

# Multidimensional Electron Imaging of Catalyst Layer Materials

Présentée le 19 juin 2023

Faculté des sciences et techniques de l'ingénieur  
Laboratoire pour la caractérisation in situ des nanomatériaux par des électrons  
Programme doctoral en science et génie des matériaux

pour l'obtention du grade de Docteur ès Sciences

par

## **Robin Pierre Alain GIROD**

Acceptée sur proposition du jury

Dr A. Hessler-Wyser, présidente du jury  
Prof. V. Tileli, directrice de thèse  
Prof. S. Bals, rapporteuse  
Dr D. Cullen, rapporteur  
Prof. C. Hébert, rapporteuse





*There is another world but it is in this one*  
*Il y a un autre monde mais il est dans celui-ci*

▪ Ignaz-Vitalis Troxler



# Acknowledgements

The making of this thesis would have been very different, a lot less joyful or quite simply impossible without the help, guidance and support of many people to whom I owe my deepest gratitude.

First and foremost I want to say the biggest thanks to Vaso, who has made it possible for me to study, live and grow in such an exceptional environment. As I get close to 6 years of coming to the INE offices and lab first weekly then (mostly) daily, it becomes clear that the trust she placed in me all these years ago for a semester project, then an internship and finally the PhD studies has shaped for the better a very significant part of my life. Her advice and mentoring have supported me in too many ways to be expressed concisely and I will carry that with me for a long time.

To say working with everyone at INE was a blessing is an understatement. It is genuinely hard to imagine a group that can go for so long without an ounce of friction and where everyone is always open for discussion with the friendliest, most welcoming and supportive behaviour. Michele, Tzu-Hsien, Reinis, Jing, Jan, Martina, Morgan, Salta, Pierpaolo, Saul and Liza: thank you, you are amazing!

I have been immensely lucky to collaborate with remarkable people within our Sinergia project and I owe a big thank you to Secil, Anne, Juan, Jens, Felix, Kinanti, Meriem and Jeremy. Special thanks go to Timon and Hubert for our fascinating discussions and for being kind enough to always put up with our demands of different samples and materials.

This work couldn't have been done without the CIME team who keep the microscopes up and running and my technical questions answered. To Davide, Victor, Marco, Fabienne, Colette and Danièle: thank you!

I have been so lucky to meet friends in Lausanne who have had no small part in keeping my morale up during these years. For this, many thanks to Roger, Mathieu, Dora, Quentin, Laetitia, Aileen, Hugo, Johannes and Claudia. A very special thank you goes to a very special person whose support has been invaluable during the last mile of this thesis; Laura, thank you so much for everything you have done.

Last but definitively not least, I want to say a heartfelt thank you to my family and especially my parents for nurturing my curiosity and my appetite for science and for their unconditional support all along.

Robin

Lausanne, May 2023

# Résumé

Les piles à combustible à membranes échangeuses de protons (PEMFC) sont une technologie prometteuse pour un futur énergétique bas-carbone au sein duquel elles pourraient permettre une mobilité lourde (camions, bus) décarbonée. Néanmoins, leur efficacité et durée de vie demeurent actuellement limitées. Ces pertes de performance trouvent en grande partie leur origine au sein de la couche catalytique (CL) cathodique où s'opère la réduction de l'oxygène (ORR), une réaction chimique clé du système. La structure nanométrique de cette couche est en effet directement liée aux flux de réactifs vers les sites catalytiques, et influe également l'évolution des catalyseurs en phase opératoire. Comprendre cette structure et celles des nanomatériaux qui la composent est donc primordiale pour la création de piles nouvelles générations.

Cette thèse a ainsi pour but d'étudier la morphologie de ces CL ainsi que celle de leurs composants à l'échelle nanométrique grâce à la microscopie électronique en transmission (MET). L'attention est portée spécifiquement sur les systèmes de CL classiques, contenant des catalyseurs Pt dispersés sur des supports carbonés poreux à grande surface et un réseau d'ionomère tétrafluoroéthylène sulfonaté. Dans un premier temps, la tomographie électronique (ET) à température cryogénique est utilisée pour obtenir une information en trois-dimensions (3D) de la structure préservée de CLs. En particulier, la préparation d'échantillon et l'acquisition de données sont optimisées afin d'éviter la majeure partie des dégâts habituellement induits par le faisceau d'électrons. En mobilisant des réseaux de neurones profonds pour le traitement d'image, une reconstruction segmentée est obtenue au sein de laquelle chaque composant et leurs interactions peuvent être analysés. Les résultats révèlent pour la première fois la complexité du réseau d'ionomère à l'échelle nanométrique. De larges hétérogénéités d'épaisseurs sont observées au sein d'un réseau par ailleurs interconnecté et continu. De plus, le réseau couvre la majorité de la surface externe des carbonés et connecte ainsi presque tous les catalyseurs Pt externes. A terme, l'utilisation de cette méthode pourra permettre des analyses fines des modifications structurelles résultant d'optimisations des CLs, par exemple par fonctionnalisation de surface des carbonés.

Afin de révéler plus en détail la structure interne des supports carbonés, une méthode de préparation d'échantillon améliorée utilisant l'électropolissage est ensuite mise au point. Celle-

ci permet la rotation complète de l'échantillon dans le microscope et ainsi l'acquisition et la reconstruction tomographique de volumes en haute résolution. Avec une résolution de l'ordre du demi-nanomètre, ces reconstructions révèlent l'intégralité du réseau de pores internes des carbones. De larges mésopores y sont observés, séparés entre eux par des quelques couches graphitiques seulement. Ces mésopores sont localisés au centre des particules de carbones seulement et sont entourés par des couches graphitiques épaisses et compactes. Au sein de ces dernières de rares micropores de diamètre inférieur au nanomètre assure la connexion entre les pores internes et externes et limite vraisemblablement la diffusion des réactifs vers le centre des carbones. Ces résultats indiquent ainsi que des supports améliorés pourraient viser une plus large mesoporosité interne tout en minimisant l'épaisseur de la couche compacte externe.

Ces analyses révèlent la structure des CL et des carbones à un temps donné seulement, mais une information en temps réel et en conditions opératoires est également d'une importance considérable pour comprendre les mécanismes de dégradations des performances des PEMFC. Afin de réaliser cet objectif, des avancées méthodologiques utilisant le MET électrochimique en phase liquide (ec-LPTEM) sont enfin présentées dans la dernière partie de cette thèse. En particulier, des méthodes pour la mesure précise des potentiels au sein du microscope ainsi que pour des acquisitions à haute résolution et faible influence du faisceau d'électrons sont proposées.

Dans l'ensemble, les avancées réalisées dans cette thèse offrent une meilleure représentation de la structure 3D des CL et de leurs composants au sein des PEMFC, ainsi que des stratégies d'améliorations pour permettre leurs analyses en conditions *operando* et à l'échelle nanométrique. Les méthodes et résultats présentées ici supportent ainsi directement le développement des prochaines générations de PEMFC.

**Mots clés :** pile à hydrogène à membrane échangeuse de proton, couche catalytique, électrocatalyseur, ionomère, support carbone, microscope électronique en transmission, tomographie électronique, cryo-microscopie, microscopie électronique électrochimique en phase liquide, traitement d'image, débruitement, segmentation.

# Abstract

The proton exchange membrane fuel cell (PEMFC) is an important technology for clean power generation in a decarbonized hydrogen system and is notably envisioned for applications in heavy-duty transportation. However, for cost and performance competitiveness, improvements are still required in efficiency and durability. Optimization of the complex structure of multicomponent cathode catalyst layers (CL), where the oxygen reduction reaction (ORR) takes place, is a promising strategy to conciliate low mass transport resistances, high kinetics, and good performance retention. Yet, much of the morphology of this layer remains poorly known. This includes the interactions of the ionomer network, the nature of the micropores, the influence of the porosity on performance losses and calls for advances in characterization of the CLs at the nanoscale.

In this thesis, I used advanced transmission electron microscopy (TEM) methods to study these questions in CLs fabricated with Pt nanocatalysts dispersed on (porous) carbon supports and perfluorinated sulfonate acid ionomers. Electron tomography (ET) at cryogenic temperature was first used to gain three-dimensional (3D) insights into the preserved morphology of intact CLs. By operating at a low electron dose and using advanced image processing methods for denoising and segmentation, accurate volumetric reconstruction with limited electron beam-induced degradation was achieved. The results reveal the intricacy of the ionomer morphology at the nanoscale and show that this is a highly continuous network with remarkable thickness heterogeneities which, furthermore, connects all Pt catalysts at the surface of the supports. Next, to gain further insights into the interior microporosity of the carbon supports, a sample preparation method enabling full-range, high-resolution ET was established. The reconstructions uncover typically large interior mesopores with few-layers carbon walls, separated from the external CL pores by compact carbon shells in which rare and mostly sub-nm pores are seen. Finally, to ultimately understand how this porosity influences degradation pathways in the CL, progress is detailed towards the study of Pt/C catalysts in real time with electrochemical liquid phase (ec-LP)TEM. As a whole, the knowledge gathered herein offers a more accurate 3D picture of the CL in PEMFC and pathways towards their *operando* characterization at the nanoscale. As such, this thesis shows how multidimensional TEM can aid the development of improved PEMFCs.

**Keywords:** proton exchange membrane fuel cell, catalyst layer, electrocatalyst, ionomer, porous carbon black, (scanning) transmission electron microscopy, (cryo) electron tomography, electrochemical liquid-phase transmission electron microscopy, image denoising, image segmentation, TEM, STEM, ET, ec-LPTM, PEMFC, CL.



# Content

<b>Acknowledgements</b>	<b>i</b>
<b>Résumé</b>	<b>iii</b>
<b>Abstract</b>	<b>v</b>
<b>1 Introduction</b>	<b>1</b>
<b>2 Background</b>	<b>5</b>
2.1 CL components .....	5
2.1.1 Metallic nanocatalysts .....	5
2.1.2 Carbon supports .....	7
2.1.3 Ionomer .....	9
2.1.4 Integrated architecture and interactions within catalyst layers .....	11
2.1.5 Degradation pathways of carbon-supported catalysts .....	13
2.2 Methods for characterizing the morphology of CL materials .....	14
2.2.1 Gas sorption and electrochemical methods .....	15
2.2.2 X-rays-based imaging techniques .....	16
2.2.3 Atomic force microscopy .....	18
2.2.4 Scanning electron microscopy techniques .....	18
2.2.5 Transmission electron microscopy techniques .....	19
2.3 <i>in situ</i> TEM to probe electrocatalysts degradation .....	24
<b>3 Methodology and Instrumentation</b>	<b>26</b>
3.1 (Scanning) Transmission Electron Microscopy .....	26
3.1.1 Principle and modes of operation .....	26
3.1.2 Contrast in the (S)TEM .....	27
3.1.3 Instrumental resolution .....	29
3.1.4 Beam-induced damage and mitigation strategies .....	30
3.1.5 TEM at cryogenic temperatures .....	31
3.1.6 Cameras for low-dose TEM imaging .....	32
3.1.7 Dose limited resolution .....	33
3.2 Electron tomography .....	33
3.2.1 Fundamental aspects .....	34
3.2.2 Projection in the TEM .....	34
3.2.3 Tilt-series geometry .....	35
3.2.4 Aligning tilt-series .....	36
3.2.5 Algorithms for 3D reconstructions .....	38
3.2.6 Resolution in ET .....	41
3.3 Image processing and analysis .....	42
3.3.1 Methods for denoising .....	43
3.3.2 Metrics of denoising performance .....	47
3.3.3 Methods for segmentation .....	48
3.3.4 Metrics of segmentation performance .....	49
<b>4 Three-dimensional Nanoimaging of Fuel Cell Catalyst Layers</b>	<b>51</b>
4.1 Abstract .....	51
4.2 Introduction .....	51

4.3	Materials and methods.....	53
4.3.1	Materials .....	53
4.3.2	Sample preparation for electron microscopy .....	53
4.3.3	Radiation damage evaluation and tilt-series acquisition.....	53
4.3.4	Tomography reconstruction and image processing .....	54
4.3.5	Resolution estimation .....	56
4.3.6	Data analysis.....	56
4.3.7	EDS analysis.....	56
4.3.8	Electrochemical measurements .....	57
4.4	Results .....	57
4.4.1	Cryo-electron tomography of catalyst layer aggregates .....	57
4.4.2	Structure of catalyst layers.....	61
4.4.3	Discussion.....	66
<b>5</b>	<b>Microporosity in High Surface Area Carbons</b>	<b>67</b>
5.1	Introduction .....	67
5.2	Materials and methods.....	69
5.2.1	Materials .....	69
5.2.2	Sample preparation for electron microscopy .....	69
5.2.3	Electron microscopy imaging .....	70
5.2.4	Tomography acquisition and reconstruction.....	70
5.2.5	3D segmentation and pore size analysis .....	71
5.3	Results .....	71
5.3.1	Heterogeneous morphology of primary aggregates in KB .....	71
5.3.2	Full-range electron tomography for Pt/C catalysts.....	73
5.3.3	Microstructure and micropores in KB supports.....	75
5.4	Discussion .....	79
5.5	Conclusions .....	82
<b>6</b>	<b>Towards High-Resolution <i>operando</i> Studies of Pt/C Catalysts with LPTEM</b>	<b>84</b>
6.1	Introduction .....	84
6.2	Materials and methods.....	86
6.2.1	Materials .....	86
6.2.2	ec-LPTEM and open-cell apparatus .....	86
6.2.3	Inert potential window measurements .....	86
6.2.4	Pd-H RE loading and testing .....	87
6.2.5	Electron microscopy imaging .....	87
6.2.6	<i>in situ</i> (S)TEM experiments.....	87
6.2.7	Data processing.....	88
6.3	Results and discussion.....	88
6.3.1	Electrodes for electrocatalytic measurements in microcells.....	88
6.3.2	Potential-induced dissolution of Pt nanocubes .....	95
6.3.3	Towards <i>in situ</i> imaging of Pt/C catalysts .....	97
6.4	Conclusions .....	98
<b>7</b>	<b>Conclusions and Outlook</b>	<b>99</b>
<b>A</b>	<b>Operational considerations for ET</b>	<b>103</b>
<b>B</b>	<b>Supplementary Information for Chapter 4</b>	<b>104</b>
<b>C</b>	<b>Supplementary Information for Chapter 5</b>	<b>121</b>
<b>D</b>	<b>Supplementary Information for Chapter 6</b>	<b>127</b>
	<b>Bibliography</b>	<b>134</b>
	<b>Curriculum Vitae</b>	<b>157</b>





# 1 Introduction

An unprecedented transition away from our carbon-intensive energy system is necessary to conciliate the energy needs of wellbeing<sup>1-3</sup> and the environmental envelope of a safe society in a warming world<sup>4,5</sup>. This calls for behavioural changes to reduce demand and technological shifts to offer credible alternatives to fossil fuels in hard-to-decarbonize sectors<sup>6,7</sup>. For the case of long-distance transport, fuel cells (FC) powered with green hydrogen are capable of providing an environmentally sustainable alternative to combustion engines<sup>8-10</sup>. However, developments are still needed for hydrogen-based technologies to become competitive and reach broad rollout.

Specifically, this thesis focuses on the proton exchange membrane (PEM)FC, which is the incumbent technology for converting hydrogen back to electricity in transport applications. Fundamentally, PEMFCs are electrochemical cells in which hydrogen is oxidized at an anode electrode in the hydrogen oxidation reaction (HOR), while the oxygen reduction reaction (ORR) takes place at the cathode<sup>11</sup>. In the acidic environment of the PEMFC, the half-cell reactions are  $\text{H}_2 \rightarrow 2\text{H}^+ + 2\text{e}^-$  (standard electrode potential  $E^0 = 0$  V vs. the reversible hydrogen electrode - RHE) at the anode, and  $\text{O}_2 + 4\text{H}^+ + 4\text{e}^- \rightarrow 2\text{H}_2\text{O}$  ( $E^0 = 1.23$  V vs. RHE) at the cathode. To balance the cell equation, protons must diffuse from one electrode to the other while electrons transfer through an electrical circuit, powering a load. To this end, PEMFC devices use a stacked assembly of gas diffusion electrodes (GDE) surrounding a polymer electrolyte membrane through which the proton transport occurs<sup>12</sup>, as depicted in Fig. 1.1. In addition, bipolar plates with gas flow channels compress this membrane electrode assembly (MEA), distribute gases evenly to the GDEs, and evacuate water and unreacted gases.

The efficiency of PEMFC devices is limited by three main contributions: 1) ohmic losses from contact resistances, 2) mass transport limitations at high current densities, 3) kinetic limitations due to the sluggish 4 electrons process of the ORR and resulting overpotential ( $\eta$ , the difference between the effective and thermodynamical electrode potential)<sup>11,13</sup>. To mitigate this third contribution and accelerate the reaction, scarce and precious metal catalysts from the platinum group (PGM) are typically employed, as they exhibit the best activity performance among pure metals<sup>14,15</sup>. As a result, the cathode catalyst layer (CL), where the ORR takes place, concentrates a major part of the cost of PEMFCs<sup>16</sup> and research efforts have sought to find competitive PGM-

free catalysts and to maximize the utilization of PGM ones<sup>17,18</sup>. As schematically depicted in Fig. 1.1, the industry standard CL now features Pt nanocatalysts (occasionally alloyed) dispersed on high surface area carbons. These Pt/C aggregates are interconnected by an ionomer network that efficiently conducts and distributes protons throughout the layer<sup>19</sup>. The interplay between these three central components strongly affects the structure of the CL from the local reactive site to the bulk scale and, in turn, the kinetics and the transport of reactant and products<sup>19–23</sup>.

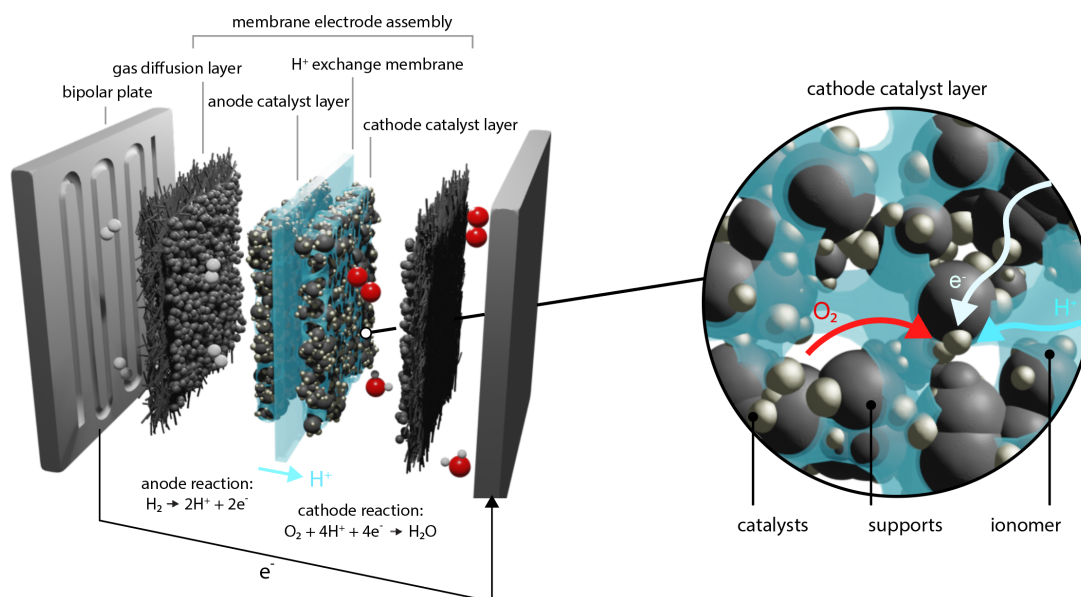


Fig. 1.1: Illustration of the PEMFC components and reactions and zoom-in depicting the morphology and reactant transport towards a reactive site in the cathode catalyst layer.

The fundamental understanding of these structure-performance relationships is key to designing the next generation of CLs with better kinetics, high-current performance and durability and enabling their widespread adoption. The task critically hinges on the ability of nanoanalytical tools to provide an accurate picture of the morphology of each component, and of their interactions, ideally during operation and across the lifetime of the FC. However, the intricacy of the CL and the dynamic nature of the events of interest renders characterization challenging.

As a platform hosting tomography and *in situ* capabilities, the transmission electron microscope (TEM) is a remarkably versatile instrument that allows to characterize materials at the nanoscale, in three-dimensions (3D) and under a variety of stimuli, including electrochemical biasing. In addition, novel, more sensitive, and faster cameras aided by ever-improving image processing algorithms now enable to probe into dynamic and fragile systems with limited observation-induced interference. Thus, the instrument appears particularly suited to characterize the delicate CL.

In this thesis, electron tomography (ET) and *in situ* TEM are used to provide detailed and accurate insights into the standard Pt/C-ionomer system. In particular, the complete morphology of the CL and of the interior porosity of the carbon supports is reported and progress is made toward the accurate biasing and imaging of Pt/C with electrochemical liquid phase (ec-LP) TEM.

Specifically, **chapter 2** details the components of the CL studied herein, with an emphasis on previous studies concerning their interactions and the resulting structures, and on strategies leveraged in recent years for improved performance. A review of the methodologies used in the literature to characterize the CL architecture and the morphology of its components at various scales follows. The focus is also brought on the degradation pathways of Pt/C catalysts and on *in situ* TEM studies of these materials under electrochemical stimuli.

**Chapter 3** describes the instrumentation and techniques I used to gain insights into CL materials. The TEM instrument is presented, along with the factors governing the resolution of the obtained images and the interactions of the highly energetic electron beam with the specimen. The principle of ET and the workflow for tilt-series acquisition and 3D reconstruction are then described. Finally, an overview of the methodology used herein for image denoising and segmentation is given.

**Chapter 4** presents an investigation of the morphology of CL samples with cryo-ET. The reconstructions obtained with limited electron beam-induced damage allow us to identify all the components, including the fragile and beam-sensitive ionomer network preserved by preparation with microtomy. Properties of the ionomer network and its interactions with the carbon supports and the Pt nanocatalysts are then investigated. In particular, large thickness heterogeneities and high continuity are found in the ionomer network that is additionally seen to cover most of the available carbon surface, while most external Pt particles are found to be connected to the network.

**Chapter 5** dives in more detail into the morphology of the porous carbon supports. A methodology for full-range tomography is described, which allows for 3D reconstruction with sub-nm resolution of the interior micropores. The results reveal a complex morphology created by carbon planes arranged concentrically with sub-nm constrictions between the interior and exterior space, which comes in contrast with conventional, cylindrical-like, porosity models.

Expanding in the temporal dimension, **chapter 6** details the methodological progress made towards accurately biasing and imaging Pt/C catalysts with ec-LP TEM. Considerations are first given to the choice of working and reference electrodes for providing accurate potential measurements, low background interference, and good contrast. Electrochemical conditions to trigger Pt degradation are then explored and used on a model catalyst to show that these events

---

can be monitored with ec-LP TEM. Finally, methods for denoising time-series acquired at low electron dose as obtained in ec-LP TEM are compared.

Finally, in **chapter 7**, I summarize the results of my thesis and offer some directions for future work involving ET and ec-LP TEM for investigating PEMFC catalyst layers and their components.



## 2 Background

This chapter begins with an introduction of the metallic nanoparticles-carbon supports-ionomer network as the typical components of catalyst layers and provides a brief review of recent developments in each toward high-performance PEMFCs. The current knowledge about their interactions, the resulting catalyst layer architecture, and how these are related to performance loss is then discussed. Finally, methods for characterizing the morphology of the catalyst layer and of the components within are reviewed, with an emphasis on studies that have leveraged the TEM and specifically ET and ec-LPTM techniques.

### 2.1 CL components

In this section, the conventional catalyst layer is presented in detail. The focus is placed on metallic nanocatalysts, supports based on carbon blacks, and perfluorinated sulfonic acid (PFSA) ionomers. Discussion on the large variety of alternative approaches for ORR catalysts (e.g., PGM-free<sup>18,24</sup> ones), catalyst supports (e.g., order-structured carbons<sup>25,26</sup> and non-carbon<sup>27</sup>) and ionomers (e.g., hydrocarbon-based<sup>28</sup>) is omitted.

#### 2.1.1 Metallic nanocatalysts

At the core of the conventional CL, metallic nanocatalysts enable good efficiencies at the device level by accelerating the reactions at both electrodes. The half-cell cathode-side ORR is a sluggish reaction suffering from high overpotential and has therefore been the focus of many studies seeking to improve PEMFC performance. Platinum is the single most active pure metal<sup>14,15</sup>, but its scarcity makes it a constraining factor of the CL price, even with predicted economies of scale<sup>20</sup>. As a result, much work has been dedicated to reducing the quantity of Pt required to meet performance targets. As far as the catalyst is concerned, strategies towards these high-performance and low-Pt catalyst layers have involved two interrelated pathways to increase the mass activity<sup>29</sup>: increasing the number of active sites with extended surface area, and increasing the site-specific activity of the catalysts.

Tuning the electrochemical surface area (ECSA) has long been recognized as a prominent strategy to readily increase the number of active sites, leading to the inception of Pt nanocatalysts, a few nm in diameter, typically supported on high surface carbons (Pt/C)<sup>23</sup>. Fig.

## 2.1 CL components

2.1a shows a secondary electrons (SE) scanning (S)TEM image of such standard catalysts, demonstrating the benefit of the support for their dispersion. These catalysts typically feature high surface area, in the order of 80-120 m<sup>2</sup>/g<sub>Pt</sub>, but exhibit limited specific activities that result in mass activities benchmarked around 0.2 A/mg<sub>Pt</sub> at 0.9 V in rotating disk electrode (RDE) measurements<sup>30,31</sup>. As shown in Fig. 2.1e, recent improvements of orders of magnitude have been achieved following materials-by-design approaches that aim at optimizing the adsorption of key, oxygen-containing, reaction intermediates. The specific activity has for instance been shown to depend on the exposed surface facet and the local electronic structure, leading to a variety of nanostructuring approaches<sup>32</sup>. For instance, core-shell NPs and nanoplates<sup>33</sup> (Fig. 2.1b), octahedra<sup>34</sup>, nanowires<sup>35</sup> (NWs, Fig. 2.1c), and nanoframes<sup>36</sup> (Fig. 2.1d) have been demonstrated with upwards of a 20-fold increase in mass activity, and state-of-the-art performance towering at 13.6 A/mg<sub>Pt</sub> (ref.<sup>35</sup>).

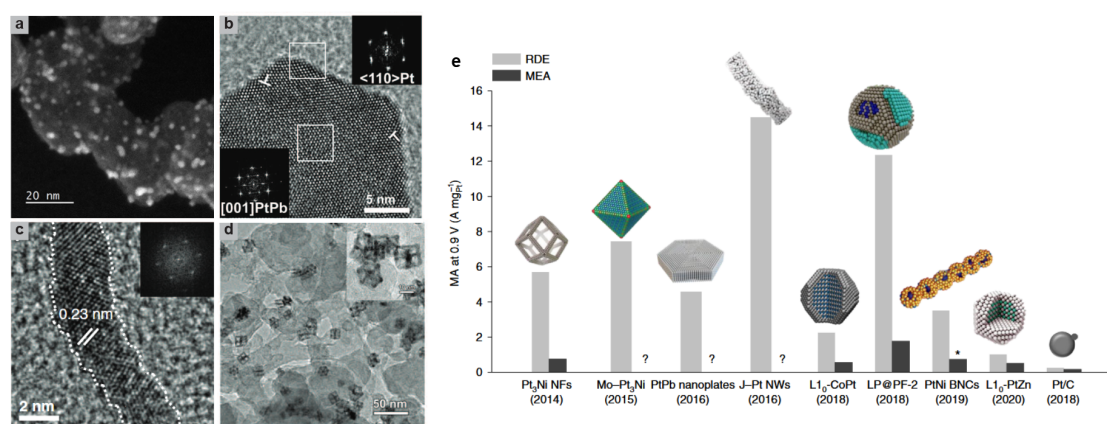


Fig. 2.1: Advanced catalysts for ORR. **a**, representative STEM-SE image of a standard Pt/C catalyst, here commercial TEC10E50, TKK. **b**, high resolution (HR)TEM image of a PtPb/Pt core/shell nanoplate. **c**, HRTEM image of performance-leading ultrafine jagged Pt nanowires (NWs). **d**, bright-field (BF)-TEM images of the intricate and high-performance PtNi<sub>3</sub> nanoframes with Pt-skin surface supported on carbon. **e**) performance of state-of-the-art catalysts against industry standard Pt/C high-performance metallic nanocatalysts. Panels reproduced with permission from: **a**, ref.<sup>37</sup>, ACS; **b**, ref.<sup>33</sup>, AAAS; **c**, ref.<sup>35</sup>, AAAS; **d**, ref.<sup>36</sup>, AAAS; **e**, ref.<sup>20</sup>, Springer Nature.

It is noteworthy that in most cases the performance of these tailored nanostructures is reported from rotating disk electrode (RDE) measurements and hardly transfer to membrane electrode assemblies (MEA, Fig. 2.1e) whose operating conditions differ drastically<sup>12,22,38</sup>. This discrepancy is partly linked to the reactant transport regimes because oxygen diffusion fluxes in RDE measurements limit the current to a few mA.cm<sup>-2</sup> at most, about 2-3 orders of magnitude lower than in MEAs. In addition, low catalyst loading has been shown to result in a comparatively increased importance of the ECSA against the specific activity. This is because below a certain number of reactive sites, the bottleneck comes from limited local oxygen

fluxes<sup>17</sup>. Finally, interactions with the ionomer and the supports further modify the local environment of the catalysts and will be discussed in more detail in Section 2.1.4.

### 2.1.2 Carbon supports

Catalyst supports provide an extended conductive surface on which the nanoparticles are deposited. They are a fundamental component of the catalyst layers that influence the nanocatalysts' size, distribution, durability and performance but also shape the layer's macro-, meso- and micro-porosity and thus reactant transports. Conventional carbon supports are based on carbon blacks (CB) which are turbostratic carbon nanoparticles of diameter 10-100 nm synthesized via pyrolysis of gaseous hydrocarbon precursors<sup>39</sup>. The process typically creates shells of non-graphitizable (i.e., with d-spacing > 0.335 nm due to mismatched stacking) carbon sheets concentrically arranged around a more disordered and porous core<sup>40</sup>. During production, primary nanoparticles with varying sizes coalesce and create extended fused aggregates whose characteristics of fineness (the primary particle size), structure (aggregate size and shape<sup>41,42</sup>), porosity and surface chemistry dictate the properties and potential applications of the final black<sup>43,44</sup>. Fig. 2.2a and b show the primary particle size distribution and a typical CB aggregate, demonstrating the range of particle size obtained in the synthesis process. In addition, blacks can be heat-treated to obtain “graphitized” particles by converting the originally disordered microstructure (Fig. 2.2c) to highly ordered turbostratic planes (Fig. 2.2d).

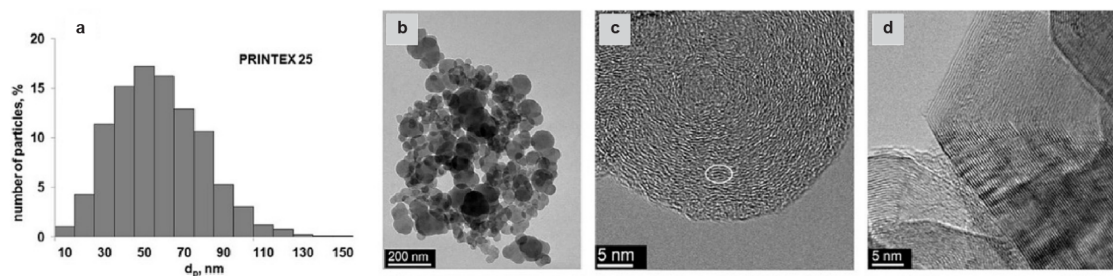


Fig. 2.2: Carbon black morphologies. **a**, particle size distribution and **d**, representative TEM image of a typical CB aggregate, here, commercial Printex 25. **c**, HRTEM image of regular and **d**, graphitized (heat-treatment in Ar and at 2600°C) carbon blacks. Panels reproduced with permission from ref.<sup>42</sup>, Elsevier.

Despite decades of research in various application fields, the exact microstructure and the origin of the porosity in carbon blacks remain uncertain<sup>44</sup>. Models and observations from x-ray diffraction (XRD) and high-resolution (HR-)TEM concord to say that non-graphitized blacks are formed of basic structural units (BSU), themselves a stack of short and misaligned carbon sheets, arranged around a more disordered core<sup>42,45</sup>. The internal microporosity would therefore arise from the random packing of BSUs in the core, as well as from mismatch at the edges in the shells, leaving gaps and channels between them. Another factor could be the presence of

## 2.1 CL components

odd-membered, non-hexagonal, carbon rings in the graphitic sheets, as reported from HR-TEM observation<sup>46</sup>. Simulations have shown that these defects lead to buckling and ripples in graphene sheets, which would translate to pore openings in the carbon blacks<sup>46-48</sup>. Nevertheless, the well-known presence of large mesopores in some blacks, sometimes up to tens of nm large, remains unexplained by these theories. As illustrated in Fig. 2.3a, the combination of the primary internal micro-/meso-pores and secondary pores between particles, agglomerates and aggregates results in a complex structure with hierarchical porosity over scales spanning two orders of magnitude.

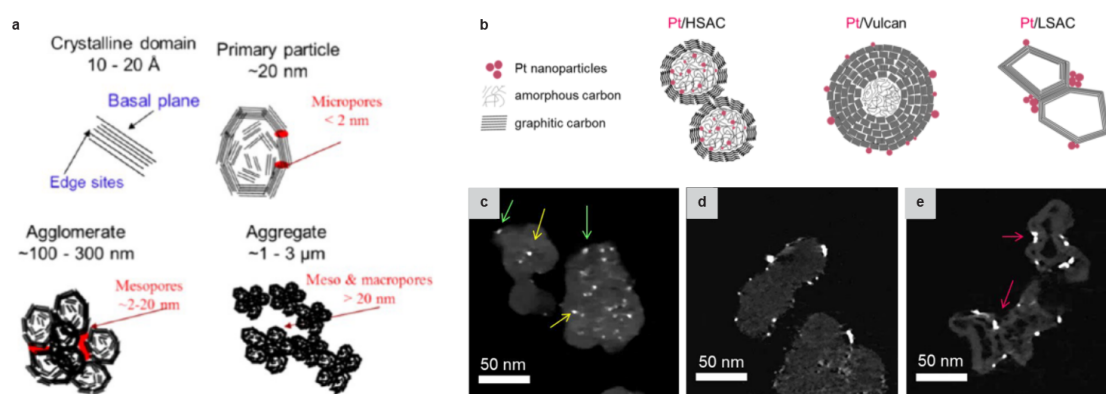


Fig. 2.3: Carbon supports for CL in PEMFC. **a**, Illustration of the hierarchical porous structure of carbon blacks. **b**, Depiction of the microstructure of a high surface area carbon (HSAC, here a Ketjenblack), Vulcan and low surface area carbon (LSAC, here a graphitized Ketjenblack), and **c-d**, corresponding tomograms from reconstructions of these carbons loaded with 20 wt% Pt demonstrating the localization of NPs as a function of the microstructure. Panels reproduced or adapted with permission from: **a**, ref.<sup>23</sup>, ACS; **b-e**, ref.<sup>49</sup>, ACS.

The most common blacks used in PEMFCs are Vulcans, Ketjenblacks, and graphitized versions of these. An illustration of their respective microstructure is shown in Fig. 2.3c. Vulcans are furnace blacks, produced by the pyrolysis of atomized aromatic oils, with primary particle size around 30 nm and low interior porosity that result in a specific surface area (SSA) in the range 200-250 m<sup>2</sup>/g (ref.<sup>49</sup>). They have been the historical choice for catalyst layers but suffer from corrosion at the high potentials > 1.0 V that can arise during start up-shut down (SUSD) of the cell. In addition, catalysts are mostly hosted at their surface (as seen in Fig. 2.3b and d) which can lead to mobility and coalescence over the course of the PEMFC lifetime and thus ECSA loss, as further discussed in Section 2.1.5. Lower catalyst mobility can be achieved using supports with higher porosity, a typical example being Ketjenblacks (KB). These carbons are obtained by pyrolysis of acetylene fluxes and possess a large SSA of around 600-1200 m<sup>2</sup>/g (ref.<sup>40,50</sup>). The large interior mesoporosity of these carbons from which the extremely high SSA originates has long been known from TEM images and mercury porosimetry measurements<sup>40</sup>, and offers interior sites to host NPs as shown in Fig. 2.3b and c. Alternatively, corrosion

resistance can be offered by graphitizing these but involves drawbacks: the inner porosity is lost during carbon plane rearrangement so that the SSA drops to around 150 m<sup>2</sup>/g and the greater hydrophobicity of the surface results in aggregation of both ionomer and Pt nanoparticles (demonstrated in Fig. 2.3b and e)<sup>49,51,52</sup>. The choice of carbon supports thus entails tradeoffs and strategies for optimization are further detailed in Section 2.1.4.

### 2.1.3 Ionomer

Ionomers are polymers with ion-conductive properties offered by ionic groups incorporated in their backbone or side chains. In PEMFCs, they allow protons to diffuse between the electrodes through the proton exchange membrane (PEM) and in the CL by forming a network of thin films and strands that cover and connect Pt/C catalysts. The standard ionomers in PEMFCs are perfluorinated sulfonic acids (PFSA). These are random copolymers with a polytetrafluoroethylene (PTFE) backbone onto which side-chains are grafted and terminated with a sulfonic acid SO<sub>3</sub><sup>-</sup> group associated with a specific cation, typically H<sup>+</sup>. The density and length of these side chains define the parameter space to modify the chemical structure of the ionomer and, in turn, their ion-conductivity and chemical-mechanical properties<sup>23</sup>. A range of commercialized chemistries is shown in Fig. 2.4a, with the trademarked Nafion being the historical representative of this class and still prominently used in PEMFCs. The coexistence of the hydrophobic backbone and hydrophilic ionic groups results in phase separation as depicted in Fig. 2.4b, which provides PFSA with their solvation capabilities and ionic transport properties. The sulfonic acid group concentration in ionomers is described by the equivalent weight (EW), defined as the mass of dried ionomer per sulfonic group in g<sub>polymer</sub>/mol<sub>sulfonic-group</sub>, and dictates the morphology of the phase separation.

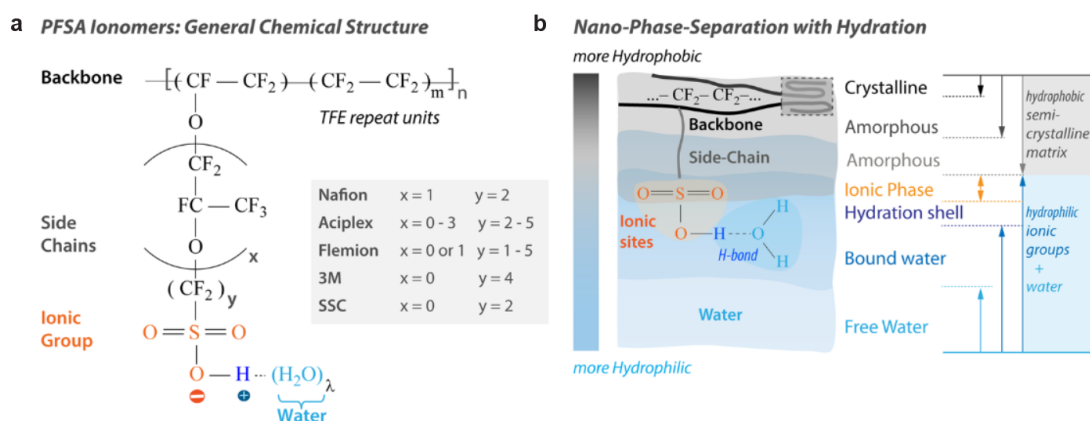


Fig. 2.4: Structure of ionomers. **a**, chemical structure of PFSA ionomers and **b**, illustration of the phase separation resulting from the physical properties of the side chains, ionic groups, and PTFE backbone of PFSA ionomers. Panels reproduced with permission from ref.<sup>53</sup> under a Creative Commons license.

## 2.1 CL components

PEMFC CLs are often fabricated by casting catalyst inks, and therefore the behaviour of PFSA ionomers in solution has long been of interest. A range of morphologies have been found, depending principally on the dielectric constant of the solvent. While ionomers are solvated in apolar organic solvents with  $\epsilon > 10$ , they aggregate in colloidal structures in solvents with  $3 < \epsilon < 10$  and precipitate when  $\epsilon < 3$ <sup>23,54</sup>. It has been proposed from small angle neutron scattering (SANS) measurements that cylindrical structures are formed in polar solvents, with radius  $\sim 2$ - $3$  nm and length  $\sim 20$  nm<sup>55,56</sup>, or that secondary swollen aggregates can form in aqueous environments<sup>57</sup>. It remains unclear to what extent these morphologies in solution are linked to the morphology of the ionomer network in the CL. How these may in turn influence the PEMFC performance is still a matter of ongoing research<sup>23</sup>.

In addition, the nano-morphology and properties of the ionomer network depend strongly on substrate and confinement effects. As shown in Fig. 2.5a and c, experiments with grazing incidence small angle x-ray scattering (GISAXS)<sup>58</sup> and energy-filtered (EF) cryo-TEM<sup>59</sup> have demonstrated that phase separation is lost when ionomer films are confined below 10-20 nm. This bears implications for proton and oxygen transport, which are decreased in such ultra-thin films<sup>53</sup>, as transport is otherwise thought to proceed through water domains in bulk membranes. In addition, the hydrophilicity of the substrate also impacts the conformation of the ionomer chains and side groups, with again exacerbated effects for thin-films where the interaction length is on the scale of the total film thickness (Fig. 2.5b and c). For instance, contact angle reversal in films below 100 nm suggested that the side chains can point inwards or outwards depending on their interactions with the substrate<sup>53</sup>.

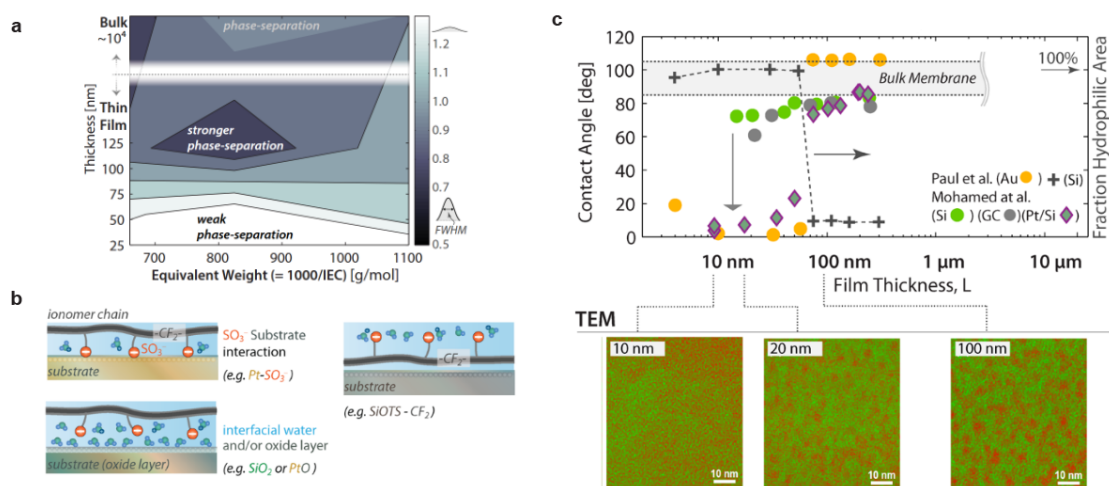


Fig. 2.5: Confinement and substrate effects on ionomer films. **a**, degree of phase separation estimated from the broadening of the ionomer peak in GISAXS measurements as a function of ionomer EW and film thickness. **b**, illustration of the ionomer interactions in the vicinity of the substrate and **c**, contact angle measurements on ionomer thin films of decreasing thickness and various substrates. EF-TEM images demonstrate the loss of phase separation in the 10-20 nm



range. Panels reproduced or adapted with permission from: **a**, ref.<sup>58</sup>, Wiley; **b-c**, ref.<sup>53</sup>, under a Creative Common license; TEM data in **c**, ref.<sup>59</sup>, ACS.

#### 2.1.4 Integrated architecture and interactions within catalyst layers

CLs are fabricated by casting from a catalyst ink, either by roll printing or spray coating<sup>60</sup>. Based on numerous studies that leveraged nano-computed tomography (nCT), SAXS, mercury porosimetry, and TEM imaging data, the resulting structure is known to exhibit hierarchical porosity with large secondary pores, up to  $\mu\text{m}$  large, formed between Pt/C-ionomer secondary aggregates. Within these, primary pores are defined by the carbon support primary particles and their interior. The ionomer network binds these aggregates together and partially fills the pores<sup>61</sup>. The overall homogeneity of this structure depends on the ink formulation, that is, the choice of each component (catalyst, supports and ionomer) but also on the dispersion medium. An ideal CL would exhibit high mass transport of gases, high proton conductivity, low water retention and would minimize resistances at the local catalyst site, in the bulk of the CL and at the MEA interfaces<sup>12</sup>. However, each of these parameters is affected by the choice of the components whose relationships and interactions make the optimization of the CLs' structure a complex task.

For instance, Pt-ionomer proximity is necessary to ensure that protons can reach the reactive sites at the so-called three-phases interface. However, the sulfonic acid groups of PFSA ionomer are known to bind preferentially to the hydrophilic Pt surface, which reduces the available active surface and, thus, Pt mass activity<sup>62</sup>. This was demonstrated by comparing the performance in the kinetic region of 3M's nanostructured thin films (NSTF) with and without ionomer, the former exhibiting better activity<sup>17,63</sup>. This is also a key interest of porous carbon supports. In these, internal Pt nanoparticles are protected from being in direct contact with the ionomer and this has been shown to increase their specific activity<sup>62,64</sup>. Another implication of the Pt-ionomer interactions is that the change of conformation leads to a rearrangement of the ionomer backbone, making it more rigid and decreasing O<sub>2</sub> permeation rates<sup>23</sup>. This effect becomes increasingly detrimental at very low Pt loading, where limited O<sub>2</sub> fluxes across thin ionomer films have been shown to become the major contribution to non-Fickian transport resistances (nFR)<sup>17</sup>. To overcome these limitations, recent research has suggested that tuning the ionomer chemistry offers a promising avenue. For example, shorter side chains reduce the flexibility of the ionomer strands and mitigate the conformation changes that enable SO<sub>3</sub><sup>-</sup> adsorption<sup>23,65-67</sup>. Other alternatives have sought to prevent direct Pt-ionomer contact by masking the nanocatalysts, either with molecular species that were subsequently removed<sup>68</sup>, or by encapsulation with few-layer carbon shells<sup>69</sup>. Benefits in terms of local O<sub>2</sub> transport in the latter case remain however uncertain<sup>19</sup>.

Studies of the impact of the support porosity on the catalyst activity also underline that the three-phase interface is not required *per se* and that proton conduction can happen within carbon pores. CO-stripping measurements at varying relative humidity (RH) and comparison with ECSA measurements derived from ET results have further demonstrated that interior catalysts within these porous carbons participate at high RH while the ECSA decreases at lower RH<sup>50</sup>. It was hypothesized that in these dry conditions, proton conduction in the carbon pores is not ensured anymore so the protocol would grant access to the internal/external fraction of catalysts. Similar studies on various carbon supports have further confirmed that the low porosity of Vulcan and graphitized carbons lead to the majority of the catalysts residing outside of the supports<sup>49</sup>. Also, while interior particles are accessible at high RH and show enhanced activity, it was demonstrated that by varying the synthesis method and the proportion of interior vs. exterior particles, the performance at high current density is reduced due to the increased transport resistances<sup>70</sup>. These results highlight the importance of the support-Pt interactions in shaping the morphology and performance of the CLs in the various current regions, but also a conundrum of CLs with conventional carbon supports. Indeed, providing high mass transports and avoiding direct Pt-ionomer contact for high activity are often orthogonal tasks. A way forward was recently proposed in the precise tuning of the pore size. Studies have shown that a controlled and localized Pt-catalyzed oxidation of porous carbon support can lead to an increase of the pore volume in the 2-5 nm range and drastically increased mass transport but also kinetics<sup>64,71-73</sup>. Current hypotheses are that channel openings in the shell of the carbon supports are increased at an optimum point where transport resistances are reduced but ionomer still does not intrude, or that the internal tortuosity of the internal carbon micropores was reduced in the process<sup>72</sup>. However, direct visualization of these pores is lacking and the large porosity variation in KB even before modification renders statistically significant results challenging.

Furthermore, the interactions between the carbon supports and the ionomer are also defining elements of the morphology and performance of the fuel cell. For example, the degree of graphitization of the carbon support and, hence, the hydrophobicity of the surface leads to different interactions with the ionomer and different degrees of aggregation in the CL, which, in turn, influence the high current density performance<sup>51,74,75</sup>. The importance of a homogenous ionomer coverage at the local site level and in the bulk of the CL has been further demonstrated by varying the ionomer morphology in catalyst ink. Extensive studies have screened different solvent mixtures and their polarity, and the amount of Pt particle loading. The results were visualized in terms of the acidity imparted by the ionomer conformation and the aggregate size in solution<sup>76,77</sup>, in the CL<sup>75,78</sup> and ultimately in the high current performance<sup>75</sup>. While optimization of the ink formulation is a major part of the CL homogeneity, it was recently demonstrated that the surface of the carbon supports could also be chemically modified



with  $-\text{NH}_x$  groups to promote interactions with the ionomer, which resulted in lowered transport resistances<sup>79,80</sup>. This improvement is believed to arise from a more homogeneous coverage and repartition of the ionomer, however, the challenges associated with the characterization of the ionomer morphology (see Section 2.2.5) have hindered the direct visualization of this effect.

### 2.1.5 Degradation pathways of carbon-supported catalysts

The PGM-based catalysts and their supports have been known to degrade during operation in several ways, resulting in turn in marked performance decay over time. A great number of studies have been dedicated to identifying the specific pathways of performance losses, with NPs ECSA loss and carbon corrosion standing out as the two main and interrelated sources, illustrated in Fig. 2.6a.

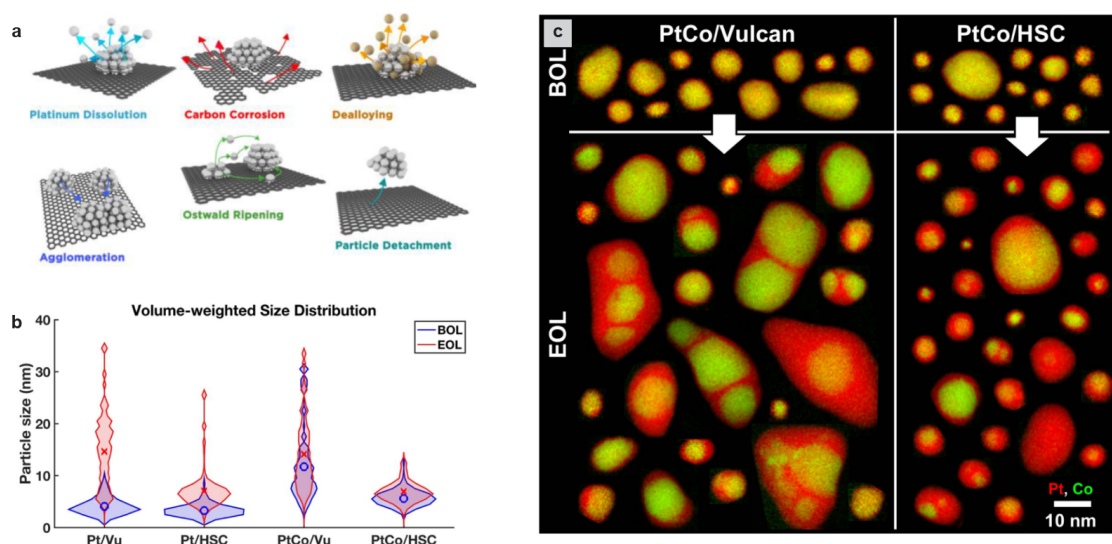


Fig. 2.6: Degradation mechanisms of Pt/C catalysts. **a**, illustration of the mechanisms of degradation for carbon-supported catalysts. **b**, Volume-weighted PSD following Pt-degradation targeted AST on Vulcan (Vu) and KB, porous carbons (HSC) and **c**, Pt and Co EELS maps of alloyed NPs at the beginning of life (BOL) and end of life (EOL) following the AST. The tailed PSD and multicore particles visualized in EELS at the EOL of the Vu-supported particles demonstrate the important of ECSA loss by coalescence. Panels reproduced with permission from: **a**, ref.<sup>81</sup>; **b** and **c**, ref.<sup>82</sup>, all under a Creative Commons license.

ECSA loss can proceed in different ways, including dissolution, coarsening and detachment of the NPs<sup>83</sup>. Dissolution can proceed either chemically or electrochemically<sup>84</sup>, in particular through cycling around the Pt oxidation potential. Electrochemical dissolution happens directly by the oxidation reaction:  $\text{Pt}^0 \rightarrow \text{Pt}^{2+} + 2e^-$ . Alternatively, an oxidized layer may form at the surface of the particles which can then be chemically dissolved or partially stripped during subsequent reduction. The Pt ions can be evacuated with the exhaust water, but also remain in the ionomer, ultimately ending in the membrane where  $\text{H}_2$  crossover chemically reduces it to form the well-known Pt-band<sup>82,83</sup>. In addition to the ECSA and therefore mass activity loss, the

resulting poisoning of the ionomer can result in increasingly high proton-transport resistances over time. Beyond Pt, NCs with multimetallic composition can also exhibit selective dissolution and dealloying, which additionally reduces the intrinsic activity over time.

Coarsening occurs as a result of two main processes, namely Ostwald ripening and coalescence<sup>82,83</sup>. The former proceeds from dissolution, whereby smaller particles preferentially dissolve owing to higher surface energy, and the generated ions are eventually redeposited on larger NPs. The process can occur in 3D with ions travelling across the electrolyte or in 2D where they would move across the carbon support. Coalescence on the other hand proceeds from mobile particles that eventually enter into contact and fuse at their interface to reduce the local curvature. Recent evidence from *in situ* and IL TEM studies<sup>85,86</sup> in combination with EELS results demonstrated that sintered alloyed particles had kept their dual core (Fig. 2.6c),<sup>82,87</sup> indicating that coalescence is a non-negligible process. In addition, the particle size distribution (PSD) is also a hallmark of the dominant mechanism, with agglomeration via ripening typically tending towards a normal distribution while coalescence events can be evidenced by a strong tailing towards larger sizes (Fig. 2.6b). Evaluating these PSD has further demonstrated that high surface area, porous, supports such as KB result in coarsening by ripening primarily, while Vulcan carbons resulted in greater NP mobility and higher occurrence of coalesced particles (Fig. 2.6b)<sup>82</sup>.

Additionally, carbon support corrosion dynamically modifies the surface the NPs reside on and can further aggravate NP mobility or directly lead to detachment<sup>83</sup>. Corrosion of carbon can electrochemically proceed above 0.207 V vs. RHE in the following reaction:  $C + H_2O \rightarrow CO_2 + 4H^+ + 4e^-$ . The operative potential range of PEMFC is typically higher but the sluggish kinetics of the corrosion reaction mean that, under regular operative conditions, the degradation is limited. However, much higher voltages can arise, for example during start-up and shut-down (SUSD), when fuel starvation and reverse current can occur<sup>88</sup> and the matter is compounded by the ability of Pt to catalyze the reaction.

## 2.2 Methods for characterizing the morphology of CL materials

The complex relationships between the interactions of the CL components and the bulk scale performance underline the need for accurate characterization methods at the nanoscale. The task is nevertheless challenged by the scale of interest, and potential heterogeneities that span over orders of magnitude in scale. Various techniques that have been applied to gain insights into the nanoscale morphology of CLs and their components are reviewed in this section.

### 2.2.1 Gas sorption and electrochemical methods

N<sub>2</sub> physisorption is used to access information on the surface area and pore size distribution of materials. The principle lies in the measure of the adsorbed volume of an inert gas on the surface of a solid maintained at cryogenic temperature (typically 77 K), at increasingly elevated pressures<sup>89</sup>. The results are  $V = f(P/P_0)$  isotherms, where  $V$  is the adsorption volume and  $P/P_0$  is the equilibrium relative pressure. Fitting the curves with models that depend on assumptions about the adsorption mechanism and the geometry and size of the pores grants access to different information about the material analyzed<sup>89</sup>. Common examples are the Brunauer-Emmett-Teller (BET) method to access the surface area and the quenched solid density functional theory (QSDFT) for pore size distribution<sup>90</sup>. The pore size distribution offers more detail and common practice is to evaluate the relative volume of micropores (< 2 nm diameter), mesopores (2-50 nm) and macropores (> 50 nm)<sup>91</sup>. Following this, the method has been used to infer the evolution of porous carbon supports upon oxidative heat treatment and revealed an increase of the microporosity in favour of the mesoporosity for the best-performing ones<sup>73</sup>. When applied to the entire CL, it was shown to provide insights on the effect on the CL morphology of the type of carbon support<sup>51,92</sup>, of the Pt and ionomer loading<sup>92,93</sup> and distribution<sup>94</sup>. By further comparing the pore distribution upon addition of catalysts and ionomer, it also allowed inferring the preferred position of Pt nanoparticles and the degree of impregnation of ionomer in micropores<sup>94</sup>.

Complementary to physisorption, an increasing number of electrochemical methods have been implemented in the past decade to probe the morphology of CLs. The common principle is the measurement of charges passed during a material-specific electrochemical reaction, which can be related to the surface area from standard values. For example, Pt ECSA measurement is often done by CO-stripping, whereby CO is allowed to adsorb onto the Pt surface and then stripped by electrooxidation<sup>95</sup>. Since the oxidation reaction requires water and a proton conduction path, measurement of the ECSA at varying RH further grants insights into the fraction of Pt surface in contact with the ionomer. Indeed, high RH conditions allow water to condensate at the surface of carbons and offer a conduction path for all particles while low RH conditions probe connected particles only<sup>96</sup>. The method has been applied in several studies to investigate the so-called dry proton accessibility as a function of ionomer content, Pt loading and carbon type, surface functionalization and porosity modification<sup>50,64,71,79,97</sup>. A limitation of the assumption that only ionomer-connected particles participate at low RH is that it is difficult to ascertain dryness of the carbon surface, and remaining adsorbed water and wet bridges could introduce uncertainties in the measurement. This is typically visualized as the RH-dependent dry proton accessibility curves never reach a plateau even down to 10% RH in the reported studies. An alternative approach consists in filling the CL with a fluorocarbon fluid, which ensures that

proton supply can only be provided through the ionomer<sup>98</sup>. In coupling this procedure with CO-stripping, the ionomer coverage in a range of carbons and the difference in activity of an ionomer-covered Pt surface to a bare one can be investigated<sup>99</sup>.

### 2.2.2 X-rays-based imaging techniques

While the methods based on molecular and electrochemical probes grant routine access to valuable information on the morphology of the CL, they rely on key assumptions and models and provide averaged bulk measurements only. To access spatially resolved information, imaging techniques are required. In particular, the large penetration depth of X-rays provides access to a statistically relevant field of view (FOV) and straightforward sample preparation. As such, lab- and synchrotron-based X-ray instruments have become key tools in the investigation of CLs. Additionally, computed tomography (CT) is now a standard tool in X-ray imaging and readily offers access to 3D reconstruction.

In the simplest case, the imaging contrast relies on the absorption difference between materials in the ray path. However, the low  $Z$ -number of most of the CL components results in limited contrast and resolution, between them and with the pores<sup>100</sup>. Instrumentation developments have made phase contrast more available in the past decade, which enables greater contrast with the pores and higher resolution in the images. This has allowed studying the porosity and aggregate size distribution at  $\mu\text{m}$ -scale with resolution approaching a few tens of  $\text{nm}$ <sup>101–103</sup>. Phase contrast nevertheless still offers limited contrast between the low- $Z$  components, especially carbons and ionomer. To overcome the challenge, subsequent studies have used the capabilities of PFSA ionomers to bind a range of counter-ions at the sulfonic acid groups. In particular, the exchange of protons with heavy-ions, such as  $\text{Cs}^+$  or  $\text{Ba}^{2+}$  leads to greater  $Z$ -contrast in absorption<sup>104,105</sup>. By using correlated phase contrast to resolve the pore-material interface and the overall morphology of the solids, and absorption contrast to locate the ion-exchanged ionomer, complementary reconstructions were obtained as shown in Fig. 2.7a and b<sup>106–109</sup>. Still, using absorption contrast to differentiate between high- $Z$  materials, i.e., ion-exchanged ionomer and Pt nanocatalysts is an issue. Even though it is assumed that the Pt volume is limited compared to the ionomer one, so that the error introduced by the Pt signal would be small, this might not be the case at high Pt loadings. To overcome this limitation, it was proposed that spectral imaging, whereby the energy of the incident beam is changed to image above and below the Pt  $L_3$  absorption edge, allows discriminating between the signals<sup>110</sup>. In addition, a complementary approach to improve the resolution has been to combine the low-resolution data of the secondary aggregates and porosity provided by nano-CT with knowledge of the primary aggregates and pores provided by  $\text{N}_2$  porosimetry (for meso- and micropores) and Pt size and loading from TEM images<sup>102,106–108,111</sup>. The method exemplified in Fig. 2.7c is particularly

interesting as it allows the construction of model data that are strongly grounded on experimental results but still rely on assumptions which are enforced for correspondence between the experiments (e.g., pore shape and ionomer coverage homogeneity).

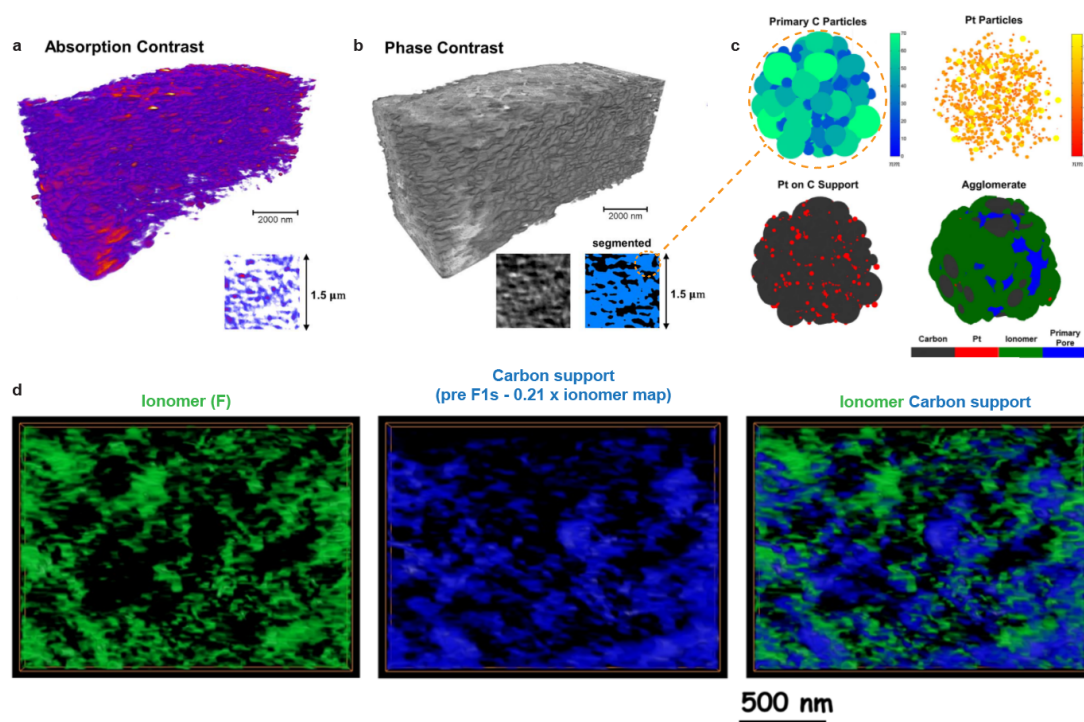


Fig. 2.7: X-Rays-based imaging of CLs. **a-c**, hybrid nCT – modelisation reconstruction workflow. **a**, Absorption nCT provides information on the high-Z materials, including Cs<sup>+</sup>-exchanged ionomer and Pt nanoparticles while **b**, phase contrast reconstruction allows to segment the air-material interface. The phase contrast volume is segmented and separated into aggregates which are populated in **c** by primary carbons and Pt nanoparticles based on TEM size distribution and by ionomer based on the absorption reconstruction. **d**, STXM spectro-tomo-ptychography reconstruction of the F 1s and C 1s spatial intensities in a microtomed CL section. Panels adapted with permission from: **a-c**, ref.<sup>106</sup>, IOP; **d**, ref.<sup>112</sup>, ACS.

An alternative approach consists in further leveraging the spectral imaging capabilities of synchrotron-based soft X-ray transmission microscopy (TXM) to image at energies with element-specific contrast, typically near an absorption edge such as the C 1s or F 1s. Owing to the greater dose associated with the multiple images required at each energy, the more intensive computation, and the limited specimen thickness dictated by the absorption at the F 1s edge, the first studies with the technique focused on microtomed cross-sections of CLs. They showed that Pt degradation after operation and ionomer inhomogeneities at the  $\mu\text{m}$  scale could be visualized with spatial resolution approaching 30 nm<sup>113–115</sup>. Furthermore, the quantitative nature of the signal has enabled detailed studies of the fluorine loss associated with the imaging process and comparison with beam-induced damages in electron microscopy<sup>116–118</sup>. In another instance, such mapping was used to provide insights into the spatial changes in Pt speciation and ionomer/Pt

distribution following durability testing<sup>119</sup>. More recently, the method was extended to volumetric reconstructions with spectro-tomography, offering insights into the morphology of CLs by spatially resolving areas of increased C (supports) and F (ionomer) concentration<sup>120,121</sup>. Subsequent development has been the implementation of ptychography, whereby a pixelated detector is used to record the 2D scattering pattern at each scan point. The redundant information between overlapping adjacent illuminations is used to solve the inverse image problem and retrieve the object function from which the scattering pattern originates<sup>122</sup>. The resolution is in principle limited by the incident wavelength rather than the optics of the imaging system and improvement down to 15 nm in 2D spectral images of CL was shown (Fig. 2.7d)<sup>112</sup>. The technique remains limited by the maximum dose allowed before radiation-induced sample degradation but holds promise to reach resolution below 10 nm with, e.g., capabilities for maintaining the specimen at cryo-temperatures<sup>112</sup>.

### 2.2.3 Atomic force microscopy

The limited resolution of X-ray instruments leaves an open door for techniques to probe CL with nanometer resolution. Atomic force microscopy (AFM) generates images by raster scanning a nanometer-thin probe at the surface of a specimen, and tracking the deflection of the probe to reconstruct topographic maps. Using dedicated stages, further signals can be obtained, such as modulus, adhesion and conductivity maps. These signals are especially interesting for the study of sections of CLs, because the ionomer domains are necessarily softer than their surroundings, while the carbon and Pt surfaces are conductive. Accordingly, the tool has been used to gain insights into the ionomer distribution and thickness in CLs, finding partial surface coverage and ionomer thickness about 7-12 nm<sup>123,124</sup>. An additional benefit of AFM is that it can easily be operated in environmental conditions and even liquids so that results are closer to what could be expected in the high humidity and 80 °C conditions which is the typical operating condition of PEMFCs. However, the intrinsic surface nature of the measurements and the resolution that is limited to a few nanometers grant limited access to the Pt nanoparticles, especially ones buried in porous supports. In addition, the necessity to image the surface of cross-sections casts doubts on results such as ionomer coverage, as the microtomy process typically employed could easily disrupt the ionomer layer.

### 2.2.4 Scanning electron microscopy techniques

With resolution approaching nm and relatively straightforward sample preparation, scanning electron microscopy (SEM) is also often used as a routine technique to investigate the surface or cross-section of CLs. It is commonly used to inspect the homogeneity of secondary aggregates or the presence of large ionomer clusters as a result of catalyst ink modifications<sup>78,80</sup>. To grant further insights into the 3D morphology of the electrodes, the combination with

focused ion beam (FIB) in FIB-SEM tomography has proven valuable. By serially sectioning with the ion probe and imaging with electrons, consecutive images are obtained that can be stacked to obtain 3D reconstructions with isotropic resolution down to a few nm. The method has been used to study the pore size distribution and carbon connectivity of pristine<sup>125</sup> and cycled samples<sup>100</sup>. A limitation of conventional FIB-SEM imaging on porous materials is the so-called shine-through artefact, whereby an image plane effectively contains information about materials in open pores deeper in the volume and ultimately complicates the segmentation and usable resolution. To overcome this, embedding with ZnO has been successfully demonstrated to fill the pores and provide adequate contrast resulting in reconstructions with enhanced quality<sup>126,127</sup>. The methodology has been applied to image the interface between the microporous layer (MPL) and the CL<sup>128</sup>. The results also showed that the Pt NPs in the CLs slightly modified the contrast in the aggregates and allowed to precisely identify the interface as well as to evaluate the local Pt density. In addition, the porosity, pores size and oxygen diffusivities were calculated, granting insights into the gas transport properties of the CL. Nevertheless, SEM does not offer the resolution for individual Pt particles, and the FIB sectioning process has been shown to result in strong morphological changes in the carbon supports and damage to the ionomer network<sup>129</sup>. The extensive damage was even leveraged in one instance to image cross sections of the CL before and after strong FIB irradiation, with the material lost in the process attributed to the ionomer<sup>130</sup>. Nevertheless, the resolution remains limited, and it is unclear whether damage is also imparted to the other components, or to which extent the porosity could be modified in the process.

### 2.2.5 Transmission electron microscopy techniques

The (sub)-nm resolution of TEM has made the tool especially valuable for the characterization of CLs and their components. It is regularly used to investigate nanocatalysts' shapes, size distribution<sup>131</sup> and elemental composition<sup>87</sup> at the nanoscale and down to the atomic scale, but also to investigate the morphology and microstructure of the carbon supports<sup>132</sup>. However, TEM conventionally acquires images in projection, which limits access to properties of interest for CLs, including inner porosity of the carbon support, pores within primary aggregates, catalyst distribution and position inside or at the surface of the support, and ionomer surface coverage and penetration within the support, which are known to influence significantly PEMFC performance.

To better discriminate between exterior and interior particles on porous carbons, a few studies have used secondary electrons (SE), whose small mean free path effectively results in surface images. By correlating BF or HAADF STEM images with SE images, NPs localization and the resulting size distribution can be accessed as demonstrated in Fig. 2.8a. This has been applied

## 2.2 Methods for characterizing the morphology of CL materials

to gain insights on the effect of various carbon supports on the Pt localization and size distribution<sup>51,79,93,94</sup>, of this Pt distribution and the resulting utilization during operation<sup>133</sup>. Other studies have tracked the NPs size distribution changes during carbon-corrosion accelerated stress test (AST) in MEAs<sup>37,134</sup> and compared it to degradation observed in aqueous cells for identical-location (IL) TEM experiments<sup>37</sup>.

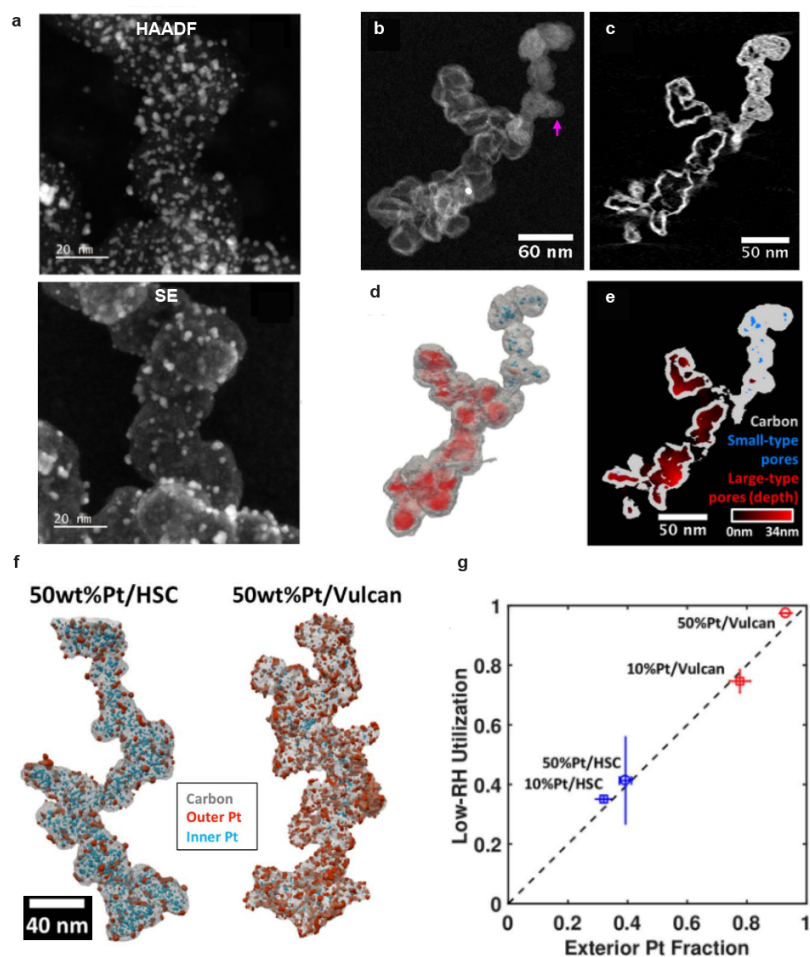


Fig. 2.8: STEM imaging of Pt/C catalysts. **a**, correlated STEM-HAADF and SE imaging of Pt/C catalysts with HSC, porous supports. **b-e**, STEM-LAADF ET of an HSC support enabling pore segmentation and demonstrating the different morphologies coexisting in these CBs. **b**, is the LAADF image, **c**, a tomogram, **d** and **e** the surface visualization and segmented reconstruction. **f**, STEM-LAADF ET reconstructions of two Pt/C aggregates comparing the localization of Pt NPs on the support. **g**, Comparison of ET external Pt fraction dry-proton accessibility measurement from CO-stripping. Panels reproduced with permission from: **a**, ref.<sup>37</sup>, ACS; **b-g**, ref.<sup>50</sup>, under a Creative Commons license.

Alternatively, ET offers further versatility and access to volumetric reconstruction. In the past 20 years, the technique has become increasingly available for investigating the three-dimensional shape of nanocatalysts and of the carbon supports<sup>135,136</sup>. A long-standing challenge in the accurate reconstruction of supported nanocatalysts concerns the strong contrast between the metallic NPs and low-Z supports. The point spread function (PSF) of tomographic



reconstruction and possible violation of the projection requirement (e.g., from diffraction contrast, see Section 3.2.2) often results in artefacts from the NPs that fall in the intensity range of the supports and challenge accurate interpretation and segmentation of the reconstructions. Still, the method has been used to study carbon-supported catalysts using either BF-(S)TEM<sup>49,72,125,137–142</sup> or low-angle annular dark field (LAADF)<sup>50</sup> to limit the intensity difference. Further improvements in the accuracy of the reconstructions have been demonstrated by correlating signals of different intensities in the so-called multimode tomography<sup>143</sup>. For example, LAADF and HAADF<sup>144</sup> or BF and HAADF<sup>145,146</sup> pairs of images have been used, possibly in combination with a masking procedure in post-processing to prevent high-intensity artefacts<sup>147</sup>. ET of Pt/C catalysts has yielded critical insights into the interactions between the catalysts and their supports. For instance, segmentation of the heterogenous inner porosity of an HSC aggregate was performed (Fig. 2.8b-e), and comparison of the Pt localization on two carbon supports with different Pt loading was achieved (Fig. 2.8f). The results were compared with electrochemical accessibility measurements and indicated that dry-proton accessibility measurement can be related to the exterior fraction of particles (Fig. 2.8g)<sup>50</sup>. In another study, the evolution of the Pt size distribution and calculated ECSA from ET reconstructions of Pt NPs on a range of carbons with increasing porosity could be tracked during ASTs and offered direct insights on the origin of ECSA losses on each supports<sup>49</sup>. Focusing solely on the metallic NPs, identical location imaging allowed visualization of coalescence events in 3D<sup>85</sup>. More recently, the inner porosity of mesoporous and modified carbon supports was investigated in greater detail and the results suggest that mass transport improvements were obtained thanks to a lower interior tortuosity<sup>72</sup>.

Typically, most ET studies focused on the investigation of isolated and dispersed aggregates, with limited considerations of the ionomer component. The main reason pertains to the challenges associated with imaging ionomers in the TEM: these are extremely beam-sensitive materials, with elemental F- loss reported from  $\sim 300$  e<sup>-</sup>/nm<sup>2</sup> (ref.<sup>117,148</sup>); they are made of elements of relatively close atomic weight (C, S, F, O) with the carbon supports, resulting in poor amplitude contrast, which is only made worse in the presence of bright metallic NPs.

To overcome the contrast challenge, elemental mapping of the F or S signal, fingerprints of the ionomer, have been valuable tools. As shown in Fig. 2.9a-c, insights into the localization and morphology of the ionomer network in microtomed sections have been reported in various studies, either using energy dispersive X-ray spectroscopy<sup>116,149,150</sup> or energy filtered (EF) and electron energy loss spectroscopy (EELS) mapping in both TEM and STEM<sup>149,151</sup>. However, the relatively high electron dose required to generate enough signal and the subsequent F-losses limit the signal and, ultimately, the resolution<sup>149</sup>.

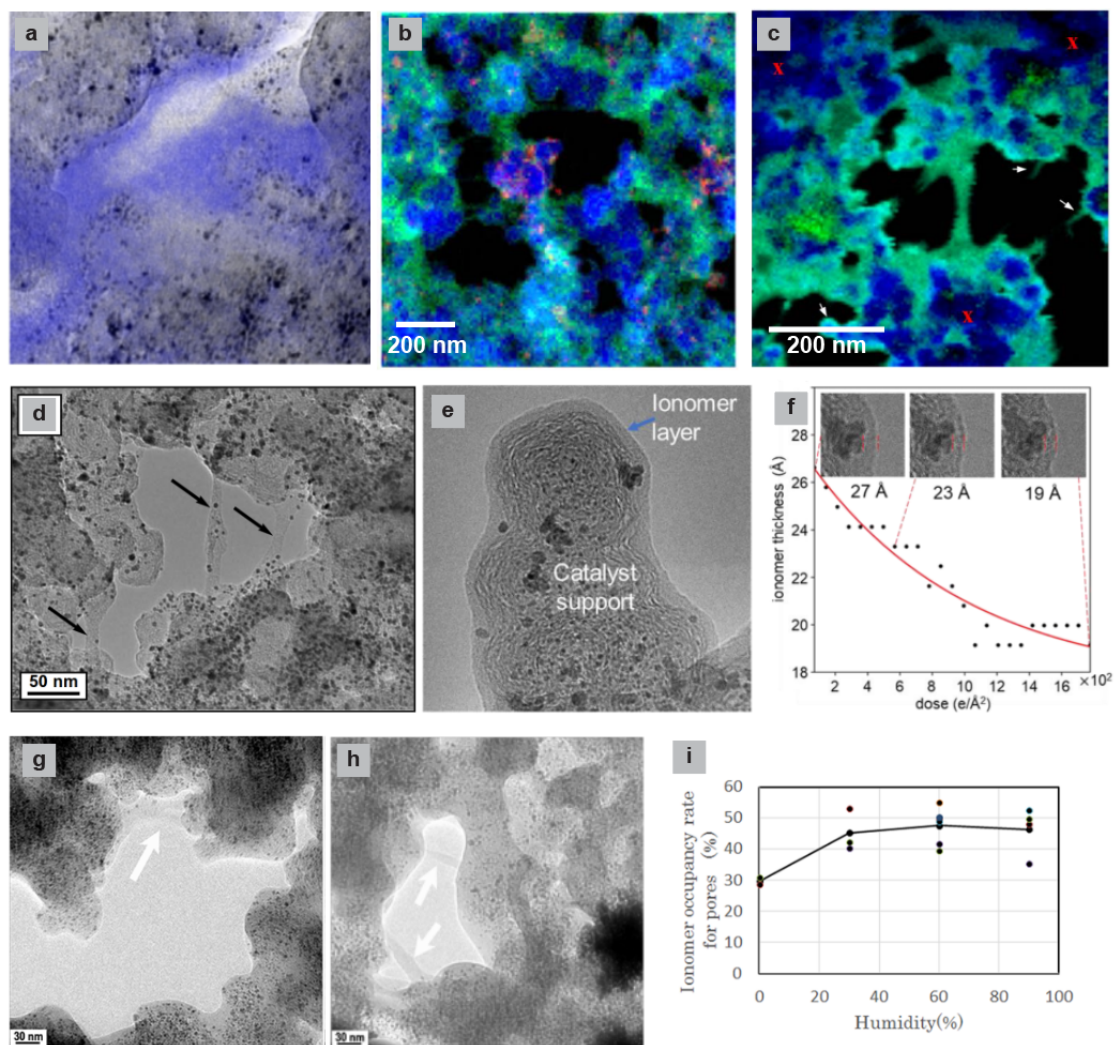


Fig. 2.9: Electron imaging of ionomers in CLs. **a**, EFTEM map of the F-K $\alpha$  line superimposed on a BF-TEM image of an embedded and microtomed CL section. **b**, EDS and **c**, EELS maps for a microtomed CL section without embedding. Green, blue and red refer to principal components extracted by multivariate statistical analysis (MVSA), with compositions relating to the ionomer, supports and Pt, respectively. **d**, HR-TEM image of a partially embedded microtomed section, demonstrating the ionomers strands in the CL. **e**, HRTEM image of a dispersed aggregate with clear identification of an anion-exchange ionomer layer. The thickness of the layer was tracked as increasing accumulated dose in **f**, and demonstrates the beam-sensitivity of the material. **g-h**, comparison of the pore-filling degree by the ionomer network plunge frozen in dry and 90% RH conditions. **i**, pore filling for a range of RH following the method. Panels reproduced with permission from: **a**, ref.<sup>104</sup>, Elsevier; **b** and **c**, ref.<sup>149</sup>, IOP; **d**, ref.<sup>61</sup>, Oxford University Press; **e** and **f**, ref.<sup>152</sup>, Oxford University Press; **g-i**, From ref.<sup>153</sup>, Oxford University Press.

At higher magnification, the HRTEM speckled contrast that originates from the amorphous nature of the ionomers renders identification easier against the concentric morphology of the supports<sup>154</sup>. This has been used in some studies to evaluate the extent of ionomer coverage on the carbon surface of dispersed aggregates<sup>51,66,155–157</sup>, and to visualize the morphology of the ionomer network in microtomed sections<sup>61,153,158</sup>, revealing heterogeneities with strands and

pure ionomer aggregates as seen in Fig. 2.9d. However, the high electron dose required for HRTEM imaging again means that such images often come with significant degradation<sup>117,148,152</sup>. Nevertheless, the use of cryo-TEM and developments in camera hardware has enabled some low-dose studies to seemingly mitigate most of the electron beam-induced damage, at least to obtain single images of a given area before degradation (Fig. 2.9e, f)<sup>152,153</sup>. In particular, a recent study combined it with freeze-plunging and cryo-transfer to lock the ionomer in the hydrated state<sup>153</sup>. The results revealed a significant difference in the filling of the secondary porosity with the dry state (Fig. 2.9g-i), coherently with the swelling of ionomers in high RH conditions<sup>53</sup>.

For these reasons and although evaluation of the ionomer interactions with the support is acutely needed, ET of CLs with ionomer has remained limited. A few ET studies have focused on pure ionomer membranes to investigate the nanostructure of the phase separation, with results granting insights into the connectivity of hydrophilic domains<sup>159-161</sup>. However, for CL materials, reports to date have mostly used ion-exchange to increase the amplitude contrast and focused on dispersed particles<sup>162,163</sup>. In one study, two samples with different ionomer-to-carbon (I/C) weight ratios were reconstructed and showed a partial but increasing surface coverage from 40% to 80% when going from 0.2 I/C to 0.5, and a mean thickness around 7 nm<sup>163</sup>. These results provided the first visual confirmation of the partial coverage of the supports (Fig. 2.10a-d), however, it remains unclear to what extent the ion-exchange procedure may modify the material, and if the resulting contrast is material-specific<sup>148,164</sup>. In addition, the increased amplitude contrast of the ionomer was interfering with the Pt NPs and led to the use of model ionomer-carbon samples only, although it is known that the ionomer interacts preferentially with the Pt surfaces and may therefore exhibit different characteristics in the actual CL<sup>60</sup>. Other studies have attempted to reconstruct the CL morphology from ET with BF images of FIB lamellae<sup>139</sup> and microtomed sections<sup>129</sup> but did not visualize the ionomer or reported too much electron beam-induced movement for accurate reconstruction. Very recently, an ET study of microtomed sections was reported with successful visualization of some ionomer pockets (Fig. 2.10e, f)<sup>158</sup>. However, the results were principally used to investigate the effect of ASTs on carbon corrosion, and the resolution did not allow to precisely visualize ionomer at the surface of the supports. Additionally, no considerations were given to electron beam-induced degradation.

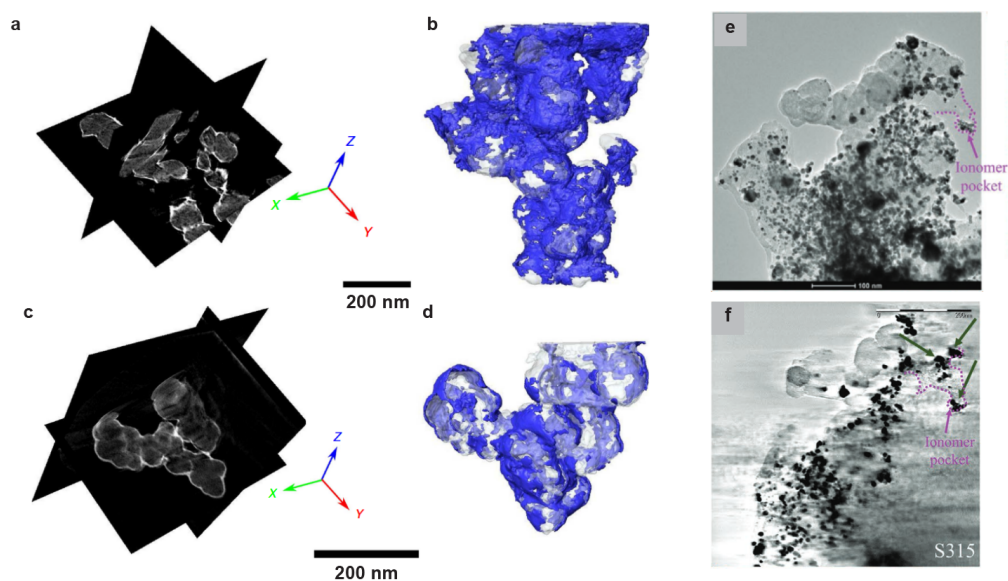


Fig. 2.10: Tomography of ionomer in CL samples. **a-d**, STEM-HAAD ET reconstruction of  $\text{Cs}^+$  ion-exchange model Vulcan-ionomer sample at 0.5 I/C (a, b) and 0.2 I/C (c, d). The ionomer is in blue in the surface-rendered segmented volumes (b, d). **e**, BF-TEM image from the tilt-series of an embedding-free microtomed CL section and **f**, corresponding tomogram in the ET reconstruction. Panels reproduced with permission from: **a-d**, From ref.<sup>163</sup>, Springer Nature; **e** and **f**, ref.<sup>158</sup>, Wiley.

### 2.3 *in situ* TEM to probe electrocatalysts degradation

The mean free path of electrons travelling in various media requires the microscope's column to be kept under vacuum and samples to be a few hundred nanometers thick. Thus, typical analytical conditions are vastly different from operating ones<sup>165–167</sup>. It was therefore recognized early in electron microscopy history that adjustments in the apparatus were required to achieve more realistic conditions in the sample vicinity<sup>168,169</sup>. Over time, two strategies have gained widespread application: the open-cell approach that uses differential pumping and pressure limiting apertures to maintain a moderately high pressure of a gas of choice around the sample, allowing for condensation to take place and/or low vapour pressure liquids to be used<sup>168,170</sup>; the closed-cell approach which uses adapted specimen holders that accommodate a small enclosure isolated from the column<sup>167</sup>. With modern microfabrication techniques, this enclosure is now typically realized by stacking two silicon chips featuring electron-transparent silicon nitride membranes, onto which electrodes can be further patterned and connected to a potentiostat for electrochemical experiments, while fluidic lines can be added to the holder and an electrolyte flow established<sup>167,171</sup>. While the open-cell approach has offered insights into the dynamics of some catalysts for energy conversion reactions<sup>172,173</sup>, the closed-cell approach is often favoured for being amenable to quantitative electrochemistry and closer to *operando* conditions for aqueous environments<sup>81,84,174–176</sup>. To date, this electrochemical liquid phase (ec-LP)TEM has

been used in several works to gain insights into the dynamics of electrocatalytic systems for the oxygen evolution reaction (OER)<sup>177,178</sup>, the ORR<sup>86,179–182</sup> and the CO<sub>2</sub> reduction reaction (CO<sub>2</sub>RR)<sup>183–186</sup>.

In particular, studies of electrocatalysts for the ORR have sought to probe into the origins of ECSA losses during operation and to disentangle the competing mechanisms reviewed in Section 2.1.5. For example, carbon-supported PtFe nanoalloys were found to exhibit a marked coarsening within electrochemical cycles and potential-dependent material dissolution and redeposition were observed during slow scans<sup>179</sup>. In studies focusing on the conventional Pt/C system, a major challenge has systematically been the resolution required to resolve the individual Pt NPs. One proposed solution to this end used custom-made chips with thinner SiN<sub>x</sub> windows and reduced overall cell thickness<sup>180</sup>. In addition, an extended area for material deposition was included, to increase the electrochemical signal. The resulting chip offered improved resolution compared to commercial solutions and led to observations of dissolution events, as well as migration and aggregation of some of the particles over the course of repeated potential cycles. The same setup further enabled to study the potential-induced dissolution of a patterned Pt electrode with atomic resolution<sup>181</sup>. Another proposition has been to dynamically control the liquid thickness via beam-induced radiolysis of the electrolyte<sup>182</sup>. Interactions of the electrons with an aqueous electrolyte generate a range of chemical species which include gaseous H<sub>2</sub> and O<sub>2</sub> and gas nucleation can be triggered at sufficiently high electron dose<sup>187–189</sup>. The effect was used to expand and retract a gas bubble in the observation area, thereby tuning the thickness under the beam. Cycling was performed with thicker liquid and imaging was performed in thin liquid conditions to maximize the resolution. As a result, a range of degradation mechanisms could be observed including detachment, coalescence, dissolution and reprecipitation. Finally, an investigation of bigger PtNi nano-octahedra supported on carbons was also performed with STEM-HAADF<sup>86</sup>. The experiments directly visualized dissolution-redeposition processes and NP displacement at the surface of the supports resulting in coalescence events when cycling at high potentials.

It is noteworthy that the final degraded state resulting from operando ec-LPTEM is likely to differ from what happens in MEA. The liquid environment is indeed different, and this factor alone is already sufficient to induce discrepancies between ASTs conducted in MEA, RDE and IL-TEM setups<sup>37,38</sup>. In addition, the electron beam modifies the environment by generating reactive radicals through inelastic interactions with water molecules<sup>188,189</sup>, even if direct beam-induced damage to the specimen can be avoided. The working and reference electrodes are also markedly different, with implications on the measurements further discussed in Section 6.3.1. Nevertheless, the direct visualization of degradation events can offer valuable insights into the fundamental processes at play.

## 3 Methodology and Instrumentation

This chapter presents the instrument (the transmission electron microscope - TEM) and the main technique (electron tomography - ET) that were used in this thesis to investigate catalyst layers (CL) and their components in three-dimensions (3D) at the nanoscale. Aspects of digital image processing are also discussed and methods to denoise and segment volumes and time-series are covered.

### 3.1 (Scanning) Transmission Electron Microscopy

#### 3.1.1 Principle and modes of operation

In a broad definition, the TEM is an instrument that uses electrons accelerated at high voltages towards a specimen thin enough to let them pass through and subsequently records signals originating from the interactions of these electrons with the specimen.

A simplified ray diagram demonstrating the path of electrons travelling down the optical column to the specimen plane is shown in conventional (C)TEM mode in Fig. 3.1a and in scanning (S)TEM mode in Fig. 3.1b. Electrons are emitted from the electron source and accelerated down the column by the electron gun with high tensions ranging conventionally from 60 to 300 kV. In this regime the wavelength of the electrons ranges from 2 to 4 pm, while they travel at speeds close to that of light (e.g.,  $\sim 0.78c$  at 300 kV)<sup>190</sup>. The mean free path of electrons and their interactions with matter have two immediate consequences: 1) the column must be kept in high vacuum in order to avoid interactions other than ones with the sample and 2) the specimen must be thin enough for electrons to be able to exit it. In practice, this limits thicknesses to a few 100s of nm. Electromagnetic lenses are used for manipulating the beam illumination and focusing of the image. Lenses are divided in three main parts. The first set is the condenser system which comes between the electron gun and the specimen and shapes the electron beam. In CTEM, a parallel and broad illumination is used (Fig. 3.1a), while in scanning (S)TEM, a probe highly focused on the specimen is formed (Fig. 3.1b). In CTEM, the objective lens (OL) placed below the specimen magnifies the specimen image up to a level of 50x. In addition, a diffraction pattern is formed in the back focal plane (BFP) of this lens (Fig. 3.1c and d). Finally, the intermediate-projector system is the last set of lenses whose role is to further magnify the image

to the desired magnification and to conjugate the camera with the plane at which the information of interest is found, i.e., the image plane of the OA or its BFP to record a diffraction pattern (Fig. 3.1c and d).

In STEM, scanning coils that can deflect the beam in x and y positions are used to scan the beam on the specimen. At each point, the intensity of directly transmitted or scattered electron beams is recorded to assemble a digital image.

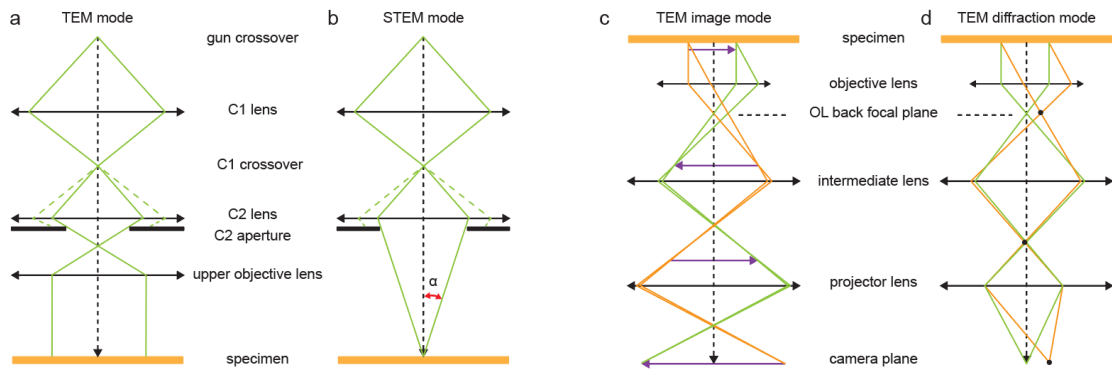


Fig. 3.1: Simplified ray diagram of (S)TEM. **a**, broad-beam illumination (CTEM) and **b**, scanning mode (STEM). **c**, CTEM operating in image and **d**, diffraction mode. Based on schematics in ref.<sup>190</sup>

### 3.1.2 Contrast in the (S)TEM

Contrast in the (S)TEM arises from electrons scattered in the specimen and possibly their interactions with the directly transmitted beam. A fundamental distinction can be made between *amplitude* contrast and *phase* contrast<sup>190</sup>. Both often participate in the final image, although imaging conditions favour one or the other.

Amplitude contrast can originate from *mass-thickness* contrast and *diffraction* contrast. The latter occurs in crystalline specimens when a set of crystal planes is close to the Bragg condition. In this case, the incident electrons can be elastically and coherently scattered at an angle  $\theta$  related to the lattice spacing  $d$  by Bragg's law:

$$n\lambda = 2d \sin \theta, \quad (1)$$

where  $\lambda$  is the electron wavelength and  $n$  is the diffraction order. In CTEM, when an objective aperture (OA) is inserted in the BFP of the OL to let only the direct beam through, crystalline regions from where diffraction occurred show lower intensity in the image. Alternatively, one of the diffracted beams can be selected with the aperture and only the diffracting areas participate in the final image. If the direct beam is selected, this mode of operation is termed bright-field (BF)TEM while the use of the Bragg diffracted electrons leads to dark-field (DF) images.



### 3.1 (Scanning) Transmission Electron Microscopy

Mass-thickness contrast arises due to electrons being elastically and incoherently scattered by the atomic nuclei, in Rutherford scattering events. Again, the OA can be used to block these scattered beams from participating in the final image, which results in a lower intensity locally (Fig. 3.2a). In addition, heavy elements scatter at angles greater than most Bragg-diffracted beams. This has led to the development of high-angle annular dark field detectors (HAADF) in the STEM, whereby a ring-shaped detector collects only these electrons scattered at high angles (Fig. 3.2b). In this case, the intensity in the final image is proportional to  $\sim tZ^{1.7}$  (ref. <sup>191</sup>), where  $t$  is the specimen thickness, providing direct mass-thickness contrast.

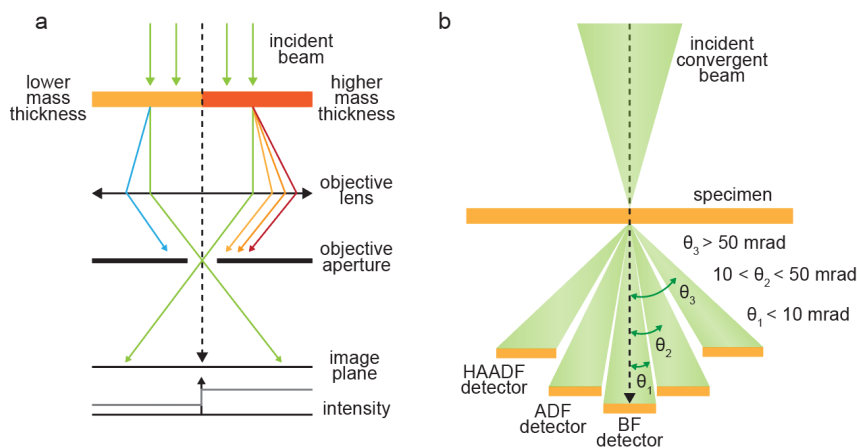


Fig. 3.2: Signal collection in (S)TEM. **a**, Mechanism of mass-thickness contrast in BF-TEM and **b**, arrangement of the detectors in STEM mode. Based on schematics in ref.<sup>190</sup>

As depicted in Fig. 3.2b, HAADF is not the only source of signal that can be recorded in STEM. The direct beam can also be used to form a BF image. In most conditions, bright field STEM images exhibit similar characteristics with BF-TEM images<sup>192,193</sup>, with contributions from mass-thickness and diffraction contrast tuned by the collection angle  $\theta_1$ .

Phase contrast arises in (S)TEM images when two or more coherent beams with a phase difference are allowed to interfere. In high-resolution (HR)TEM, this difference comes from the effect of defocus and lens aberrations on Bragg scattered beams and gives rise to fringes that carry information about the lattice spacing<sup>190</sup>. In addition, Fresnel contrast is also a prominent source of contrast in defocused images and arises at interfaces between materials exhibiting large differences in inner potential. Since the objective lens is focused on a plane close to the specimen, the image is obtained in the near-field or Fresnel regime. Therefore, the interfaces in the image show Fresnel fringes whose intensity and width are related to defocus, inner potential difference and electron wavelength<sup>190,194</sup>.

Apart from using electrons to form images, spectroscopic imaging is also possible. Specifically, elemental analysis using characteristic X-rays is available in the so-called energy-dispersive



spectroscopy (EDS). X-rays are generated by transitions of outer shell electrons to inner shell holes created by the ejection of core electrons from inelastic interactions with the incident beam. The energy of these X-rays is a fingerprint of the electronic structure of the atoms in the specimen since only specific transitions are allowed. When combined with STEM, the origin of X-rays can be spatially resolved to obtain elemental maps.

### 3.1.3 Instrumental resolution

The TEM lenses and the electron sources suffer from aberration and partial spatial and temporal coherence and this degrades the achievable resolution. With some approximations, the effect of the microscope on the CTEM image can be described with a spatial resolution response function<sup>195</sup>. The recorded image intensity  $G(u)$  can then be written in Fourier space as the product of a contrast transfer function (CTF)  $H(u)$  with the object function  $F(u)$ . The CTF features three components that act on the way information is transferred to the image: an aperture function  $A(u)$  that introduces a cutoff at high frequencies, an envelope function  $E(u)$  that results from various contributions damping the high frequencies and an aberration term  $B(u)$  resulting from the imperfections of the lenses:

$$H(u) = A(u)E(u)B(u). \quad (2)$$

The aberration term of the CTF is a sinusoidal function that depends strongly on the defocus and the spherical aberration of the TEM lenses. Consequently, for a given microscope and defocus, bands of spatial frequencies exhibit a positive contrast (the object function is directly transmitted) while other frequencies show negative (reversed) contrast. To maximize direct interpretability the contrast should be consistent over a wide range of frequencies and this optimum is found at the so-called Scherzer's defocus<sup>196</sup>.

The envelope term in Eq. (2) arises from various multiplicative contributions including from the limited spatial and temporal coherence of the source. As electrons are emitted and accelerated with slight variations in energy, the chromatic aberration of the TEM lenses results in delocalization at the image plane. The fact that the source is not point-like, the specimen drift and vibrations, the quality of the detector and electron beam-induced damage also affect the high frequencies and add to the damping envelope. The CTF allows to define two points related to resolution: the first crossover at Scherzer's defocus is the point-to-point resolution, i.e., the highest spatial frequencies that can be directly interpreted, and the tail of the damping envelope defines the information limit. Interpretation of information between the point-to-point resolution and the information limit typically requires image simulation or CTF correction.

### 3.1.4 Beam-induced damage and mitigation strategies

Unfortunately, the electron-matter interactions can also result in adverse effects that alter the sample under investigation. This can impose limitations on the imaging conditions and, in turn, deter the quality of the images. Conventionally, these electron-irradiation damages are classified by the type of electron scattering that produces it (i.e., elastic or inelastic)<sup>197</sup>.

In inelastic scattering events, energy from the incident electron is directly transferred to the specimen notably via ionization of the inner or outer atomic shells<sup>198</sup>. If the specimen is conductive, this vacancy can be filled by another electron from the system. However, in the case of an insulator, this can result in radiolysis and bond scission, leading to the formation of new volatile molecules and, eventually, mass loss. In addition, when secondary electron generation is significant, electrostatic charges can build up on the specimen surface. In insulating materials like polymers, the surface potential can become strong enough to lead to dielectric breakdown and material sputtering. Heat generation also occurs due to the energy transfer during inelastic scattering. In most samples, however, the radial conduction away from the illuminated area typically limits the temperature rise to a few Kelvin (e.g., about 1 K in a carbon film illuminated with a 5 nA electron probe) even on insulating polymers<sup>190</sup>.

As the rate of this type of damage depends on the inelastic cross section (which decreases with the acceleration voltage<sup>198</sup>), a direct mitigation pathway consists in working at higher voltages. However, the cross-section for elastic scattering is also reduced at higher acceleration voltage, so the compromise between lower image contrast and lower damage is not necessarily beneficial<sup>198</sup>. Cooling the specimen at cryogenic temperature is also a prominent strategy that has often been used to enable imaging of beam-sensitive ionomers<sup>117,148</sup>. It directly limits the temperature rise and also reduces the rates of the chemical processes and diffusion that lead to mass or elemental loss by radiolysis<sup>199</sup>. Other strategies have involved dedicated sample preparation steps to increase heat or electrical conduction. This can for example include carbon coating<sup>197</sup>, careful consideration of the substrate<sup>117</sup>, or encapsulation in few-layers 2D materials<sup>199</sup>.

Elastic scattering can lead to atomic displacement or knock-on damage. It results from the conservation of energy and momentum that dictates the amount of energy transferred by an incident electron as a function of the scattering angle. For backscattering events ( $\theta > 90^\circ$ ) the energy transfer can be significant. Materials possess threshold displacement energies, above which an atom from the specimen can be expelled if such high-angle scattering occurs<sup>197</sup>. In effect, the rate of these knock-on events depends on the excess high tension and the electron dose<sup>200</sup> (that is, the charge density in the beam, typically in  $C/cm^2$  or  $e/nm^2$ ). If significant, knock-on damage can result in atomic rearrangement and sputtering of surface atoms, severely

altering the specimen. This type of damage is the dominant mechanism of degradation in carbon supports as found in CLs and is mitigated by working at low electron dose and voltages (e.g., the graphite threshold voltage is  $\sim 140$  kV, ref.<sup>197</sup>).

Either way, the degradation rate is directly dependent on the electron dose, so that minimizing it is often the best course of action. Occasionally, there may exist a nonlinear relationship of damage to the dose-rate so that better results can be obtained with short exposure at high current or long exposure at low current<sup>198</sup>. This may in turn favour the use of TEM or STEM<sup>201</sup>.

### 3.1.5 TEM at cryogenic temperatures

The control of cooling temperatures in the microscope is enabled by dedicated cryo-holders whose use in TEM dates back as far as 1954 (ref.<sup>202</sup>). The standard side-entry model typically uses metal conduction, with an external dewar containing liquid nitrogen (LN<sub>2</sub>). In this design, a conductor rod connects the dewar to the tip of the holder inside the column and a heater element provides precise control over the temperature<sup>203</sup>.

A severe problem that arises from maintaining the specimen at cryogenic temperature is that the tip of the holder effectively acts like a cryo-pump and can gather moisture and contamination even in the evacuated TEM column<sup>190</sup>. This is especially prominent when using cryo-transfer holders because some moisture from the air condenses during the transfer and is directly brought into the column<sup>203</sup>. Even with more regular materials science operations where the holder is usually cooled in-column, moisture previously introduced and traces from contaminated ionic pumps may eventually lead to the growth of a thin ice layer on the specimen<sup>203</sup>. Cryo pole-pieces that feature a dedicated double-blade anticontamination device in the form of a cold shield closely surrounding the specimen are highly beneficial in that regard<sup>203,204</sup>. This design can remarkably limit the rate of ice growth (Fig. 3.3a), although contamination still happens after a few hours. Fig. 3.3b shows such an ice layer that had grown on a graphitized carbon black aggregate supported on lacey carbon despite the use of a double-blade anticontaminator and illustrates how this can deceptively resemble thin ionomer layers. To mitigate the risk of misinterpretation, experiments performed at cryo-temperatures in this thesis were limited to 3-5 hours within which the presence of ice was regularly controlled by checking the edges of lacey carbon strands (see additional methods in section 4.3.3).

An additional challenge is the thermal drift that results from the contraction of the holder during cooling and imposes time limitations to reach equilibrium and, historically, the vibrations of the boiling LN<sub>2</sub>. The latter point is now well mitigated by the excellent insulation of modern dewars<sup>203</sup>.

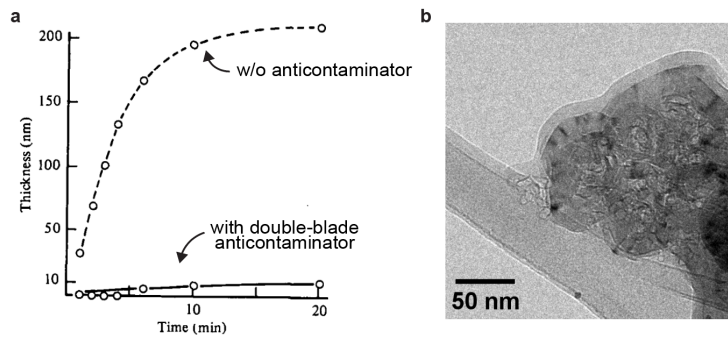


Fig. 3.3: Ice contamination in the TEM. **a**, thickness of the ice contamination over time on a cryo-transferred specimen maintained at  $-170\text{ }^{\circ}\text{C}$ , from the moment of insertion. Adapted with permission from ref.<sup>204</sup>, Wiley. **b**, ice contamination on a graphitized Vulcan and Nafion aggregate supported on lacey carbon. The amorphous layer covering the carbon strand and the carbon surface is only contamination.

### 3.1.6 Cameras for low-dose TEM imaging

The main technology for TEM cameras nowadays employs complementary metal-oxide semiconductor (CMOS)-based sensors which enable higher readout speeds than previous charge-coupled devices (CCD)<sup>205,206</sup>. The sensors can be photosensors coupled to a scintillator – an interface at which photons are generated upon interactions with electrons – or, as allowed recently with the advent of radiation-hard CMOS-based sensors<sup>207,208</sup>, direct electron (DE) detection units. The propagation of the high-energy electrons in the sensing layers results in signal delocalization, which is further spread out when travelling to the detection elements in scintillator-based cameras. This delocalization directly reduces the resolution of the image at the highest spatial frequencies and participates in the CTF envelope of Eq. (2). Some of the latest developments involve using back-thinned pixels so that electrons can cross the sensing elements with limited backscattering, thereby limiting the delocalization of signal-generating events<sup>205</sup>. It is this reduced delocalization in back-thinned DE cameras and their fast readout that is at the origin of the so-called resolution revolution in structural biology<sup>209</sup> and, for the materials science, enables the imaging of beam-sensitive samples at higher resolution with lower dose and *in situ* processes at faster rates. The modern detectors are also maintained at low temperatures (typically  $-30\text{ }^{\circ}\text{C}$ ), which reduces the noise associated with thermal jumps and activation. The noise imparted by a camera on the signal can be quantitatively assessed by the detective quantum efficiency (DQE) which measures the ratio  $\text{SNR}_{\text{in}} / \text{SNR}_{\text{out}}$  as a function of the spatial frequency of the signal (usually displayed as fractions of the Nyquist frequency)<sup>210</sup>. Fig. 3.4 demonstrates the improvement brought by modern DE cameras in this regard, but also shows that DQEs remain perfectible. A more complete description of the origins of noise in TEM images and its treatment in post-processing is given in Section 3.3.1.

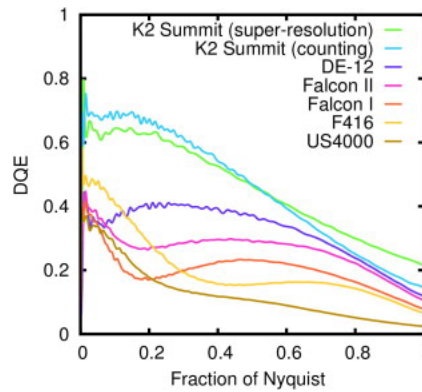


Fig. 3.4: DQE of various detectors at 200kV, including scintillator (US4000 and F416) and direct electron (Falcon I and II, DE-12 and K2 Summit) based. Reproduced with permission from ref.<sup>210</sup>, Elsevier.

### 3.1.7 Dose limited resolution

Considerations in Section 3.1.3 set the resolution with regard to instrument characteristics and assume thin samples and high SNR. In this case, *resolution* is understood in the sense of the Rayleigh criterion, that is, in terms of *resolvability* between features. However, the beam-induced damage can limit the total electron dose available and result in low SNR. This sets a *detection* problem. Indeed, a feature should exhibit a SNR above the Rose criterion, which is typically 3-5, to be detected. Hence, the smallest features that can be resolved are a function of the contrast of that feature imaged with a given technique, the efficiency of signal generation with the technique, and the efficiency of signal detection (the DQE). Egerton has proposed that this dose-limited resolution<sup>198</sup> can be expressed as:

$$\delta = \text{SNR} \cdot \sqrt{2} \cdot (\sqrt{\text{DQE} \cdot F \cdot D_e} \cdot |C|)^{\frac{1}{2}}, \quad (3)$$

where  $D_e$  is the electron dose,  $F$  is a signal efficiency relating the number of recorded electrons to the fluence (or dose) required to generate them,  $\delta$  is the (dose-limited) resolution,  $C$  is the Weber contrast of the feature relative to the adjacent background and the SNR is set by the Rose criterion. A practical use of this approach for determining the dose required for sufficient contrast and resolution to align tilt-series of CL is demonstrated in Annex B.1.1.

## 3.2 Electron tomography

The (S)TEM allows to form an image from a variety of signals and collection processes. However, the images directly obtained at the microscope are limited to two dimensions. When complex morphologies such as that of CL materials need to be visualized and analyzed, accessing three-dimensional (3D) information is required. In this thesis, ET was used to solve that problem.

### 3.2.1 Fundamental aspects

Broadly speaking, the meaning of tomography refers to the visualization of slices, e.g., across a volume. In microscopy, the term describes the process by which a volume can be reconstructed from a set of projections acquired at different angles to form a tilt-series. In this sense, tomography consists in inverting the projection operation to recover the original object that generated the recorded images.

The operation of projecting a  $N$ -dimensional structure in a  $N-1$  dimensions space can be described mathematically by the Radon transform that defines each point of a projection as the line integral along a path parallel to the axis of projection (Fig. 3.5a). Projecting a structure at different angles results in a sampled representation of the structure in the Radon space, which is typically displayed as a sinogram with axes of the projection surface (a line, in 2D object to 1D projection, or a plane, for a 3D object projected to 2D) and angle of projection (Fig. 3.5b). Additionally, there is a close link between the representation of an image in the Fourier space and in the Radon space, as stated by the Fourier slice theorem: the Fourier transform of the projection of an object at an angle equals a slice at that angle through the Fourier transform of the object. It follows that two routes can be classically chosen for tomographic reconstruction: via Fourier space by populating the Fourier space with the Fourier transforms of the acquired projection, then taking its inverse Fourier transform; or via real space by simulating the inverse effect of a projection and “smearing” the intensities recorded in the image in a back-projection operation. These methods are further discussed in Section 3.2.5.

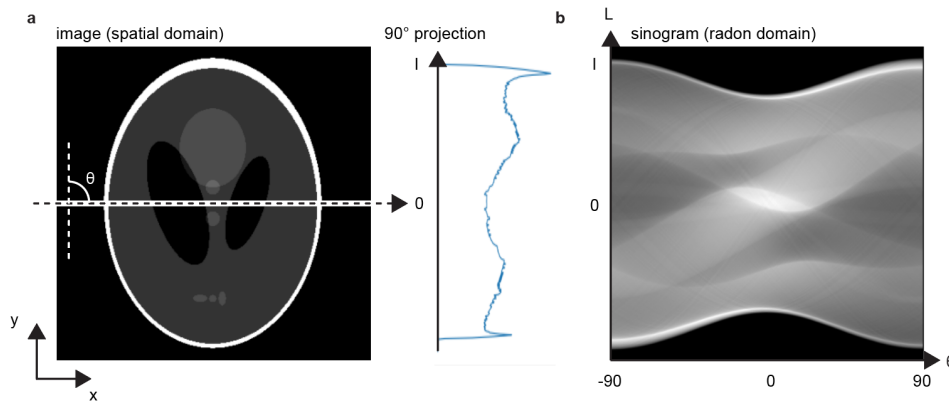


Fig. 3.5: Radon transform and sinogram. **a**, projection geometry of the Radon transform and **b**, corresponding sinogram representing the image in the Radon domain.

### 3.2.2 Projection in the TEM

The projection requirement for tomographic reconstruction states that the acquired signal should vary monotonically with some physical properties of the specimen to be reconstructed. This, in principle, limits the combination of signal and sample that can be used to acquire tilt-

series of a specimen in the (S)TEM. As presented in Section 3.1.2, mass-thickness contrast is directly related to a projection of the density through the sample<sup>211</sup> and satisfies the projection requirement. However, the BF-(S)TEM signal also includes effects from diffraction in crystalline specimens. This contrast appears at rotation angles where some sets of planes are close to Bragg conditions and is therefore unrelated to a projection of the structure. Alternatively in the case of phase contrast, it can be shown that under the projection assumption and the weak phase object approximation (WPOA - the specimen potential is small compared to the acceleration voltage, and the accumulated effect of the specimen can be replaced with a simple integral along the optical path), the intensity  $g$  in the recorded image exhibits a monotonic relationship to the projected specimen potential  $v_z$ :

$$g(x) \approx 1 + 2\sigma_e v_z(x) \otimes h_{WP}(x), \quad (4)$$

where  $\sigma_e$  is a scaling factor,  $h_{WP}$  the PSF for BF imaging which corresponds to the effect of the CTF in real space. However, these assumptions fail beyond a few tens of nm for light elements as found in biological macromolecules<sup>211</sup> and down to sub-nm thicknesses for heavy elements<sup>190</sup>. Additionally, care should be taken to image within a CTF passband or to correct for CTF phase flips in post-processing to avoid contrast reversal. Phase contrast is also more sensitive to changes in defocus. These change the CTF and, thus, the spatial frequency at which contrast reversal occurs but also the intensity and width of Fresnel fringes. This in turn creates contrast changes in the tilt-series that are unrelated to the projection operation.

These considerations show that the projection requirement is satisfied for mass-thickness contrast in BF-(S)TEM with amorphous specimens and for phase contrast with thin and light specimens. As a result, for materials science applications where crystalline specimens containing heavy elements are common, STEM-HAADF is typically preferred<sup>212,213</sup>. It was noted however that even under conditions where the projection requirement fails, the exterior shape of objects may still be accurately recovered, although the interior intensities would be subject to erroneous effects<sup>214</sup>.

### 3.2.3 Tilt-series geometry

A challenge specific to ET is related to the limited space available in the pole piece gap for the specimen to rotate and to the shadowing created by the side-bars of the specimen holder at high angles. In addition, planar specimen induces a strong increase of the thickness under the beam at higher angles, eventually imposing a signal-to-noise limit. The angles that cannot be recovered create a wedge of missing information that can be easily visualized in the Fourier transform of an ET reconstruction. Furthermore, the mechanical precision, experiment time, and total electron dose the specimen can withstand also impose a limit on the total number of

projections that can be acquired and, thus, on the angular sampling. The combination of a missing wedge and limited angular sampling results in a decreased and anisotropic resolution as demonstrated in Fig. 3.6.

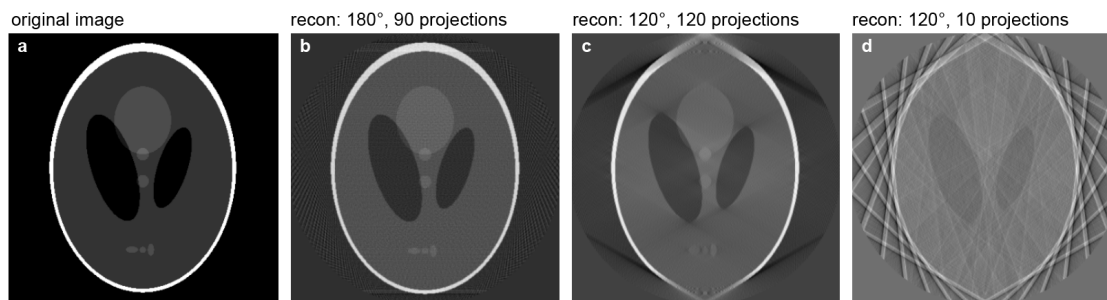


Fig. 3.6: Effect of limited angular sampling and tilt range on the tomographic reconstruction of the Shepp-Logan phantom. **a**, original object. Reconstructed from projections in range **b**,  $[-90^\circ, 90^\circ]$  with  $2^\circ$  angular sampling, **c**,  $[-60^\circ, 60^\circ]$ ,  $1^\circ$  sampling, **d**,  $[-60^\circ, 60^\circ]$ ,  $12^\circ$  sampling.

Strategies to mitigate this missing wedge have involved dedicated holders and modified acquisition schemes, for example with dual-axis acquisition or laminography. If the specimen is amenable to this, shaping or deposition at the end of a needle in combination with the use of specialist holders can allow rotation through the full  $\pm 90^\circ$  range without shadowing<sup>215</sup>. This strategy is used in Chapter 5 to enable high-resolution reconstruction of carbon supports. Alternatively, data processing methods can leverage prior knowledge and assumptions about the specimen to constrain the solutions to the reconstruction problem and limit the smearing effect of the missing wedge. These will be discussed in greater detail in Section 3.2.5.

### 3.2.4 Aligning tilt-series

Another challenge of ET arises from the fact that the field of view is close to the tolerance of the mechanical stage that rotates the specimen. Optimized alignments and automated tracking and focus allow to maintain the region of interest (ROI) in the image during acquisition (see operational considerations in Annex A). However, finer alignments are required in post-processing to achieve the highest spatial resolution available from the acquired data. Typically, misalignments lead to delocalization and blurring of the features and imprecise reconstruction. Beyond these shifts between projections of a tilt series, it is also important to ensure that the rotation axis is at the centre of the images and straight. As illustrated in Fig. 3.7, an off-centre tilt axis results in bent features and arc artefacts in the reconstruction that can strongly limit the final resolution<sup>216</sup>.



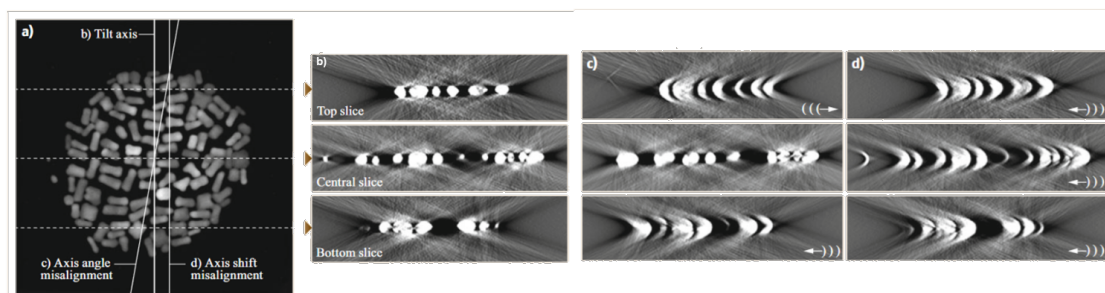


Fig. 3.7: Depiction of the effects of tilt axis alignment on tomographic reconstruction. **a**, STEM HAADF image of a nanoparticle aggregate indicated the tilt-axis assumed for reconstruction and the position of three reconstruction slices in **b-c**. **b**, reconstruction with centred tilt-axis, **c**, tilted and **d**, shifted. Adapted with permission from ref.<sup>216</sup>, Springer Nature.

Correcting for misalignment can be done manually by tracking a feature throughout the tilt series. The method is however labour intensive and time-consuming, may lack precision, and requires sufficient SNR and well-defined features.

Other (semi-)automated methods can be divided in marker-based and marker-less strategies. Marker-based strategies use the semi-manual detection of high-contrast *ad-hoc* markers, often gold beads of a few nm diameters. These are deposited on the TEM grid and the specimen during sample preparation and can be tracked throughout the tilt series<sup>217</sup>. The position of these features is then used to solve the set of equations describing the geometry of the projection. This includes the shifts, but also the exact rotation about the tilt-axis and additional sources of displacement such as sample shrinkage, changes in magnification or out-of-plane tilts<sup>211</sup>. A benefit from this class of methods is therefore that angular refinement is provided by design and allows to compensate for goniometer inaccuracies or non-rigid modifications of the specimen during acquisition. However, the markers may result in strong contrast artefacts in the reconstruction and shadow the features of interest. This method is typically challenging for samples containing Pt/C catalysts as used here because markers can be misinterpreted for the nanocatalysts. Alternatively, the catalysts themselves can be used as tracking features but their typically high spatial density on the supports often leads to failure of the automated tracking and necessitates tedious manual corrections. Either way, these tracking methodologies rely on the accurate detection of as many features as possible, which has often proved difficult with the typically low SNR of the images acquired in this thesis.

A different class of methods operates on averaged information across the whole image and may therefore show accurate results even with noisy data or less distinct features. A typical strategy involves a first pre-alignment with cross-correlation to limit jumps between adjacent images<sup>211,218</sup>. If the object imaged is well-isolated (that is, with only background surrounding all sides), if it remains within the FOV with no parts moving in or out, and if the projection

requirement is strictly met, then the centre of mass can be used as a central point of alignment for all projections in the tilt-series<sup>219,220</sup>. However, since these conditions are often only partially met, more robust alignment methods have been devised. For example, the “common-line” or “vertical-mass fluctuation” methods operate on the principle that in perfectly aligned tilt-series, 1D projections on the axis of rotation should be the same for all images<sup>211,218</sup>. This strategy has been shown to solve shifts on the axis parallel to the rotation axis with sub-pixel accuracy. However, it is ineffective for shifts on the axis perpendicular to the rotation axis. For these situations, “iterative reprojection” or “projection-matching” alignment approaches can be powerful<sup>211,218,221</sup>. They operate on the basis that the reprojections of a perfect reconstruction exhibit minimum shifts to the projections that allowed its computation in the first place. It is then possible to write the cost function of an optimization task that iteratively reduces the shifts until the projections and reprojections match and to solve the optimization problem with, e.g., gradient descent methods.

Finally, determination of the tilt axis can be done directly by manual measurements of feature trajectories or using the Fourier transform of a maximum intensity z-projection of the full tilt series. Alternatively, the task can also be solved iteratively on the same basis as the projection-matching approach<sup>222</sup>.

### 3.2.5 Algorithms for 3D reconstructions

The next step in the tomography workflow consists in reconstructing the 3D object from the acquired projection. Traditional algorithms for reconstruction can be classified in two groups: direct transform methods that include backprojection (BP) along with Fourier-based techniques; and algebraic iterative methods such as the simultaneous iterative reconstruction (SIRT). More recently, methods have been developed that incorporate knowledge of the specimen for regularized reconstructions or assumptions about the image formation process in model-based reconstructions.

The backprojection algorithm performs operations that lead to smearing of the intensities in the projections back into the space that holds the reconstruction, from the angle they were acquired. Through summation, the local build-up of intensities defines the features from which the projections were originally formed. However, as the Fourier slice theorem dictates, tomography suffers from a relative undersampling of high spatial frequencies and BP reconstructions appear blurred because of this effect. Classically, a weighing filter in Fourier space is applied in order to decrease the contribution of the low spatial frequencies and improve the sharpness of features. On the other hand, direct Fourier inversion uses the Fourier slice theorem to directly populate the Fourier space of the reconstruction, before applying an inverse Fourier transform to recover the original object. The process involves an interpolation step to convert data from the polar

coordinates in which the tilt-series are acquired to the cartesian grid of the Fourier space that holds the reconstruction. This interpolation results in a loss of resolution that has typically inhibited the use of the Fourier-based methods.

The tomographic reconstruction task can also be mathematically stated (in matrix form) as an inverse problem aiming at recovering the object that gives rise to an observation (the projection images acquired in the TEM) via a forward transform (the projection operation)<sup>216,223</sup>:

$$y = \Phi x, \quad (5)$$

where  $y$  and  $x$  are vectors containing the observation and the original object, respectively, and  $\Phi$  is a matrix representing the projection operation. In an ideal case, there are sufficiently many observations and solving the system of equations yields a unique solution. In reality, however, the observations come in limited numbers and without the missing wedge, are rarely perfectly aligned and are degraded by noise. It follows that the problem is underdetermined and ill-posed and many solutions may exist that approximatively satisfy Eq. (5). To better approach a unique solution, algebraic iterative methods and more recent regularized and model-based approaches have been devised. These techniques aim at constraining the reconstruction to match the experimental data, while possibly embedding prior knowledge about the object or the image formation process along the way<sup>224,225</sup>.

A common algorithm from the iterative class is the simultaneous iterative reconstruction technique (SIRT). It can be formulated in the additive form as:

$$\hat{x}^{k+1} = \hat{x}^k + \rho_k \cdot \Phi^*(y - \Phi \hat{x}^k), \quad (6)$$

where  $\hat{x}^k$  is the reconstructed object at the  $k$ -th iteration;  $\rho_k$  is the relaxation parameter which influences the strength of the update;  $\Phi$  performs a projection via, e.g., discrete Radon transform;  $\Phi^*$  its transpose which performs an approximation of an inverse Radon transform implemented, e.g., via backprojection. An iteration of this reconstruction method reads as follows: starting from the reconstruction at the  $k$ -th iteration, this reconstruction is reprojected computationally and the difference between these projections and the reference, original data  $b$  is calculated. These *difference projections* are used to compute a *difference reconstruction* which is weighted by  $\rho_k$  and added to the current state of reconstruction. The SIRT algorithm therefore enforces data fidelity to find an estimate of the object. Given enough data, the SIRT algorithm effectively solves the optimization task:

$$\hat{x} = \arg \min_{\hat{x}} \|\Phi \hat{x} - y\|_{l_2}^2. \quad (7)$$

However, in the underdetermined case of ET, there may in effect be many solutions  $\hat{\mathbf{x}}$  that minimize Eq. (7). Also, the data are themselves corrupted, so that the difference  $(\mathbf{y} - \Phi\hat{\mathbf{x}}^k)$  in Eq. (6) eventually contains mostly noise. This highlights the issue of semi-convergence of the SIRT algorithm, with initial iterations leading to better approximations of the exact solution, but lower quality above a certain number of iterations. Furthermore, the SIRT algorithm cannot address the missing wedge elongation as no information is available in the observed data to constrain the reconstructions. Still, the algorithm is relatively computationally inexpensive and often yields good contrast.

The SIRT limitations underline the fact that in a problem as under-constrained as ET reconstruction, data fidelity alone is often not enough to retrieve a unique solution. A way to improve the quality of the estimated object is to simultaneously enforce other constraints defined by *a priori* knowledge of the object to be reconstructed. This class of methods operate by including regularization term(s) in the formulation of the problem and balancing their strength to obtain a reconstruction that possesses desirable characteristics while still satisfying data fidelity. A common approach is the compressed sensing framework, which assumes that the signal to be reconstructed is sparse in some basis. That is, there is a (sparsifying) transform that allows to represent the signal with only few non-zero coefficients<sup>224</sup>. The mathematical formulation of the problem then becomes:

$$\hat{x}_\lambda = \arg \min_{\hat{x}} (\|\Phi\hat{x} - y\|_{l_2}^2 + \lambda \|\Psi\hat{x}\|_{l_1}), \quad (8)$$

with  $\|\mathbf{x}\|_{l_2} = \sum_i \sqrt{x_i \cdot x_i}$  the  $L_2$  or Euclidian norm of a vector  $\mathbf{x}$  used to constrain the reconstruction with data fidelity,  $\|\mathbf{x}\|_{l_1} = \sum_i |x_i|$  the  $L_1$  or Manhattan norm used on  $\psi$ , the sparsifying transform, and  $\lambda$  the regularization strength parameter. The use of the  $L_1$  norm on the regularization term promotes sparse solutions because it penalizes many small coefficients and favours a few large ones so that Eq. (8) minimizes both the distance to the acquired data and the number of coefficients in the sparse basis. A plethora of sparsifying transforms has been implemented for ET to date, depending on the assumptions that can be made about the specimen. For example, a physically motivated prior that is often leveraged in materials science is that the original object has sharp boundaries and homogeneous atomic density within these. As such, the representation in the image gradient domain of such an object becomes sparse, because there should be only a few large gradients at the edges of the object and minimal contrast variation within or outside of it. The  $L_1$  norm of the image gradients is often referred to as the total variation (TV) of an image and the problem is that of TV minimization, which has found widespread application in ET<sup>224,226</sup>. Another common case is that of a few objects surrounded by an extended dark background, e.g., in the case of nanoparticles imaged in STEM-

HAADF. In this case, sparsity can be directly enforced in the image domain since only some pixels of the image are non-zero. Here, the sparsifying transform is simply the identity and this has often been applied in combination with TV minimization<sup>227</sup>. Herein, TV minimization alone was typically used because tilt-series were mostly acquired in BF-TEM mode resulting in non-zero background.

While regularized reconstructions incorporate knowledge about the specimen, it is also possible to include further assumptions about the mechanism of image generation in model-based methods. The goal is here to use a forward model ( $\Phi$  in Eqs. (5)-(8)) that may better represent the image formation process than a simple geometric projection. This is of particular interest if the projection requirement for ET is known to fail predictably but also when combining other signals beyond imaging or to provide more robust solutions to noisy data. Successful implementations have explicitly included a model for noise-generating processes<sup>228</sup> or non-linear effects<sup>229</sup> in HAADF tomography. The strong contrast variations introduced by diffraction in BF-TEM have also been taken into consideration<sup>230</sup>. In another instance, multislice simulation was used as the forward model to account for multiple scattering and enabled atomic ET of heavy elements in HRTEM tomography<sup>231</sup>.

### 3.2.6 Resolution in ET

Ideally, the resolution of tomographic reconstructions would be that of the acquired images. However, the constraints imposed by the TEM on ET acquisition (geometry, limited electron dose, ...) result in an often significantly degraded resolution in 3D. Assuming perfect alignment, the reconstruction resolution  $d_y$  in the axis parallel to the tilt axis should be equivalent to the image resolution, while the resolution  $d_x$  in the axis perpendicular to the tilt axis is constrained by the number of projections  $N_p$  acquired and the diameter  $D$  of the object to be reconstructed, as given by the Crowther criterion<sup>232</sup>:

$$d_x = \frac{\pi D}{N_p}. \quad (9)$$

This criterion was derived on the basis of angular sampling considerations for sufficient filling of the Fourier space. If the sampling is additionally done at  $180^\circ$ , then resolution in the  $z$  direction should be identical to  $d_x$ , however, in most situations, the missing wedge creates an elongation  $e$  that depends on the maximum angle  $\theta_{\max}$ :

$$e = \sqrt{\frac{\theta_{\max} + \sin \theta_{\max} \cos \theta_{\max}}{\theta_{\max} - \sin \theta_{\max} \cos \theta_{\max}}} \quad (10)$$

And the resolution in the  $z$ -direction is degraded following:

$$d_z = d_x \cdot e_{xz}. \quad (11)$$

While this criterion provides an indication for experimental design, it may in effect differ radically from the resolution achieved in the reconstruction. Indeed, reconstruction methods other than direct ones have the potential to overcome sampling limitations, while strong noise effects and artefacts arising from misalignments or other imaging factors (Fresnel fringes and focus variations, diffraction) have a negative impact. It is therefore interesting to be able to experimentally measure the resolution in the reconstruction. Various methods have been devised to this end depending on what limits the resolution (a PSF, reconstruction artefacts, the noise, ...). In noise-limited data, a measure of the resolution can leverage Fourier Shell Correlation (FSC) curves. The FSC aims at comparing the consistency of two independently reconstructed datasets containing the same signal but corrupted by independent (and theoretically additive) noise as a function of spatial frequency. In effect it measures the cross-correlation coefficient between two corresponding 3D shells in Fourier space<sup>233</sup>:

$$FRC(r) = \frac{\sum_{r_i \in r} F_1(r_i) \cdot F_2(r_i)^*}{\sqrt{\sum_{r_i \in r} |F_1(r_i)|^2 \cdot \sum_{r_i \in r} |F_2(r_i)|^2}}, \quad (12)$$

where  $F_j$  is the Fourier transform of image  $j \in [1,2]$  and  $r$  is the radius of the shell considered. The FSC can be directly related to the spectral signal-to-noise ratio (SSNR) allowing to define a measure of the resolution as the spatial frequency beyond which the SSNR falls below a given threshold<sup>211</sup>. A variety of arbitrary thresholds have been proposed, which relate to different ways of estimating at which point a voxel contains sufficiently enough signal to raise above the noise. A common choice is the half-bit threshold which corresponds to the point at which the average information content of a voxel in Fourier space is half a bit<sup>233</sup>.

If the resolution is set mainly by the instrument and the reconstruction artefacts, then measuring the sharpness or, conversely, the blur of features in the volume is more relevant. A straightforward way to do this involves taking an edge intensity profile and measuring the full width at half maxima (FWHM) of its derivative<sup>234</sup>.

### 3.3 Image processing and analysis

The effective analysis and interpretation of 3D data and time-series of beam-sensitive materials imaged at low-electron dose within this thesis required optimization of data processing pipelines for denoising and segmentation. This section gives an overview of some of the methods I used to this end.

### 3.3.1 Methods for denoising

The digital 2D or 3D images obtained on a computer are only distorted versions of the true (latent) signal. These distortions include blurring due to the CTF of the microscope, elongation due to the PSF of tomographic reconstruction with limited angular sampling and noise caused by the electronic circuit and the randomness of signal generation in the TEM. The problem is therefore to recover the latent image given only the degraded version and, possibly, knowledge of the physical processes from which the distortion arises. Specifically, noise in electron microscopy (and more generally most imaging technologies) can be modelled as arising mainly from the contribution of a Poisson term and a Gaussian one<sup>235</sup>. The resulting image  $y$  can then be stated as a function  $y = f(x)$ , with  $x$  the true image and  $f$  the forward model:

$$f(x) = Poi(x) + \eta, \quad (13)$$

with Poisson noise *applied* via  $Poi(.)$  and Gaussian noise *added* with  $\eta$ . Poisson (mainly shot) noise arises from the fact that recording an image involves counting events that are produced by random Poisson processes. In the TEM case, these are prominently related to emission from the electron source and scattering in the specimen. As shown in Fig. 3.8, a characteristic of Poisson noise is that the standard deviation increases with a higher expected value (true signal,  $\lambda$  in Fig. 3.8a). More specifically, the variance of a Poisson distribution is equal to the expected value and thus the standard deviation and the SNR are  $\sigma = SNR = \sqrt{\lambda}$ . In other words, the standard deviation of Poisson noise changes with the local image brightness. In contrast, the main source of Gaussian noise is the thermal agitation of electrons in the electronics and is therefore added after the initial acquisition of the image. It is zero-mean and parameterized by a standard deviation that is a characteristic of the detector, is uniform across the image, and is signal-independent.

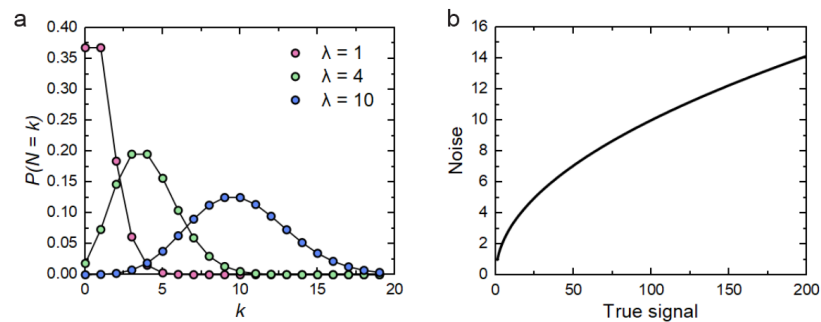


Fig. 3.8: Characteristics of Poisson noise. **a**, Poisson distribution for different expected values  $\lambda$  and **b**, standard deviation of Poisson noise for increasing true signal.

Either way, the SNR increases at higher counts and this motivates the simplest denoising strategies: binning or applying a (linear) filter<sup>236</sup>. Filtering in image processing involves the 2D

convolution of a kernel with the image, which is the basis of many more advanced methods. A kernel is a square matrix whose elements define the weights of a linear combination of surrounding pixels used to compute the new value of a pixel. While it allows many operations (e.g., approximating image gradients with Sobel filters), some simple and often used kernels are the local mean and gaussian ones, which directly increase the SNR by averaging pixel values in a given neighbourhood.

Beyond these simple filters, other methods include non-local means strategies that seek pixels similar to the targeted one to average them and patch-based approaches such as BM3D that searches redundant subsets of an image to assemble these in a 3D transform domain and denoise them together<sup>237,238</sup>. Another popular approach is to formulate the denoising task as an optimization problem that seeks (following notations in Eq. (13)) to find an estimate  $\hat{x}$  of the original signal  $x$  from noisy data  $y = f(x)$  by minimizing a cost function  $E$  so that:

$$\hat{x} = \operatorname{argmin}_{\lambda} E(\hat{x}, y) \text{ with } E(\hat{x}, y) = D_f(\hat{x}, y) + \lambda R_{\Psi}(\hat{x}). \quad (14)$$

In this formulation,  $D_f$  is a data fidelity term that ensures the estimation adheres to the observation via the forward model and is typically the Euclidian distance so that  $D_f(\hat{x}, y) = \|F(\hat{x}) - y\|_{l_2}^2$ .  $F$  is a model of the forward transform and, in the case of a denoising task, is identity.  $R_{\Psi}$  is a regularization term weighted by  $\lambda$  that enforces assumptions about the latent image by promoting some desirable properties of  $\hat{x}$  in the basis  $\Psi$ . For instance, smoothness can be promoted with Tikhonov regularization where  $R_{\Psi}(\hat{x}) = \|\hat{x}\|_{l_2}^2$ , or sparsity can be enforced in the spatial gradient domain to promote sharp edges in TV-minimization<sup>239</sup> so that, similarly to the problem of tomographic reconstruction,  $R_{\Psi}(\hat{x}) = \|\nabla \hat{x}\|_{l_1}$ .

A recent alternative consists in formulating the problem as a *learning* task<sup>240</sup>, where the goal is to find an approximation  $g$  of the inverse model so that:

$$\hat{x} = g(y) \sim f^{-1}(y), \quad (15)$$

where, for imaging problems,  $g$  is often set as a convolutional neural network (CNN) and is trained on the basis of sufficiently large sets of input-target pairs  $(y, x)$ . This assumes that, for training, true images are accessible, and that the learned model is capable of generalization so as to perform well on unseen corrupted data.

Neural networks are sequences of simple linear and non-linear mathematical operations organized in layers. Each layer produces an output that is then picked up by the next one as input and *deep* networks are those containing many such layers<sup>241</sup>. The core concept in neural network training is that each of these building blocks performs a differentiable function so that



their parameters (the *weights*) can be iteratively updated to minimize a loss function. This loss quantifies the discrepancy between the desired output  $x$  and the actual output  $\hat{x}$ . The update is performed using stochastic gradient descent and allows to fit models with millions of parameters, provided enough observations are available in the dataset.

Many types of layers and operations are available and some common ones are depicted in Fig. 3.9a. In CNNs, most layers are convolutions, i.e., filters with kernels typically  $3 \times 3$ , where each kernel is parameterized by its (trainable) weights<sup>242</sup>. By stacking many such convolutional layers, training a CNN can therefore be thought of as designing the best sequence of filters for a given task. Other typical operations include transfer functions (or *activation*) that allow learning non-linear relationships; down-sampling operations such as max-pooling that compress the signal and produce low-dimensional representations of the images; up-sampling operations, e.g., dilations, that allow to enlarge the images and increase the resolution. By interleaving these layers, many different network architectures have been designed and optimized for a variety of tasks. In this thesis, tools using the U-Net model have been mainly used<sup>243</sup>. As schematized in Fig. 3.9b, U-Nets feature an encoder-decoder architecture with the input being first progressively compressed in smaller, lower resolution maps, in hope that the model learns to pick up global and high-level features and excludes the noise. In the decoder part, the selected features are then up-sampled to obtain an output that matches the input resolution. This up-sampling alone would however result in blurred images, and skip-connections are therefore added to transfer some information from the high-resolution input and the first layers to the decoder side.

Critically, the many degrees of freedom of CNNs allow them to learn a variety of functions but also warrant caution against overfitting, i.e., the ability of networks to memorize the one-to-one correspondence of training pairs rather than learning a generic model<sup>242</sup>. Therefore, part of the training dataset must be kept for validation, whereby some of the pairs are used for inference only and the loss computed on the predicted output is used to track the performance of the models on unseen data. In addition, this challenge also highlights the need to build extensive training datasets in order to limit the chances of overfitting.

### 3.3 Image processing and analysis

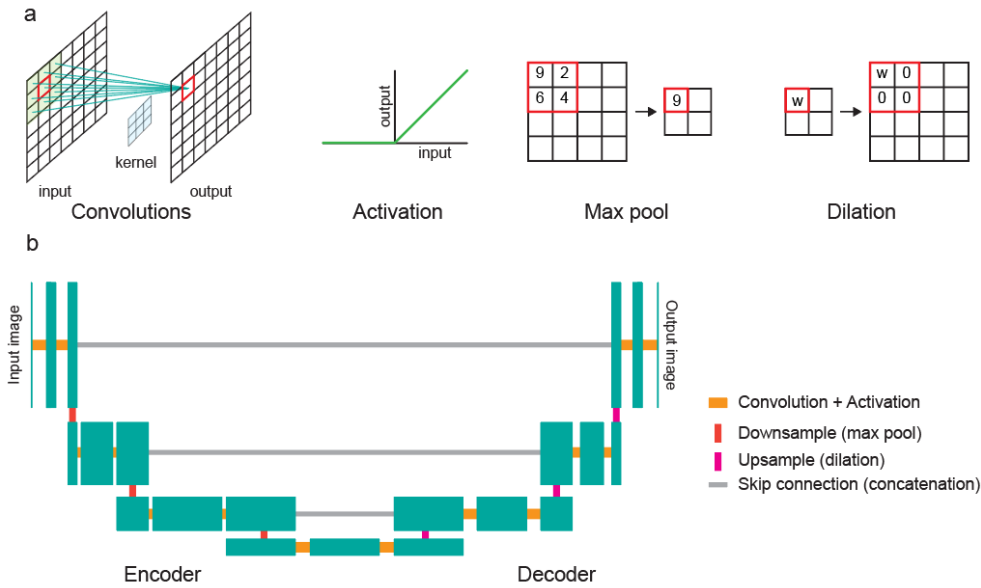


Fig. 3.9: CNNs and U-Net. **a**, Basic operations in (convolutional) neural networks and **b**, U-Net architecture.

The prototypical training strategy involves assembling pairs of corrupted and ground truth images (GT), with the latter being acquired e.g., with longer exposure time or higher dose if the specimen allows<sup>241,244,245</sup>. Alternatively, synthetic datasets can be constructed from image simulation. Cases where a GT is directly used for training are instances of *supervised* learning, but often, an empirical GT is not accessible and simulation might be too complex or might not adequately represent the real process of imaging. Various strategies have been devised to offer *unsupervised* or *semi-supervised* learning whereby only degraded data are used. Two examples and variations thereof that have found applications in microscopy are the Noise2Noise<sup>246</sup> and the Noise2Void<sup>247</sup> approaches. The former uses pairs of independently corrupted images featuring the same signal, which could be consecutive frames in a time series or independent tomographic reconstructions in the so-called cryo-CARE scheme<sup>248</sup>, depicted in Fig. 3.10; the latter aims at predicting the value of a given pixel based on its surrounding, requiring a single noisy image for training. Importantly, the performance of DL models output hinges on the quality of the training dataset, and it is required to be representative of the original images. Inadequate training can result in significant performance degradation and artefacts. It is also noted that in most cases, a neural network performs highly nonlinear operations and the output might not be appropriate for quantification of image intensities.

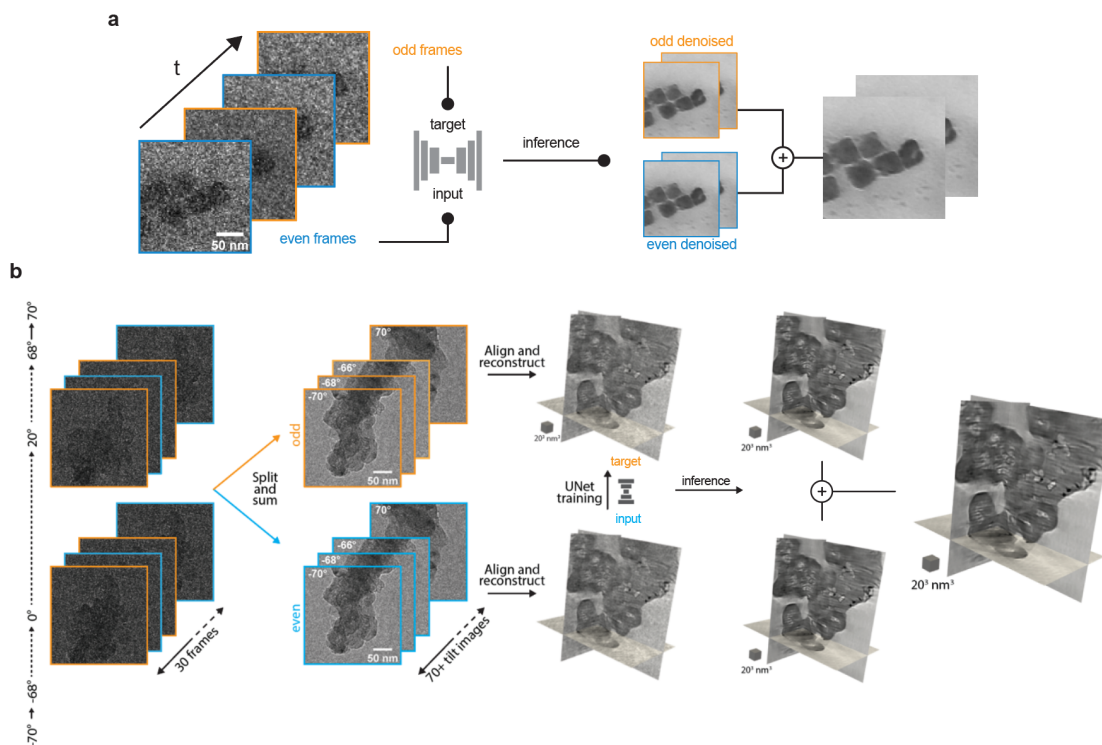


Fig. 3.10: Workflows for training a U-Net-based denoiser in the Noise2Noise regime from **a**, time series as acquired in ec-LP TEM and **b**, tilt-series with multiframe acquisitions as obtained from DE detectors. Raw image used in (a) courtesy of S. Toleukhanova.

### 3.3.2 Metrics of denoising performance

Many of the advanced denoising approaches require extensive manual tuning of hyperparameters to achieve the best performance. As a result, the operator is left with a large parameter space to explore, which is compounded by the variety of approaches to choose from. Metrics that reflect performance are therefore interesting and allow quantified comparisons between methods or parameterization of an algorithm. In supervised cases, a plethora of metrics is available that gives a sense of the quality of an estimate when compared to the true image. Some of these metrics include the normalized root mean squared error (NRMSE), the peak signal-to-noise ratio (PSNR), or the structural similarity index metric (SSIM) that reflects the degree of similarity between two images based on contrast, luminance and structural content<sup>249</sup>. In unsupervised training, no true image is available for comparison and estimation may then rely on *no-reference* metrics. One example that has been implemented for this thesis is the Q-metric, which was originally designed to automate parameter selection in denoising algorithms<sup>250</sup>. This metric computes an estimation of the sharpness of anisotropic features in an image from the singular values of the image gradients (see Fig. 3.11). It has proven to be well-behaved to blur and noise and can therefore be used as a descriptor of image quality. As the metric is, to date, not implemented in image processing toolboxes, a python version was

developed for this thesis. The Fourier ring/shell correlation curve described in Section 3.2.6 is also informative as it relates to the SNR as a function of spatial frequencies and it directly reveals whether improvements are made to the noise-limited resolution. Finally, the goal of denoising is often to prepare a dataset for segmentation and, therefore, segmentation quality is a hallmark of denoising performance.

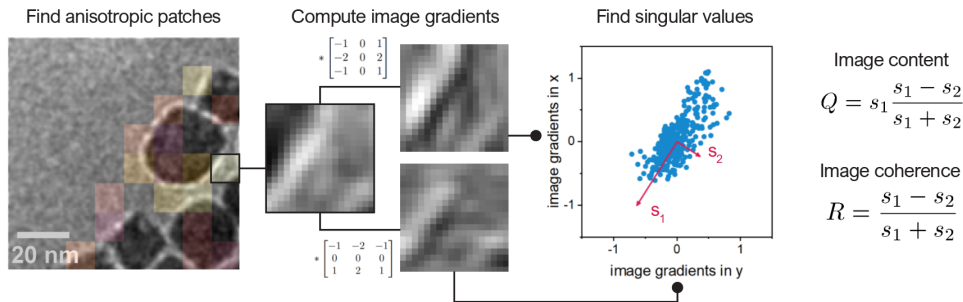


Fig. 3.11: Workflow for metric  $Q$  calculation<sup>250</sup>. The image is first divided into patches whose local image gradients in  $x$  and  $y$  are computed by convolution with Sobel filters. Singular value decomposition of the gradient intensities is used to compute the strength of the dominant orientation in the patch (first singular value  $s_1$ ) and of the orthogonal orientation (second singular value  $s_2$ ).  $s_1$  scales directly with the slope of the edge intensity and may be used as a measure of sharpness. The coherence  $R$  describes how anisotropic a given patch is and scales with the noise variance, the content  $Q$  multiply this value by  $s_1$  to obtain to metric that scales with edge blur and noise. Image for demonstration courtesy of S. Toleukhanova.

#### 3.3.3 Methods for segmentation

Segmentation is often the final processing step required to extract information from a 2D or 3D image and may be typically a task of *semantic* segmentation (identifying the different classes of pixels within an image) or *instance* segmentation (or *labelling* - separating each instance of a given object in an image). Fundamentally, it is therefore a task of classification and clustering of pixels together and is amenable to many algorithms developed for this purpose.

The simplest segmentation method is global thresholding, which effectively classifies pixels on the basis of their grey value being above or below a given intensity threshold. The threshold value can be set arbitrarily or in automated ways. For instance, histograms featuring a binomial distribution are well-suited for Otsu's threshold<sup>251</sup>, which aims at minimizing the intra-class intensity variance, while histograms with a dominant background peak and ideal threshold at the base of that peak may use the triangle threshold. In any case, global thresholding assumes that each class within an image possesses relatively homogeneous grey values and therefore is challenged in cases of strong noise, non-homogeneous background and objects with strong intensity variations within their boundaries. In these cases, it may be interesting to prefilter the image, not only for denoising but also to remove a possible background or to enhance edges with difference of gaussians<sup>252</sup>.

However, even if the difference between objects or classes might look obvious, optimization of the sequence of pre-thresholding operations can be a tedious task and this has led to the development of more automated methods. For example, pixel classifiers aim at learning the underlying classification logic from a few manual annotations<sup>253</sup>. They perform this by constructing *feature stacks* in which the original image is concatenated with  $n$  filtered versions at varying resolution. The operation can be thought of as positioning each pixel in a  $n$ -dimensions feature space with coordinates of grey values following each filter or sequence thereof. Using the inputs from manual annotations, this space is amenable to supervised clustering or classification using methods such as random trees or artificial neural networks. Subsequently, the class of other pixels in the image can be inferred from their position in the now-segmented feature space. These methods can prove very effective in many tasks but generally perform best when classes exhibit relatively homogeneous characteristics, e.g., of texture, grey levels or shape, that is, low intra-class variance in the feature space. In addition, classification is still performed using relatively low-level features, i.e., local context, and the construction and classification of the feature stack becomes computationally expensive for large datasets.

Deep learning methods can there again provide strong performance and greater generalizability at a lower computational cost (at least during inference). As with denoising, CNNs perform best for segmentation tasks<sup>254</sup>. Specifically, encoder-decoder architectures as found in the U-Net allow to create high-level features through down-sampling and to leverage non-local information due to the activation layers<sup>243</sup>. In comparison with the pixel classifier described above, a DL classification can be thought of as a way to create the most appropriate features, i.e., to find the best way to apply a sequence of filters, themselves tuned during training, on an image so that the result can be easily classified in the different phases the image contains. Training data are generated typically with manual labelling of many images<sup>241</sup> or using synthetic datasets<sup>255</sup>. It is important to note that manually labelled images do not constitute an exact ground truth and may be subject to errors and bias. Therefore, DL segmentation trained on annotations should perhaps be best considered as an extension of manual labelling.

### 3.3.4 Metrics of segmentation performance

A plethora of metrics are available to assess the performance of segmentation<sup>256</sup>. In this thesis, the precision, recall, and F1 (or Dice) scores have been specifically used, and these are calculated as follows:

$$precision = \frac{Nb_{TruePositive}}{Nb_{Predictions}} \quad recall = \frac{Nb_{TruePositive}}{Nb_{TruePositive} + Nb_{FalseNegative}} \quad (16)$$

$$F1 = 2 \cdot \frac{\textit{precision} \cdot \textit{recall}}{\textit{precision} + \textit{recall}}$$

The recall of the model for a given class is the fraction of ground truth pixels correctly labelled as such. A high recall means that most pixels attributed to a given class in the training data are effectively classified as belonging to this same class by the model; conversely, a low recall means that the model misses some pixels that are attributed to this class. The precision of a model for a class is the fraction of pixels of this class correctly labelled in the prediction, i.e., the fraction of true positives in all predictions. A high precision means that predictions of the model for a given class are often correct; a low precision indicates numerous false positives. Finally, the F1 score is the harmonic mean of recall and precision and provides an integrated view of the performance.

# 4 Three-dimensional Nanoimaging of Fuel Cell Catalyst Layers\*

## 4.1 Abstract

Catalyst layers in proton exchange membrane fuel cells consist of platinum group metal nanocatalysts supported on carbon aggregates, forming a porous structure through which an ionomer network percolates. The local structural character of these heterogeneous assemblies is directly linked to the mass-transport resistances and, hence, its three-dimensional visualization is critical for understanding the origins of performance losses. Herein, we implement cryogenic transmission electron tomography aided by deep learning methods for image restoration to quantitatively investigate the 3D structure of catalyst layers at the scale of the local reaction sites. The analysis reveals that the surfaces are typically covered by a 3 nm thick ionomer film while a highly continuous network results in the majority of exterior Pt catalysts being accessible to ionomer. We expect that our findings and methodology for evaluating the catalyst layer architecture will contribute towards linking the morphology to transport properties and overall fuel cell performance.

## 4.2 Introduction

The design of catalyst layers (CL) for proton exchange membrane fuel cells (PEMFC) involves an optimal interplay between metallic nanoparticles (2-3 nm, heavy-element, and crystalline) and the carbon supports (amorphous mostly, porous structures) in relation to the coverage provided by an ionomer network (down to a couple of nanometers, amorphous, and highly sensitive to radiation damage)<sup>13,20</sup>. This structure dictates mass-transport and, hence, performance losses<sup>19</sup>, but its complexity renders visualization in three dimensions of the interactions of the CL components very challenging, across the spectrum of imaging methodologies. Previously, the location of the nanosized metallic catalysts on the carbon supports was successfully imaged using electron tomography (ET) in transmission electron

---

\* This chapter is adapted from the accepted manuscript version of [Girod, R., Lazaridis, T., Gasteiger, H. A. & Tileli, V. Three-dimensional Nanoimaging of Catalyst Layers. *Nature Catalysis* **6**, 383–391 (2023)]. Author contributions: RG performed the sample preparation, TEM data acquisition, processing and analysis and wrote the manuscript with contributions from all co-authors.

microscopy (TEM) or scanning TEM (STEM) mode<sup>49,50,72,85</sup>. ET is an inherently dose-intensive technique and, hence, these studies omitted information on the extremely electron-beam sensitive ionomer phase<sup>117,148,257</sup>. Additionally, the poor contrast between the ionomer and the carbon support<sup>163,258</sup> makes quantitative analysis a difficult computer vision problem. Ion-exchange with heavy metals has been used as an enhancing preparation step for techniques based on mass-contrast such as high angle annular dark-field (HAADF)-STEM<sup>162,163</sup> or X-Ray absorption for nano-computed tomography (nCT)<sup>106,107,109,110</sup>. However, the nanocatalysts cannot be resolved in this case because the intensities of the different phases overlap or for lack of resolution. Moreover, the impact on the morphology of the ionomer layers and on their interaction with radiations remains unclear<sup>148,164</sup>. Other studies employed fluorine chemical mapping to gain insights into the ionomer morphology within CLs, using either electrons<sup>104,149,259</sup> or photons<sup>112,116,119,121</sup> as ionizing radiation but were systematically faced with trade-offs between resolution and radiation damage for access to three-dimensional data. Recently, atomic force microscopy (AFM) was implemented to characterize the evolution of ionomer layers during operation<sup>123,124</sup>, but its surface nature inherently brings limitations to imaging of buried nanocatalysts. To date, no single microscopy method has been successful in providing structural characterization of CLs and quantitative analysis of the interactions of the components directly.

To achieve three-dimensional nanoimaging of catalyst layers, we implement electron tomography at cryogenic temperatures (cryo-ET) on dispersed or microtomed samples, while leveraging deep learning methods for denoising and segmentation to obtain quantitative information. We start by investigating catalyst layers with graphitized supports and varying content of ionomer and find that microtomy is critical to preserve the ionomer morphology. This enables to characterize in full a section of a CLs fabricated with porous supports, in which the ionomer network is seen to cover 80% of the exterior carbon surface, typically with thin ionomer films, 3nm in thickness, but also with strands and aggregates and up to 24 nm wide. Because protons and gases are expected to diffuse through different pathways, we further differentiate between the thickness on surfaces and that within the network, with results underlying the different ionomer morphologies encountered by the reactants. Further, we investigate the accessibility of Pt surfaces by the network and relate this to electrochemical measurements in low relative humidity. Most external NPs are seen to be accessible but partially covered by the network, resulting in 15% of all Pt surfaces in direct contact with the ionomer. The findings demonstrate the potential of cryo-ET to enable investigations of the morphology of CLs.



## 4.3 Materials and methods

### 4.3.1 Materials

Samples used in this study were Pt/C catalyst layers (CL), prepared by Mayer rod-coating catalyst slurries onto PTFE sheets. All characteristics of the catalyst layers are summarized in Table B.3.1. Two carbon black support types were used: a compact, graphitized VA-type carbon (gVu in the following), and a high surface area, porous, Ketjenblack carbon black (KB in the following). Both were supplied by Tanaka Kikinokogyo (TKK). For the gVu carbon, Pt was deposited *via* a polyol reduction method<sup>70</sup> at a loading of 8.7 wt%, quantified by thermogravimetric analysis. Three CLs were prepared with those, using Nafion D2021 and ionomer-to-carbon weight ratios (I/C) of 0.35, 0.7 and 1.2. For the KB-based catalyst, the as-received material contained 19.8 wt% Pt that had been deposited by the manufacturer and a CL was prepared using a 3M 800EW ionomer (EW  $\equiv$  equivalent weight in units of  $\text{g}_{\text{ionomer}}/\text{mol}_{\text{SO}_3\text{H}}$ ), at I/C 0.7. The choice of using a lower equivalent weight ionomer was found to improve coating homogeneity, as seen from a backlight observation of the layers.

### 4.3.2 Sample preparation for electron microscopy

Samples for transmission electron microscopy (TEM) were prepared by dry-dispersion (samples gVu3, 7 and 12) or ultramicrotomy (KB7). For the dispersed samples, stripes of a CL were scraped with a scalpel blade and the resulting powder was lightly crushed between two glass slides to further break up larger clumps. TEM grids, typically lacey carbon, 200 mesh (Electron Microscopy Sciences), were repeatedly placed onto the powder until enough aggregates had been transferred as observed from optical microscopy. Microtomed cross-sections were prepared with partial or full embedding of small triangular stripes cut from the CLs, as described elsewhere<sup>61,260</sup>. For partial embedding, the first resin layer was a pre-cured Gatan's G2 and, for forming the blocks, the Embed 812 epoxy (Electron Microscopy Sciences), cured at 60°C overnight, was used. Microtomy was done at room temperature on a Leica EM UC7, using a Diatome cryo 35° diamond knife with a boat. 100-150 nm thin sections were cut and floated on water before transferring to TEM grids. The thickness choice was guided by the need to preserve the integrity of the sections.

### 4.3.3 Radiation damage evaluation and tilt-series acquisition

Tilt- and dose-series were acquired on a ThermoFisher Scientific F20 equipped with a Falcon III direct electron camera (ThermoFisher Scientific), and operated at 200 kV in bright field (BF) mode and using a 40  $\mu\text{m}$  objective aperture. The sample holder was a Gatan 914. When working in cryogenic conditions the holder was cooled in-column to -175°C (98 K) and contamination

by ice growth was regularly controlled, with an operating window usually lasting 3-5 h for each grid, depending on humidity conditions.

For radiation damage evaluation, dose-series of microtomed samples from the KB7 sample were acquired at a dose of  $1300 \text{ e}^- \cdot \text{nm}^{-2}$  per image, with an initial  $120 \text{ e}^- \cdot \text{nm}^{-2}$  required for positioning and focusing. The thickness of the ionomer coverage was manually measured as a function of the accumulated dose in 11 positions, with initial thicknesses ranging from 3 to 7.5 nm. The plots were linearly fitted, and the dose was corrected to ensure a 0 intercept.

For tomographic acquisition, tilt-series of  $4096 \times 4096$  pixels images were acquired at 50 kx magnification, resulting in a 0.2 nm pixel size. ThermoFisher Scientific's TEM tomography software was used to acquire images as sequences of 30 frames, each 50 ms, totalling 1.5 s of exposure time per angle. The electron dose rate was typically  $20\text{-}33 \text{ e}^- \cdot \text{nm}^{-2} \cdot \text{s}^{-1}$ , that is  $30\text{-}50 \text{ e}^- \cdot \text{nm}^{-2}$  per angle. On average, an initial irradiation with a dose of  $100 \text{ e}^- \cdot \text{nm}^{-2}$  was required to position the region of interest, optimize the focus, and obtain a snapshot of the initial state before acquisition. Each tilt-series then consisted of 65-75 projections in  $2^\circ$  increments. Focus was manually adjusted on-the-fly using no other image acquisitions and the region of interest (ROI) was tracked automatically by the software using cross-correlation between each tilt image and the previous angle. Tracking was typically lost once or twice during the tilt-series and the ROI was re-centred manually on these occasions. The dose rates, total accumulated dose, and sampling range for each acquisition are detailed in Table B.3.2. Due to the thickness of the sections, imaging was performed in thinner areas where a monolayer of carbon primary aggregates was identified from low-magnification images. Typically, a 600-700 nm-wide field of view without thick areas was required to prevent shadowing within a  $120\text{-}140^\circ$  range.

### 4.3.4 Tomography reconstruction and image processing

Before reconstruction, frames at each angle were aligned using the MotionCor2 software<sup>261</sup> and split in two interleaved even / odd stacks, each containing half of the frames. Frames were summed to a single image and  $2 \times 2$  binned, and the procedure was repeated for all angles before assembling in two tilt-series image stacks. We found that the combination of low signal-to-noise ratio, BF mode, lacey carbon grids, and microtomed cross-sections when employed, resulted in automated alignment methods such as centre-of-mass, cross-correlation or even IMOD's marker tracking performing poorly. Consequently, alignments were performed semi-manually, using a Pt nanoparticle visible at as many angles as possible and a tool for the FIJI software written in-house in ImageJ macro language<sup>262,263</sup>. Briefly, the macro allows users to place markers tracking a feature of interest throughout the tilt-series and subsequently translates the images to align these markers. Shifts can be recorded and applied to other stacks so that the same alignments were done to the even and odd acquisition series. Tilt-series alignments were

further refined manually down to pixel accuracy using the Tomviz software<sup>264</sup>. Finally, the rotation axis was identified by tracking the trajectories of nanoparticles throughout the tilt-series and corrected for centre and orthogonality.

Tomographic reconstruction was performed using the Astra toolbox<sup>265,266</sup> with code implemented in python. The cuda version of the simultaneous iterative reconstruction technique (SIRT) with 20 to 30 iterations was used to reconstruct two volumes from the even and odd tilt-series. Volumes were then used to train a deep learning model for denoising in a Noise2Noise regime<sup>246</sup>. Our code made heavy use of the open-source notebooks created by Bucholtz *et al.* for the CryoCARE workflow and we therefore refer the reader to the relevant publications<sup>248,267</sup> and GitHub repository<sup>268</sup>. Parameters were identical to those used by the authors and training was run typically for 150-200 epochs. The model was then applied to both even and odd volumes, before summing the output predictions into the final reconstruction.

Segmentation was performed using the YaPiC python toolbox<sup>269</sup>. The platform performs as a pixel classifier, allowing to train deep learning models from sparse annotations. For each reconstruction, a training dataset was generated by sampling one in ten z-sections throughout the volumes. Each section was annotated manually using the QuPath software<sup>270</sup> to obtain ground truth data. For the annotation procedure, all components could be identified by eye, following features described herein. However, reconstruction artefacts, the missing wedge elongation and remaining noise occasionally challenged this task. In such cases, close inspection of the surrounding volume allowed to make an informed decision.

The neural network used for segmentation had the classic U-Net (2D) architecture<sup>243</sup>, and minibatch-wise normalization, data augmentation by flipping, 20% validation and 50 training steps per epoch were used. Training was typically run for 500 epochs. We chose to work with segmentation in 2D rather than 3D for ease of annotation and speed of training, as 3D models have significantly more parameters to be optimized, which increases the risk of overfitting in our data-scarce regime. After training, the performance was evaluated on the training dataset and the annotations were completed as necessary to fine-tune the models, before applying them to the entire reconstructed volumes. The models have a soft-max activation as the final layer so that each pixel is returned as a vector whose elements are the scores associated with each class and have been normalized between 0 and 1, resulting in a probability-like map per class. Consequently, each map was binarized using Otsu's method<sup>251</sup> and the resulting volumes were reduced to a single stack with a singular grey level per class. Finally, a median filter with a kernel size of 1x1x4 voxels was applied to account for the anisotropy of the 2D segmentation.

### 4.3.5 Resolution estimation

Resolution of the reconstruction before and after denoising was estimated using Fourier shell correlations (FSC) between the volumes reconstructed from the even and odd stacks. Computation was performed using the FSC program from Image Science<sup>271</sup>. The resolution was estimated at the half-bit criterion.

### 4.3.6 Data analysis

From the segmented volumes, a range of metrics was computed, including volume fractions, carbon surface area and coverage by ionomer, connected components, ionomer network thickness, size distribution of the Pt nanoparticles and their accessibility and surface area. All operations and measurements were performed with FIJI and the MorpholibJ<sup>272</sup> and BoneJ2<sup>273,274</sup> plugins or in python using mainly the scikit-image, SciPy and PoreSpy<sup>275</sup> libraries. Volumes and multi-orthoslice views were rendered with Tomviz<sup>264</sup>. The detailed methodology and software used for each metric are described in Annex B.1.2.

Where applicable, an error measurement was estimated by calculating the mean absolute error between measurements from the processed volume and from an evaluation dataset, which was a set of densely and manually annotated tiles that were not used for training.

### 4.3.7 EDS analysis

Energy dispersive spectroscopy (EDS) hypermaps were acquired on a ThermoFisher Scientific Osiris TEM operated at 200kV at room temperature, with samples prepared by ultramicrotomy. For the fluorine distribution at the CL level, the F K $\alpha$  and Pt L $\alpha$  and  $\beta$  lines were fit to obtain net counts maps with a 50<sup>2</sup> nm<sup>2</sup> pixel size. The fluorine to platinum weight fraction was calculated from k-factor quantification performed in Velox (ThermoFisher Scientific). Under the assumption that platinum distribution is homogeneous throughout the electrode, the resulting map is representative of the ionomer distribution. For statistics, the mean fluorine weight fraction was measured in sub-areas of 500<sup>2</sup> nm<sup>2</sup> tiled over the entire acquisition. For the analysis of the KB7 tilt-series acquisition site, a map with 0.62<sup>2</sup> nm<sup>2</sup> pixels was acquired with a 0.6 nA probe, and a resulting total accumulated dose of 4.9x10<sup>7</sup> e<sup>-</sup>/nm<sup>2</sup>. For net counts, the maps were processed with the Velox software again, with the F K $\alpha$ , C K $\alpha$  and Pt L $\alpha$  and  $\beta$  lines fitted after a 3  $\sigma$  gaussian pre-filter. Decomposition was carried out with the Hyperspy python toolbox, after a 4x spatial binning preprocessing step and using the non-negative matrix factorization algorithm. To prevent interference from a Si contamination (see discussion in Annex B.1.3), the Si K $\alpha$  was masked before the operation.

### 4.3.8 Electrochemical measurements

MEAs with an active area of 5 cm<sup>2</sup> were prepared using the Pt/KB-based catalyst layers (KB7) described in Section 1.1 as cathodes, whereas anodes were fabricated based on a commercial 20.0 wt% Pt/Vulcan catalyst (TEC10V20E, TKK). The MEAs were prepared by hot-pressing anode/cathode decals at 155°C for 3 min onto a 15 μm reinforced membrane. Platinum loadings were determined by weighing decals before and after hot-pressing.

Fuel cell measurements were carried out in a stainless-steel single-cell hardware (Fuel Cell Technologies, USA) fitted with 5 cm<sup>2</sup> active area graphite flow fields (0.5 mm wide channels and lands, Poco Graphite). For the anode and cathode, Freudenberg H14C10 was used as a diffusion medium with a compression of 14%. Testing was performed on an automated Greenlight G60 test station. All MEAs were conditioned before electrochemical characterization using a voltage-controlled break-in procedure (H<sub>2</sub>/air at 1390/3320 nccm, 80°C, 100% relative humidity, and 150 kPa<sub>abs inlet</sub>), following a sequence of 0.6 V (45 min), open circuit voltage (5 min) and 0.85 V (10 min) for 10 cycles.

The Pt utilization was then determined by CO stripping voltammetry at 80°C and relative humidities of 10%, 20%, 30%, 50%, 70%, and 95%. Briefly, the cathode compartment, equilibrated to a set temperature and relative humidity, was flushed with CO (10 vol%, balance N<sub>2</sub>) for 10 minutes, followed by an N<sub>2</sub> purge of the entire test station and its gas supply. Three consecutive cyclic voltammograms were recorded by scanning the electrode potential between 0.1 – 1.0 V<sub>RHE</sub> at 10 mV.s<sup>-1</sup>. The charge corresponding to CO electro-oxidation, apparent in the first anodic scan at potentials above 0.6 V<sub>RHE</sub>, was obtained by integrating the current using the second anodic scan as a baseline, where no further CO oxidation occurred. The integrated charge can be converted into an electrochemically active Pt surface area using a charge density of 420 μC.cm<sup>-2</sup><sub>Pt</sub> for linearly bound CO. Finally, the RH-dependent Pt utilization is calculated by dividing the electrochemically active Pt surface at a given RH by its pendant at full humidification, i.e., the electrochemically accessible Pt surface area at 95% RH.

## 4.4 Results

### 4.4.1 Cryo-electron tomography of catalyst layer aggregates

Electron imaging of organic specimen<sup>198,276</sup>, including ionomers<sup>117,148,149</sup>, is typically performed at cryogenic temperature because it reduces the rate of radiolysis, which is the prime source of electron beam-induced damage in such materials. To access volumetric information, we combine it with electron tomography, where series of projection images are acquired over incremented specimen tilt angles and used to compute a three-dimensional reconstruction of the

## 4.4 Results

specimen. A schematic of the microscope configuration operated under these conditions is depicted in Fig. 4.1a, and examples of bright-field (BF) TEM images of a Nafion-graphitized Vulcan-Pt aggregate at increasing tilt-angles are shown in Fig. 4.1b. As demonstrated in Fig. 4.1c and Fig. B.1, operating at 98 K with a cumulative electron exposure of  $80 \text{ e}^- \cdot \text{\AA}^{-2}$  results in a 10 – 40 % thickness loss in the nanometers-thick layers found in the CLs. We note that within this dose range, the shrinkage-dose relationship appears linear and with limited influence of the initial ionomer layer thickness (Fig. B.1b). This indicates that for thicknesses up to  $\sim 8 \text{ nm}$  as investigated here, damage would be primarily related to radiolysis rather than charging as a direct relationship to ionomer thickness would have been expected otherwise.

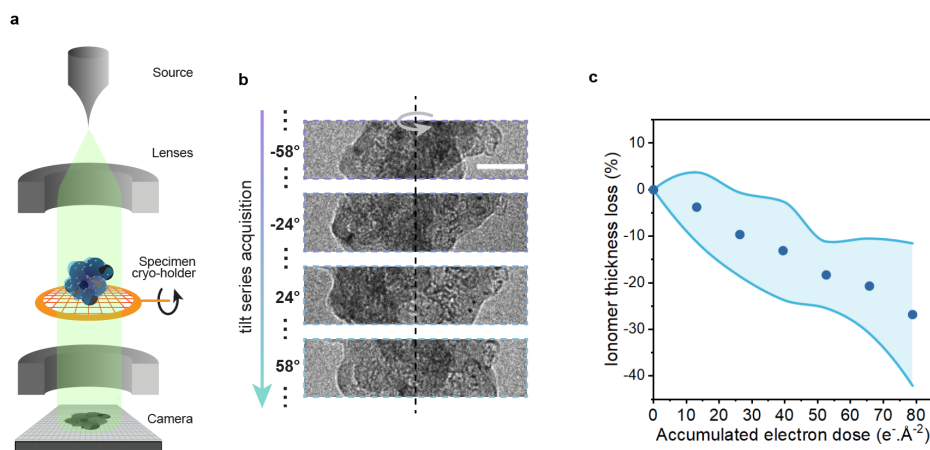


Fig. 4.1: Cryo-ET workflow. **a**, Schematic demonstrating the electron tomography acquisition. Aggregates are dispersed on a grid and imaged over  $> 70$  angles in  $2^\circ$  increments. **b**, Representative projections acquired during the tilt-series. Scale bar is 50 nm. **c**, Average beam-induced degradation measured from thickness loss of ionomer layers imaged at 98 K. Data points are the mean and shaded area one standard deviation ( $N = 11$ ).

To achieve a tradeoff between signal and electron beam-induced damage, tilt-series were acquired at low accumulated electron dose  $< 40 \text{ e}^- \cdot \text{\AA}^{-2}$  (see minimum signal calculations in Annex B.1.1 and details in Methods), thus inducing only limited degradation as demonstrated in Fig. B.2. Volumetric reconstructions were then computed with the cryo-CARE method<sup>244,248</sup>, which integrates a denoising procedure (see details in Methods and data preparation). Line profiles and image quality quantification in Fig. B.3a-d demonstrate that this workflow performed significantly better than other methods.

The result of this reconstruction and denoising procedure on an aggregate from a catalyst layer fabricated with Nafion ionomer, graphitized Vulcan (gVu) carbon supports, and Pt nanoparticles (sample gVu7 in Table B.3.1) is shown in Fig. 4.2a and b. Evaluation of the resolution using Fourier shell correlation plots (FSC, Fig. B.3e) showed that the denoising procedure resulted in an improvement from  $23.7 \text{ \AA}$  to  $16.9 \text{ \AA}$ <sup>211</sup>. Close inspection of the

reconstruction reveals that all three phases in the aggregate can be identified based on a complex combination of contrast and textural changes. As exemplified by the tomogram and line profile in Fig. 4.2b, the dense and highly graphitized shell of the carbon particles results in a darker contrast that surrounds a typically hollow and bright porous core. This shell was found to vary from a few carbon layers to tens of nanometers, which was further corroborated by high resolution (HR)-TEM images (Fig. B.4). Pt nanoparticles exhibit the darkest contrast with a characteristic size of 2 – 5 nm. The ionomer is identified by exclusion, as a smooth, typically continuous and slightly lighter binding phase surrounding or between the carbon and Pt particles.

Gaining quantitative insights from the reconstructions further requires segmenting the different phases. Since all components are discernible to the human eye, this task could be done entirely manually, but the size and complexity of the volume make segmentation effectively intractable at scale. Automation is then desirable, however, as demonstrated by the line profile in Fig. 4.2b, conventional grey-level thresholding is challenged by the low inter-component contrast. In addition, the remaining reconstruction artefacts can result in strong intra-component contrast variation and areas of uncertainty. To overcome this challenge, we investigated whether machine learning methods utilizing deep learning (DL) models could learn from manual annotations and subsequently perform as well as a human operator to segment unseen data. Specifically, and for each reconstruction, we trained a U-Net convolutional neural network, whose architecture has been shown to perform particularly well on microscopy images and in data-scarce regimes<sup>243</sup>. Each training dataset was obtained by manually annotating one-in-ten z-sections, as depicted in Fig. B.5a. We note that these annotations are central to the accuracy of the segmentation pipeline and care was taken to ensure their quality. Where artefacts created ambiguities, an informed choice was made by closely inspecting the surrounding region.

After training, each model was validated by evaluating the performance against manually segmented tomograms that were unused for training (see details of the data preparation, training scheme and validation in Methods). Fig. B.5c and d demonstrate that the method overall provides accurate segmentation of all components and shows performance on par with human annotations on most phases. Specifically, the ionomer was segmented with a 0.86 precision, meaning that 86% of ionomer predictions from the DL model were similar to human ones, i.e., only 14% were false positives in this volume. Applying the model to the entire reconstruction allows to visualize the segmented volumes, as shown in Fig. 4.2c and d. We note that each reconstruction in this work was segmented by a unique DL model and that the training is not universal.

## 4.4 Results

In Fig. 4.2e and Fig. B.6, we demonstrate that processed reconstructions can provide qualitative and quantitative information by investigating aggregates obtained by dry-dispersion of three model catalyst layers with varying ionomer-to-carbon (I/C) weight ratio (0.35, 0.7 and 1.2 w/w, see fabrication and preparation details in Methods and Table B.3.1). Volumes in Fig. B.6 allow to clearly visualize the morphology of the aggregates and the localization of the different components with respect to each other. In addition, the segmented reconstructions allow to compute a range of morphological metrics characterizing the ionomer-Pt-carbons interactions (see Methods and Annex B.1.2 for details on the calculations). With an increasing I/C ratio of the gVu electrodes, a monotonic uptrend of the local I/C weight ratio and of the computed carbon coverage is observed, as shown in Fig. 4.2e. However, the computed I/C ratio was systematically lower than expected, which we mainly attribute to disruptive effects from sample preparation by dispersion. To mitigate this, partial embedding<sup>61</sup> and sectioning in ultra-microtomy were used in the following.

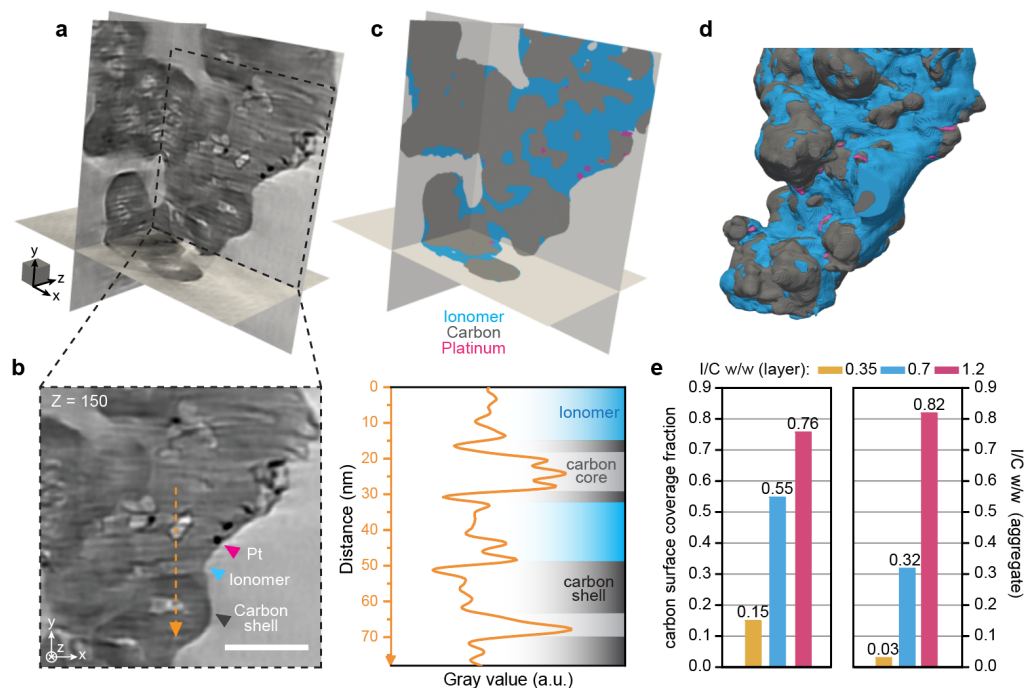


Fig. 4.2: Analyses of Nafion-gVu-Pt aggregates. **a** and **b**, Multi-orthoslices view and representative tomograms of a 0.7 w/w Nafion/gVu, with 8.7 wt% Pt on carbon (sample gVu7 in B.3.1). Scale bar is 50 nm and scale cube is  $20^3 \text{ nm}^3$ . A line profile of the grey levels is plotted along the orange dashed arrow in **b** to point out the different features. Shaded areas are provided as guides to identify regions corresponding to the ionomer phase (blue), carbon shells (dark grey) and carbon hollow cores (light grey). **c**, Segmentation results from the same aggregate and **d**, corresponding surface rendered view. **e**, Quantitative analysis of the carbon coverage and effective I/C w/w ratio in aggregates from the CL prepared with different ionomer content (samples gVu3, gVu7, and gVu12 in Table B.3.1).



#### 4.4.2 Structure of catalyst layers

To gain insights into the morphology of a typical PEMFC cathode, we then studied a catalyst layer with 19.8 wt%<sub>Pt</sub> supported on a high surface area, porous Ketjenblack carbon, and fabricated at 0.7 w/w I/C ratio with a 3M 800EW ionomer (sample KB7 listed in Table B.3.1). Sample preparation with microtomy was found to maintain a well-preserved open porosity while being amenable to tomography. FSC curves indicate a 17.5 Å resolution in the reconstructed volume.

Segmentation was performed following the same methodology established on gVu samples. In this case, the outermost, pseudo-graphitic layer of the carbons was usually well evidenced due to the greater inter-layers spacing compared to gVu. In addition, the internal porosity causes textural variations in the carbons, as opposed to the ionomer which was typically smoother. Side-by-side comparisons between grey-scale tomograms and segmentation results are presented in Fig. B.5e and f. There again, the DL model trained for this volume was found to perform well compared to manual annotations as shown in Fig. B.5g. Performance metrics were found to be close to the ones computed on the gVu7 sample, demonstrating the reproducibility of the method in matching human performance across different samples. In addition, EDS analysis on the site of the tomographic reconstruction was performed and is detailed in Fig. B.7. We find that signals associated with the ionomer are seen throughout the layer and overall match with the segmentation results, despite limitations in imaging thin ionomer layers with EDS and a low signal in the area (further discussed in Annex B.1.3).

A surface rendering of the segmented reconstruction is presented in Fig. 4.3a. Relatively small and oriented carbon aggregates formed of primary beads of 20-40 nm in diameter are observed, similar to the structures seen in TEM images of dispersions of the Pt/C catalyst (some examples of which are shown in Fig. B.8). The external surface area of the primary carbon particles is calculated to be  $120 \text{ m}^2 \cdot \text{g}_{\text{carbon}}^{-1}$ , not accounting for internal porosity of Ketjenblacks, which is in the range of typical solid, non-porous carbon supports<sup>42</sup>. Internal Pt nanoparticles as well as some carbon pores can be visualized in the reconstruction (Fig. B.9), however, a significant 50% of the surface fraction of this porosity is known to be held in pores smaller than the resolution of our data<sup>73</sup> and, therefore, pore analysis was excluded from this work. The ionomer network is visible as strands and thick patches connecting carbon aggregates and we calculate an I/C weight ratio of 0.73 (see Fig. 4.3b), in excellent agreement with the bulk value of 0.7. In comparison with results from dispersions, this demonstrates the importance of adequate sample preparation for analysis of the ionomer phase.

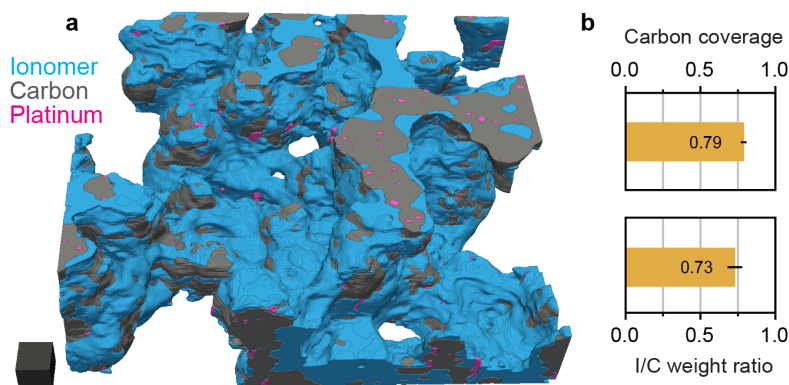


Fig. 4.3: Cryo-ET reconstruction of a microtomed 3M ionomer-KB-Pt catalyst layer. CL prepared with a 0.7 I/C weight ratio and a 19.8 wt%<sub>Pt</sub> catalyst (sample KB7 in Table B.3.1). **a**, Segmented reconstruction and **b**, measurements of I/C weight ratio and carbon surface coverage. Error bars represent the measurement error due to segmentation (see Methods). Scale cube is  $20^3 \text{ nm}^3$ .

We then studied the ionomer network morphology, an important characteristic of catalyst layers linked to reactant mass transport resistances and fuel cell performance<sup>23,79,80</sup>. A connected components analysis of the ionomer phase (Fig. B.10) indicates high connectivity with the single largest component accounting for 99.4 % of the ionomer volume. Coverage of the external carbon surfaces is found to reach 78% in this area, indicating that at this ionomer content, the majority of exterior carbon surfaces are in contact with the ionomer phase. To investigate the thickness and homogeneity of the network, we first computed the ionomer network thickness distribution using the local thickness algorithm<sup>277</sup> which accounts for the thicker areas and strands and relates therefore to proton transport within the network. We compare this to the carbon coverage and platinum coverage thickness distributions, obtained by calculating the distance from their respective surface to the nearest pore between the primary carbon particles (see Methods for details) which pertain more directly to oxygen transfer through the ionomer film. A colour-coded 3D map of the local thickness is presented in Fig. 4.4a, alongside close-ups taken from the volume and illustrating the difference between the two calculation strategies. The corresponding distribution plots are shown in Fig. 4.4b. We find a wide range of ionomer thicknesses, as observed previously from 2D micrographs<sup>278</sup> and hybrid simulation-observation methods<sup>106</sup>, with the network being on average 9.2 nm thick. The map and distribution also demonstrate the presence of large ionomer areas, up to 24 nm thick. Interestingly, complementary results obtained with ion-exchange (and discussed in more detail in Annex B.1.4 and Fig. B.14) indicate that phase separation likely exists within these large aggregates. In comparison, the platinum and carbon coverage extracted data exhibit narrower and close distributions, with mean thicknesses of 4.9 and 5.7 nm respectively, and a mode centred around 3 nm in both cases. This comes close to a geometrical estimation of the average

ionomer thickness of 3.8 nm at 0.7 w/w I/C,  $120 \text{ m}^2 \cdot \text{g}_{\text{carbon}}^{-1}$  and 78% coverage on a hypothetically planar carbon surface, with a higher value anticipated for results from tomography due to the more complex geometry. Furthermore, inspection of BF-TEM images of the same microtomed sample (Fig. B.11a-e) demonstrates that similar ionomer morphologies are observed across the section, while measurements of the thickness of the ionomer coverage are closely matching the tomography results (Fig. B.11f).

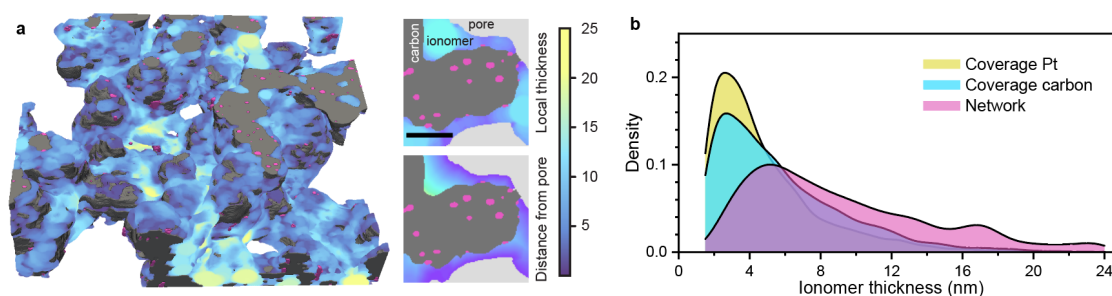


Fig. 4.4: ionomer network analysis. **a**, 3D map of the ionomer local thickness, and close-ups illustrating the difference in calculation with the local thickness algorithm and a graph-based distance calculation from the pores. Scale bar is 20 nm. **b**, Distribution of the ionomer thickness plotted for different sampling and calculation methods. The network thickness is sampled randomly throughout the ionomer in the local thickness map, the carbon and Pt coverage are sampled randomly at their respective interfaces with ionomer in the distance from pore maps. A cutoff at 1.5nm was introduced to account for the resolution limit.

To further study the representativeness of these results, the I/C weight ratio, carbon coverage fraction, and carbon coverage thickness were computed on three sub-areas from the volume used in Fig. 4.3 and Fig. 4.4. Results are plotted in Fig. B.12. The I/C weight ratio was found to differ significantly in the smaller area, coherently with the few large ionomer aggregates accounting for a significant fraction of the ionomer volume. The carbon surface coverage and coverage thickness were found to closely match the measurements that included the entire volume. Furthermore, we performed energy dispersive spectroscopy (EDS) analysis of the microtomed section (Fig. B.13), which indicates that at  $1\sigma$ , the Pt-normalized fluorine signal varies by less than 8.4% from its mean over areas of  $0.5^2 \mu\text{m}^2$ . Under the assumption that Pt is well distributed in the electrode, this suggests that ionomer distribution throughout the layer was relatively homogeneous. Taken together, these results suggest that analyses performed at the scale accessible in electron tomography can be considered representative.

In comparison with other attempts to characterize the ionomer film thickness in catalyst layers, we therefore find results coherent with Cetinbas and co-workers<sup>106</sup> at this ionomer content, but values significantly smaller than reported previously from STEM tomography<sup>163</sup> and *in situ* AFM<sup>123</sup>. These discrepancies could arise due to the difference in sample preparation with the former studies (see Annex B.1.4 on ion-exchange for contrast enhancement), and to the

## 4.4 Results

hydrated state of the ionomer and a possibly higher ionomer content in the later. Our measurements nonetheless form a coherent picture with the morphology of ionomer dispersions which are known to exhibit primary rod-like aggregates of radius 1.5 to 2.5 nm depending on the equivalent weight and side-chain length<sup>55,56</sup>, and secondary ones up to hundreds of nanometers depending mainly on the dispersion environment<sup>57,76</sup>. This agreement suggests that at this ionomer content, the carbon and platinum surfaces would be most frequently covered by a single primary ionomer aggregate, and therefore that the state of ionomers in dispersion and final morphology in CLs would be strongly linked.

The reconstructed volume further allows studying the morphology and interactions of the Pt nanoparticles with the carbon support and ionomer network. Fig. 4.5a shows a 3D visualization and a close-up tile of a sub-volume taken from the reconstruction in Fig. 4.5, where the interior Pt nanoparticles are labelled in pink and the exterior in green. A significant fraction (46 %) of the nanoparticles are found to reside in the nanopores within the carbon primary particles, in agreement with previous work on this type of high surface area carbons<sup>50,72</sup>. The distributions of interior and exterior Pt sizes are depicted in Fig. 4.5b. Both populations show similar morphology with an average diameter of 2.7 and 3.0 nm for interior and exterior, respectively, and a slightly wider distribution for the exterior particles ( $\sigma_{\text{interior}} = 0.7$  nm,  $\sigma_{\text{exterior}} = 1.0$  nm), likely due to particle growth constrained by the inner porosity of the carbon support during synthesis.

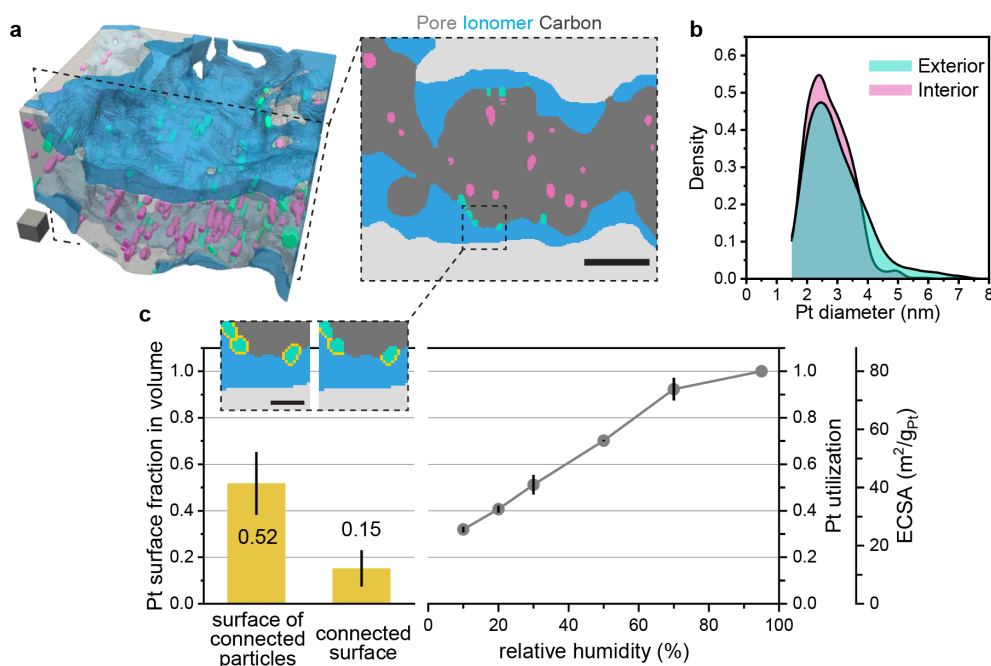


Fig. 4.5: Platinum-related morphology analysis in the microtomed 3M ionomer-KB-Pt catalyst layer. **a**, Sub-volume and 2D close-up maps from the segmented reconstruction in Fig. 4.3 demonstrating the localization of Pt nanoparticles inside (pink) or outside (green) of the porous carbon supports. Scale cube is  $10^3$  nm<sup>3</sup>, scale bar is 20 nm. **b**, Distribution of the platinum

diameters as a function of their localization. A cutoff at 1.5nm was introduced to account for the resolution limit. **c**, Comparison of Pt surface measurements from tomography and electrochemistry. Following the example in the close-ups, measurements from tomographic reconstruction are the Pt surface fraction in direct contact with ionomer (connected surface), and the fraction of Pt surface from particles in contact with ionomer (surface of connected particles). Electrochemical measurements are the ECSA and Pt utilization from CO-stripping surface area measurements as a function of RH in the MEA, scanned from 0.1-1.0 V at 10 mV/s and 80 °C. Scale bar in the close-ups is 5 nm. Error bars represent the measurements error due to segmentation for tomography (see Methods), and the min-max values of  $N = 2$  measurements for electrochemical data. Line is a guide to the eye and grey dots are the average of  $N = 2$  measurements.

Focusing on the exterior Pt particles and their connectivity to the ionomer network, we then compared surface areas that were computed from the tomograms to bulk measurements. Fig. 4.5c shows that different quantities can be obtained from tomography. As depicted in the close-ups in Fig. 4.5c, the connected surface is defined as the Pt surface in direct contact with the ionomer, which accounted for  $15 \pm 8 \%$  of the total Pt surface in the reconstruction. In comparison, the surface of connected particles is the measure of the total surface of all particles in contact with the ionomer and was  $52 \pm 13 \%$  of the total Pt surface in the reconstruction. The discrepancy between these quantities can be partly attributed to a tendency in the segmentation results to embed Pt more deeply than would be realistic, which is captured by our error estimation from mean absolute error calculations with the evaluation dataset (see Methods for detail). To compare with electrochemical measurements, we measured the electrochemical surface area (ECSA) by CO-stripping at varying relative humidity (RH), a method routinely used to assess Pt utilization<sup>64,97</sup>. Since oxidation of CO requires water and proton-conducting pathways, measurement of the ECSA in high RH conditions provides information on all Pt surfaces within the layer due to condensation of water on the carbon surface and within the carbon nanopores. Conversely, measurements at low RH would exclude surfaces that are not connected to the ionomer phase, which contains water and conducts protons even in dry conditions. The plot shown in Fig. 4.5c demonstrates the decrease in Pt utilization (the ratio of ECSA at a given RH to the measurement at 95% RH) as measurements are performed at lower RH. We note that the measurements do not reach a plateau within the investigated range, an observation that is further discussed in Annex B.1.5. The ECSA at 95% RH averages  $79.9 \text{ m}^2 \cdot \text{g}_{\text{Pt}}^{-1}$ , correlating well with the  $76.2 \text{ m}^2 \cdot \text{g}_{\text{Pt}}^{-1}$  total surface area from tomography and indicating that at these high RH conditions all Pt is accessible for CO-stripping<sup>50</sup>, including Pt particles buried within the nanopores of the primary carbon particles. At 10% RH, CO-stripping measurements indicate a Pt utilization of 31 %, which lies in between the values of the connected surface and of the surface of the connected particles computed from tomography. This suggests that a larger area than the one in direct contact with the ionomer participates in the ECSA measurements even in low RH conditions. As further discussed in Annex B.1.5, this

could indicate remaining interfacial and bound water<sup>279</sup>, or proton surface diffusion<sup>280</sup> in CO-stripping measurements at low RH.

### 4.4.3 Discussion

In summary, we elaborated on an approach that provides access to quantitative, three-dimensional data at nanometer resolution, allowing detailed observation of the PEM fuel cell catalyst layer structure with all its components. It was demonstrated that, while not completely suppressing e-beam-induced damage to the ionomer, performing cryogenic electron tomography sufficiently mitigates these effects and allows for volumetric reconstruction. In addition, advanced image processing methods provided access to quantitative measurements of all components while sample preparation with ultramicrotomy allowed observation of a highly continuous network and to study its characteristics. We confirmed that a wide range of ionomer thicknesses exist within the layer, up to 20-24 nm, with the majority of the Pt particles on the exterior of the carbon supports being covered by single ionomer aggregates, 3-4 nm thick. Additionally, the high coverage of the external carbon surfaces results in the ionomer network connecting the majority of exterior Pt nanoparticles when deposited on a porous carbon support.

More generally, routine investigations of catalyst layers with cryo-ET require further technique advancements. In this work, we relied extensively on human operators while leveraging machine learning as an extension to manual segmentation. This is a laborious process, which, in combination with the remaining reconstruction artefacts and noise, can entail a degree of uncertainty. Nevertheless, our results from the comprehensive nanoimaging study of the catalyst layers were systematically corroborated by bulk sample measurements and properties, including I/C ratio, ionomer average thickness and Pt-specific area. Looking forward, to limit uncertainty and streamline the image processing pipeline, methods for improving the signal-to-noise ratio in the acquisitions are imperative. Envisioned enhancements could leverage the advancements in instrumentation that includes more sensitive cameras and phase plates. In addition, strategies for reducing the operator's involvement in the segmentation procedure could build on a generic model trained on synthetic images that would be fine-tuned to each reconstruction requiring only a few annotations.

Thus, our results pave the way towards comparison of different catalyst layer morphologies at the nanoscale. Further investigations building on this approach could offer valuable insights into the effects of carbon-ionomer interface engineering, which have been recently implemented to develop improved carbon coverage<sup>79,80</sup>, and could help unravel the relationships between the state of ionomer in dispersions and catalyst slurries, and their final film and network morphology in catalyst layers.

# 5 Microporosity in High Surface Area Carbons\*

## 5.1 Introduction

In the catalyst layers (CL) of proton exchange membrane fuel cells (PEMFC), carbon black (CB) supports serve a three-fold function. They offer an extended surface area for dispersing metallic nanocatalysts (NC), an electrical conduction path to and from the reactive sites, and a tunable porosity for gaseous reactants to diffuse through<sup>19,23</sup>. The properties of the CBs and their interactions with the metallic nanoparticles (NPs) have a critical influence on the performance of the fuel cell<sup>23,281</sup>. For instance, their degree of graphitization dictates the corrosion resistance of the supports and, in turn, their durability over extended start-up/shut-down cycles<sup>282,283</sup>. However, the lower surface area of graphitized supports results in more aggregated NCs and, thus, reduced electrochemical surface area (ECSA)<sup>49,51</sup>. On the other hand, high surface area carbons (HSAC) such as Ketjenblacks (KB) offer an extended internal porosity in which NCs can be deposited<sup>49-51</sup>. This porosity confines the NCs and reduces their mobility and coalescence during operation, leading to better ECSA and mass activity retention at the end of life<sup>82</sup>. In addition, interior NPs exhibit an increase in specific activity, which arises from the protection offered by the porosity from direct contact with the sulfonic acid groups of the ionomer conventionally employed in PEMFC CLs<sup>62,64</sup>.

Yet, the use of KB comes with tradeoffs. Their high specific surface area (SSA) and disorder result in more carbon corrosion<sup>282</sup>, and the increased tortuosity that results from their primary porosity leads to higher oxygen mass transport resistances, especially at low Pt loadings<sup>71</sup>. This last point has been recently tackled with procedures that aim at locally modifying the KB porosity in order to optimize the tradeoff between ionomer protection for high kinetics and improved porosity for better mass transports<sup>71,73</sup>. N<sub>2</sub> physisorption analyses have revealed that, at optimal CL performance, the treatment results in an increase in the volume of both micropores < 2 nm and mesopores 5.5-14 nm in diameter<sup>73</sup>. As a result, current hypotheses link the performance improvements to either an increase of the pore size to an optimum value that

---

\* This chapter presents the results of a research work in collaboration with Timon Lazaridis and Hubert A. Gasteiger and is meant to be submitted for publication. Author contributions: RG conceived the research, performed the data acquisition and analysis and wrote the chapter.

does not restrict mass transport but still prevents ionomer intrusion<sup>50,71,73</sup>, or to a reduction in the interior tortuosity of the supports enabled by the removal of microporous constrictions<sup>72</sup>. In addition, the observation that Pt NPs are often tightly surrounded by narrow carbon pores has also suggested that Pt NPs may experience restricted local oxygen fluxes and hence, that the oxidation of carbon in the immediate surrounding of the particle would directly reduce mass-transport resistances<sup>72</sup>.

Either way, a detailed understanding of the transport properties in both the carbon supports and their modified counterparts requires an accurate picture of the CB microstructure. However, the diversity of morphologies within a single type of CB as well as the scale of the relevant features (a significant fraction of KB pore volume is held in micropores  $< 1$  nm in width<sup>73</sup>) have challenged the CB characterization efforts<sup>50</sup>. Historically, images have been typically obtained in high-resolution transmission electron microscopy (HRTEM)<sup>284–286</sup>. The technique has previously brought insights into the CB microstructure, revealing that most CBs host micropores and some, like KBs, large interior mesopores<sup>40</sup>. Some studies have further attempted to segment these HRTEM micrographs to gain insights into the arrangement of the graphitic planes seen in the exterior shell of CBs<sup>39</sup> and of resembling soot particles<sup>286</sup>. Yet, a common limitation is that 2D micrographs offer limited information on complex 3D structures. Electron tomography (ET) has therefore been used in a number of studies to investigate the distribution of Pt NPs on porous carbons<sup>49</sup> and has further revealed that different morphologies can be seen in KB carbons<sup>50</sup> and a seemingly increased mesoporosity in modified KBs<sup>72</sup>. However, the resolution in ET is typically limited by the missing wedge that smears the reconstructed features in the  $z$ -direction. Despite the findings highlighted here, the morphology of the smallest features and pores of CB structures has thus remained elusive.

In this study, we sought to uncover the nature and morphology of the interior meso- and micropores in KBs and to understand how the interior porosity in these carbons connects to the external space. To this end, we demonstrate an improved sample preparation method for full-range tomography and optimize the alignment and reconstruction procedure to achieve sub-nm resolution in tomographic reconstructions of a range of KB particles. We find that interior mesopores are separated from the exterior space by compact carbon shells in which only rare and small, sub-nm, openings are observed. These results are discussed in terms of the CB microstructure and implications for gas transport to interior reactive sites.



## 5.2 Materials and methods

### 5.2.1 Materials

The catalysts studies in this work were as-received, commercially available, 19.8 wt% Pt/KB (TEC10E20E, Tanaka Kikinokoku K.K., Japan), that had been platinized by the manufacturer. KB are highly porous carbon supports, and the SSA of this Pt/C material was previously measured to be  $\sim 500\text{-}550\text{ m}^2/\text{g}$  (ref.<sup>73</sup>). Modified versions of this catalyst were obtained by Pt-catalyzed oxidation. Briefly, the procedure involved placing samples in a tube furnace heated to the desired oxidation temperature for 12h, under a mixture of synthetic air and argon. Here, we used samples obtained from treatment at 290°C (KB290). Details about the treatment and performance of the resulting materials are given in ref.<sup>73</sup>.

### 5.2.2 Sample preparation for electron microscopy

For conventional TEM imaging and ET acquisition, inks were prepared by dispersing the catalyst powders in isopropyl alcohol (analytical grade, Sigma Aldrich) or chloroform (ACS reagent, Sigma Aldrich), at 0.1 mg/mL concentration. The inks were systematically sonicated in an ultrasonic bath and 2-3  $\mu\text{L}$  were placed and left to dry on ultrathin lacey carbon copper grids (200 mesh, electron microscopy science) or 5 nm silicon nitride window grids with 50 x 1500  $\mu\text{m}^2$  slots (model 76042-45, electron microscopy science).

For full-range ET, we used tungsten probes fabricated in-house by electropolishing, which is a fast and inexpensive way to obtain sharp tips down to the nm range<sup>287,288</sup>. Typically, a  $\sim 2\text{-}3\text{ cm}$ -long section was cut from a 1 mm diameter tungsten wire (99.99%, ref. 267562-15G, Sigma Aldrich). One end of this section was polished until flat and shiny on progressively finer sandpaper and SiC grinding paper.  $\sim 5\text{-}7\text{ mm}$  of this tungsten probe was then immersed in a 5 mL beaker filled with 3M KOH. The other end of the tungsten probe was connected to a potentiostat (SP-300, BioLogic) as the working electrode (WE) of the electrochemical system used for electropolishing. The counter electrode (CE) of this system was a Pd wire shaped as a coil,  $\sim 2\text{ cm}$  in diameter, that was placed in the beaker to surround the immersed end of the tungsten probe. A 4 V bias was applied to the tungsten WE with respect to the CE to induce electrochemical dissolution. At this potential, the reaction at the WE is typically limited by mass-transport, and the solution was agitated by a magnetic stirrer at 100 rpm to accelerate this etching process. We note that stirring should be gentle enough to maintain a still meniscus around the immersed tip, and the rotation speed should therefore be adjusted depending on the container used for the reaction. It is also important to ensure that the WE is well-centered in the CE coil to obtain a homogeneous current distribution and symmetric etching. In addition,  $\text{H}_2$  is evolved at the CE during the etching process, and therefore the coil should be large enough for

the bubbles to not disturb the meniscus around the probe. The immersed surface area of the CE should also be sufficiently large to not limit the currents in the system. For reference, with the geometry used here, currents at the beginning of the process were  $\sim 50$ - $100$  mA without stirring, and  $\sim 500$ - $600$  mA with. At this rate, the cylindrical end of the wire is narrowed to a  $\mu\text{m}$ -sized probe within 10-15 minutes. This was tracked with a camera placed at the height of the meniscus, but could also be followed from the decreasing currents as the tungsten surface area is progressively reduced. In our experience, currents were down to around 100-200 mA (with agitation) when the reaction was stopped.

Before deposition, the probes were primed with a thin layer of Nafion by dipping in a Nafion D520 solution (Sigma-Aldrich), to enhance surface adhesion with Pt/C aggregates. For deposition, each probe was immersed in a freshly sonicated catalyst ink (1 mg/mL in IPA) and the results were inspected in SEM (Quattro, ThermoFisher Scientific). We have found that a probe radius at the apex around 0.5-1  $\mu\text{m}$  was best and maximized the chances of having an aggregate clearly extending out.

### 5.2.3 Electron microscopy imaging

HRTEM imaging was performed at a ThermoFisher Scientific F20 equipped with a Falcon III camera (ThermoFisher Scientific) and operated at 200 kV. Images for KB morphology screening and tilt-series acquisitions were acquired at 150 kx magnification (4096<sup>2</sup> pixels, 0.68 Å pixel size), with a 40  $\mu\text{m}$  objective aperture.

For tomography in STEM mode, a Titan Themis (ThermoFisher Scientific) was operated at 200 or 300 kV with a 20-100 pA probe current, a 50  $\mu\text{m}$  condenser aperture and an 8-15 mrad convergence angle. The annular dark field (ADF) detector was used, with a camera length (collection angle) between 285 mm ( $\sim 20$ -125 mrad) and 910 mm ( $\sim 6$ -39 mrad) to adjust the balance of low angle (LA)ADF contrast and phase contrast.

### 5.2.4 Tomography acquisition and reconstruction

All tilt-series were acquired in 2° increments. For conventional ET, the specimen holder was a Fischione 2020, and for full-range ET a Fischione 2050 probe holder fitted with the on-axis cartridge for 1 mm probes.

Before acquisition and to limit carbon contamination, a  $\sim 15$  minutes beam-shower was performed for all samples at a 10-20  $\text{e}^-/\text{nm}^2/\text{s}$  dose. The tilt-series were acquired with ThermoFisher (S)TEM tomography software.

The full-range ET acquisitions were done in two steps, with a  $[-50^\circ, +50^\circ]$  tilt range each time and a  $\sim 90^\circ$  manual tilt of the internal rotation mechanism of the holder in between. The exact

internal rotation angle was determined in a custom-made automated procedure described in Annex C.2 and the full series were subsequently assembled in one. Alignment of the series was performed with the fully automated method and software developed by Odstrčil *et al.* in ref.<sup>218</sup>. The rotation axis was determined manually by tracking a particle visible at multiple angles and was corrected to be vertical.

Reconstructions were computed with the filtered back projection (FBP), conjugate gradient least square (CGLS), simultaneous iterative reconstruction technique (SIRT), total-variation minimization (TVM) or model-based iterative reconstruction (MBIR) algorithms. A comparison is presented in Fig. C.4 and their respective qualities are discussed in Annex C.4. The method used for each reconstruction presented here is specified in the caption of the corresponding figure. Reconstructions with the FBP, CGLS and SIRT algorithms were performed with their cuda versions of the Astra toolbox<sup>265,266</sup>, with code implemented in Python. For the CGLS and SIRT reconstruction, 30-60 iterations were run. TVM reconstructions were performed using the operator discretization Python library (ODL). The L2 norm was used on the data fidelity term and the L1 norm on the TV operator, with a regularization weight  $\lambda_{TV}$  typically 0.02-0.1. The Douglas-Rachford solver was used with default step size and was typically run for 8-12 iterations. The forward and back projections were handled with the ASTRA cuda backend. Before the reconstruction, the tilt-series intensities were normalized to a mean and standard deviation of 1 to be able to use approximately the same hyperparameters for different reconstructions. The MBIR algorithm is available in a standalone software described in ref.<sup>228,230</sup>.

### 5.2.5 3D segmentation and pore size analysis

Segmentation was performed in 3D with a pixel classifier implemented in the Ilastik software<sup>289</sup>. All intensity, edge and texture features were selected with sigma 1, 3, and 10. The pore thickness was evaluated with the local thickness algorithm implemented in Fiji's plugin BoneJ<sup>273</sup>. Surface renderings were done with Tomviz<sup>264</sup>.

## 5.3 Results

### 5.3.1 Heterogeneous morphology of primary aggregates in KB

To understand the microporosity in KB, we started by screening dispersed particles with HRTEM. A striking feature of these carbons, evidenced in Fig. 5.1a with more examples in Fig. C.1, is the large heterogeneity of morphologies observed in primary particles. The primary KB particles range from 5-10 nm *hollow* particles with large interior mesopores and thin, few-layers carbon shells, to > 50 nm *full* particles with very low Pt loading that indicates a poorly accessible

interior. In between, *porous* particles most often have a high Pt loading but a less clear mesoporosity in HRTEM. The transition between these populations is unclear which indicates a continuum of morphologies with poorly-defined modes rather than definite categories. With this limitation in mind, an evaluation of the prevalence of each type from manual counts in HRTEM micrographs indicates that the *full* morphology is less observed (Fig. 5.1b), reflecting  $N_2$  physisorption results that show that interior porosity must exist in most of these carbons in order to explain their high SSA.

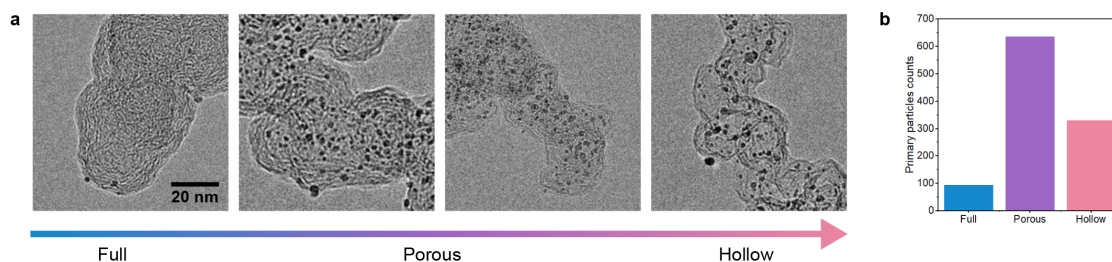


Fig. 5.1: Overview of Pt/C aggregate morphologies. **a**, Representative HRTEM images of pristine Pt/C aggregates. **b**, Morphology distribution extracted from manual counts.

To gain further insights into the morphological characteristics of these typical populations, we performed STEM-LAADF electron tomography acquisition and reconstruction of three particles. We note that these were modified KB-290 aggregates, not pristine ones, but the same kind of morphologies were observed in these carbons as well. Tomograms showing cross-sections across the reconstructed volumes are displayed in Fig. 5.2a-c along with surface renderings of the segmented particles and measurements of Pt-related characteristics (Fig. 5.2d). The full aggregate has few interior Pt NPs, which results in a 78% exterior surface fraction of Pt, similar to previously reported in non-porous, Vulcan carbon blacks<sup>50</sup>. In contrast, the porous and hollow particles both feature a high number of interior NPs, as shown in the tomograms and surface reconstructions. We find the exterior Pt surfaces to be 31 and 35% respectively, which matches with previously reported measurements in KB<sup>50</sup>. In addition, the greater interior porosity is correlated with a three-fold increase in Pt loadings compared to the full particle, with Pt loadings around 30 wt% vs. ~10 wt% for the full particle. Interestingly, we have observed these different morphologies to largely coexist in close vicinity, sometimes even within the same primary aggregates as demonstrated in Fig. 5.2e-h. The tomograms also reveal different interior morphologies of the porous and hollow carbons. Up to 10 nm-wide mesopores can be seen in the hollow particle while no clear interior pores are visible in the porous particles, whose porosity is only evidenced by the presence of interior Pt NPs. We note that dark intensities deceptively looking like micropores in Fig. 5.2c and f are attributed to reconstruction artefacts arising from the missing wedge and the point spread function of tomography. This indeed

creates fan-like features around the bright Pt NPs, with dark deficiency areas in the direction perpendicular to the tilt-axis<sup>290</sup>.

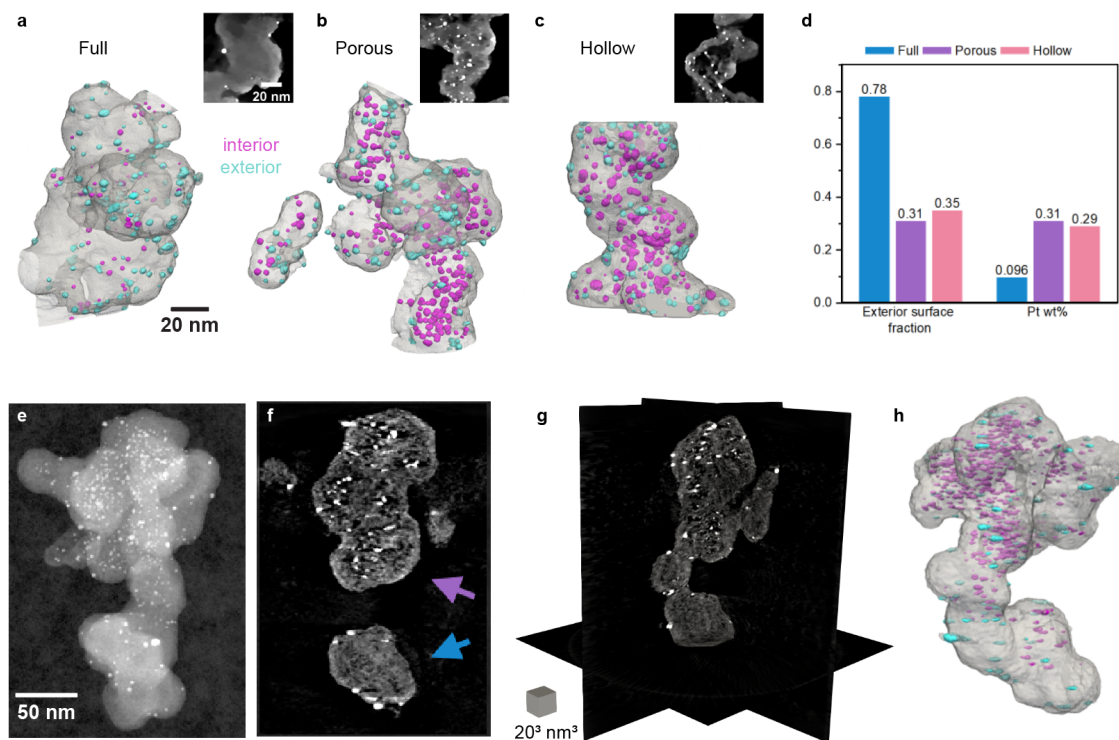


Fig. 5.2: STEM tomography of Pt/KB aggregates. **a-c**, STEM-LAADF electron tomography of representative KB-290 and **e-h**, and KB particles. Insets in **a-c** are tomograms demonstrating the morphological characteristics of the corresponding aggregate. **d**, Pt-related characteristics of the full, porous and hollow particles reconstructed in **a-c**. **e**, STEM-LAADF image from a tilt-series and **f**, tomograms from the reconstruction of the corresponding aggregate. The arrows indicate the parts of the aggregate exhibiting the full or porous morphology. **g** and **h**, multiorthoslices view and surface rendering of the reconstruction. **a-c** were reconstructed with the MBIR algorithm, **f-h** with TVM.

These results highlight two challenges in the TEM investigations of Pt/C catalysts. First, ADF reconstructions are prone to artefacts in the presence of a missing wedge and investigations of the microporosity in these materials require optimizations. Second, the large variance in morphology means that studies of carbon structural modifications (such as Pt-catalyzed oxidation for accessible carbons) should either build on robust statistics, which is hardly accessible with tomography or should utilize identical location measurements.

### 5.3.2 Full-range electron tomography for Pt/C catalysts

To improve the resolution in ET reconstructions, we first optimized the data acquisition part by using full-range tilting as a direct way of mitigating the missing wedge issue. The challenge, however, then lies in the sample preparation required to ensure the region of interest does not get shadowed at any angle. For materials amenable to focused ion beam (FIB) manipulation,

this has been commonly achieved by shaping a needle and transferring it to a dedicated substrate. The choice of the substrate is conditioned by the instrument and specimen holder, which, for full-range tomography, commonly hosts a probe. NPs on the other hand must be embedded for this method to be applicable, which is often inconvenient, limits the resolution, and may result in undesired interactions. Other methodologies rely either on dispersion and deposition<sup>138,215</sup>, or in-SEM transfer of a given NP or aggregate with dedicated methods<sup>287,291</sup>. In principle, dispersion is the most widely applicable method since it requires no dedicated equipment as opposed to the micromanipulators used for in-SEM transfer. Yet, the deposition of particles onto a sharp probe is inherently random, and commercial probes for full-range ET have an apex that is typically too large to reliably obtain particles extending out of surrounding material. Padgett *et al.* used nanofibers to provide an augmented surface onto which particles could then be deposited<sup>215</sup>, but we have found that Pt/C particles very rarely adhered to the fibres. In addition, the fibres are well-suited supports for metallic particles imaged in HAADF but may result in strong diffraction contrast and defocus fringes in BF- and HRTEM. As a result, no method in the literature was well-suited and straightforward for preparing Pt/C samples for full-range BF- or HRTEM ET.

Herein, we implemented a preparation method that relies on electropolishing a tungsten wire down to a nanosized probe and used a thin coating of Nafion as a priming layer to increase the adhesion of particles to the needle. The electropolishing protocol is described in the methods and importantly, only requires a DC power source and conventional chemicals. The final dimension of the needle can be finely tuned, and we have found that a radius around 0.5 – 1  $\mu\text{m}$  at the apex was ideal for Pt/C deposition. A typical probe obtained with this preparation is depicted in Fig. 5.3a, showing that a good surface coverage was achieved, with an aggregate extending out of the needle tip. Two reconstructions from tilt-series acquired in BF-TEM using a conventional specimen holder in the range  $[-72^\circ, +68^\circ]$  and the developed preparation are shown in Fig. 5.3b and d, along with Fourier transforms of a central tomogram in the  $xz$  plane. The full-range sampling directly mitigates the missing wedge as seen in the Fourier transforms, which results in a reduced elongation in the  $z$ -axis of the reconstructions.

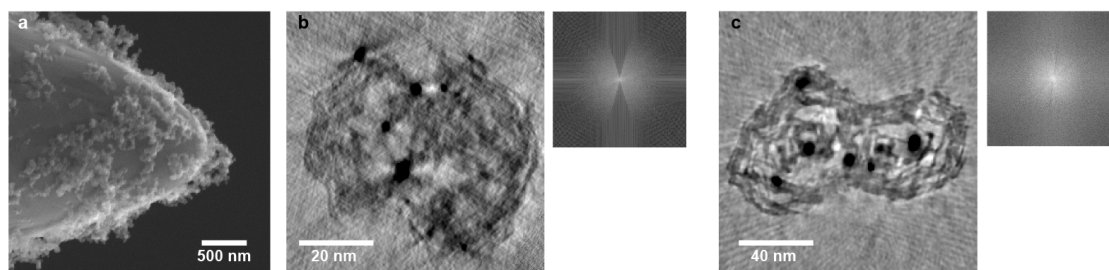


Fig. 5.3: Sample preparation and effect of full-range tomography. **a**, SEM image of a probe prepared for full range ET. **b**, tomograms in the  $xz$  plane of a KB aggregate in conventional BF-

TEM ET reconstructed with the SIRT algorithm from a tilt-series with a  $[-72^\circ, +68^\circ]$  angular span and corresponding Fourier transform. **c**, Tomogram of a KB aggregate reconstructed with TVM from a full range tilt-series and corresponding Fourier transform.

### 5.3.3 Microstructure and micropores in KB supports

To gain insights in the microstructure of KB supports, we reconstructed five primary particles or aggregates with the methodology described above. The particles cover a range of morphologies, as seen from the overview in Fig. 5.4. Three were reconstructed from BF-TEM acquisitions (Fig. 5.4b, c and e) and two from LAADF-STEM (Fig. 5.4a and d). The acquisition parameters were tuned to provide a combination of mass-thickness and phase contrast and an assessment of their respective qualities is given in Annex C.3 and Fig. C.3. A comparison of reconstructions algorithms is also done in Annex C.4, and we have typically used CGLS, SIRT or TVM as indicated in the captions. In this section, the contrast of TEM reconstruction was inverted to facilitate comparison and the aggregates are referred to by the letter (A-E) of their panel in Fig. 5.4.

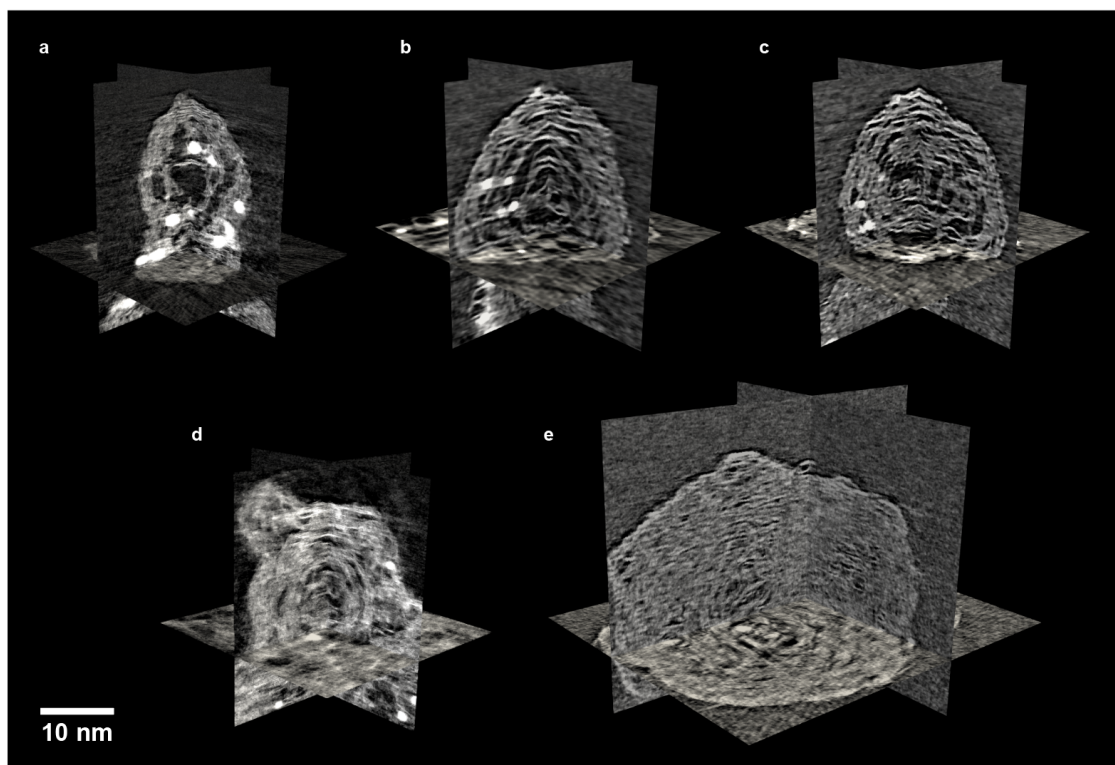


Fig. 5.4: Multiorthoslice overview of the reconstructions. **a** and **d**, STEM acquisition, SIRT reconstruction. **b** and **c**, TEM acquisition, TVM reconstruction. **e**, TEM acquisition, CGLS reconstruction. All volumes are shown to scale, and the contrast of the TEM reconstructions was inverted to facilitate comparison.



The first STEM particle (particle A, Fig. 5.4a and Fig. 5.5) could be categorized as *hollow*, following the classification established in Fig. 5.1. In it, large interior mesopores, up to 12 nm in width and widest at the centre of the particle, are enclosed by a relatively compact carbon shell,  $\sim 5\text{-}7$  nm thick in most places. Some medium-sized pores, typically 1-2 nm wide but also down to 0.5 nm, run through this shell (Fig. 5.5b and c, magenta markers). These are in most instances slit-shaped and can be seen in some places to arise from the imperfect stacking and peeling-off of carbons planes. Importantly, these pores do not seem to percolate and connect to the exterior. Pt NPs are dispersed throughout this porosity, most often in the medium pores of the carbon shell (Fig. 5.5c). The resolution of this STEM reconstruction also shows that the interior mesopores are separated by thin carbon walls, typically 1-4 loosely stacked and crumpled graphene sheets (Fig. 5.5b and c, green markers). These carbon walls can bend very strongly in the centre of particles. In some places, this creates quasi-spherical and hollow nodules, 3-4 nm in diameter, that occupy the central cavity (cyan markers in Fig. 5.5b and multiorthoslice close-up in Fig. 5.5d).

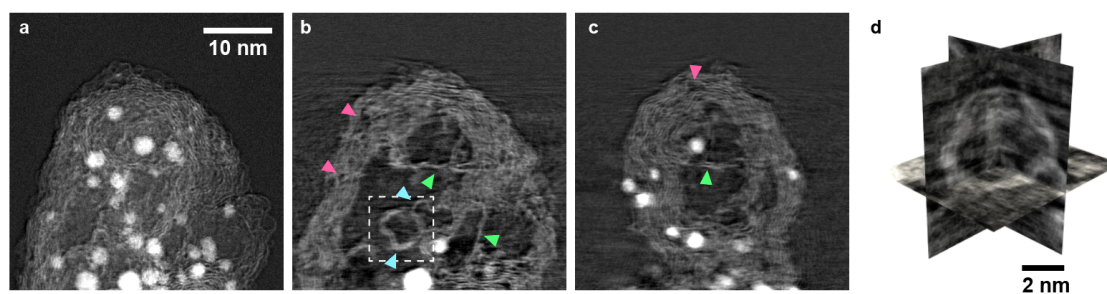


Fig. 5.5: Reconstruction of particle A. **a**, STEM ADF image, **b**, **c** tomograms from the corresponding SIRT reconstruction showing representative features. Magenta arrows indicate pores, green arrows interior 1-2 layers walls and cyan arrows carbon pseudo spherical structure. **d** shows a multiorthoslice close-up of such a structure (dotted square in **b**).

The next two reconstructions were done on the relatively similar particles B and C, which would be categorized as *porous*, and are displayed in more detail in Fig. 5.6. Here, a different, more homogeneous and concentric porosity is visible with a less compact and poorly defined outer shell. Still, the pores tend to be larger towards the centre, where carbon walls are highly disordered, warped and bent. This also creates different morphologies, with pores being closer to ellipsoids at the centre, sometimes forming the same pseudo-spherical features seen in particle A. To the sides, they are rather curved and slit-shaped. Visualized in 3D, these slits have the shape of oblate spheroids, sometimes dish-like with an additional curvature along the two main axes of the spheroids for the biggest pores (an example is displayed in Fig. 5.6c). The length of the slits ranges from 1 to  $> 10$  nm, without a clear mode. Pore width range from up to 3.5 nm but most often  $\sim 1\text{-}2$  nm for interconnected micro-mesopores, to very frequent deep sub-



nm openings as small as 0.5 nm between carbon layers (Fig. 5.6d). The graphene sheets were not clearly resolved individually, but the width of the pore walls was commonly down to a 0.4-1.1 nm range, indicating 1-3 carbon layers. Due to the resolution of the acquisition, the BF-TEM noise background, contrast mechanism, and reconstruction artefacts (see related discussion in Annex C.3), it is somewhat difficult to ascertain the origin of all intensity variations in the sub-nm range and, thus, the full extent of the smallest micropores. Still, many pores exhibited high contrast and were resolved without ambiguity (Fig. 5.6d).

Importantly, very few pores are found to open to the exterior, and these were almost systematically sub-nm in diameter (magenta markers in Fig. 5.6e). We stress that, despite the reconstruction uncertainties, pores in the nm-range and above are unambiguously resolved and yet, we only found a single instance of such a pore,  $\sim 1.2$  nm wide, connecting to the exterior in of these two particles (green marker in Fig. 5.6f). In addition, tracking the pathways between the possible sub-nm entry points and larger pores where the Pt NPs reside was challenging, with many sub-nm constrictions at the limit of the achieved resolution.

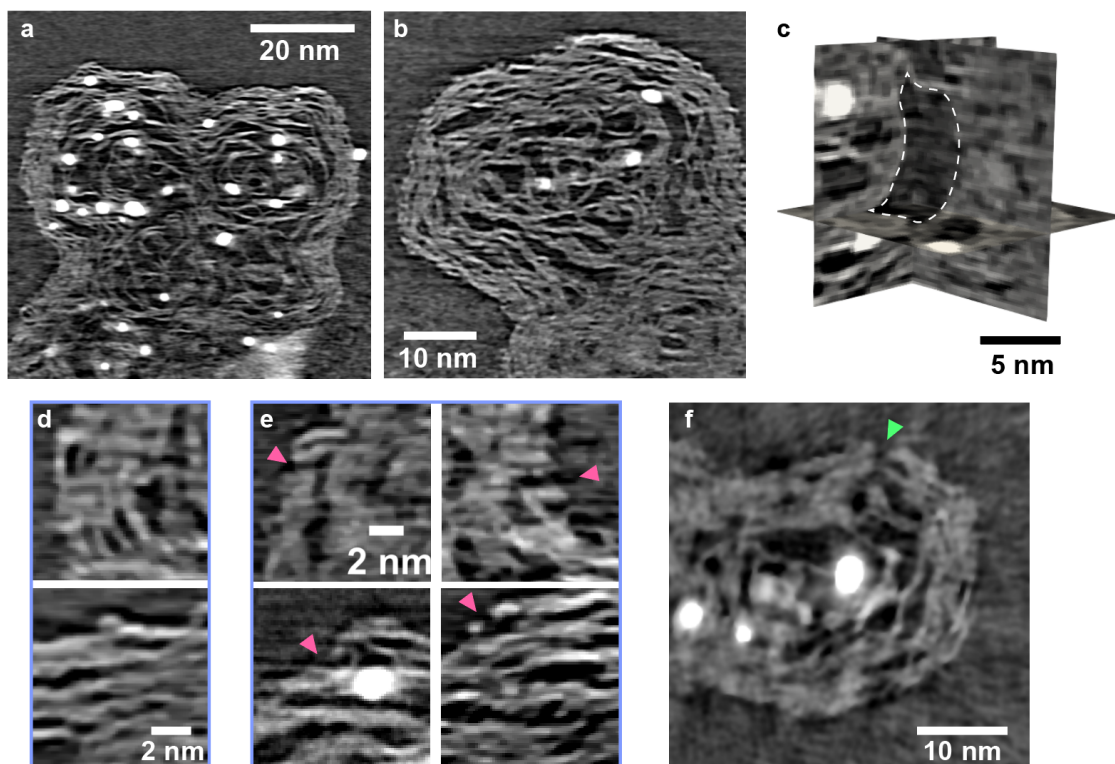


Fig. 5.6: Tomograms from the TVM reconstructions of particles B (a) and C (b). c, multiorthoslice view of an oblate slit-shaped pore. d, representative examples of well-resolved deep sub-nm pores. e, representative examples of entry pores in the carbon shell. f, Unique instance of  $> 1$  nm entry pore, here  $\sim 1.2$  nm wide.

Fig. 5.7 depicts the segmentation of porosity on a sub-volume from particle B. The results do not include the smallest pores but are reasonably accurate on pores in the range of 0.8-4 nm.

### 5.3 Results

The pore diameters were evaluated with the local thickness method, which calculates the diameter of the largest inscribed sphere at a given point. Visualization of the pore thickness in 3D (Fig. 5.7b) demonstrates the global distribution of the pores and their tendency to be wider towards the centre of the particle. The corresponding (volume-weighted) pore size distribution (Fig. 5.7c) peaks around 1-2 nm in diameter. In comparison, manual measurements of the diameter of 340 pores in the two reconstructed particles show a prevalence by counts of sub-nm pores with a mode at 0.6-0.7 nm (Fig. 5.7d), while the corresponding volume-weighted distribution exhibits a mode around 2 nm (not shown).

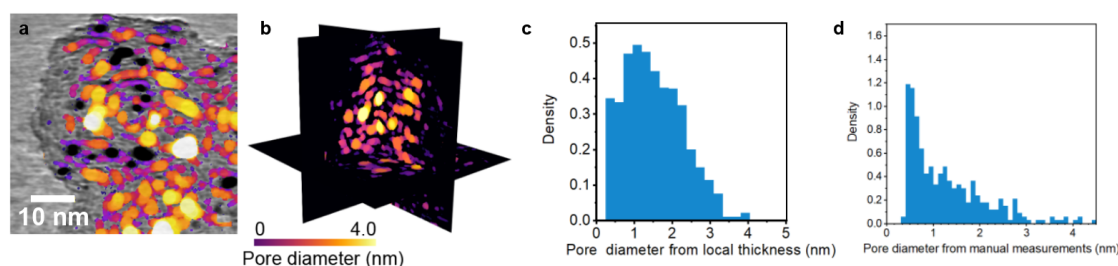


Fig. 5.7: Porosity segmentation. **a**, overlaid tomogram from particle C and segmented porosity result after local thickness calculation. **b**, 3D view of the pore local thickness of the pores and **c**, resulting pore size distribution. **d**, comparison with pore size measured manually.

Next, the aggregate D was imaged in STEM and included a particle mostly devoid of Pt NPs in its interior pores (Fig. 5.8a and b). The morphology of the aggregate otherwise resembles particles B and C, but with a thicker carbon shell, 10-12 nm in thickness, through which 0.5-1.5 nm wide slit-shaped pores are running (Fig. 5.8c). The centre is also disordered and meso-microporous with pores mostly in the 1-3 nm range. In some places, the interior space is seen to be filled with the same pseudo-spherical nodules as seen in particle A, but stacked at a higher density (Fig. 5.8d). In most places, it resembles the centre of particles B and C where the transition between this disordered centre and the increasingly stacked shell is not distinct, but it is clear that the pores get smaller and the carbon walls between them become thicker towards the outer edges. Interestingly, this aggregate features partially fused primary particles which have the same overall morphology but a different number of interior Pt NPs (clearly seen in Fig. 5.8a). Because all these primary particles seemingly feature an identical outer shell, this suggests that the precursors for Pt NPs synthesis did not diffuse through it. Instead, they may have come from other large openings not observed here, and then diffused through the wider interior pores. The carbon particle in Fig. 5.8 would then be Pt-empty because it sits at the end of a perhaps too tortuous pathway.

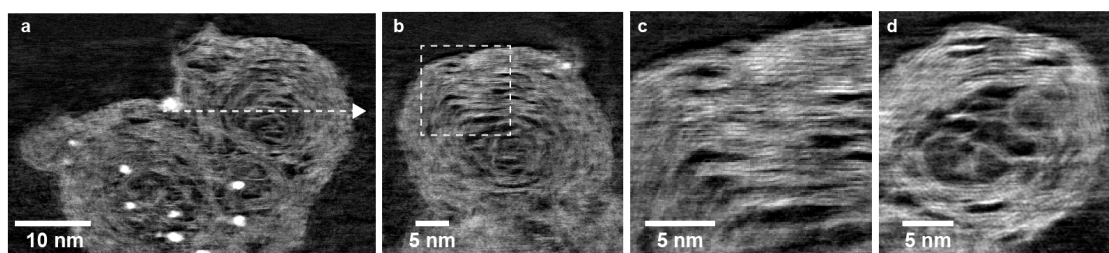


Fig. 5.8: ET of particle D. **a**, tomogram from a SIRT reconstruction. **b**, is a cross-section view along the arrow in **a** showing a particle without Pt from this aggregate. **c**, close-up of the dense carbon shells and slit-shaped pores in **b**. **d**, Satellite particle of the aggregate showing buckled and spherical, few-layers carbon features in its interior.

For completeness, we finally reconstructed a *full* particle (particle E in Fig. 5.9), which at  $\sim 70$  nm in diameter is larger than all previous reconstructions. It is without interior Pt NPs as observed on similar morphologies in Fig. 5.2. Here, the dense carbon shell is about 20-25 nm in thickness. Slit pores run through it as well but are smaller on average than observed in the other particles, at most 1-1.2 nm and typically 0.5-1 nm in thickness. A disordered core is also observed, which resembles that of particles B-D, although with smaller pores, up to 2 nm and typically 1-1.5 nm wide.

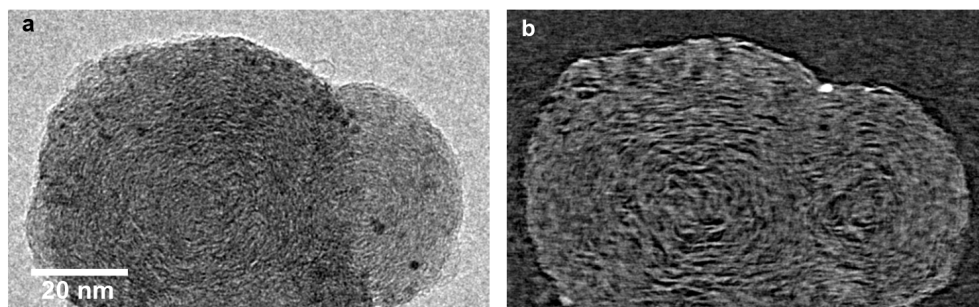


Fig. 5.9: ET of particle E. **a**, TEM image from the tilt-series and **b**, corresponding tomogram from a CGLS reconstruction.

## 5.4 Discussion

Overall, it is clear that the microstructure of KB carbons is varied. The observations made here bear implications for the fuel cell performance but also for the understanding of the synthesis of these blacks and the microstructure of porous carbons in general.

The microstructure of CBs and the origin of their microporosity is a long-debated topic<sup>42,292</sup>. The first models have postulated that the compact exterior shell observed in HRTEM could be composed of basic structural units (BSU) which would be few-layers (5-7) graphitic stacks arranged concentrically around the more disordered center<sup>285</sup>. Refinements have promoted the idea of BSUs structuring the shells, but with larger hexagonal or elliptical units, 2.5-5 nm in

diameter, in which a small degree of curvature may arise<sup>45,293</sup>. More recently, the evidence of pentagonal and heptagonal defects in activated carbons has suggested that the curvature of CB could also be related to fullerene structures<sup>46,47</sup>, in which odd-membered rings give rise to warped and bent carbon sheets<sup>47,292</sup>.

In the large carbon shells reconstructed here, we observed compact and arranged stacks of carbon planes, particularly in aggregate D, which would be coherent with the BSUs view. On the other hand, the shell of particle A appears less structured and lacks such units. This may suggest a progressive ordering when shells grow thicker<sup>286</sup>. The strongly bent and few-layers carbon planes in the core of the particles reconstructed herein also support the presence of defects and fullerene-like structures, which are required to give rise to these pseudo-spherical structures. In addition, some of the slit-shaped pores seem to arise from carbon plane “peeling-off” (e.g., Fig. 5.8c), which suggests warped graphene sheets and odd-membered ring defects rather than an imperfect stacking of rigid and planar units.

Further, the interior morphology can provide insights into the synthesis pathway of the porous KB. For denser CBs that resemble the *full* morphology reported here, particle aggregates are thought to form in three steps<sup>292</sup>. Firstly, aromatic layers in the vapour phase condense to form nuclei, which then coalesce randomly giving rise to a disordered core. In the second step, surface deposition occurs and defines the more ordered carbon shells. Finally, these particles aggregate without coalescing in long chains joined by necked interfaces. It is unclear however if the synthesis of mesoporous carbons follows the same pathway. In the particles imaged here, the pseudo-spherical nodules that populate some of their core suggest that better-defined structures, perhaps fullerene-like, pre-exist an initial coalescence step, and may give rise to the large interior pores at the core of these carbons. Furthermore, the apparent connectivity of the central pores and the continuity of the external shell between primary particles, seen for example in particle D, shows that aggregation may happen at an earlier step already only then followed by surface growth. Better segmentation and further analysis of the interior mesoporosity would be required to quantitatively study the characteristics of the interior pore network, e.g., its connectivity and tortuosity. The lack of Pt NPs in parts of particle D shows in any case that the connectivity is not systematic even with a relatively homogeneous interior porosity.

Concerning the apparent tortuosity of the pores in these reconstructions and the sub-nm constrictions in the shells, they question the nature of diffusion pathways to the interior Pt catalysts. In similar carbons, Padgett *et al.* have previously reported the existence of ~1 nm channels connecting to the exterior in particles similar to our *porous*, and of larger, 2-5 nm openings connecting large interior pores in *hollow* particles to the exterior using LAADF-STEM ET. In a follow-up study, Ko *et al.* revisited these results with BF-TEM ET of KB and other

mesoporous carbons, in which only very few such  $> 2$  nm openings were observed, which they deemed insufficient to support high oxygen diffusion rates. Instead, they highlighted the presence of silt-shaped micropores, 1-2 nm wide and 5-10 nm long, arranged concentrically in onion-like structures, although it is unclear if these were directly seen to percolate and connect to the exterior. They further postulated from  $N_2$  physisorption measurements that the constrictions created by these micropores in the carbon shell regulate the oxygen diffusion fluxes between the exterior and interior mesopores. Our results support this second view, as we observed similar slit-shaped pores throughout our reconstructions. However, we find two fundamental differences. First, only the widest slit-shaped pores we visualized were as large as reported by Ko *et al.* Instead, a highly significant fraction of our slit-shaped pores is sub-nm in width, as shown in Fig. 5.7d, and 3-6 nm in length. Further, we did not find  $> 1$  nm micropores to reach the exterior of the particles in this study and a single  $\sim 1$  nm pore. Openings observed here were otherwise sub-nm, 0.5-0.8 nm in diameter, and relatively cylindrical over 1-2 carbon layers. These numerous sub-nm micropores, whether opening to the exterior or being inside the carbon shells, are also consistent with  $N_2$  physisorption measurements of KB particles, from which a significant volume fraction of micropores  $< 1$  nm in width was seen (Fig. 3a in ref.<sup>73</sup>). Overall, these constrictions are consistent with the idea of Ko *et al.* that a smaller carbon shell implies a less tortuous and restricted diffusion pathways and benefits fuel cell performance but also highlight that diffusion of gases through these shells would be even more restricted than previously thought. An alternate view suggested by the inhomogeneous population of Pt NPs in the primary particles of aggregate D (despite their similar morphology) is that these sub-nm pores may be of limited relevance to diffusion and that, instead, rare and larger openings not visualized here support high diffusion fluxes to the interior mesopores. Once in this presumably well-connected pore network, reactants could then rapidly diffuse through and reach most (but not all) of the aggregate's interior. The fact that Pt NPs are seen inside the compact but relatively thin shell of particle A, but not in that of particle D where they are only found inside the core mesopores also suggests that, past a certain thickness, the shells are not systematically the preferred diffusion pathways and support this idea.

These results demonstrate that diffusion pathways in porous carbons are highly complex and that both the morphology and thickness of the carbon shell and that of the interior porosity may be of importance. This also bears implications for simulations which relied on carbon models with cylindrical boreholes<sup>108,294</sup>, or randomly scattered spherical holes<sup>45</sup>. As put forward in previous studies, it is also clear that ionomer would not intrude in these sub-nm pores<sup>294</sup>.

We note that the resolution, occasional diffraction artefacts, and interactions with the beam in STEM tomography could affect the interpretation of the high-resolution features discussed herein (see discussion in Annex C.3). Further progress towards (near) atomic resolution STEM-

ET is required to resolve each graphitic plane and unambiguously analyze the CB microstructure. This could be achieved by focusing on smaller particles to ensure the projection requirement is better met or by utilizing model-based reconstruction algorithms that can account for multiple scattering in phase contrast<sup>231</sup>. Aberration-corrected HRTEM could also reduce the influence of diffraction artefacts. In addition, beam-induced displacements observed during the STEM acquisitions reduced the quality of the reconstructions and possibly modified the structure. Performing the measurements with low acceleration voltage and dose could offer a way forward. In the STEM case, maximizing the resolution at low kV would require a larger convergence angle and here again a small particle would be key to ensure that the smaller depth of field does not impede tomography.

Finally, we reflect on more accurate descriptors for the microstructure of porous carbons. For simplicity, we have so far employed a *hollow*, *porous*, and *full* classification, on the basis of the presence of an interior mesoporosity and that of interior Pt NPs as visible from 2D HRTEM images. The complexity of the structures observed here in 3D shows that this classification is simplistic, since the *full* particles (e.g. particle E) effectively possess micropores, while a *porous* particle (particle D) with interior pores up to the mesopore range did not feature interior Pt NPs. We propose that a better treatment of the variability of KB primary particles could be done on the basis of two characteristics: thickness of the compact external shell and average width of pores in the core of the particle. This effectively allows more precise description the particles herein.

## 5.5 Conclusions

In summary, we have implemented a simple method for full-range ET of CBs and optimized the acquisition and reconstruction parameters to gather insights into a range of KB primary particles and aggregates. We showed that the microstructure of the KB carbons is highly complex and is well described in terms of the morphology of the exterior shell and the nature of the central porosity. Based on these observations, we have also discussed questions regarding the nature of the structuring units of carbon blacks and the origin of their porosity in terms of their synthesis. This demonstrates the potential of ET for fundamental studies of CBs and shows that further investigations with atomic ET could shine a new light on these decades-old questions.

Our main findings relevant to PEMFCs concern the connectivity of KB interior pores to the exterior space, and we have found that in all particles investigated, the connections were made through rare and almost systematically sub-nm entry openings. These observations question the nature of the diffusion pathways in fuel cell CLs and show that these are either more restricted

than previously assumed or that diffusion would be supported by rare and larger pores (not observed here) that would directly feed into the interior mesopores. Assuming these phenomena coexist, maximum diffusion rates would be achieved with thin carbon shells and large interior pores. We have further seen these interior pores to be typically separated by few-layers graphitic shells, which may be easily oxidized by Pt-catalyzed corrosion during heat-treatment. This would support the idea that accessible carbons synthesized with this pathway perform well due to a lower tortuosity in the central porosity. Overall, these results pave the way towards a complete understanding of the characteristics of the interior porosity in porous carbons, their implication on the tortuosity and constrictions faced by diffusing gases, and their relationship to mass-transport resistances in PEMFC electrodes.

# 6 Towards High-Resolution *operando* Studies of Pt/C Catalysts with LPTEM\*

## 6.1 Introduction

Designing catalyst layers (CL) for proton exchange membrane fuel cells (PEMFC) with improved durability for transportation applications necessitates a fundamental understanding of the mechanisms governing their performance losses during operation<sup>12,19</sup>. A major contribution to these losses comes from the potential-driven decrease of the electrochemical surface area (ECSA) of Pt/C catalysts in the cathode CL<sup>83</sup>. Its origins have been conventionally studied with a combination of electrochemical diagnosis and globally-averaged chemical analyses<sup>295–297</sup>. However, these methods lack the spatial resolution required to directly visualize nanoparticle evolution at the nanoscale and to study parameters of importance such as their interaction with porous carbon supports during operation<sup>298</sup>. Identical-location (IL)-(S)TEM has been widely used to overcome this challenge, and has previously brought insights into the respective contributions of coalescence, Ostwald ripening, Pt dissolution, and carbon corrosion to the ECSA losses<sup>37,85,299,300</sup>. The technique however offers limited temporal resolution because the experiment must be interrupted and the grid transferred to the TEM for each image. Therefore, the dynamics of the degradation events can hardly be accessed. In addition, some phenomena such as Pt redeposition, movements and coalescence may be difficult to differentiate in images comparing materials at beginning of life (BOL) and end of life (EOL) only.

More recently, the development of electrochemical liquid phase transmission electron microscopy (ec-LPTEM) has offered an opportunity for monitoring a range of electrochemical processes in real-time and under credible conditions<sup>167,298</sup>. The technique is enabled by a miniaturized closed-cell hosted at the tip of a TEM holder (Fig. 6.1a), in which a small amount of electrolyte can be held in isolation from the column's vacuum<sup>165</sup>. Thin film electrodes reach within the cell and are available for electrochemical biasing<sup>174</sup> (Fig. 6.1a and b). The approach has previously been used to study commercial and state-of-the-art ORR catalysts in conditions

---

\* Parts of this chapter were adapted from the candidate's contribution to the submitted manuscript version of [Shen, T., Girod, R., Vavra, J. & Tileli, V. Considerations of liquid-phase transmission electron microscopy applied to heterogeneous electrocatalysis. *J. Electrochem. Soc.* **170**, 056502 (2023)]. Author contributions: RG acquired, processed and analyzed electrochemical and TEM data, and wrote the chapter.



relevant to PEMFCs<sup>301</sup>, revealing mechanisms of metal dissolution, dealloying, coalescence and ripening, while also providing insights into corrosion of the catalyst support material<sup>180,182,302–304</sup>. Despite these findings, experiments in ec-LPTEM remain challenging. The difficulties pertain to the accuracy of the electrochemical bias and to the differences with the processes at play in bulk-scale devices, but also to the achievable spatial resolution in liquid cells in relation to the dose imparted by the electron beam<sup>166</sup>. Consequently, interpretation of the results requires knowledge of and control over numerous factors at play while the study of phenomena at the smallest scale, e.g., Pt-carbon interactions, still requires developments towards increasing the achievable resolution.

Herein, we present a range of methodological advances towards accurately imaging and biasing Pt/C catalysts with ec-LPTEM and discuss some considerations of importance for performing these measurements *in situ*. On the basis of inert potential window measurements and an extensive discussion of materials for ec-LPTEM working electrodes, we first show that glassy carbon (GC) thin films are adequate substrates for the study of electrocatalysts, including Pt/C. Discussion of the counter and reference electrodes in these systems is also provided and a Pd-H reference electrode is demonstrated as an avenue towards more reproducible potential measurements in the closed cell. Second, we study the conditions for inducing Pt NPs degradation within a reasonable timeframe accessible in ec-LPTEM experiments. We apply the protocol to demonstrate *in situ* monitoring of the electrochemically-induced dissolution of model Pt nanocubes. Lastly, to enable higher resolution imaging at lower electron dose, we evaluate an unsupervised deep learning method for denoising ec-LPTEM time series.

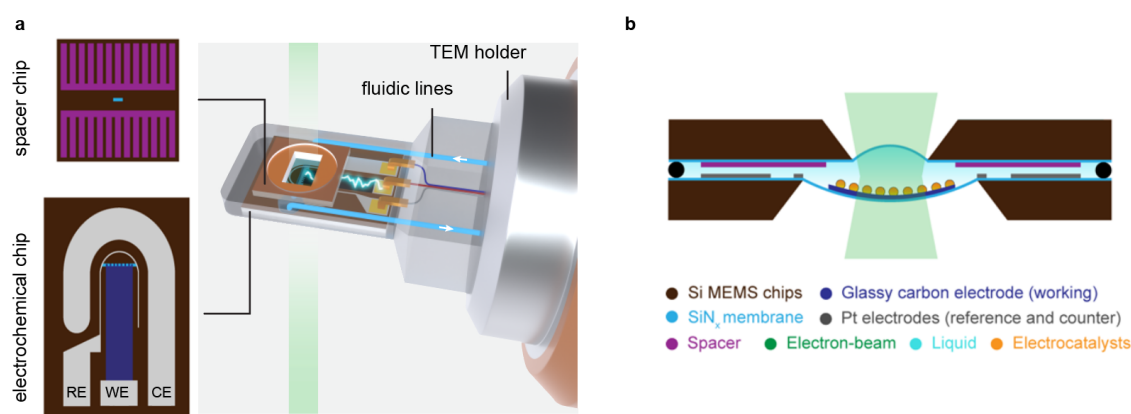


Fig. 6.1: ec-LPTEM apparatus. **a**, schematic illustration of a LPTEM holder and top-down view of the two microelectromechanical (MEMS) chips that form the liquid cell enclosure. RE: reference electrode, WE: working electrode, CE: counter electrode. **b**, cross-section of the assembled cell. Chips and cross-section illustrations courtesy of T.H. Shen.

### 6.2 Materials and methods

#### 6.2.1 Materials

Two catalysts were used in this study. The Pt/C was a 19.8 wt% Pt on Ketjenblack (KB) porous carbons (TEC10E20E, Tanaka Kikinzoku K.K.). Pt nanocubes were synthesized in-house by conventional colloidal chemistry protocols<sup>305</sup>.

#### 6.2.2 ec-LPTEM and open-cell apparatus

The experiments were performed in an ec-LPTEM specimen holder or in a benchtop open cell. Our ec-LPTEM system was a Hummingbird Scientific liquid electrochemistry specimen holder. The tip of the holder is designed to host an electrochemical chip with patterned electrodes, stacked with a spacer chip to create a cavity isolated from the TEM column (Fig. 6.1). The open cell setup was custom-made and is described in detail in ref.<sup>306,307</sup>. Briefly, the open cell hosts electrochemical chips and has metal contacts connecting to the pads of the chips. Once assembled, the window area of the chips is exposed to a ~ 4 mL cavity where conventional reference (RE) and counter (CE) electrodes can be inserted. The CE was a Pt wire, and the RE was an Ag/AgCl (3 M NaCl, BASi), a leak-free miniature Ag/AgCl (3.5 M KCl, Innovative Instruments), a Hg/HgO (BASi) or another Pt wire. The electrodes used in each experiment are detailed in the captions of the corresponding figures.

The electrochemical chips were micro-electromechanical systems (MEMS) fabricated in-house with clean-room processes. Fig. 6.1a depicts the typical arrangement of the electrodes patterned on the chips. The CEs were Pt metal and the REs were Pt or Pd metal. For the WEs, we used Pt metal or glassy carbon (GC) fabricated by pyrolysis of SU-8 photoresist. The Pt WEs were passivated, except for a small area in the vicinity of the window, and the GC WEs were not. The chips and their fabrication are further described in ref.<sup>307,308</sup>. For the spacer chips, we used 250 or 500 nm commercial chips (Hummingbird Scientific).

Electrochemical measurements were performed with a BioLogic SP-300 potentiostat, and recorded with the EC-Lab software.

#### 6.2.3 Inert potential window measurements

The inert potential windows of GC and Pt WE electrochemical chips were determined from cyclic voltammetry measurements (CV) in the open-cell setup. Electrochemical features and gas evolution onsets were compared in 0.1 M KOH (Sigma Aldrich) and 0.1 M HClO<sub>4</sub> (Sigma Aldrich). Differences arising from the surface Pt-O layer thickness were assessed from measurements after a 30 s air plasma at 100 W (Henniker, HPT-100).

#### 6.2.4 Pd-H RE loading and testing

For the Pd-H RE testing, electrochemical chips featuring a 50 nm thick Pd RE, with or without passivation, were mounted in the open cell setup. The total area of the Pd RE was  $\sim 0.5 \text{ mm}^2$  for fully exposed chips without passivation and  $8000 \text{ }\mu\text{m}^2$  with passivation. The open cell was filled with 0.1 M HCl previously purged with  $\text{N}_2$ . Hydrogen loading was performed by evolving hydrogen at the electrode in chronopotentiometry (CP) with cathodic currents (-200 nA) or in chronoamperometry (CA) at cathodic potential (-100 mV vs. RHE). The loading was carried until 50  $\mu\text{C}$  of hydrogen evolution reaction (HER) charges had passed. The durability and potential of the electrodes were assessed by monitoring their open circuit voltage (OCV) directly after loading. The electrolyte in the open cell was constantly purged with  $\text{N}_2$  to prevent  $\text{O}_2$  absorption which is known to reduce the lifetime of Pd-H REs<sup>309</sup>.

#### 6.2.5 Electron microscopy imaging

For IL-TEM experiments, the microscope was a ThermoFisher Scientific Talos operated at 200 kV and in bright field (BF) TEM mode. The same instrument was used for ec-LPSTEM *in situ* experiments. It was operated at 200 kV and imaging was performed with high angle annular dark field (HAADF) in STEM. For ec-LPTEM *in situ* experiments in transmission mode, a JEOL 2200 FS was operated at 200 kV in zero-loss BF-TEM imaging conditions with a 10 eV energy slit and 100  $\mu\text{m}$  objective aperture. Time-series were recorded with a DE-16 camera (Direct Electron).

#### 6.2.6 *in situ* (S)TEM experiments

All chips and spacers were activated with an air plasma at 100 W for 15 s to enhance their wettability. The catalysts were drop-cast on the chips by placing 2-4  $\mu\text{L}$  of a catalyst ink (IPA for Pt/C, hexane for Pt nanocubes) and leaving them to dry. The chips were GC WE electrochemical chips, with Pt CE and RE. Before mounting the chips in the holder, the deposited nanocubes were electrochemically cycled in the open cell to clean their surface from remaining ligands used in synthesis (Fig. D.1). The microcells were then assembled in the holder, inserted in the TEM, and 0.1 M  $\text{HClO}_4$  electrolyte was flown in until wetting could be seen in the window. The electrolyte was not flown during electrochemical experiments. The Pt REs were calibrated in-holder at the beginning of each *in situ* experiment by using the hydrogen underpotential deposition (HUPD) features of the Pt catalysts at the WE (Fig. D.2) and was typically  $\sim 0.8\text{-}1.0 \text{ V}$  vs. RHE in 0.1 M  $\text{HClO}_4$ . The exact calibration of each chip can be found in the captions of the corresponding figures.

Electrochemical degradation was done in CV, at 500 mV/s in the voltage range of [0.4-1.45] V vs. RHE. Every  $\sim 100$  degradation cycles, a full Pt signature CV ([0.05-1.2] V vs. RHE) was

acquired for 5 cycles. During degradation cycling, images were acquired every minute ( $\sim 14$  cycles) in order to limit electron irradiation while maintaining adequate temporal resolution to track changes. ec-LPSTEM of cubes was done with a 100 pA probe and 1  $\mu$ s dwell time resulting in 3000  $e^-/\text{nm}^2/\text{image}$ . ec-LPTEM of cubes was done at 120  $e^-/\text{nm}^2/\text{s}$ , with 1 s acquisition. ec-LPTEM of Pt/C catalysts was done at 25  $e^-/\text{nm}^2/\text{s}$ , with two consecutive 1 s images every minutes.

### 6.2.7 Data processing

For monitoring the Pt nanocubes degradation, each frame was lightly denoised with a  $2\sigma$  Gaussian filter and segmented using Otsu's threshold in FIJI<sup>251,262</sup>. The total area of this segmented phase was measured to plot the relative area loss during cycling.

For Pt/C denoising benchmark, we compared a median filter (2 px, in FIJI), the PURE-LET plugin<sup>310</sup> in FIJI with 10 cycles and automated parameters adjustment, the BM3D algorithm<sup>238</sup> implemented in Python with noise standard deviation estimated from the background, the Noise2Void (N2V, ref.<sup>247</sup>) plugin in FIJI, and the Noise2Noise (N2N, ref.<sup>246</sup>) python implementation in the CSBdeep python toolbox. The N2N models were trained using the pairs of consecutive frames acquired during the ec-LPTEM experiments. The training dataset was typically 2000  $64^3$  patches with 200 more for validation. We used a batch size of 32, 62 steps, the mean squared error loss and typically trained for 200-500 epochs with the Adam optimizer and a 0.0004 learning rate. Benchmarking was done on the basis of the standard deviation of a background patch, the image quality metric Q (ref.<sup>250</sup>) calculation in the 25 most anisotropic 15 x 15 px patches of each image and Fourier ring correlation (FRC) curves calculated with FIJI's FRC plugin.

## 6.3 Results and discussion

### 6.3.1 Electrodes for electrocatalytic measurements in microcells

In the closed cells for ec-LPTEM, electrochemical stimulus is provided through a dedicated electrochemical chip onto which co-planar thin-film electrodes are patterned by microfabrication techniques. Conventionally, three electrodes are used as working, reference and counter electrodes (Fig. 6.1a). To understand how design and material choices affect the performance of these electrodes, we start by discussing the attributes of each in the context of a range of electrocatalytic experiments that include the  $\text{CO}_2$  reduction reaction ( $\text{CO}_2\text{RR}$ ), the oxygen evolution reaction (OER), and the oxygen reduction reaction (ORR).

### ***Working electrode***

The substrate used at the working electrode supports the catalysts and is therefore subject to the same electrochemical conditions. Key attributes for ec-LPTEM that are shared with bulk cell design should be (electro)chemical stability, good conductivity, mechanical stability and ideally, absence of interfering electrochemical processes, to allow for straightforward identification and analysis of electrochemical features of the loaded catalytic material<sup>311</sup>. Additional considerations are to be made in the context of ec-LPTEM: the possibility to pattern the material at nanoscale with established microfabrication techniques, and the TEM contrast influenced by crystallinity, and atomic weight of the element(s). Finally, it is often beneficial to use a dielectric material with good adhesion properties as passivation layer, to cover the peripheries of the cell. Typically, SiO<sub>2</sub> or SiN<sub>x</sub> insulating layers are used to restrict electrochemical events to the observable area, but also to reduce the background signal from the substrate arising from capacitive current, change of phase, or other background electrocatalytic processes. Regarding the shape of the electrode, considerations should be given to the observable area, for example maximizing the length of the electrode edge which provides suitable imaging conditions in the case of a non-electron transparent substrate. It is also useful to keep part of the observed area free of conductive material, which provides a control to compare catalysts that were not influenced by the primary electrochemical process.

The common substrate materials are gold, platinum, and glassy carbon (GC). Gold and platinum offer the advantage of metallic substrates: good conductivity, low charge transfer resistance and well-established microfabrication procedures. They can be plasma cleaned to tune the surface hydrophilicity without damage and offer good adhesion to passivation materials. Gold however tends to exhibit island growth<sup>312</sup>, requiring a minimum thickness of around a few tens of nm while platinum can more easily be fabricated down to a thickness of ~ 15 nm while maintaining continuity. They both exhibit electrochemical features related to their surface oxidation, which limit their inert potential range in the anodic region to about 0.8 V vs. RHE for Pt and 1.3 V vs. RHE for Au<sup>311,313-316</sup>. While such features do not prevent the use of these substrates at more anodic potentials, care should be taken to separate the electrocatalytic processes. It is recommended to become accustomed to the substrate signals by running blank experiments to measure substrate current and identify background features prior to *in situ* experiments. Furthermore, repeated cycling above the oxidation potential in longer experiments can result in significant dissolution of the substrate<sup>317</sup>. The dissolved species can then be redeposited in the area of observation by beam-induced reduction<sup>318</sup>, or electrodeposition if the potential is cycled down to sufficiently cathodic values<sup>318</sup>. Ultimately the evolution of oxygen and hydrogen at these surfaces limits the usable potential range in the anodic and cathodic regions respectively, as gas evolution disrupts imaging conditions. Gold is poorly active towards HER<sup>319,320</sup>, making

it a potential candidate for the study of catalysts at mild cathodic potentials<sup>319</sup>. On the other hand, platinum is one of the most active materials towards HER<sup>319,320</sup> but shows comparatively poor activity towards OER<sup>321</sup>. It is also known that OER activity at platinum surfaces exhibits a dependency on the thickness of its surface oxide film<sup>322,323</sup>. In practice, we have found that after an air plasma treatment such as commonly done to improve hydrophilicity and allow for wetting in the TEM, the increased oxide layer allowed Pt electrodes to be used for *in situ* experiments in alkaline conditions at up to 2.0 V vs. RHE. To demonstrate this, Fig. 6.2a compares the cyclic voltammetry results of a Pt thin film electrode with and without an oxide film in 0.1 M HClO<sub>4</sub> and 0.1 M KOH. The oxide film was formed after a 30 seconds exposure to a 100 W air plasma and exhibits a 180 mV higher overpotential towards OER at 0.5 mA/cm<sup>2</sup> than the same electrode previously reduced electrochemically. Thus, Pt substrates are particularly convenient for studies of OER catalysts. Finally, glassy carbon is another common substrate for *in situ* experiments. It is a non-graphitizing allotrope of carbon<sup>324</sup>, that can be fabricated in thin films by controlled pyrolysis of photoresist materials<sup>325</sup>. Its wide inert potential range and stability<sup>311,326</sup> renders it indispensable in the studies of electrocatalysts<sup>327</sup>. Even as thin films, no features are observable besides hydrogen and oxygen evolution, both occurring at high overpotentials as shown in Fig. 6.2b for acidic and alkaline electrolytes. Furthermore, it also provides minimal electron scattering and low background contrast, often making it the substrate of choice for ec-LPTEM. It is however significantly more fragile, requiring care in handling and deposition of catalysts, and suffers from poor adhesion to the substrate and passivation layers.

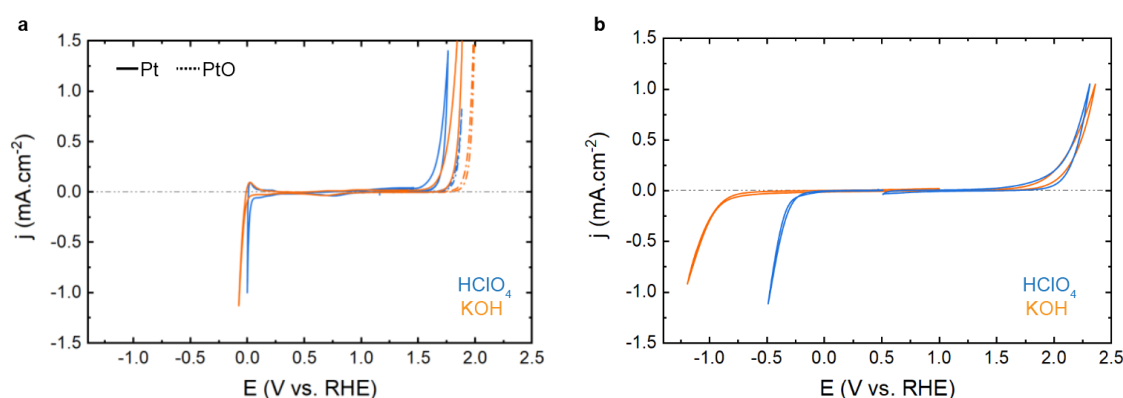


Fig. 6.2: Evaluation of the inert potential window of electrochemical chips. Cyclic voltammetry of (a) glassy carbon and (b) platinum thin film electrodes patterned on a chip for LPTEM, in 0.1 M KOH and 0.1 M HClO<sub>4</sub>, scan rate: 20 mV/s. In the case of Pt, the activity towards OER was evaluated for an electrode passivated by an oxide film after an air plasma treatment (dotted line, 30 s, 100 W) and for the same Pt electrode after electrochemical reduction of the oxide film (plain line). The chips were fabricated in-house and the voltammograms were recorded in a benchtop, ex-situ, apparatus with a true reference electrode (Ag/AgCl for HClO<sub>4</sub> electrolytes or Hg/HgO for KOH electrolytes).

For the study of ORR catalysts, we have typically employed the GC substrates for their absence of overlapping features in the range of accelerated stress tests (AST, typically up to  $\sim 0$ -1.5 V vs. RHE). We note however that GC thin-films have a higher resistivity and charge-transfer rate at the electrode interface than their bulk counterparts, which are usually pre-treated electrochemically or by polishing to reduce this effect<sup>328,329</sup>. As we have shown in ref.<sup>330</sup> and further demonstrate for the Pt/C system in Fig. D.3 the ohmic a, the result was an increased redox peak separation and a slanted baseline for catalysts on a carbon substrate when compared to a gold one. This effect is likely to be an important driver of similar deviations reported in many studies<sup>304,331,332</sup>, in addition to the commonly assumed ohmic drop due to thin liquid cross-sections and increased resistances in the microcell. Indeed, the uncompensated resistance  $R_u$  at the origin of the ohmic drop depends on the conductivity of the solution and the distance between the RE and WE. In the MEMS chip configuration, the reference electrode is relatively close to WE with a distance of around several hundred micrometres since they are all patterned on the same chip. The values of  $R_u$  in such configuration, measured by electrochemical impedance spectroscopy (EIS), are around several tenths to several hundred ohms in aqueous electrolytes. With the current ( $i$ ) in the range of several hundred nA in the microcell, the ohmic drop ( $iR_u$ ) then falls in the range of several hundred  $\mu$ V and should usually be negligible. In fact, in our experiments, the CV of a pure Pt electrode in the ec-LPTEM cell did not show the commonly observed slanted baseline of GC electrodes (Fig. D.3b), even in thin liquid layer conditions.

### ***Reference electrode***

Choice of the reference electrode is equally important to the success of an ec-LPTEM experiment and knowledge of the reference potential is essential for accurate interpretation of electrochemical results. Numerous studies have been dedicated to detailing the fundamental and practical aspects of reference electrodes<sup>333,334</sup>, including a recent review in ref.<sup>335</sup> focusing on their use in the context of microscale systems for *in situ* and *operando* studies of electrocatalysts. Herein, we outline a few general guidelines and recommendations to keep in mind regarding this component of the liquid cell. The main requirements for the reference electrode are that its potential should be stable over time and ideally known (calibrated) for a given system and that it should not contaminate the electrolyte<sup>335-337</sup>. Fundamentally, this implies that the electrolytic process determining the electrode potential should be well-defined, simple, and fast (has a high exchange current density), and should obey the Nernst equation<sup>336-338</sup>. Furthermore, the species partaking in the process (e.g., ionic species in solution, metallic electrode, etc.) should remain at equilibrium without changes in thermodynamic activities (concentration or partial pressure). This has led to conventional reference electrodes working in saturated conditions, separated from the external test solution by a liquid junction<sup>337</sup>. Such

systems are necessarily complex, and despite efforts to scale down electrodes such as the Ag/AgCl reference to sizes amenable to microsystems<sup>334,336</sup>, integration within chips for ec-LPTEM remains out of reach. Choice of the reference electrode is equally important to the success of an ec-LPTEM experiment and knowledge of the reference potential is essential for accurate interpretation of electrochemical results. A number of works have been dedicated to detailing the fundamental and practical aspects of reference electrodes<sup>333,334</sup>, including a recent review in ref.<sup>335</sup> focusing on their use in the context of microscale systems for *in situ* and *operando* studies of electrocatalysts. Herein, we outline a few general guidelines and recommendations to keep in mind regarding this component of the liquid cell. The main requirements for the reference electrode are that its potential should be stable over time and ideally known (calibrated) for a given system and that it should not contaminate the electrolyte<sup>335-337</sup>. Fundamentally, this implies that the electrolytic process determining the electrode potential should be well-defined, simple, and fast (has a high exchange current density), and should obey the Nernst equation<sup>336-338</sup>. Furthermore, the species partaking in the process (e.g., ionic species in solution, metallic electrode, ...) should remain at equilibrium without changes in thermodynamic activities (concentration or partial pressure). This has led to conventional reference electrodes working in saturated conditions, separated from the external test solution by a liquid junction<sup>337</sup>. Such systems are necessarily complex, and despite efforts to scale down electrodes such as the Ag/AgCl reference to sizes amenable to microsystems<sup>334,336</sup>, integration within chips for ec-LPTEM remains yet out of reach.

Instead, ec-LPTEM systems conventionally feature a quasi-reference electrode in the form of a noble metal thin-film, typically gold or platinum. The main difference of these electrodes is their direct contact with the environment of the cell so that their potential does not result from a single, well-defined redox couple but instead from a combination of all electrolytic processes occurring in the vicinity of the electrode, resulting in a situation of mixed potential<sup>333,335</sup>. In practice, these electrodes can be particularly stable if provided with enough time to reach equilibrium and a stable liquid environment. However, because their potential cannot be determined from the Nernst equation, they require calibration before and/or after each experiment, with radical changes expected based on the actual composition of the electrolyte and the state of the electrode surface.

As an avenue for solving the miniaturization, stability, and reproducibility problem in ec-LPTEM, we have studied the capabilities of a Pd-H microelectrode to provide accurate potential measurements. The overarching strategy consists in using an alloy system fabricated *in situ* that exhibits stable potentials over a wide range of compositions. Some examples include the gold-lithium system for Li-ion batteries<sup>339,340</sup> and, for aqueous systems, the Pd-H system<sup>309,341</sup>. In PdH<sub>x</sub> alloys, the remarkably large  $\alpha+\beta$  two-phase region (from  $0.017 < x < 0.6$ , ref.<sup>342</sup>) can be



leveraged by pre-loading hydrogen in a Pd electrode (typically via HER)<sup>343</sup>. As H<sub>2</sub> subsequently slowly desorbs, the potential of the electrode remains stable at  $\sim 50$  mV over the  $\alpha+\beta$  phase, which lead to its use as a reference in different spatially constrained systems<sup>309,341</sup>. To assess the suitability of this system for ec-LPTEM application, we fabricated MEMS chips featuring a Pd RE, an example of which is shown in Fig. 6.3a. Potential measurements after H<sub>2</sub> loading are reported in Fig. 6.3b. We found that electrodes fully exposed to the electrolyte showed limited potential stability (blue curve, Fig. 6.3b), which was attributed to the thin-film nature of the electrode (here, 50 nm-thick) and, hence, high surface-to-volume ratio and fast hydrogen desorption. In contrast, passivating the Pd surface and leaving two 50 x 80  $\mu\text{m}^2$  openings resulted in drastically increased stability (orange curve, Fig. 6.3b and image of the passivation in Fig. 6.3a). The potential of this stability window was  $60 \pm 5$  mV across different chips (Fig. 6.3c), showing good reproducibility and values close to the expected for Pd-H electrodes. The length of the stability plateau ranged from 60 to  $\sim 110$  minutes and increased with the duration of the loading phase, even while the total number of charges for loading was kept the same. This is indicative of limited hydrogen loading due to the diffusion rate inside the electrode rather than hydrogen availability at the electrode-electrolyte interface. While improvements in durability are still needed for practicality, these results show that the Pd-H electrode is a promising electrode for ec-LPTEM and, importantly, would not require calibration. Future pathways could explore longer charging times and optimization of the electrode and passivation shape to increase the capacity of the hydride reservoir. In addition, the reported Nernstian relationship of the Pd-H potential to the hydrogen activity means that these electrodes are efficient pH sensors and this could bring insights into chemical processes inside the ec-LPTEM liquid cells<sup>309</sup>.

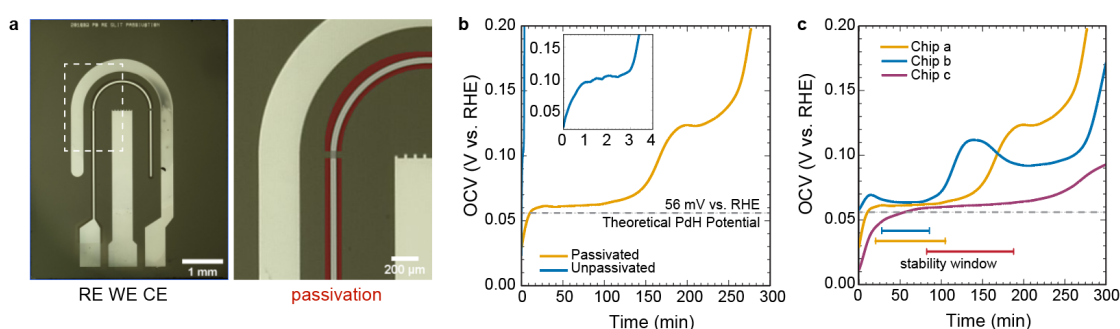


Fig. 6.3: Pd-H microchip and evaluation of potential stability. **a**, top view optical microscopy image of a MEMS chips fabricated in-house with a Pd RE. This chip features a SiO<sub>x</sub> passivation layer covering most of the RE, which provided increased potential stability at open circuit (**b**) after hydrogen loading as compared to a non-passivated electrode. **c**, comparison of the OCV of three Pd-H electrodes demonstrating the variability in stability window, defined as the longest time within a 4 mV span. Chip a and b loaded with 50  $\mu\text{C}$  in 20 min, chip c with 50  $\mu\text{C}$  in 40 min. **b** and **c** were measured in 0.1M HCl. The chips were fabricated in-house and the voltammograms were recorded in a benchtop, ex-situ, apparatus with a true Ag/AgCl reference electrode.

We note, however, that this pH dependency could affect the final use as a RE in the ec-LPTEM system because of the small scale and proximity of all electrodes in the cell. This is also the case for conventional quasi-reference electrodes as, for example, it is expected that the  $\text{H}^+_{(\text{aq})}/\text{H}_{2(\text{g})}$  and  $\text{PtO}_{(\text{s})}/\text{Pt}_{(\text{s})}$  redox couples contribute to the potential of a Pt quasi-reference electrode, implying a relationship to the partial hydrogen pressure and pH<sup>335,344,345</sup>. This bears implications for the shape and distance of the electrodes in experiments where electrocatalytic processes at the working or counter electrodes can result in local pH change or hydrogen evolution. The reference should therefore be placed sufficiently far away from the other electrodes, ideally up-flow if possible, but also sufficiently close to maintain the uncompensated resistances to the small values discussed above. Apart from the stability of the redox couples on the Pt quasireference electrode, the possible exposure of the Ti or Cr adhesion layer underneath the Pt quasireference electrode can also influence the stability of the reference potential<sup>334</sup>.

Finally, it is worth mentioning that previous studies have demonstrated with success the implementation of an external true reference, typically placed in a container outside of the specimen holder and connected to the microcell via the fluidic lines<sup>302,346,347</sup>. This configuration does however add significant ohmic resistance and noise due to the length and small cross-section of the fluidic lines, and we have typically found its implementation impractical for this reason. The next-generation *in situ* TEM holders that feature a dedicated cavity in close vicinity of the tip to host a miniaturized bulk reference are promising in that regard.

### ***Counter electrode***

The counter electrode of the electrochemical chips used in ec-LPTEM experiments is also important and like the other electrodes, the scale of the apparatus bears implications for the choice of material and geometry, which should be considered with attention. The counter electrode provides – or sinks – the charges required for a reaction to happen at the working electrode. Therefore, its size should be properly tailored to ensure that processes at the working electrode are not limited by poor reaction or diffusion rates at the counter<sup>327</sup>. Furthermore, because its potential is uncontrolled and is established as a result of the working electrode being driven by the potentiostat, care should be given that no parasitic reactions interfere with the observations and results. For instance, an easily oxidized counter may suffer from anodic dissolution when cycling catalysts at cathodic potentials relevant to HER or CO<sub>2</sub>RR at the working electrode. This, in turn, can result in the reduction and redeposition of the dissolved ions on the catalyst thereby altering the observation<sup>348</sup>. In conventional benchtop cells, this problem is easily solved by using an ion conductive membrane, separating the cell in two chambers, and preventing contamination<sup>327</sup>, but this so far remains out of reach for ec-LPTEM

setups. Another issue can arise from gas evolution, typically happening when high anodic potentials are applied at the working for instance to study OER catalysts. In such case a small platinum counter would quickly reach potentials negative enough to induce HER, possibly disrupting the observations or modifying the quasireference electrode potential. For these reasons, it is a good practice to monitor the potential of the counter electrode versus the reference during experiments. Two strategies can be employed to avoid these effects. First, an electrochemically inert material (e.g., glassy carbon) can be used to evolve gas instead of partaking in dissolution/oxidation, while ensuring that the surface area ratio to the working is large enough, and the current densities at the counter therefore low enough to avoid gas nucleation. Second, an electrode with a relatively high capacitance (e.g., carbon black, platinum with large area) can be used with a carefully controlled surface area ratio, so that all charges required for reactions to happen at the working electrode can be provided or stored by the counter electrode double layer capacitance. There again, holders accommodating for small cavities allowing to place an external counter electrode in the vicinity of the tip but outside of the micro cell are promising. Herein, we relied on large Pt CEs as depicted in Fig. 6.1a, and monitored their potential during cycling to verify they did not undergo severe Pt-PtO redox cycling.

### 6.3.2 Potential-induced dissolution of Pt nanocubes

To investigate the capabilities of ec-LP(S)TEM to probe the evolution of ORR catalysts, we then performed degradation experiments on model, 12 nm, Pt nanocubes. Electrochemical stimulus was applied by cyclic voltammetry (triangular waves) at 500 mV/s, with a potential range set from 0.4 to 1.45 V vs. RHE for 360 cycles. The test was meant to resemble the start-up/shut-down ASTs and the high potentials that can be experienced in the cathode CL during these events<sup>349</sup>. The potential range and scan rate were optimized from IL-TEM preliminary experiments (Fig. D.4) and we found that this protocol resulted in degradation of the catalysts within a timeframe suitable for *in situ* TEM experiments.

*In situ* imaging was performed in BF-TEM mode, with zero-loss energy filtering and thin-film wetting conditions to maximize resolution<sup>332</sup>. Prior to the experiment, stable imaging conditions were determined, with an upper electron dose rate limit set at 120 e<sup>-</sup>/nm<sup>2</sup>/s where no beam-induced damage could be observed to the sample within the timeframe of the experiment. In comparison, the tradeoff between resolution, dose and induced damage was found to be too restrictive in STEM-HAADF (Fig. D.5).

Fig. 6.4a-g shows a time series of images from an aggregate of nanocubes under cycling. Modification of the catalyst is observed over time, with particles becoming increasingly rounded and aggregating. Segmentation of each frame allows constructing the projection map

### 6.3 Results and discussion

shown in Fig. 6.4h, which further demonstrates the morphological changes of the catalyst during the consecutive cycles of Pt oxidation and reduction (Fig. 6.4i). Quantification of the relative area loss as a function of cycles was performed on 5 different aggregates and is plotted in j. Two kinetic regions are visible, with the rate of area loss increasing after  $\sim 240$  cycles. Two control measurements were also performed to assess the effect of the electron beam (Fig. D.6). First, an area was exposed to the electron beam under illumination conditions similar to the degradation experiment, but without biasing. As shown in Fig. 6.4j, green line, no apparent evolution of the morphology was observed within the 10 minutes of control experiment. Second, an aggregate outside of the electron-illuminated area was imaged before and after the degradation experiment and was found to have experienced similar degradation to the particles in the time-series, as shown from their relative area loss in Fig. 6.4j, black data point.

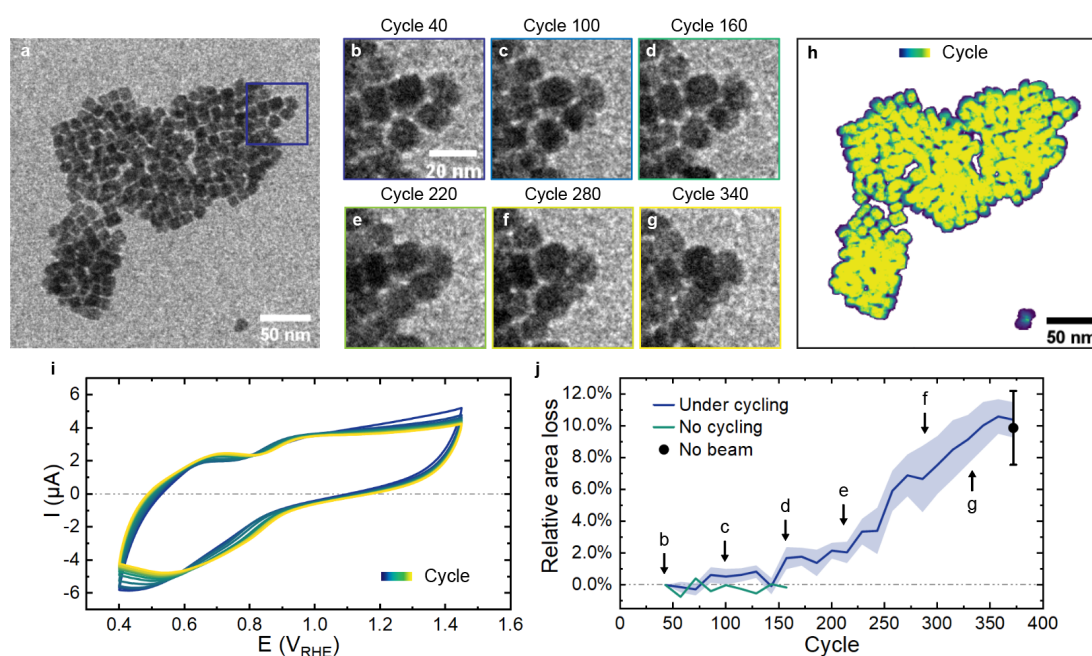


Fig. 6.4: Dissolution and aggregation during AST of Pt nanocubes catalysts for ORR. **a**, BF-TEM overview of an aggregate loaded on an electrochemical chip with GC WE, Pt CE and Pt RE ( $V = 0.8$  vs. RHE). **b-g**, time series of a close-up from (a) during cyclic voltammetry in range  $[0.4, 1.45]$  V vs. RHE at  $500$  mV/s in  $0.1M$   $HClO_4$ . Representative voltammograms throughout the cycling procedure are shown in (i). **h**, Segmented particle projection visualizing the dissolution and aggregation event and the resulting area loss. **j**, Relative area loss of Pt NPs aggregates plotted as a function of cycling advancement. Blue line and shaded area are the mean and one standard deviation over five aggregates. Green line (single measurement) and black point (mean, error bars are one standard deviation,  $N = 5$ ) are control measurements performed in the absence of bias or of beam illumination, respectively. In the absence of bias, the time series was converted to equivalent cycles for comparison. Electron fluence per image =  $120 e^-/nm^2$ .

With these controls, we conclude that the observed evolution of the Pt nanocubes results from cycling the catalyst under potential, inducing platinum dissolution. This kind of experiment can

therefore provide valuable information into the degradation pathways and kinetics of catalysts for ORR and their shape dependency. We note that the degradation protocol used here and the ec-LPTEM environment may differ from the conditions experienced in MEA or RDE geometries. The differences in the local electrochemical environment (no ionomer, for instance), diffusion rates in liquid and Pt loading have for example been shown to result in different degradation profiles<sup>37,38,296</sup>. In addition, the interactions of the electron beam with the electrolyte generate reactive radicals<sup>188,189,350,351</sup>, which have been reported to accelerate catalyst degradation when combined with potential cycling<sup>86</sup>. Further investigation may help optimise the cycling conditions for ec-LPTEM (potential range, scan rate, wave shape, electrolyte ...) in order to best recreate the degradation profiles observed in MEA while, at the same time, maintaining an adequate timeframe for *in situ* experiments. We note in passing that we have seen in IL experiments that the presence of Cl<sup>-</sup> ions in the electrolyte remarkably increased the rate of Pt dissolution<sup>352,353</sup> (Fig. D.7), and this may be promising to accelerate Pt degradation at lower potential range for *in situ* experiments.

### 6.3.3 Towards *in situ* imaging of Pt/C catalysts

We then applied the conditions demonstrated on the Pt nanocubes to image conventional Pt/C catalysts *in situ* (2-3 nm Pt NPs on KB supports). While the cycling range was adequate to induce degradation in a reasonable timeframe, even with a reduced scan rate (see IL location results in Fig. D.7), the combined electron beam effects and high upper potential limit induced corrosion of the carbon supports (Fig. D.8) which had not been observed in IL location experiments. Reducing the electron dose rate to mitigate these effects strongly limited the resolution so that individual Pt NPs could not be resolved.

To enable higher resolution at low electron dose, we studied the capabilities of a deep-learning (DL) based approach to denoise the time-series. Specifically, we investigated an unsupervised training scheme that did not require obtaining ground truth data from experimental or synthetic sources as otherwise conventionally used<sup>244</sup>. The method uses the Noise2Noise (N2N) framework, in which only pairs of noisy images containing identical signal are used to train a DL model with a CNN architecture<sup>246</sup>. Herein, we used two consecutive frames of *in situ* time-series acquired with sufficiently large temporal resolution for these frames to assume redundant signal (see Methods).

Results of the procedure on time-series of Pt/C catalysts in ec-LPTEM are displayed in Fig. 6.5, along with a benchmark against a range of denoising algorithms. We also tested the method on larger Cu nanocubes with results shown in Fig. D.9. From the denoised images on both samples, the N2N approach provided lower background noise levels and better contrast of the catalysts than other algorithms. These observations were further supported by quantification of the

## 6.4 Conclusions

background standard deviation (Fig. 6.5b), image quality metric (Q, Fig. 6.5c), and FRC curves showing noise levels as a function of spatial frequency (Fig. 6.5d). Although individual Pt NPs were not resolved in these results, they show that the N2N approach is a promising strategy to use in ec-LPTEM low-dose imaging experiments.

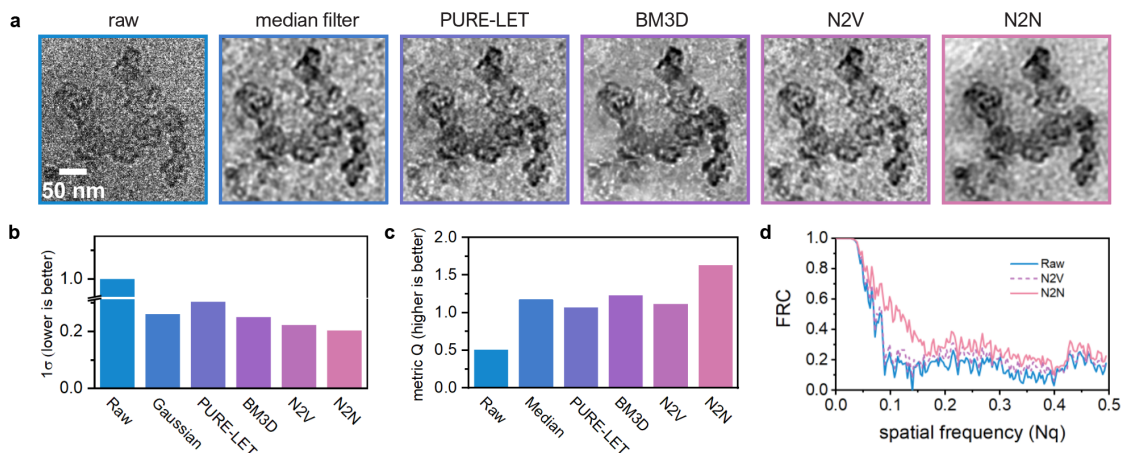


Fig. 6.5: Benchmark of denoising methods on Pt/C ec-LPTEM time-series. **a**, representative images from denoising strategies. **b**, standard deviation of a background part of the image across the denoised images. **c**, image quality metric Q measured on the 25 most anisotropic  $15 \times 15$  pixel tiles in each image. **d**, FRC curves computed between two consecutive frames.

We note that the improvement from N2N denoising was quantitatively and qualitatively better with the Cu nanocubes. We attribute this to the higher frame rate of this acquisition, which resulted in a higher redundancy of the signal between consecutive frames. This shows that the acquisition rate should be tailored to the denoising strategy. Further investigation may help to optimize this parameter and, in turn, the electron dose vs. resolution tradeoff.

## 6.4 Conclusions

In this study, we explored how ec-LPTEM could be used to study Pt/C catalyst degradation in real-time. Considerations were given to the choice of electrodes in the ec-LPTEM apparatus, and we demonstrated the adequacy of GC thin-films as a catalyst substrate. In addition, we showed that a Pd-H reference electrode may offer a way towards potential measurements in ec-LPTEM without calibration. Finally, we imaged nanocatalysts during cycling experiments and showed that Pt dissolution could be tracked in real time. We also presented promising denoising strategies for low SNR time-series, to achieve higher resolution at lower electron dose and limited beam-induced effects. Taken together, these results pave the way towards accurate *operando* studies of the catalyst-support interactions and show ec-LPTEM may have the potential to shine a light on fundamental mechanisms of performance losses in PEMFCs.

## 7 Conclusions and Outlook

The complex structure of the catalyst layers (CL) in proton exchange membrane fuel cells (PEMFC) calls for investigations beyond conventional imaging to access volumetric and/or time-resolved information. In this thesis, the interactions of the Pt-carbon-ionomer system were investigated using transmission electron microscopy (TEM) as a versatile platform for multidimensional imaging.

Starting with complete CLs, I first developed a methodological pathway to reveal their structure at the nanoscale. The challenges associated with the task are primarily related to the highly electron beam-sensitive ionomer and its weak contrast with the carbon supports. To overcome this, cryo-electron tomography (ET) was used to mitigate radiolysis damage and an advanced image processing pipeline was established to quantitatively analyze the low contrast, low signal-to-noise (SNR) reconstructions. Microtomy was found to preserve the CL open pore morphology and allowed to reconstruct a volume in which the interactions between all the components could be investigated. The results showed that ionomer covered most of the carbon exterior surface and formed in a highly connected network. This coverage was most often about 3 nm thick, but also with larger ionomer aggregates and strands up to 24 nm large. This highlighted that the ionomer morphologies encountered by protons and gases to reach the three-phase interface reactive sites are significantly different. Focusing on the Pt catalysts, they were found to reside inside and outside of the carbon, with the large majority of the exterior ones being in direct contact with the ionomer. However, comparison with electrochemical data suggested that the surfaces participating in the reactions would be greater than those in direct contact with the ionomer. These findings demonstrate the potential of cryo-ET to gain an accurate picture of the CL structure and open the way towards structure-performance studies in a range of PEMFC systems. This could be used to probe, for example, the effect of varying Pt and ionomer contents, different carbon types and carbon surface functionalization<sup>79,80</sup>. The operator's involvement remains however significant at present, and further developments are needed for this kind of quantitative analysis to become routine. In the future, instrumental (more sensitive cameras, phase plates, ...) and data processing improvements (automated alignment, deep learning with more versatile and pre-trained segmentation models, ...) could enhance the contrast and SNR and facilitate analysis at different points in the pipeline. Finally, the CLs in PEMFC are operated in high humidity, and this is well known to modify the ionomer

---

morphological properties, e.g., due to swelling<sup>53,153</sup>. Therefore, a direct follow-up may leverage freeze-plunging which is already well-integrated in many cryo-electron microscopy centres and could provide an even more accurate picture of the morphology of the CL as they exist in fuel cells.

Although cryo-ET offered remarkable insights into the CL structure, the dose-damage tradeoff remains a limiting factor in terms of resolution. To gather insights into the microstructure of the carbon supports, which are known to play a critical role in the mass-transport properties of the electrodes, I then focused specifically on Pt/C catalysts. To enable full-range, high-resolution, ET of these catalysts, a sample preparation method based on probe fabrication by electropolishing was implemented. This allowed us to resolve the interior micro- and mesoporosity of the porous carbon supports. The central mesoporosity was found to be created by strongly warped, few-layers, carbon graphitic planes, surrounded by a more compact shell. In it, carbon planes with greater ordering are occasionally mismatched and peel off to create narrow, slit-shaped, micropores. These micropores create sub-nm constrictions for gas diffusion from the exterior to the interior of the supports and question the relative importance of the gas diffusion pathways in the shells vs. in the interior mesopores. These findings directly suggest that optimized carbon blacks for CL should feature large, connected and low tortuosity interior mesopores and thin shells. Work is ongoing to enable the segmentation of the interior porosity, and could bring a more quantitative evaluation of the morphological characteristics of the pores network, using for instance novel descriptors developed for PEMFC diffusion electrodes<sup>354</sup>. In addition, the implementation of this technique within an identical location (IL) workflow has the potential to answer in full the question of the porosity modifications induced by novel protocols for Pt-catalyzed carbon oxidative treatment<sup>71,73</sup>. This is important to understand the origin of the improved performance of these carbons and could offer clear design rules for novel mesoporous supports that currently enable high Pt activity and high mass transports. Further, technical developments could reach near-atomic resolution in ET in order to resolve each carbon plane. Such a complete picture of the carbon arrangement in carbon blacks (CB) has the potential to shine a new light on old and unresolved questions regarding the fundamental nature of the CB structure, the origins of their porosity and their inception inside reactors. Improvements in this direction could be achieved for instance by using advanced alignment<sup>355-357</sup> and reconstructions algorithms<sup>231</sup> for aberration-corrected high-resolution TEM.

Finally, the interactions within CLs are not only three-dimensional in nature but also dynamic. Pt NPs and carbon supports degrade during operation in complex interrelated pathways, and visualizing these events in real-time is key to understanding the fundamental mechanisms of performance losses that limit the PEMFC durability. In the last section of this thesis, I focused on the electrochemical liquid phase (ec-LP)TEM technique, which holds potential to study



catalysts for PEMFCs in real-time. By investigating methods for more accurate biasing of the catalysts *in situ* and improved temporal and spatial resolution, the chapter paves the way towards studying the Pt-C interactions during operation and their respective degradation processes. Ultimately, a deep understanding of these interactions would require drawing the strands of this thesis together by combining 3D and real-time information. Although some forms of *in situ* and 4D, time-resolved, ET have been demonstrated<sup>358–364</sup>, a strong tradeoff remains between spatial and temporal resolution, the environment (liquid, gas), and the stimulus that can be applied. By combining ET and ec-LPTEM, it is envisioned that degradation of Pt NPs could be directly associated with their localization on the carbons, for which post-mortem ET would be sufficient. Further, IL-ET at the beginning and end of the ec-LPTEM process, perhaps with finer intervals at different cycling steps, could use the information from 2D time-series to interpolate between the 3D reconstructions. In essence, as an ultimate goal, this would lead to the development of electrochemical liquid phase electron tomography.

In summary, the knowledge gathered herein offers a more accurate picture of the CL in PEMFC and introduces pathways towards their high-fidelity *operando* characterization at the nanoscale. This thesis, thus, demonstrates that multidimensional TEM can provide unique insights in the field of energy materials and can aid the development of improved, low-carbon, technologies.



## A Operational considerations for ET

Maintaining the region of interest (ROI) in the field of view and in focus throughout tilt-series acquisition poses challenges because the scale of the field of view is close to the tolerance of the mechanical stage that rotates the sample. Firstly, minimization of these drifts requires two main alignments, depicted in Fig. A.1, to ensure the optical axis of the microscope falls on the rotation axis of the stage (Fig. A.1a) and for the specimen to lie at the eucentric plane (Fig. A.1b). Ideally, the stage is optimized for the holder used in tomography so that these alignments bring limited improvements. However, if the stage has been tuned for a different holder, significant misalignments can persist and need to be determined. The eucentric plane can be found by wobbling the goniometer between small angles and minimizing drifts with the z-height. Alignment of the optical axis requires finding the *optimized position* by shifting concurrently the beam with the beam deflectors and the image shifts until movements and defocus changes of a sample at eucentric height are minimized. Even if alignments are optimized, mechanical imprecisions can result in remaining drifts. If these drifts stem from remaining minor misalignments in the eucentric height or optimized position, they would be systematic and can therefore be calibrated ahead for a given holder, or predicted on-the-fly<sup>217</sup> using extrapolation of the drifts at the first angles. For remaining random misalignments that originate in e.g., vibrations during tilt, procedures that use a pre-acquisition alignment step, e.g., using cross-correlation, to shift the beam in order to centre the ROI with greater accuracy are useful. Finally, these steps can ensure that the ROI remains within the field of view but are not precise enough to guarantee accurate tomographic reconstruction. These final alignments are done in post-processing as presented in Chapter 3.

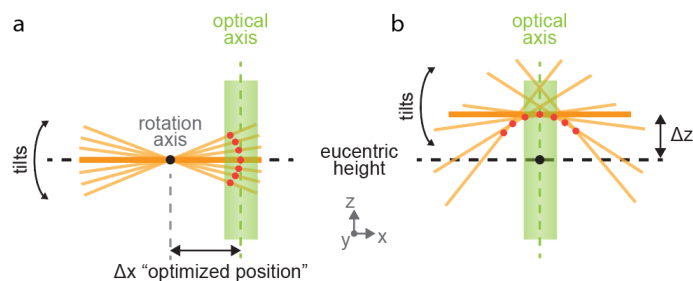


Fig. A.1: Schematized shifts experienced by a region of interest (red dot) as a result of a) misaligned optical axis with respect to the rotation axis of the goniometer by  $\Delta x$  and b) specimen away from eucentric height by  $\Delta z$ .

## B Supplementary Information for Chapter 4

### B.1 Supplementary Notes

#### B.1.1 minimal electron dose for complete tilt-series

To estimate the minimal electron dose that could be used for tilt-series acquisition, we considered that the most critical step for the final resolution was the manual alignment procedure, in which at least one Pt nanoparticle had to be identifiable at all tilt angles with adequate resolution and contrast. When operating in a dose-limited regime, Egerton proposed that the resolution is governed by the following equation<sup>198</sup>:

$$\delta = (SnR) \times (DQE)^{-1/2} \times F^{-1/2} \times D_e^{-1/2} \times \frac{\sqrt{2}}{|C|} \quad (B1)$$

So that

$$D_e = \frac{2}{DQE \times F} \times \left( \frac{SnR}{\delta \times C} \right)^2 \quad (B2)$$

Where  $D_e$  is the electron dose, DQE the detector quantum efficiency, F a signal efficiency relating the number of recorded electrons to the fluence required to generate them, SnR the signal-to-noise ratio,  $\delta$  the (dose-limited) resolution, and C the Weber contrast of the feature relative to the adjacent background.

In a first approximation, we considered a 2 nm resolution requirement for accurate localization of an average Pt nanoparticle in a Pt/C catalyst, with a Rose criterion for the SnR of 3. In our defocused phase contrast imaging conditions, we measured a Weber contrast  $\sim 0.5$ , and used a signal efficiency of 0.87, as proposed by Egerton<sup>198</sup>. The DQE of our camera had been previously measured to be 0.46 at half the Nyquist frequency.

Introducing these values in equation (B2) gives a minimal electron dose requirement of  $44 \text{ e}^-/\text{nm}^2$ , so that we have typically operated in a range of a few tens of  $\text{e}^-.\text{nm}^{-2}$  per image in the tilt-series acquisitions, as detailed in the methods. In effect, it was observed that these conditions allowed for manual alignment of about half of the acquired tilt-series and that the task remained highly challenging, qualitatively confirming that this dose is close to the lower operable limit.

### B.1.2 detailed methods for data analysis

All operations and measurements for the following metrics were performed with FIJI and the MorpholibJ<sup>272</sup> and BoneJ2<sup>273,274</sup> plugins or in Python using mainly the scikit-image, SciPy and PoreSpy<sup>275</sup> libraries.

*Volume and mass fractions, carbon surface area:* volumes and surfaces of the binary volumes were calculated with MorpholibJ, and related to mass fractions and surface assuming an ionomer and carbon density of 2000 kg.m<sup>-3</sup>.

*Carbon surface coverage:* voxels at the carbon interfaces were identified by creating a mask of the carbon phase dilated by one voxel, then subtracting the original carbon phase from it. This edge mask was used to sort carbon-neighbouring voxels as a function of their value, i.e., their class. The surface coverage was computed as the fraction of edge voxels belonging to the ionomer phase, over all edges.

*Connected components:* The connected component analysis was performed using the component labelling tool of the MorpholibJ plugin with a lower volume threshold at 1.5<sup>3</sup> nm<sup>3</sup> to account for limitations in resolution.

*Ionomer network thickness:* The ionomer network thickness was computed with the local thickness algorithm implemented in PoreSpy, which returns for each voxel the diameter of the biggest sphere inscribed within the phase while containing the voxel. To plot a distribution, 10000 points were randomly sampled within the ionomer phase.

*Pt and carbon ionomer coverage thickness:* Following Cetinbas *et al.*<sup>106</sup>, the coverage thickness was computed using a graph-based approach to calculate the geodesic distance between a sample of points at the Pt or carbon surface and the closest pore exterior to the primary carbon particles. Briefly, an adjacency matrix was created from the ionomer phase, where each voxel was connected to its 26 neighbours by edges whose weights were their Euclidian distance. Dijkstra's algorithm was then repeatedly used to search the shortest path between all voxels of the ionomer phase and any voxel of the ionomer/pore interface, effectively creating a distance-from-pore map. To make the computation tractable within a reasonable time, the volume was subdivided in 200<sup>3</sup> vx<sup>3</sup> patches that were subsequently reassembled in a single map after distance calculations. Distributions were obtained by sampling 10000 points at the surface of Pt or carbon within this map.

*Pt size distribution:* Prior to analysis, Pt nanoparticles contacting each other were separated and individually labelled using a distance transform watershed segmentation. The particles were then fitted with ellipsoids, and diameters were calculated by averaging the intermediate and minor diameters of the ellipsoids in order to account for missing wedge elongation that

---

artificially increases the major diameters. The distributions were truncated below  $1.5^3 \text{ nm}^3$  to account for the resolution.

*Pt position and accessibility:* For each platinum nanoparticle, the number of contacting voxels with the background or the ionomer was first quantified. Particles were classified as exterior if their edges contacted another phase than carbon and further defined as connected if contacting the ionomer phase. As described above, we restrict the definition of contact to areas above  $1.5^2 \text{ nm}^2$  to account for the resolution. For surface fractions, the total contact areas (with background or ionomer) were summed and divided by the total Pt area. The surface fraction of the connected particles was computed similarly, taking into account the entire surface of all connected particles as depicted in Fig. 4.5a of the main manuscript

### **B.1.3 EDS analysis on the site of the KB7 reconstruction**

EDS analysis was carried out to confirm the ionomer presence in the area reconstructed in Fig. 4.3 of the main text. The analysis was done on a different microscope and, while the precise location could be found, changes were apparent between the images at the end of the tilt-series acquisition and those prior to the EDS analysis. Clear material displacement (e.g., bottom-left corner of the image in Fig. B.7b) and overall shrinkage can be seen in Fig. B.7b-c. This is likely due to the abrupt thawing and condensation/deposition the sample/grid was subjected to when removing the cryo-holder from the column, and/or to beam-induced damage during the first positioning frames prior to the EDS analysis, which was performed at RT and relatively high dose (see Methods). However, the majority of the tilt series area was intact and could be compared to the EDS results.

As seen in the integrated EDS spectrum depicted in Fig. B.7e and e, the fluorine signal was overall low in this area. This could be attributed to degradation during the positioning frames and, possibly, to F-losses during tilt-series acquisition that were not apparent in the images (as seen in Fig. B.2f). In addition, the area suffered strongly from carbon buildup during EDS acquisition, which could arise from contamination during condensation/deposition on the cold grid, and this also limited the acquisition time and SNR. Finally, based on previous studies<sup>149</sup>, it is uncertain that a 2-3 nm-thick ionomer layer can generate enough counts before most of the fluorine is lost.

We note that the whole sample/grid suffers from Si contamination (Fig. B.7e), which was not detected in previous EDS on this catalyst layer, as shown for example in Fig. B.13. Upon further investigation, we have found it to be often present when re-acquiring data on year(s)-old samples, as was the case for this analysis. In comparison, the data in Fig. B.13 was acquired on

a grid that had not been stored for such a long time. Therefore, this Si contamination most likely originates from the long-term storage in non-inert conditions inside typical grid-storage boxes.

To improve the SNR, we also applied multivariate statistical analysis by way of decomposition with non-negative matrix factorization. Results are displayed in Fig. B.7i-k, and show that the identified components have compositions that can be related to the Pt catalyst, the ionomer and the carbon supports and that marginal improvements are gained in the SNR.

Comparing the projected segmentation results with the EDS data therefore demonstrate that ionomer is present throughout the area and in locations agreeing with tomography results.

#### **B.1.4 ion-exchange of ionomer layers for enhanced mass contrast**

One of the difficulties of resolving the ionomer distribution in fuel cells using X-ray or electron microscopies is related to the low mass-thickness contrast with respect to the carbon substrates. Conventionally, this has been addressed using contrast-enhancing sample preparation steps such as staining<sup>365</sup> or ion-exchange<sup>104,105,163</sup>, or analytical techniques sensitive to fluorine, e.g., energy dispersive spectroscopy (EDS)<sup>116,149</sup>, electron energy loss spectroscopy (EELS)<sup>149</sup>, energy-filtered (EF)-TEM<sup>104,160</sup>, and X-ray spectromicroscopy<sup>112,116,117,119,121</sup>. Analytical techniques are usually highly dose-intensive which can result in severe ionomer degradation from radiolysis. Therefore, ion-exchange was previously used in combination with electron tomography and high-angle annular dark field scanning (HAADF-S)TEM to map ionomer coverage on carbons<sup>163</sup>. It nevertheless bears inherent limitations due to the intensity of the ion-exchanged ionomer phase, which prevents the analysis of samples with nanocatalysts. This complicates conclusions as ionomers interact preferentially with the Pt surface<sup>60</sup>, potentially leading to discrepancies between model samples and catalyst layers. Moreover, the effect of the ion-exchange step on the ionomer (nano-)morphology remains uncertain, and discrepancies and swelling have been observed after ion-exchange<sup>160</sup>. We have also found that this protocol leads to a variety of results in catalyst layer samples, which we demonstrate in Fig. B.14 with two representative areas of a model, Pt-free, catalyst layer fabricated with Nafion D2021 and Vulcan carbon blacks at 0.7 w/w I/C, ion-exchanged with Cs<sup>+</sup> ions following a procedure discussed elsewhere<sup>109</sup>, and imaged in HAADF-STEM. These areas exhibited two distinct morphologies which we term here “continuous” and “clustered”. In the clustered case, crystallites, 2-3 nm wide, are observed. High-resolution images (not shown) indicate a lattice spacing corresponding to CsF and point towards a byproduct of e-beam induced degradation, release of fluorine radicals by radiolysis, and reaction with the metal cations. Alternatively, some areas exhibited the expected continuous morphology, with no crystallites observable but evidence of a relatively homogeneous and amorphous layer surrounding the carbons. We hypothesize these discrepancies arise from the presence of locally thicker ionomer layers and patches, as shown

---

in the main manuscript, which would provide sufficient reactant for CsF to arrange in crystallites. Additionally, a locally different ionomer nanomorphology could also have an influence, as ionomers are known to exhibit a transition between 10 and 20 nm from bulk-like behavior with phase separation to dispersion-like with weak phase separation, characteristic of ultra-thin layers<sup>53,59</sup>.

It appears therefore that a representative investigation of the ionomer coverage using such a sample preparation procedure is complex. Indeed, the crystallites would challenge the analysis of samples that contain Pt nanoparticles due to their similar shape. Moreover, they do not appear in tomographic reconstructions as a continuous phase (Fig. B.14), potentially inhibiting the precise identification and segmentation of the ionomer phase. As a consequence, our work focused on using bright field TEM and phase contrast as a means to image pristine catalyst layers without contrast-enhancing sample preparation steps that can lead to erroneous interpretation of the results.

### **B.1.5 Pt utilization in low RH conditions**

The electrochemical oxidation of CO chemisorbed onto a Pt surface, *CO stripping*, is well-suited to reliably determine the electrochemically accessible surface area (ECSA) of Pt/C catalysts, because the adsorption strength of CO ensures near-complete coverage<sup>95</sup>. As CO cannot be electrooxidized in the absence of water and a proton-conducting pathway, the obtained ECSA is dependent on the availability of both within the Pt/C catalyst layer, which is typically controlled *via* the relative humidity.

Three processes are primarily responsible for the availability of liquid water in a Pt/C catalyst layer: Water uptake by the ionomer's sulfonate end groups, capillary condensation in the carbon particles' internal pores, and wetting of the Pt surface via water vapour adsorption<sup>96</sup>. The ionomer's sulfonic acid sites are solvated by a hydration shell even at very low RH (<20 %), and thus a Pt surface in direct contact with the ionomer can electrochemically oxidize (strip) chemisorbed CO at such low humidification levels. For solid carbon supports, where Pt nanoparticles are predominantly present on the external surface of carbon particles and thus fully in contact with the ionomer phase, all Pt nanoparticles are active for CO stripping throughout the entire relative humidity range, i.e., the Pt utilization is always close to 100%.

In porous, high surface area carbon supports, such as the Ketjenblack carbon used in this study, a significant fraction of Pt nanoparticles is hosted within internal pores, which are not accessible to ionomer strands due to size exclusion. At high RH above 70%, capillary condensation in these pores ensures that all Pt particles are contacted by liquid water and capable of CO stripping, even though the ionomer is not present everywhere. This equates to a Pt utilization of



100%. Upon decreasing RH, the extent of capillary condensation is gradually reduced and ceases completely between 40-60% RH<sup>366</sup>. Below this RH, one would expect the ECSA, and accordingly, the Pt utilization, to reach a plateau corresponding to the fraction of external Pt surface in direct contact with the ionomer. This, however, is virtually never observed in the existing literature<sup>50,64,97</sup>. In most cases, the Pt utilization starts to decrease at intermediate RH and then falls monotonically until it reaches the lower experimental cutoff value for the RH (10-25% RH), typically determined by the technical limits of the humidifying system. Chowdhury and co-workers explained this phenomenon through continuous water bridges between adsorbed thin films on Pt nanoparticles. If the interparticle distance of dispersed Pt, scaling with the Pt weight fraction, is sufficiently small, these bridges may supply water and protons to Pt surfaces that are not in direct contact with the ionomer. Crucially, this occurs at much lower RHs than would be required for capillary condensation of liquid water, because both ionomer water uptake and Pt wetting are non-zero even below 20% RH. A plateau in Pt utilization is therefore only observed when the bridging function is hindered by sufficiently large Pt interparticle distances (e.g., a 10 wt%<sub>Pt</sub> catalyst<sup>50</sup>) or severely disrupted ionomer coverage (e.g., I/C ratio of 0.1<sup>92</sup>).

We thus suggest that Pt utilization measurements at low RH only approximate the true dry state corresponding to 0% RH, which is inaccessible to the CO stripping methodology because the oxidation reaction requires water. Above 0% RH, Pt surfaces not immediately contacted by the ionomer gradually become accessible *via* water bridges, even before the onset of liquid water condensation on the carbon surface itself. The Pt utilization therefore never reaches a true plateau equivalent to the connected surface found in cryogenic TEM tomography. Our obtained Pt utilization of 31% at 10% RH suggests that at these levels of humidification, the electrochemically accessible Pt surface area is slightly larger than that found to be in direct ionomer contact in TEM, i.e., 15% at 0% RH, but below the value of the total surface of connected particles, yielding 52% Pt utilization, as detailed in Fig. 4.5 of the main text.

## B.2 Supplementary Figures

### B.2.1 dose-series

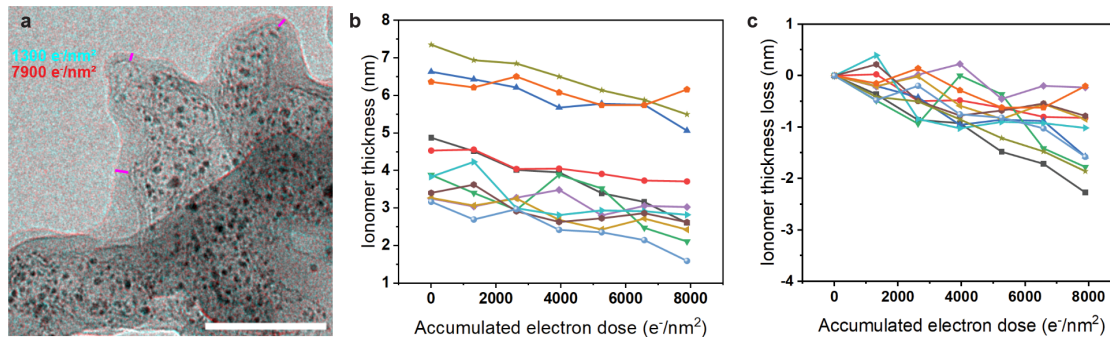


Fig. B.1: Ionomer degradation analysis at cryo-temperature. **a** Composite BF-TEM image of a typical area used for measurements of the ionomer thickness as a function of accumulated electron dose. Some of the points of the measurements are highlighted by magenta makers. Cyan channel is the image at 1300 e<sup>-</sup>/nm<sup>2</sup>, Red channel is at 7900 e<sup>-</sup>/nm<sup>2</sup>. Scale bar is 50 nm. **b** Ionomer layer shrinkage for N = 11 measurements and **c** corresponding average thickness loss.

### B.2.2 e-beam induced damages during tilt-series acquisition

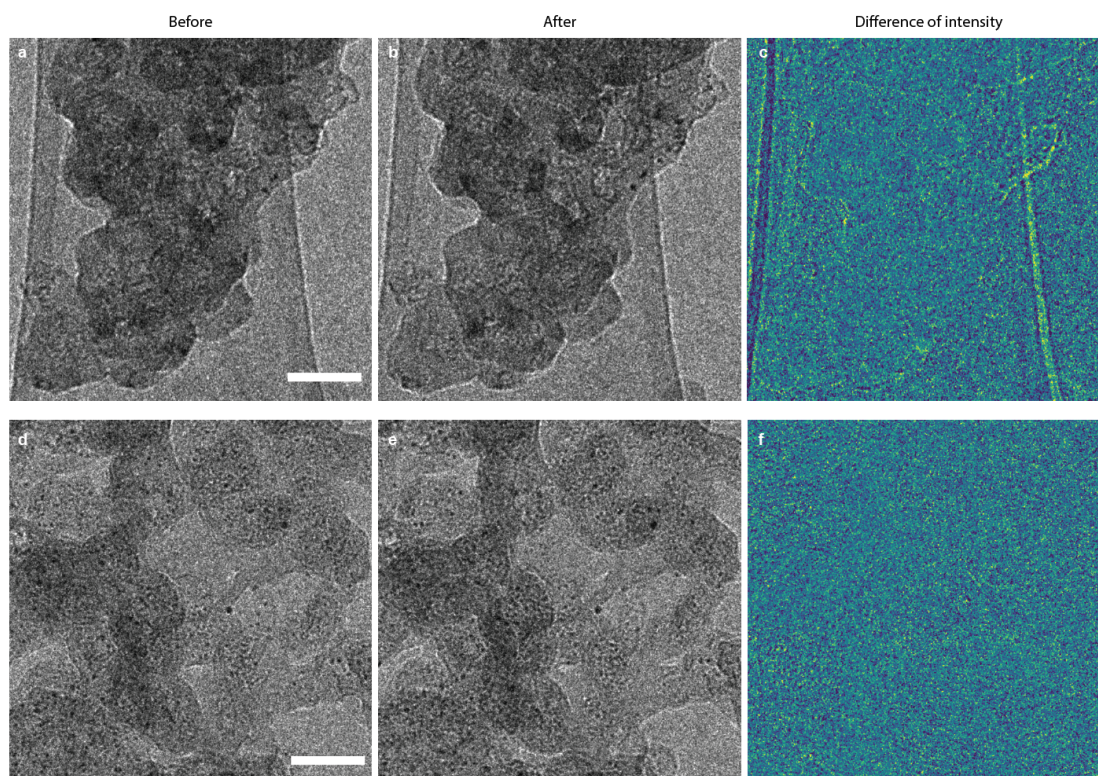


Fig. B.2: Comparison of sample shrinkage from e-beam irradiation during tilt-series acquisition. **a-c**, Aggregate from a dispersion of the gVu7 sample imaged before **a** and after **b** tilt-series acquisition, totalling 3600 e<sup>-</sup>·nm<sup>-2</sup>, and **c** difference of intensity between the two images after alignment. Increasing contrast indicates a greater shift during acquisition. Similarly, **d-f** depicts

the area of a microtomed section from the KB7 sample before **d** and after **e** tilt-series acquisition, totalling  $3450 \text{ e}^- \cdot \text{nm}^{-2}$ , and **f** difference of intensity between the two images. Scale bars are 50 nm.

### B.2.3 Denoising performance

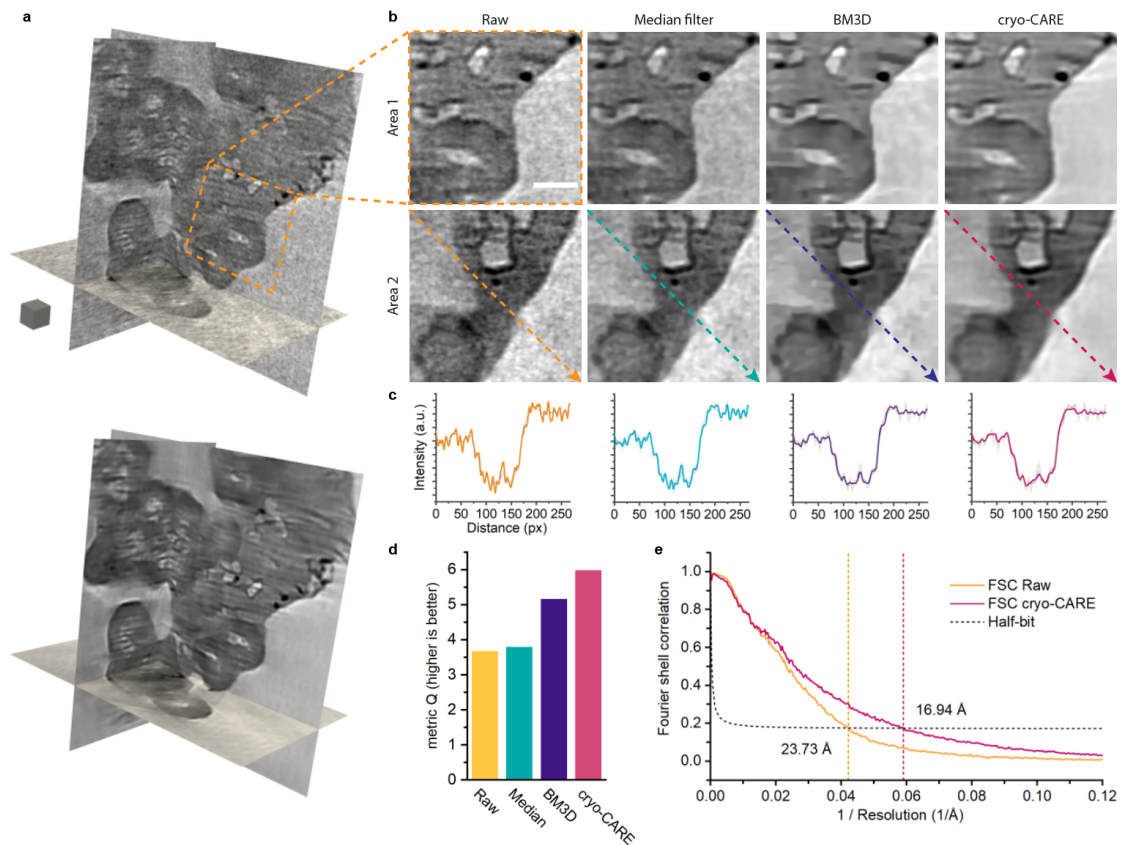


Fig. B.3: Comparison of denoising methods for tomographic reconstruction and resolution estimation. **a**, multi-orthoslice overview of a raw reconstruction of an aggregate from the gVu7 sample and comparison with the same volume denoised with the cryo-CARE method. Scale cube is  $20^3 \text{ nm}^3$ . **b**, representative areas from the reconstruction and denoising results following a median filter with a  $2 \times 2$  pixels kernel, the BM3D algorithm<sup>238,367</sup>, and the cryo-CARE method. Median and BM3D were applied plane-by-plane while cryo-CARE is a volumetric method. Scale bar is 20 nm. **c**, line profiles plotted from area 2 as shown by the corresponding arrows in (B). **d**, metric  $Q$  comparison<sup>250</sup>. Higher values indicate lower levels of noise and blur in  $25^2 \text{ px}^2$  anisotropic patches of an image. **e**, Fourier shell correlation plots computed from the even and odd volumes before (raw) and after denoising with cryo-CARE. The resolution was estimated at the half-bit criterion.



## B.2.4 morphology of graphitized Vulcans

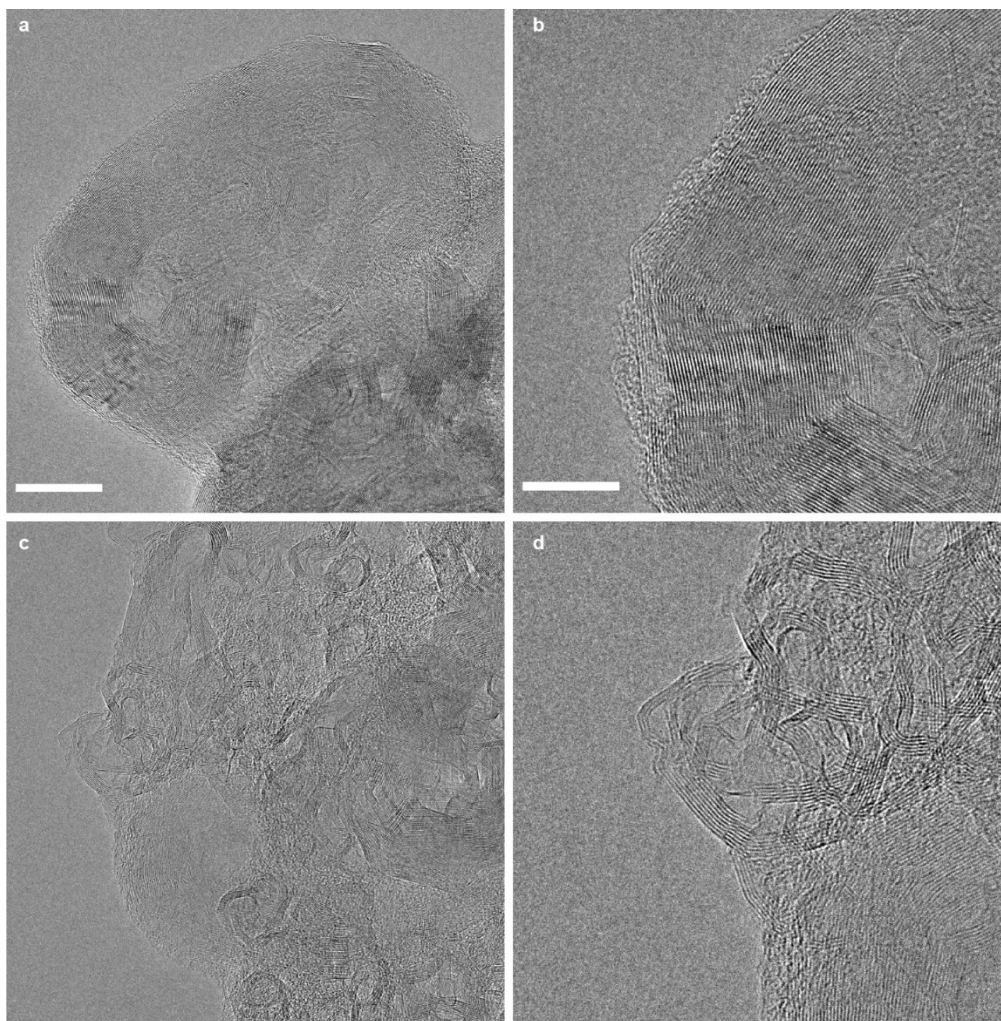


Fig. B.4: graphitized Vulcan morphologies. **a, c**, HRTEM micrographs of aggregates and particles representative of the various morphologies in a graphitized VA-type carbon black as used to fabricate samples gVu3, 7 and 12. Scale bar is 20 nm. **b, d**, Corresponding close-ups. Scale bar is 10 nm. The sample was prepared by dispersion from a model catalyst layer containing ionomer and imaged at high electron dose ( $> 10^7 e^- \cdot \text{nm}^{-2}$ ). Some highly degraded ionomer material is visible in **b** and **d**.

## B.2.5 Segmentation workflow and performance

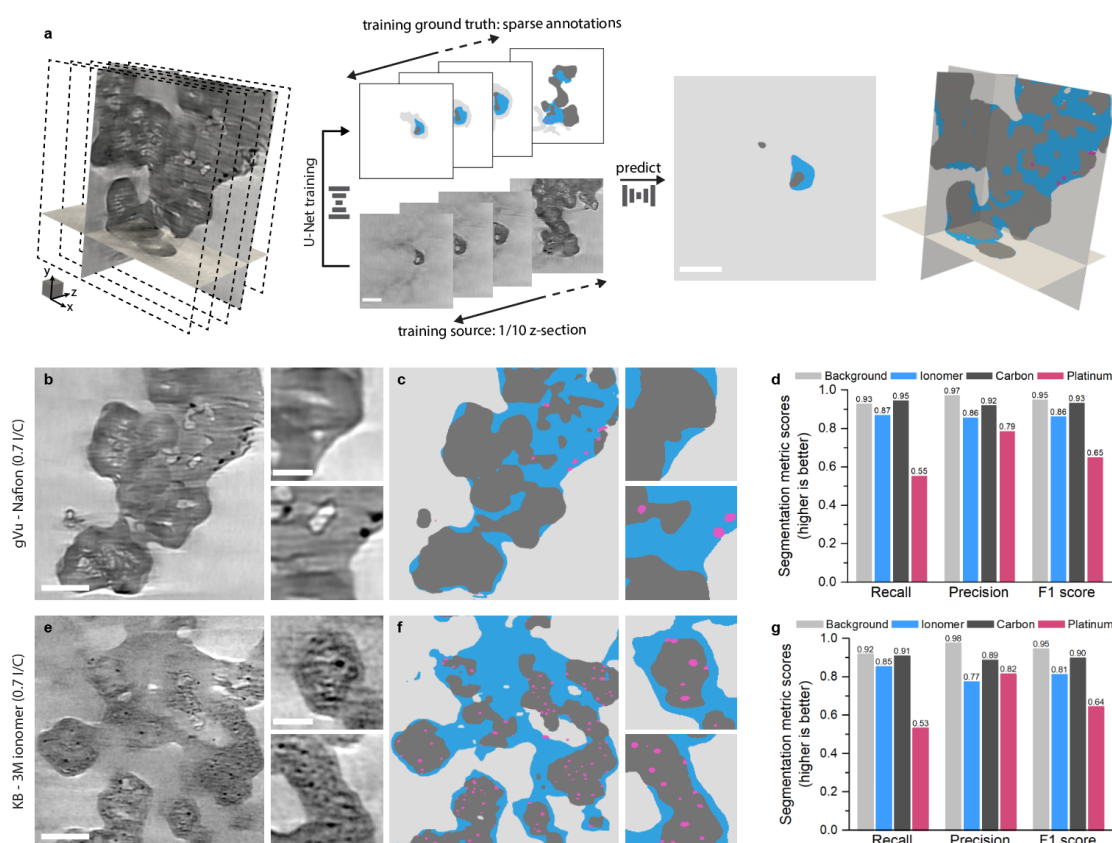


Fig. B.5: Methodology and performance of the segmentation process. **a**, schematic depiction of the training strategy as described in Methods on the gVu7 sample. For each denoised reconstruction, 1/10 z-sections are extracted and sparsely annotated by hand in 2D. This dataset is used for training a U-Net model which is then applied to predict the segmentation maps of every z-sections, that is, plane-by-plane, in the denoised volume, before reassembling in 3D. Scale cube is  $20^3 \text{ nm}^3$  and scale bars are 50 nm. **b**, **e**, example tomograms and close-ups taken from the reconstructions and **c**, **f**, corresponding segmentation output for the gVu7 (**b**, **c**) and KB7 (**e**, **f**) samples. Scale bars are 50 nm, 20 nm in the close-ups. **d**, **g**, Comparison of segmentation metric scores computed from a validation dataset held out from training. For each class, recall is defined as the fraction of ground truth pixels of this class correctly labelled as such in the output, and precision is the fraction of output pixels of this class correctly labelled. The F1 score incorporates both metrics in one.

## B.2.6 Aggregates at different I/C content

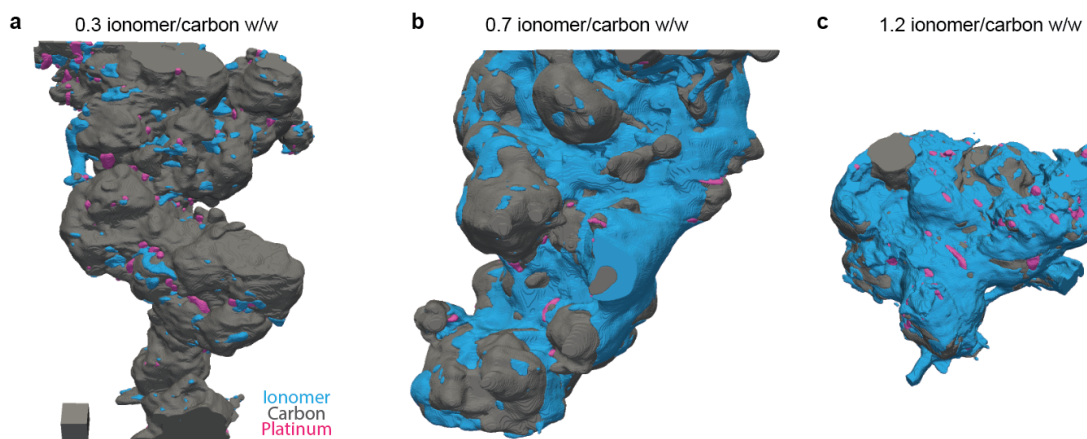


Fig. B.6: Cryo-ET reconstructions of Nafion-gVu-Pt aggregates with increasing I/C ratio. **a-c**, segmented volumes of aggregates from the gVu3, 7 and 12 samples, respectively. All volumes are shown at the same scale, the scale cube is  $20^3 \text{ nm}^3$ .

## B.2.7 EDS on KB7 site

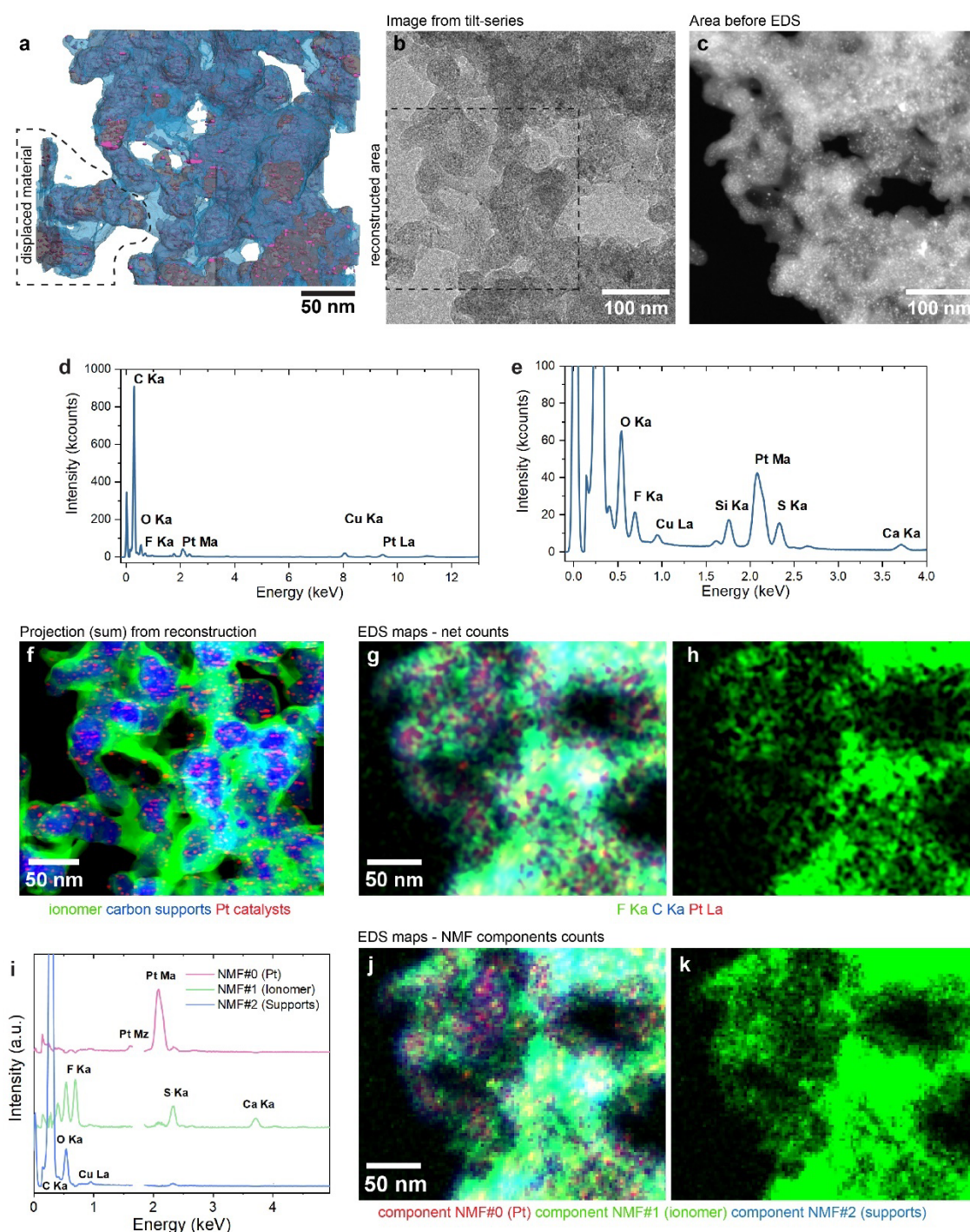


Fig. B.7: EDS analysis of the site of the KB7 reconstruction. a) 3D visualization of the reconstructed volume, oriented to match the geometry and orientation of the EDS acquisition. Comparison of the area as acquired b) in BF-TEM during the tilt-series and c) in STEM-HAADF before the EDS acquisition. e) EDS spectrum integrated over the whole area corresponding to the reconstruction and h) zoom-in on low-energy region. f) projection as the sum along the z-axis of the reconstructed volume. g) Composite EDS map with F Ka (green), C Ka (blue) and Pt L (red) net counts. h) isolated EDS map of the F Ka net counts. Acquisition at RT and 200 kV, with a 0.6 nA probe current, 100  $\mu$ s dwell time and 0.6 nm pixels. The total dose was  $4.9 \times 10^7$   $e^-/\text{nm}^2$ . Data was processed with a spatial Gaussian pre-filter ( $\sigma = 3$ ) and polynomial background removal. i-k) Results from decomposition with non-negative matrix



factorization on data spatially binned by 4 in preprocessing. The Si Ka line was masked to avoid interference. i) components identified by the decomposition, with composition related to Pt catalysts (NMF#0), ionomer (NMF#1) and carbon supports (NMF#2). j) composite map of the spatial distribution of the identified components and k) isolated map of the component associated with ionomer.

## B.2.8 morphology of Ketjenblacks aggregates

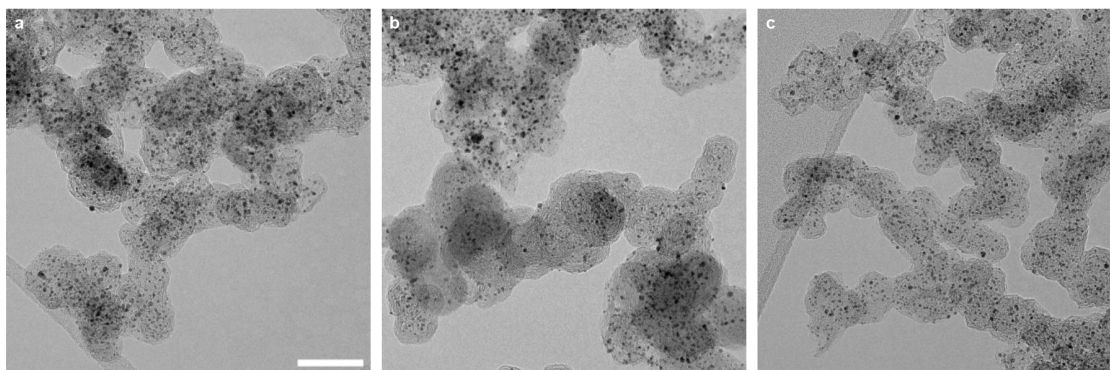


Fig. B.8: Morphology of Ketjenblack catalysts. **a-c**, representative HRTEM of dispersed 19.8 wt%<sub>Pt</sub> Ketjenblacks as used in sample KB7. Scale bar is 50 nm.

## B.2.9 pores in Ketjenblacks

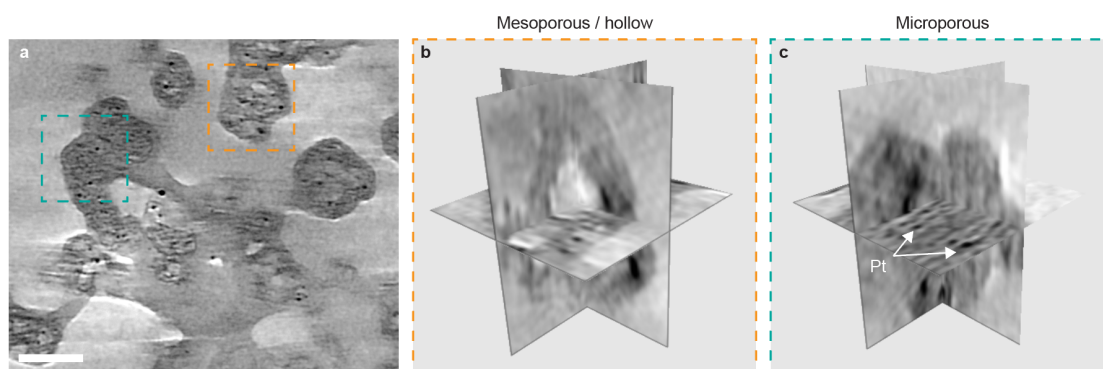


Fig. B.9: Interior morphology of Ketjenblack catalysts. **a**, Tomogram from the cryo-ET reconstruction of the KB7 sample presented in Fig. 4.3 of the main manuscript. Scale bar is 50 nm. Two categories of carbon particles can be found, with **b**, a mesoporous/hollow core directly visible and **c**, an interior microporosity demonstrated by the presence of Pt. Due to contrast and resolution limitations, the porosity was not segmented.



### B.2.10 connected components analysis of the ionomer network

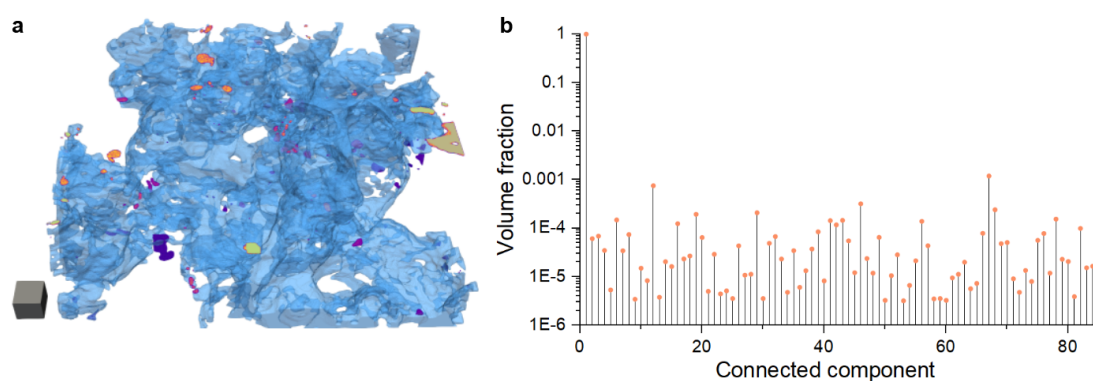


Fig. B.10: Connected components analysis of the ionomer network. **a**, Labeled connected components in the ionomer phase of the cryo-ET reconstruction of the KB7 sample presented in Fig. 4.3 of the main manuscript. Scale cube is  $20^3 \text{ nm}^3$ . **b**, Plot of the volume fraction for each identified component.

### B.2.11 ionomer morphologies in KB7 catalyst layer

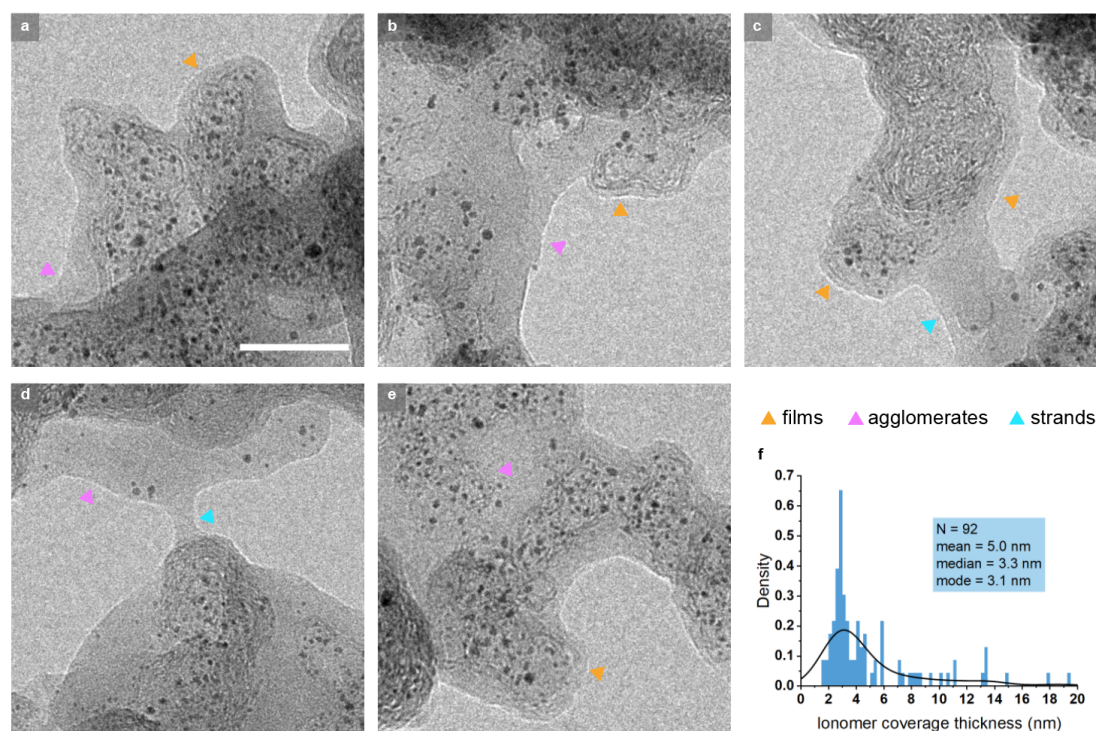


Fig. B.11: Ionomer morphologies in catalyst layers. **a-e**, representative BF-TEM images of a microtomed section of the KB7 sample, acquired in cryogenic conditions. The dose was  $1200 - 1500 \text{ e}^-/\text{nm}^2$  per image. Morphologies similar to those observed in the tomographic reconstruction are identified with coloured markers. Scale bar is 40 nm. **f**, Histogram of the ionomer coverage thickness measured from the BF-TEM images. Black line is a kernel plot of the histogram.

## B.2.12 representativeness of measurements within KB7 volume

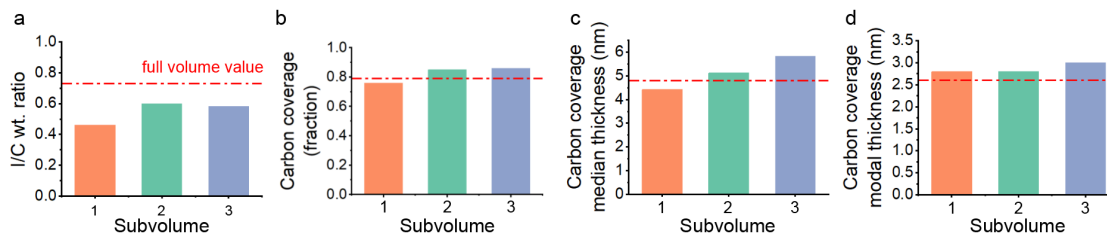


Fig. B.12: Analysis of the representativeness of the measurements in the KB7 reconstruction. Measurements of a) the I/C ratio, b) carbon surface coverage, c) median and d) modal thicknesses of the ionomer coverage on carbon surfaces. Measurements were performed on three sub-volumes of size 140 x 250 x 40 nm taken at the beginning, centre, and end of the volume (total size: 300 x 250 x 180 nm) used for Fig. 4.3 of the main manuscript, along the z direction.

## B.2.13 electrode homogeneity

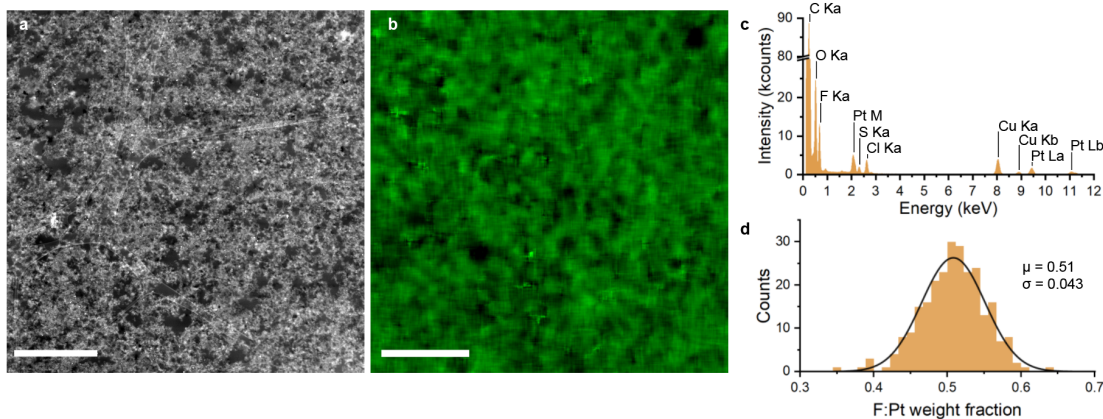


Fig. B.13: Assessment of the ionomer distribution at the catalyst layer scale. **a**, HAADF-STEM image and **b**, corresponding F:Pt weight fraction map quantified from STEM-EDS. Acquisition was done on a microtomed cross-section of the KB7 sample. Scale bars are 2  $\mu\text{m}$ . **c**, Representative STEM-EDS spectrum. **d**, F:Pt weight fraction distribution calculated from 500<sup>2</sup> nm<sup>2</sup> tiles (N = 256) sampled from the map in **d**. Black line is a fitted normal distribution parameterized by its mean  $\mu$  and standard deviation  $\sigma$ .

### B.2.14 ionomer morphology after ion-exchange

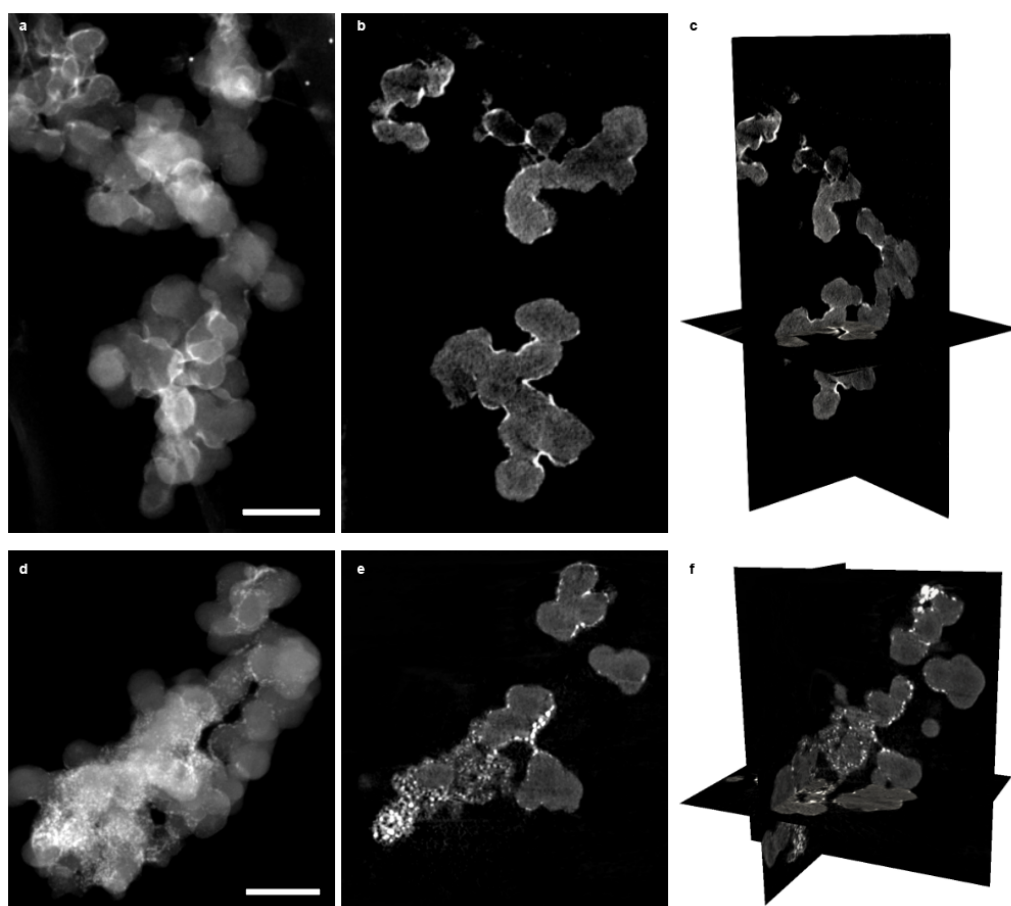


Fig. B.14: Representative ionomer morphologies after ion-exchange. **a, d**, HAADF-STEM images from ionomer/carbon aggregates from a model, Pt-free catalyst layer fabricated with Vulcan XC72 carbon black and Nafion 2021 at 0.7 w/w I/C ratio and ion-exchanged with  $\text{Cs}^+$  as discussed in Supplementary Text. Ionomer layers typically appeared “continuous” **a**, or “clustered” **d**. Scale bars are 100 nm. **b, e**, Corresponding tomograms showing a central section through the reconstructed volumes of the aggregates. **b**, Reconstruction performed by the weighted back projection (WBP) algorithm implemented with the ASTRA toolbox<sup>265,266</sup> and **e** with the model-based iterative reconstruction (MBIR) method<sup>228</sup>. **c, f**, Multi-orthoslice view of the reconstructions.

## B.3 Supplementary Tables

### B.3.1 composition of various catalyst layers

Sample denomination	Figure of reference	Carbon type	Pt loading (wt% / $\text{mg}\cdot\text{cm}^{-2}$ )	Ionomer type	Ionomer loading (I/C wr)
<b>gVu3</b>	Fig. B.6a	Graphitized Vulcan (TKK)	8.7 / $\sim 0.04$	Nafion D2021	0.35
<b>gVu7</b>	Fig. B.6b	Graphitized Vulcan (TKK)	8.7 / $\sim 0.04$	Nafion D2021	0.7
<b>gVu12</b>	Fig. B.6c	Graphitized Vulcan (TKK)	8.7 / $\sim 0.04$	Nafion D2021	1.2
<b>KB7</b>	Fig. 4.3	Ketjenblack (TKK)	19.8 / $\sim 0.08$	3M 800EW	0.7

---

### B.3.2 tilt-series acquisition parameters

Sample denomination	Figure of reference	Sampling range (°) [acquired] / [used for reconstruction]	Dose rate (e <sup>-</sup> .nm <sup>-2</sup> .s <sup>-1</sup> )	Total accumulated dose, incl. pre-irradiation (e <sup>-</sup> .nm <sup>-2</sup> )
<b>gVu3</b>	Fig. B.6a	[-66, +74] / [-66, +72]	33	3600
<b>gVu7</b>	Fig. B.6b	[-68, +76] / [-66, +76]	33	3750
<b>gVu12</b>	Fig. B.6c	[-66, +74] / [-66, +66]	20	2230
<b>KB7</b>	Fig. 4.3	[-62, +70] / [-62, +70]	33	3450

## C Supplementary Information for Chapter 5

### C.1 HRTEM images of Pt/KB

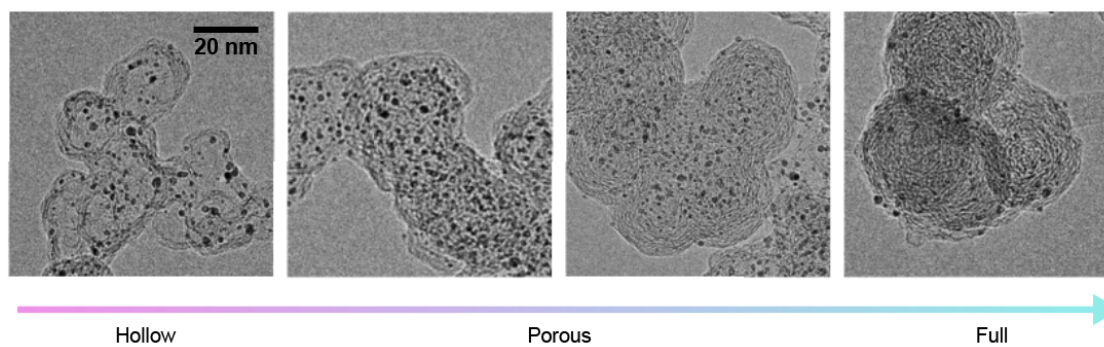


Fig. C.1: Representative HRTEM micrographs of Pt/KB aggregates

## C.2 Internal rotation determination

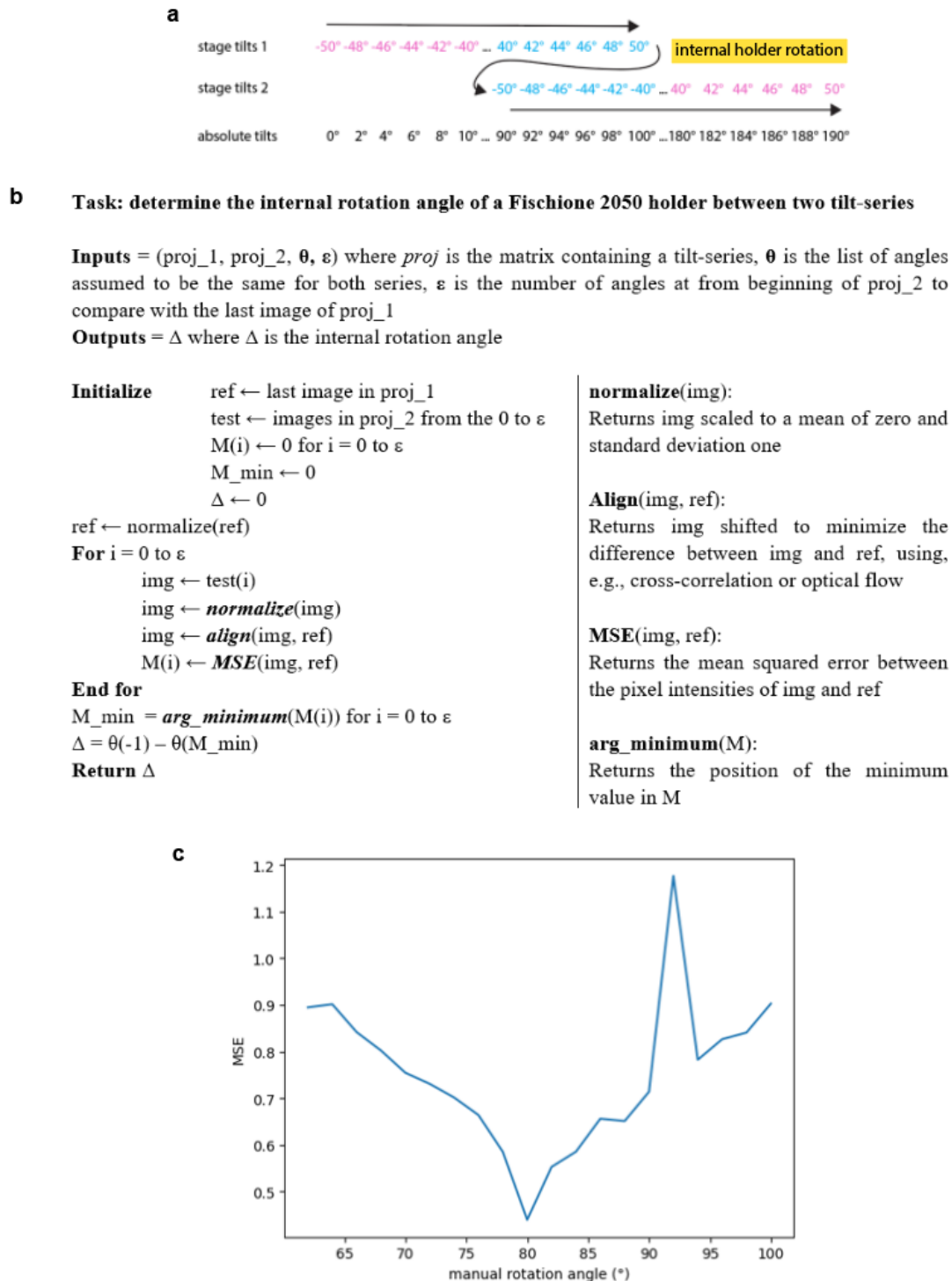


Fig. C.2: Internal rotation in probe specimen holder for full-range ET. **a**, depiction of the internal rotation angle and angular overlap in tilt-series of 100° span and 2° increment. **b**, pseudo-code of the algorithm for automated determination of the internal rotation angle. **c**, typical result from the procedure showing that MSE measurement is clearly minimum at the actual internal rotation angle, here 80° instead of the otherwise assumed 90°.

A key feature of the probe holder used in this study is the internal rotation mechanism, which allows to cover the full  $180^\circ$  tilting range with limited stage tilts. The acquisition is performed by acquiring a first tilt-series where the TEM stage is tilted in range  $[-50^\circ, +50^\circ]$ . An internal rotation of  $90^\circ$  is then done before a second tilt-series is acquired. In principle, the resulting complete series covers  $190^\circ$  with  $10^\circ$  of overlap on each end of the tilt-series as shown in Fig. C.2a. However, the internal rotation lacks precision and in effect always differs from the expected  $90^\circ$ , sometimes by up to  $10^\circ$ , so that the overlap concerns slightly different angles for every acquisition. To retrieve the actual internal rotation for each experimental acquisition, an automated procedure described in pseudo-code in Fig. C.2b was implemented. It aims at screening a few images from the beginning of the second tilt-series to find the one that best matches a pre-selected image from the end of the first tilt-series. The match was evaluated on the basis of the mean square error (MSE) between each image pair. As shown in Fig. C.2c for a typical acquisition, the MSE consistently decreases until the best match is found before rising again. Occasional outliers can be easily detected from the MSE curves, and we have never found them to prevent a clear result from being obtained. Once the true internal rotation and the actual overlapping range are determined, the complete tilt-series can be reassembled, with only one of the images kept at overlapping angles.

We have also assessed different tilt-series alignment strategies, including manual, cross-correlation, tracking-based<sup>211</sup>, and iterative methods<sup>218,222</sup>. The fully automated method developed by Odstrčil *et al.*<sup>218</sup> provided the best tradeoff between user involvement and results, and was used in the rest of this study. We note that the method was initially implemented for nano-computed tomography (nCT) data and performed well with our full-range data, but may be challenged in its current implementation for more conventional ET datasets, e.g., with objects entering/leaving the field of view and slab-like geometries.

### C.3 TEM vs. STEM ET

Next, we evaluated the results obtained with different acquisition modes. Key features were that the contrast between the Pt NPs and the carbon should not be too strong, and carbon as well as carbon pores should have sufficient visibility. To this end, we investigated (S)TEM modes that provide a combination of mass-thickness and phase contrast, starting with HRTEM. In this case, phase contrast arises from the interference of the direct and Bragg diffracted beams under slightly defocused conditions, while mass-thickness contrast is provided by a relatively large objective aperture (see methods) that removes electrons incoherently scattered at high angles. A typical image from a tilt-series is shown in Fig. C.3a, along with a close-up of a tomogram from the corresponding reconstruction. The contrast allows to clearly identify Pt NPs, carbon planes and pores. However, some elongated artefacts in the  $x$  direction can be observed in the



reconstructions. We attribute these, at least partially, to diffraction contrast and to slight defocus changes that caused variations in Fresnel fringes size and intensity which break the projection requirement in the tilt-series.

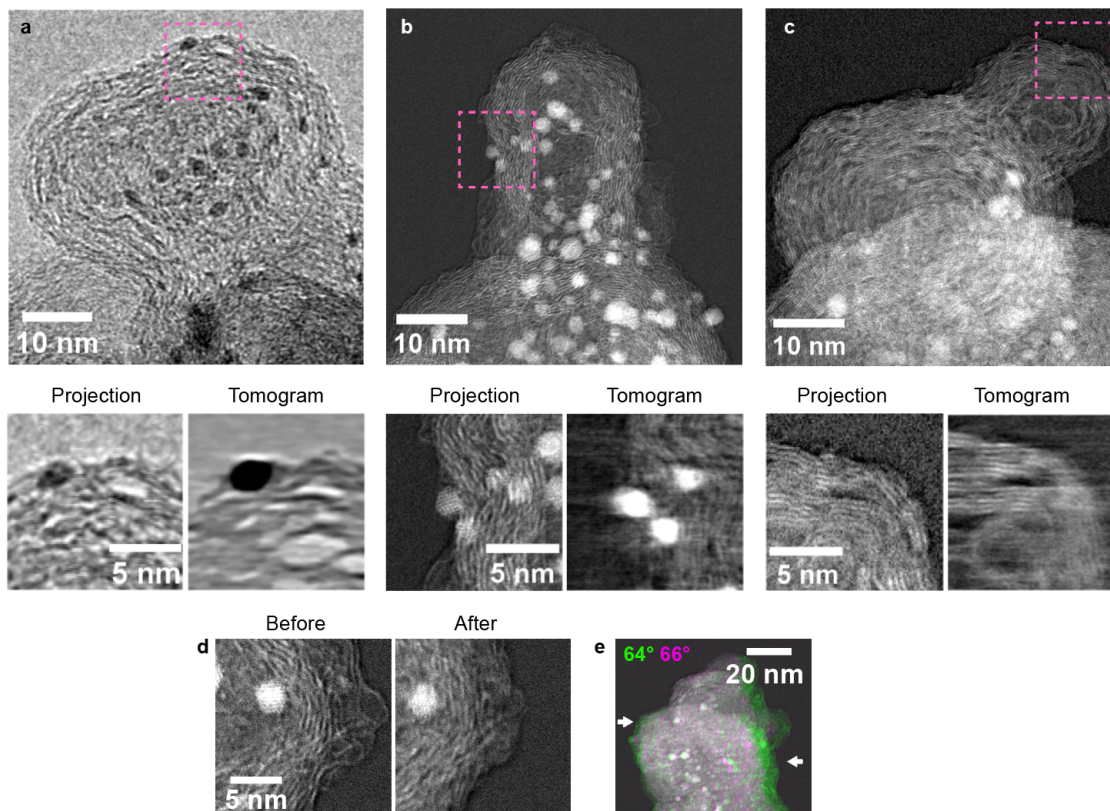


Fig. C.3: Comparison of acquisition modes for ET of KB. **a**, TEM image, close-up, and corresponding tomogram from a TVM reconstruction. **b** and **c**, STEM ADF images, close-up, and corresponding tomograms from SIRT reconstructions. **d**, comparison of beam-induced damage during a tilt-series acquisition. **e**, composite image demonstrating scanning anomalies which caused the image at  $66^\circ$  to be compressed in the  $x$  direction.

In addition, acquisitions with a probe-corrected STEM instrument were also performed. We used the ADF detector with a low collection angle (see methods) and a slight overlap with the direct beam, so that here again, the signal stems from a combination of mass-thickness contrast (in LAADF conditions) and phase contrast from the interfering direct and Bragg beams. Images with high resolution could be obtained, as demonstrated in Fig. C.3b and c, but the reconstruction quality remained limited in comparison. We attribute this to three effects: first, the total dose for a STEM acquisition was about an order of magnitude, at least, higher than in TEM. Since the acquisitions were done at 200 kV, which is higher than the threshold acceleration voltage for displacement of carbon in graphite<sup>197</sup>, knock-on damage was non-negligible. As shown in Fig. C.3d for an extreme case, this resulted in significant beam-induced damage over the course of the tilt-series. While we have also made attempts at 80 kV, we have



typically found that the resolution was too limited at the low convergence angle required for sufficient depth of focus. Second, scanning anomalies were seen in ~15% of the acquisition images, which resulted in significant distortions as shown in Fig. C.3d. These images could be removed from the series or kept if the distortions were minor but, either way, they reduced the final quality of the reconstruction. In future investigations, the problem could perhaps be solved with non-rigid alignment schemes<sup>355</sup>. Third, the particles investigated here may be too large already for the projection requirement to be met by phase contrast, although this effect would also participate in the TEM reconstruction.

Overall, pores were typically better resolved in TEM owing to the absence of beam-induced displacement. On the other hand, STEM data locally showed higher resolution, especially for carbon planes, in places where beam-induced displacements were not so severe. Thus, both acquisition modes provided valuable insights as further discussed in Section 5.3.3.

#### **C.4 Comparison of reconstruction algorithms**

We investigated the effect of the reconstruction algorithms on the full-range acquisitions Fig. C.4 compares tomograms obtained from a TEM acquisition and reconstructed with the FBP, CGLS, SIRT (not shown here) and TVM algorithms. The FBP resulted in higher noise levels and denoising with the cryo-CARE approach was tested, following methods described in sections 3.3.1 and Fig. C.4 of this thesis. The results are displayed in Fig. C.4b and show that the denoising procedure was effective. However, the resolution and contrast were still inferior to the other reconstruction techniques. This suggests that resolution in this TEM reconstruction is not limited by the noise of the projections but rather by the acquisition parameters (mainly spherical aberration of the microscope and defocus) and the angular sampling of the tilt-series. We note that the horizontal artefacts previously mentioned are more prominently visible in the CGLS, SIRT and TVM reconstructions (Fig. C.4c and d)). These are however not seen in the FBP reconstruction, which may arise from the filtering (or weighting) operation in Fourier space that is intrinsic to the method. The operation dampens the low spatial frequency (here with a Han window) in order to recover a pseudo-even sampling of the Fourier space<sup>216</sup>, and this effectively acts like a high-pass filter which could remove the artefacts, although a tradeoff is greater noise. Overall, the CGLS, SIRT and TVM provided relatively similar results with better contrast for the pores than FBP, and TVM showed slightly lower noise and sharper boundaries. We have used these alternatively in the Main of the chapter.

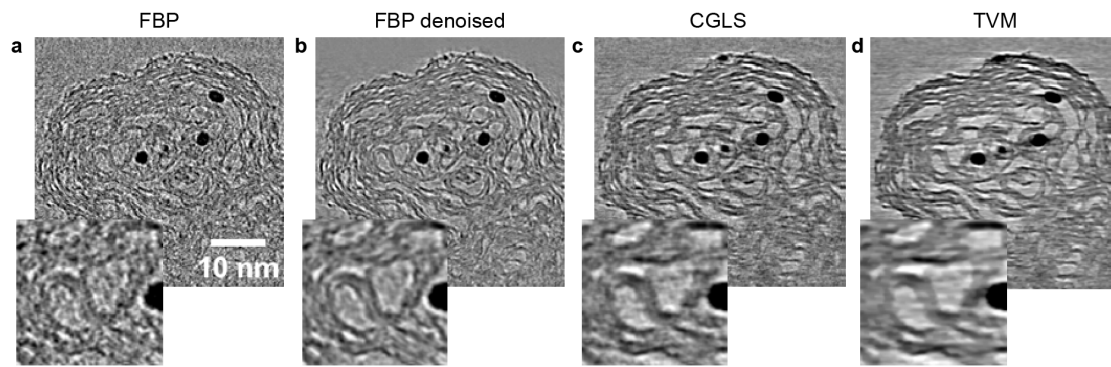


Fig. C.4: Comparison of reconstruction algorithms on a TEM acquisition.

## D Supplementary Information for Chapter 6

### D.1 Electrochemically cleaning Pt nanocubes

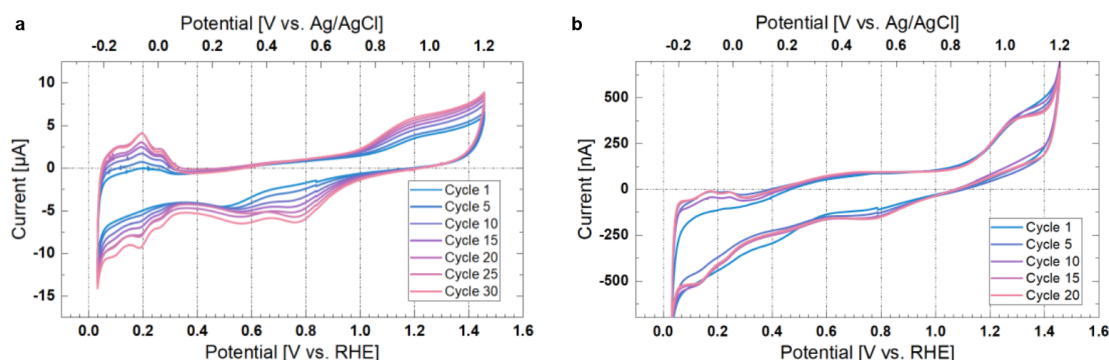


Fig. D.1: Typical electrochemical cleaning procedure for Pt nanocubes. The procedure is demonstrated here for NPs on (a) a bulk RDE electrode and (b) on a GC WE chip cycled in open cell *ex situ*. Cycling was performed at 50 mV/s, in 0.1 M  $\text{HClO}_4$ . The fine HUPD features, characteristic of faceted NPs<sup>368,369</sup>, are increasingly resolved throughout the procedure.

### D.2 Pt nanocubes signature and potential calibration in ec-LPTM

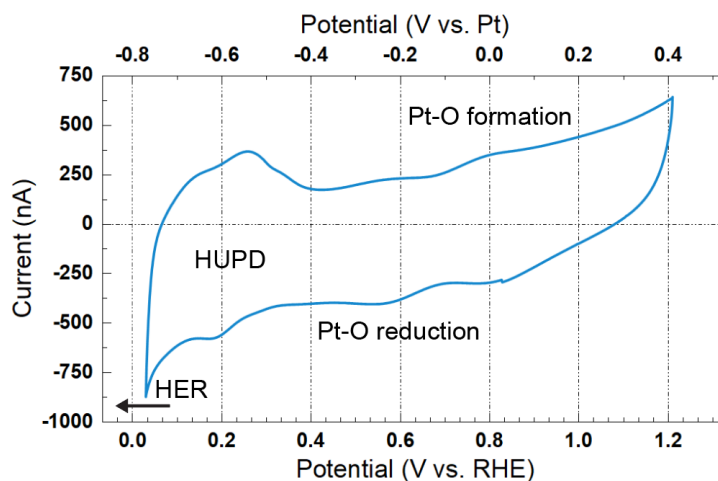


Fig. D.2: Typical Pt signature CV obtained for Pt nanocubes on a GC WE chip in ec-LPTM. The Pt features were used to calibrate the Pt RE of the chip (here,  $V_{\text{Pt}} = 0.8$  vs. RHE). CV obtained at 50 mV/s in 0.1 M  $\text{HClO}_4$ , in-holder.

### D.3 Increased resistance at GC thin-film electrodes

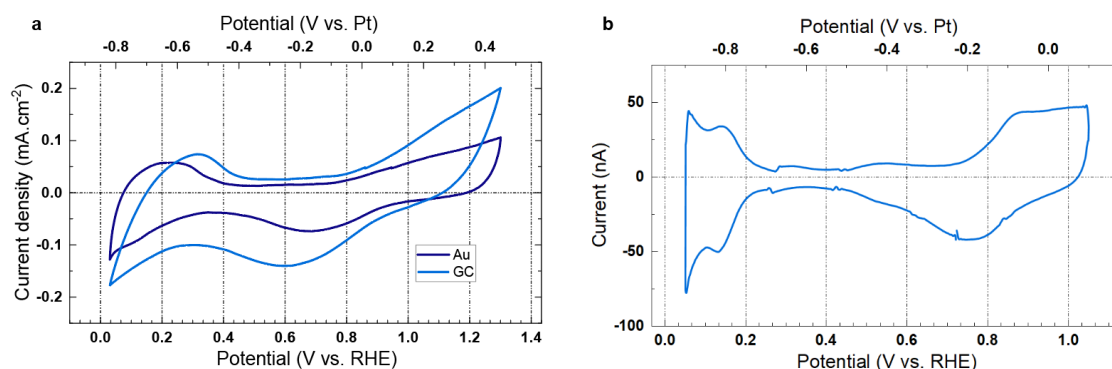


Fig. D.3: Electrochemical characteristics of thin-film WE electrodes. **a**, CV of Pt/C catalysts on Au (dark blue) and GC (light blue) electrodes patterned on ec-LPTEM MEMS chips. Scan rate: 50 mV/s. Measurements were done in the benchtop *ex situ* cell with a Pt RE ( $V = 0.85$  V vs. RHE) and a Pt CE. The currents were normalized using the integrated HUPD anodic charges and a specific value of  $210 \mu\text{C}/\text{cm}^2_{\text{Pt}}$ . The absolute currents at the Au electrode were larger than the GC one (peak HUPD cathodic current  $\sim 8 \mu\text{A}$  vs.  $4 \mu\text{A}$ ), which shows that the increased peak separation in the GC curve is necessarily attributed to higher resistances (lower resistances but much higher current could have resulted in a greater peak separation too, for instance). **b**, CV of a Pt thin film electrode in the ec-LPTEM holder. Scan rate = 50 mV/s. The chip featured a Pt RE ( $V = 0.95$  V vs. RHE) and a Pt CE.

### D.4 Pt nanocubes degradation timeframe

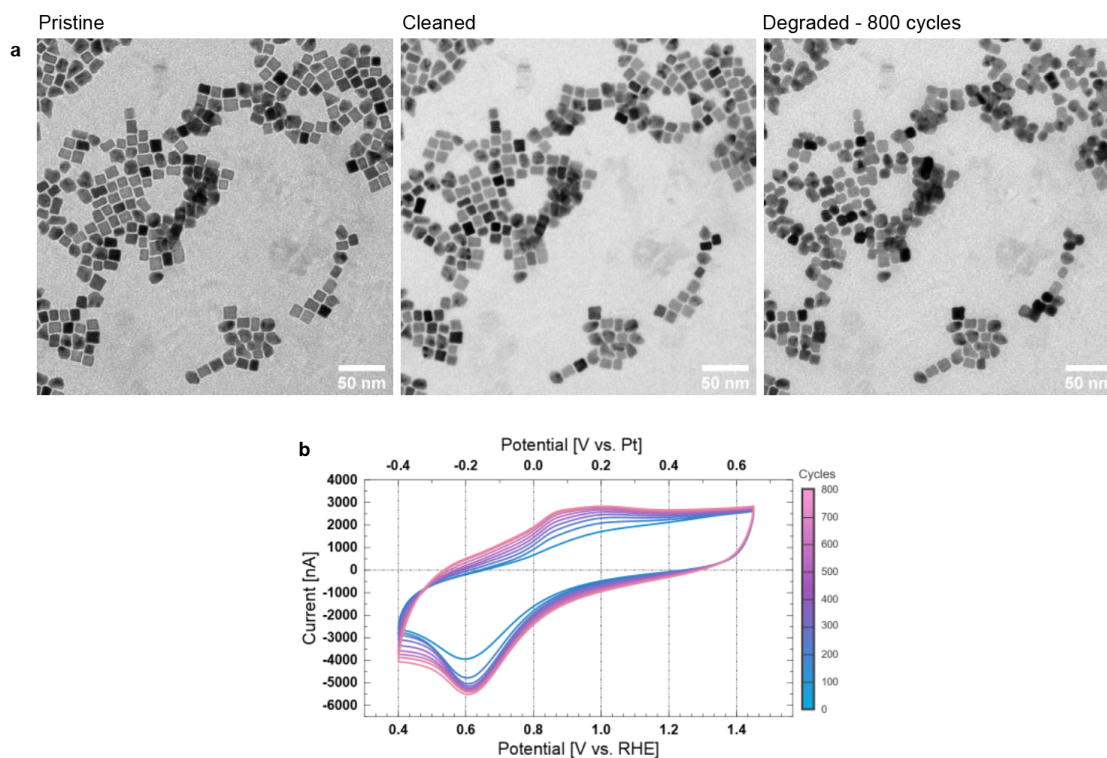


Fig. D.4: IL-TEM test of the degradation protocol for Pt nanocubes: 500 mV/s triangular waves in range  $\sim [0.4-1.45]$  V vs. RHE, in 0.1 M  $\text{HClO}_4$ . **a**, IL-TEM images of pristine cubes, after

electrochemical cleaning and after 800 cycles of the degradation protocol. **b**, Representative degradation cycles. Cycling was performed in the *ex situ* open cell, with a Pt CE and a Pt RE ( $V = 0.8$  vs. RHE).

### D.5 *In situ* STEM of Pt nanocubes

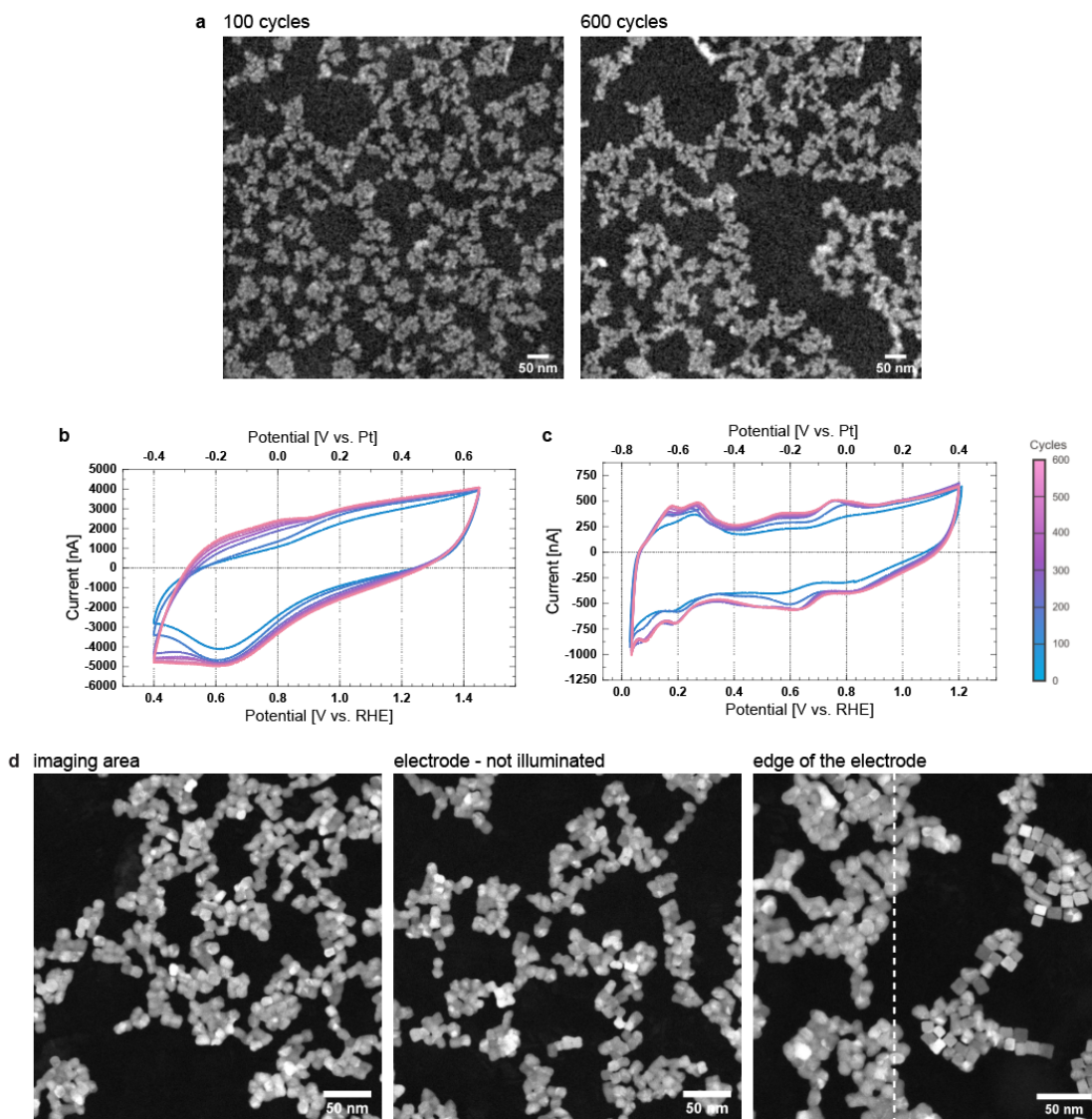


Fig. D.5: ec-LPSTEM cycling experiment of Pt nanocubes. **a**, the region of interest at the beginning and end of the degradation protocol. Images taken in STEM-HAADF with a 100 pA probe and 1  $\mu$ s dwell time (3000  $e^-/\text{nm}^2/\text{image}$ ) with 1 frame per minute and beam blanking in between. **b**, the degradation protocol was 600 triangular waves in range  $\sim [0.4-1.45]$  V vs. RHE at 500 mV/s. **c**, a 50 mV/s CV was recorded every  $\sim 100$  cycles to track the evolution of Pt features during degradation. **d**, post-mortem control images on the area of *in situ* imaging, an area on the electrode but not illuminated and the edge of the electrode.

We performed *in situ* STEM experiments with the degradation protocol described in the Main (Fig. D.5a-c). Although the protocol resulted in clear potential-induced degradation as seen at

---

the edge of the electrode (Fig. D.5d), comparison of the area that was imaged during cycling with one that was not (Fig. D.5d) shows greater particle mobility and attachment of all the aggregates in the illuminated field of view. The electron beam therefore modified the nature of the Pt nanocube degradation.

## D.6 Pt nanocubes degradation – beam interactions control

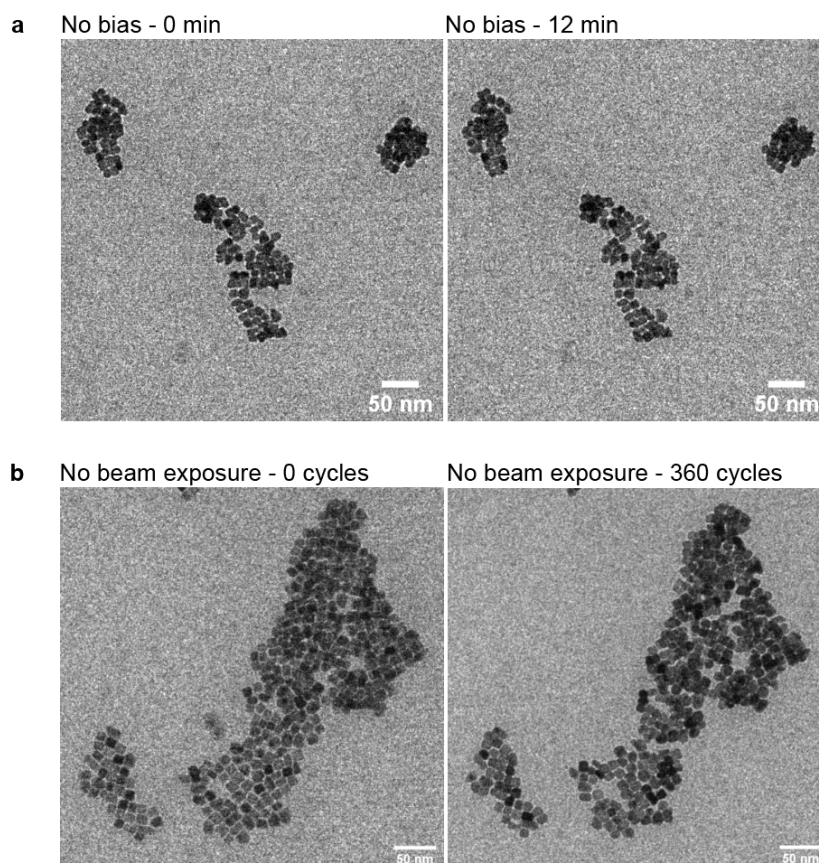


Fig. D.6: Controls of beam-related effects in ec-LPTEM of Pt nanocubes. **a**, area imaged without biasing, showing no visible movement and beam-induced degradation. **b**, aggregate cycled outside of the beam-illuminated area, showing potential-driven degradation. Quantitative comparison of illuminated vs. non-illuminated is presented in the Main.



## D.7 Effect of Cl<sup>-</sup> ions on Pt dissolution

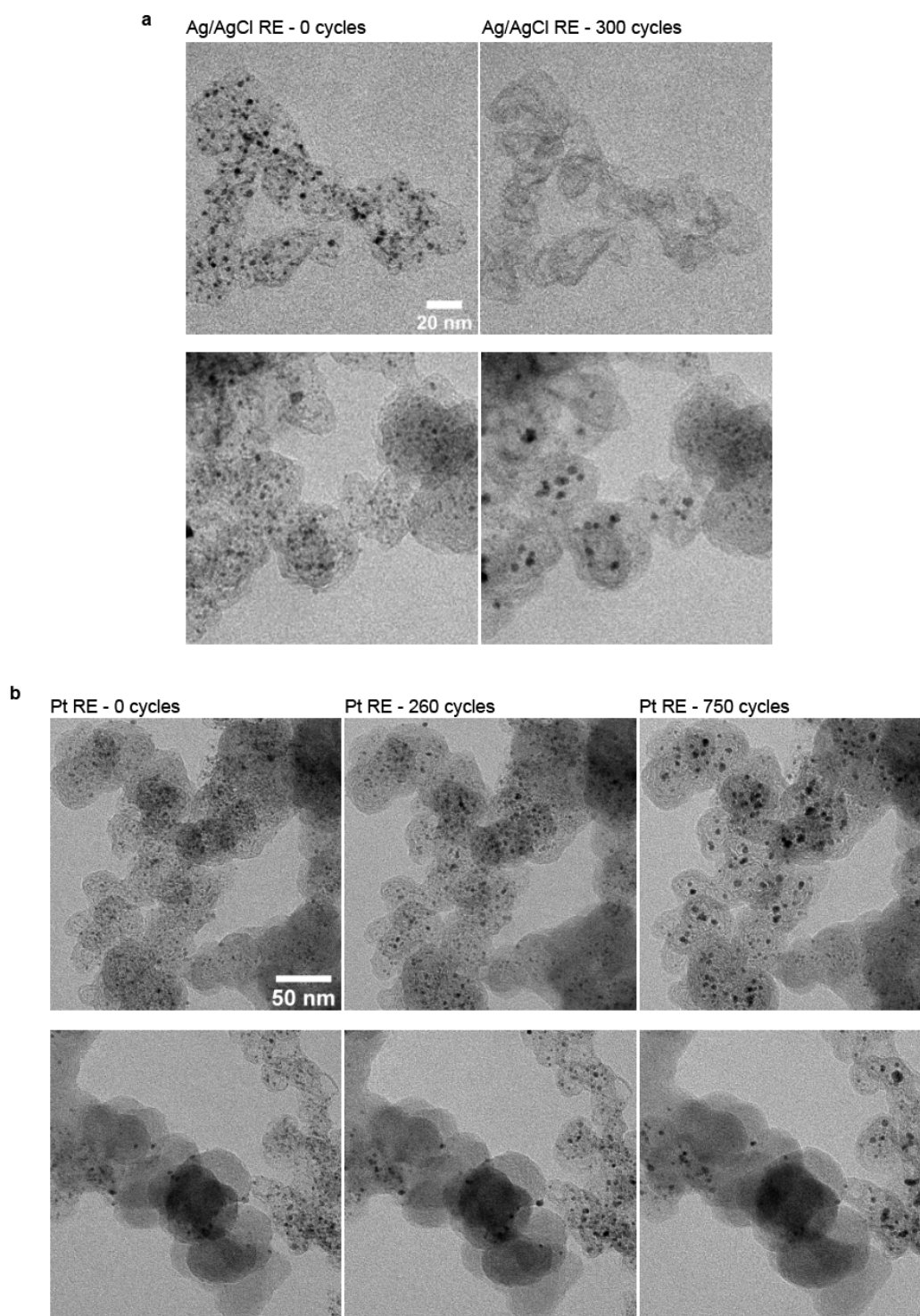


Fig. D.7: IL-TEM degradation study of Pt/KB catalysts on a GC WE chip with the open cell setup, in range [0.6-1.4] V vs. RHE and 100 mV/s scan rate. **a**, results of cycling with Ag/AgCl true RE. **b**, results of cycling with a Pt RE. The Ag/AgCl RE resulted in trace amounts of Cl<sup>-</sup> ions in the electrolyte and, in turn, in heightened rates of Pt dissolution<sup>352,353</sup>.

## D.8 *In situ* TEM of Pt/KB catalysts

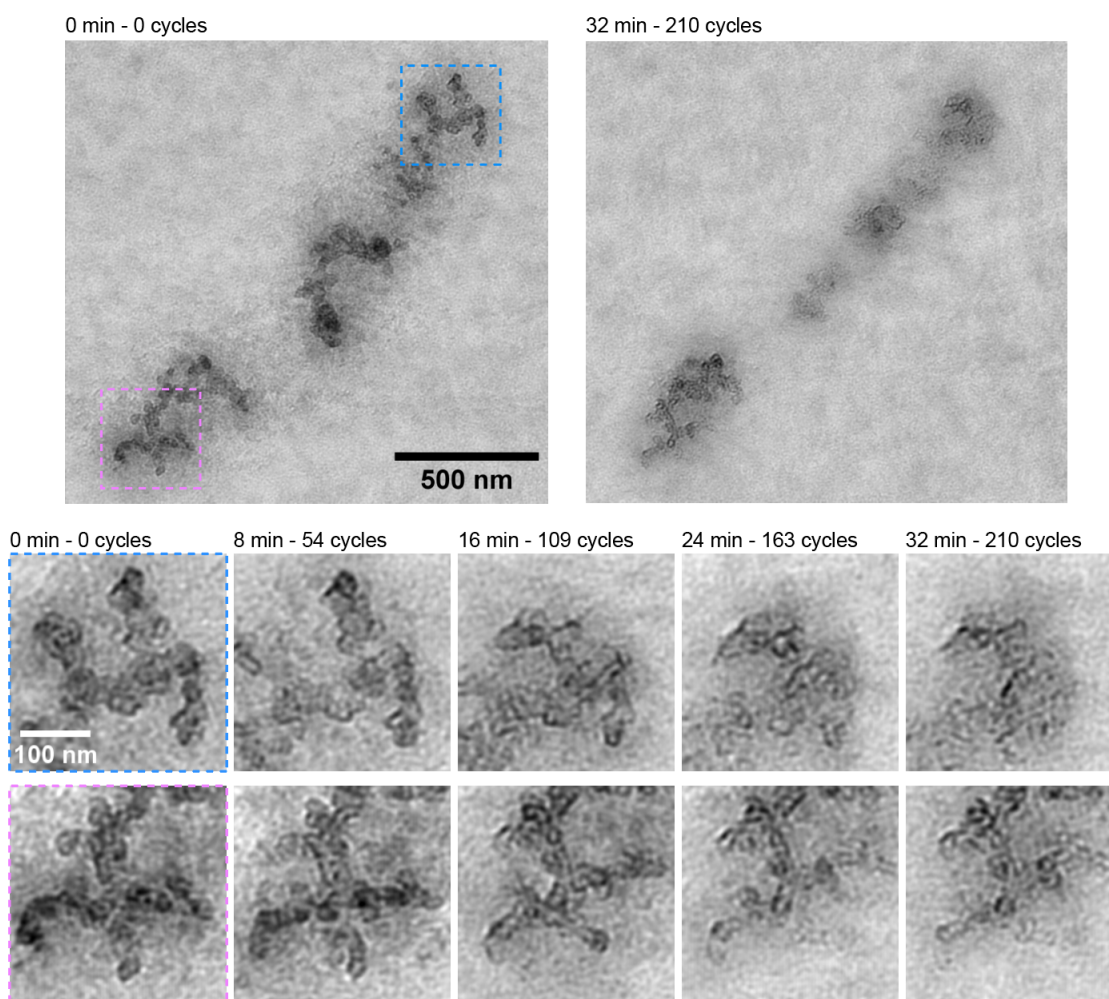


Fig. D.8: *ec*-LPTEM experiment with 19.8 wt% Pt/KB catalysts on a chip featuring a GC WE, Pt CE and Pt RE. 210 cycles were performed in range  $\sim [0.4-1.45]$  V vs. RHE with triangular waves and 500 mV/s. Imaging in BF-TEM with a 10 eV slit around the zero-loss peak,  $25 \text{ e}^-/\text{nm}^2/\text{image}$ , 1 frame/min with  $2 \times 1 \text{ s}$  exposure for N2N training. Clear corrosion of the carbon supports was observed, although this effect was not seen in IL-TEM experiments.



## D.9 Denoising ec-LPTM time-series of Cu nanocubes

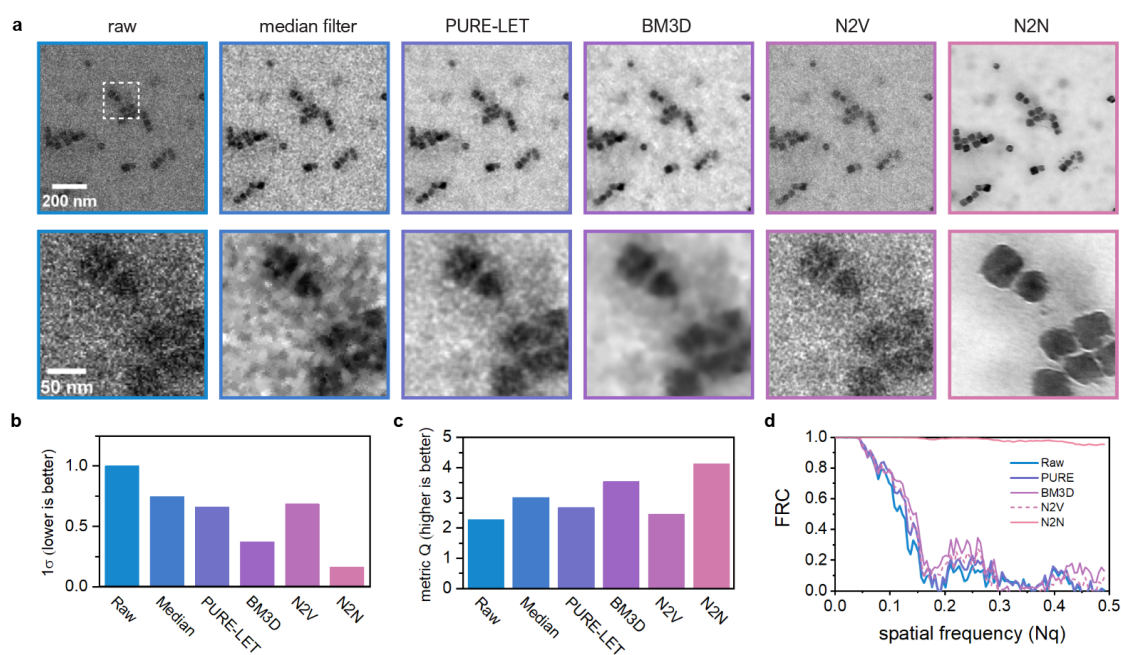


Fig. D.9: Denoising benchmark on Cu nanocubes in ec-LPTM. **a** and **b**, results of a range of denoising strategies on Cu nanocube catalysts imaged in ec-LPTM during cycling in 0.1M  $\text{KHCO}_3$ , at  $100 \text{ e}^-/\text{nm}^2/\text{s}$  and 20 frames per second. **b**, standard deviation of a background part of the image across the denoised images. **c**, image quality metric Q measured on the 25-30 most anisotropic  $8 \times 8$  pixel tiles in each image. **d**, FRC curves computed between two consecutive frames.

# Bibliography

1. Arto, I., Capellán-Pérez, I., Lago, R., Bueno, G. & Bermejo, R. The energy requirements of a developed world. *Energy for Sustainable Development* **33**, 1–13 (2016).
2. Vogel, J., Steinberger, J. K., O'Neill, D. W., Lamb, W. F. & Krishnakumar, J. Socio-economic conditions for satisfying human needs at low energy use: An international analysis of social provisioning. *Global Environmental Change* **69**, 102287 (2021).
3. O'Neill, D. W., Fanning, A. L., Lamb, W. F. & Steinberger, J. K. A good life for all within planetary boundaries. *Nature Sustainability* **1**, 88–95 (2018).
4. Millward-Hopkins, J., Steinberger, J. K., Rao, N. D. & Oswald, Y. Providing decent living with minimum energy: A global scenario. *Global Environmental Change* **65**, 102168 (2020).
5. Riahi, K. *et al.* Mitigation Pathways Compatible with Long-term Goals. in *IPCC, 2022: Climate Change 2022: Mitigation of Climate Change. Contribution of Working Group III to the Sixth Assessment Report of the Intergovernmental Panel on Climate Change*.
6. Wiedmann, T., Lenzen, M., Keyßer, L. T. & Steinberger, J. K. Scientists' warning on affluence. *Nat Commun* **11**, 3107 (2020).
7. IPCC. Emissions Trends and Drivers. in *Climate Change 2022: Mitigation of Climate Change. Contribution of Working Group III to the Sixth Assessment Report of the Intergovernmental Panel on Climate Change* (2022).
8. Seh, Z. W. *et al.* Combining theory and experiment in electrocatalysis: Insights into materials design. *Science* **355**, eaad4998 (2017).
9. Davis, S. J. *et al.* Net-zero emissions energy systems. *Science* **360**, eaas9793 (2018).
10. International Energy Agency. *The Future of Hydrogen*. (2019).
11. Winter, M. & Brodd, R. J. What Are Batteries, Fuel Cells, and Supercapacitors? *Chemical Reviews* **104**, 4245–4270 (2004).
12. Cullen, D. A. *et al.* New roads and challenges for fuel cells in heavy-duty transportation. *Nat Energy* **6**, 462–474 (2021).
13. Debe, M. K. Electrocatalyst approaches and challenges for automotive fuel cells. *Nature* **486**, 43–51 (2012).
14. Stamenkovic, V. R., Strmcnik, D., Lopes, P. P. & Markovic, N. M. Energy and fuels from electrochemical interfaces. *Nature Materials* **16**, 57–69 (2017).

15. Nørskov, J. K. *et al.* Origin of the Overpotential for Oxygen Reduction at a Fuel-Cell Cathode. *The Journal of Physical Chemistry B* **108**, 17886–17892 (2004).
16. Groger, O., Gasteiger, H. A. & Suchsland, J.-P. Review—Electromobility: Batteries or Fuel Cells? *Journal of The Electrochemical Society* **20** (2015).
17. Kongkanand, A. & Mathias, M. F. The Priority and Challenge of High-Power Performance of Low-Platinum Proton-Exchange Membrane Fuel Cells. *J. Phys. Chem. Lett.* **7**, 1127–1137 (2016).
18. Shao, M., Chang, Q., Dodelet, J.-P. & Chenitz, R. Recent Advances in Electrocatalysts for Oxygen Reduction Reaction. *Chem. Rev.* **116**, 3594–3657 (2016).
19. Jiao, K. *et al.* Designing the next generation of proton-exchange membrane fuel cells. *Nature* **595**, 361–369 (2021).
20. Fan, J. *et al.* Bridging the gap between highly active oxygen reduction reaction catalysts and effective catalyst layers for proton exchange membrane fuel cells. *Nat Energy* **6**, 475–486 (2021).
21. Sun, Y. *et al.* Advancements in cathode catalyst and cathode layer design for proton exchange membrane fuel cells. *Nat Commun* **12**, 5984 (2021).
22. Kodama, K., Nagai, T., Kuwaki, A., Jinnouchi, R. & Morimoto, Y. Challenges in applying highly active Pt-based nanostructured catalysts for oxygen reduction reactions to fuel cell vehicles. *Nat. Nanotechnol.* **16**, 140–147 (2021).
23. Holdcroft, S. Fuel Cell Catalyst Layers: A Polymer Science Perspective. *Chem. Mater.* **26**, 381–393 (2014).
24. Shao, Y., Dodelet, J.-P., Wu, G. & Zelenay, P. PGM-Free Cathode Catalysts for PEM Fuel Cells: A Mini-Review on Stability Challenges. *Advanced Materials* **31**, 1807615 (2019).
25. Lee, Y. J. *et al.* Ultra-Low Pt Loaded Porous Carbon Microparticles with Controlled Channel Structure for High-Performance Fuel Cell Catalysts. *Advanced Energy Materials* **n/a**, 2102970.
26. Yarlagadda, V., Ramaswamy, N., Kukreja, R. S. & Kumaraguru, S. Ordered mesoporous carbon supported fuel cell cathode catalyst for improved oxygen transport. *Journal of Power Sources* **532**, 231349 (2022).
27. Wang, Y.-J., Wilkinson, D. P. & Zhang, J. Noncarbon Support Materials for Polymer Electrolyte Membrane Fuel Cell Electrocatalysts. *Chem. Rev.* **111**, 7625–7651 (2011).
28. Elabd, Y. A. & Hickner, M. A. Block Copolymers for Fuel Cells. *Macromolecules* **44**, 1–11 (2011).
29. Cai, B., Henning, S., Herranz, J., Schmidt, T. J. & Eychmüller, A. Nanostructuring Noble Metals as Unsupported Electrocatalysts for Polymer Electrolyte Fuel Cells. *Advanced Energy Materials* **7**, 1700548 (2017).
30. Gasteiger, H. A., Kocha, S. S., Sompalli, B. & Wagner, F. T. Activity benchmarks and requirements for Pt, Pt-alloy, and non-Pt oxygen reduction catalysts for PEMFCs. *Applied Catalysis B: Environmental* **56**, 9–35 (2005).

- 
31. Garsany, Y., Ge, J., St-Pierre, J., Rocheleau, R. & Swider-Lyons, K. E. Analytical Procedure for Accurate Comparison of Rotating Disk Electrode Results for the Oxygen Reduction Activity of Pt/C. *J. Electrochem. Soc.* **161**, F628–F640 (2014).
  32. Mistry, H., Varela, A. S., Kühl, S., Strasser, P. & Cuenya, B. R. Nanostructured electrocatalysts with tunable activity and selectivity. *Nat Rev Mater* **1**, 1–14 (2016).
  33. Bu, L. *et al.* Biaxially strained PtPb/Pt core/shell nanoplate boosts oxygen reduction catalysis. *Science* **354**, 1410–1414 (2016).
  34. Huang, X. *et al.* High-performance transition metal-doped Pt<sub>3</sub>Ni octahedra for oxygen reduction reaction. *Science* **348**, 1230–1234 (2015).
  35. Li, M. *et al.* Ultrafine jagged platinum nanowires enable ultrahigh mass activity for the oxygen reduction reaction. *Science* **354**, 1414–1419 (2016).
  36. Chen, C. *et al.* Highly Crystalline Multimetallic Nanoframes with Three-Dimensional Electrocatalytic Surfaces. *Science* **343**, 1339–1343 (2014).
  37. Yu, H. *et al.* Recreating Fuel Cell Catalyst Degradation in Aqueous Environments for Identical-Location Scanning Transmission Electron Microscopy Studies. *ACS Appl. Mater. Interfaces* (2022) doi:10.1021/acsami.1c23281.
  38. Lazaridis, T., Stühmeier, B. M., Gasteiger, H. A. & El-Sayed, H. A. Capabilities and limitations of rotating disk electrodes versus membrane electrode assemblies in the investigation of electrocatalysts. *Nat Catal* **5**, 363–373 (2022).
  39. Singh, M. & Vander Wal, R. L. Nanostructure Quantification of Carbon Blacks. *C* **5**, 2 (2019).
  40. Kinoshita, K. Carbon: electrochemical and physicochemical properties. (1988).
  41. Nelson, J. R. & Wissing, W. K. Morphology of electrically conductive grades of carbon black. *Carbon* **24**, 115–121 (1986).
  42. Khodabakhshi, S., Fulvio, P. F. & Andreoli, E. Carbon black reborn: Structure and chemistry for renewable energy harnessing. *Carbon* **162**, 604–649 (2020).
  43. Serp, P. & Figueiredo, J. L. *Carbon Materials for Catalysis*. (John Wiley & Sons, 2008).
  44. Serp, P. & Machado, B. *Nanostructured Carbon Materials for Catalysis*. (2015). doi:10.1039/9781782622567.
  45. Ban, S., Malek, K., Huang, C. & Liu, Z. A molecular model for carbon black primary particles with internal nanoporosity. *Carbon* **49**, 3362–3370 (2011).
  46. Harris, P. J. F., Liu, Z. & Suenaga, K. Imaging the structure of activated carbon using aberration corrected TEM. *J. Phys.: Conf. Ser.* **241**, 012050 (2010).
  47. Guo, J. *et al.* Topological Defects: Origin of Nanopores and Enhanced Adsorption Performance in Nanoporous Carbon. *Small* **8**, 3283–3288 (2012).
  48. Kawasumi, K., Zhang, Q., Segawa, Y., Scott, L. T. & Itami, K. A grossly warped nanographene and the consequences of multiple odd-membered-ring defects. *Nature Chem* **5**, 739–744 (2013).
  49. Sneed, B. T. *et al.* 3D Analysis of Fuel Cell Electrocatalyst Degradation on Alternate Carbon Supports. *ACS Appl. Mater. Interfaces* **9**, 29839–29848 (2017).

50. Padgett, E. *et al.* Connecting Fuel Cell Catalyst Nanostructure and Accessibility Using Quantitative Cryo-STEM Tomography. *J. Electrochem. Soc.* **165**, F173–F180 (2018).
51. Park, Y.-C., Tokiwa, H., Kakinuma, K., Watanabe, M. & Uchida, M. Effects of carbon supports on Pt distribution, ionomer coverage and cathode performance for polymer electrolyte fuel cells. *Journal of Power Sources* **315**, 179–191 (2016).
52. Qi, Y. *et al.* Insight into carbon corrosion of different carbon supports for Pt-based electrocatalysts using accelerated stress tests in polymer electrolyte fuel cells. *Journal of Power Sources* **551**, 232209 (2022).
53. Kusoglu, A. & Weber, A. Z. New Insights into Perfluorinated Sulfonic-Acid Ionomers. *Chem. Rev.* **117**, 987–1104 (2017).
54. Uchida, M., Aoyama, Y., Eda, N. & Ohta, A. New Preparation Method for Polymer-Electrolyte Fuel Cells. *J. Electrochem. Soc.* **142**, 463–468 (1995).
55. Loppinet, B. & Gebel, G. Rodlike Colloidal Structure of Short Pendant Chain Perfluorinated Ionomer Solutions. *Langmuir* **14**, 1977–1983 (1998).
56. Loppinet, B., Gebel, G. & Williams, C. E. Small-Angle Scattering Study of Perfluorosulfonated Ionomer Solutions. *J. Phys. Chem. B* **101**, 1884–1892 (1997).
57. Welch, C. *et al.* Nafion in Dilute Solvent Systems: Dispersion or Solution? *ACS Macro Lett.* **1**, 1403–1407 (2012).
58. Kusoglu, A., Dursch, T. J. & Weber, A. Z. Nanostructure/Swelling Relationships of Bulk and Thin-Film PFSA Ionomers. *Advanced Functional Materials* **26**, 4961–4975 (2016).
59. Modestino, M. A. *et al.* Self-Assembly and Transport Limitations in Confined Nafion Films. *Macromolecules* **46**, 867–873 (2013).
60. Hatzell, K. B., Dixit, M. B., Berlinger, S. A. & Weber, A. Z. Understanding inks for porous-electrode formation. *J. Mater. Chem. A* **5**, 20527–20533 (2017).
61. More, K. & Reeves, S. TEM Specimen Preparation of Partially-Embedded Electrodes From Proton Exchange Membrane Fuel Cell Membrane Electrode Assemblies. *Microscopy and Microanalysis* **11**, 2104–2105 (2005).
62. Shinozaki, K., Morimoto, Y., Pivovar, B. S. & Kocha, S. S. Suppression of oxygen reduction reaction activity on Pt-based electrocatalysts from ionomer incorporation. *Journal of Power Sources* **325**, 745–751 (2016).
63. Kongkanand, A. *et al.* Development of Dispersed-Catalyst/NSTF Hybrid Electrode. *J. Electrochem. Soc.* **159**, F676 (2012).
64. Ramaswamy, N., Gu, W., Ziegelbauer, J. M. & Kumaraguru, S. Carbon Support Microstructure Impact on High Current Density Transport Resistances in PEMFC Cathode. *J. Electrochem. Soc.* **167**, 064515 (2020).
65. Kreuer, K. D. *et al.* Short-side-chain proton conducting perfluorosulfonic acid ionomers: Why they perform better in PEM fuel cells. *Journal of Power Sources* **178**, 499–509 (2008).
66. Park, Y.-C., Kakinuma, K., Uchida, H., Watanabe, M. & Uchida, M. Effects of short-side-chain perfluorosulfonic acid ionomers as binders on the performance of low Pt loading fuel cell cathodes. *Journal of Power Sources* **275**, 384–391 (2015).

- 
67. Ramaswamy, N. *et al.* Editors' Choice—Ionomer Side Chain Length and Equivalent Weight Impact on High Current Density Transport Resistances in PEMFC Cathodes. *J. Electrochem. Soc.* **168**, 024518 (2021).
  68. Lee, J. H. *et al.* Controlling Ionomer Film Morphology through Altering Pt Catalyst Surface Properties for Polymer Electrolyte Membrane Fuel Cells. *ACS Appl. Polym. Mater.* **2**, 1807–1818 (2020).
  69. Ji, S. G., Kwon, H. C., Kim, T.-H., Sim, U. & Choi, C. H. Does the Encapsulation Strategy of Pt Nanoparticles with Carbon Layers Really Ensure Both Highly Active and Durable Electrocatalysis in Fuel Cells? *ACS Catal.* **12**, 7317–7325 (2022).
  70. Harzer, G. S., Orfanidi, A., El-Sayed, H., Madkikar, P. & Gasteiger, H. A. Tailoring Catalyst Morphology towards High Performance for Low Pt Loaded PEMFC Cathodes. *J. Electrochem. Soc.* **165**, F770–F779 (2018).
  71. Yarlagadda, V. *et al.* Boosting Fuel Cell Performance with Accessible Carbon Mesopores. *ACS Energy Lett.* **3**, 618–621 (2018).
  72. Ko, M., Padgett, E., Yarlagadda, V., Kongkanand, A. & Muller, D. A. Revealing the Nanostructure of Mesoporous Fuel Cell Catalyst Supports for Durable, High-Power Performance. *J. Electrochem. Soc.* **168**, 024512 (2021).
  73. Lazaridis, T. & Gasteiger, H. A. Pt-Catalyzed Oxidation of PEMFC Carbon Supports: A Path to Highly Accessible Carbon Morphologies and Implications for Start-Up/Shut-Down Degradation. *J. Electrochem. Soc.* **168**, 114517 (2021).
  74. Andersen, S. M. *et al.* Adsorption Behavior of Perfluorinated Sulfonic Acid Ionomer on Highly Graphitized Carbon Nanofibers and Their Thermal Stabilities. *J. Phys. Chem. C* **118**, 10814–10823 (2014).
  75. Berlinger, S. A. *et al.* Impact of Platinum Primary Particle Loading on Fuel Cell Performance: Insights from Catalyst/Ionomer Ink Interactions. *ACS Appl. Mater. Interfaces* **14**, 36731–36740 (2022).
  76. Berlinger, S. A. *et al.* Impact of Dispersion Solvent on Ionomer Thin Films and Membranes. *ACS Appl. Polym. Mater.* **2**, 5824–5834 (2020).
  77. Berlinger, S. A., McCloskey, B. D. & Weber, A. Z. Inherent Acidity of Perfluorosulfonic Acid Ionomer Dispersions and Implications for Ink Aggregation. *J. Phys. Chem. B* **122**, 7790–7796 (2018).
  78. Orfanidi, A., Rheinländer, P. J., Schulte, N. & Gasteiger, H. A. Ink Solvent Dependence of the Ionomer Distribution in the Catalyst Layer of a PEMFC. *J. Electrochem. Soc.* **165**, F1254–F1263 (2018).
  79. Ott, S. *et al.* Ionomer distribution control in porous carbon-supported catalyst layers for high-power and low Pt-loaded proton exchange membrane fuel cells. *Nat. Mater.* 1–9 (2019) doi:10.1038/s41563-019-0487-0.
  80. Orfanidi, A. *et al.* The Key to High Performance Low Pt Loaded Electrodes. *J. Electrochem. Soc.* **164**, F418–F426 (2017).
  81. Hodnik, N., Dehm, G. & Mayrhofer, K. J. J. Importance and Challenges of Electrochemical in Situ Liquid Cell Electron Microscopy for Energy Conversion Research. *Acc. Chem. Res.* **49**, 2015–2022 (2016).

82. Padgett, E. *et al.* Mitigation of PEM Fuel Cell Catalyst Degradation with Porous Carbon Supports. *J. Electrochem. Soc.* **166**, F198–F207 (2019).
83. Shao-Horn, Y. *et al.* Instability of Supported Platinum Nanoparticles in Low-Temperature Fuel Cells. *Topics in Catalysis* **46**, 285–305 (2007).
84. Soleymani, A. P., Parent, L. R. & Jankovic, J. Challenges and Opportunities in Understanding Proton Exchange Membrane Fuel Cell Materials Degradation Using In-Situ Electrochemical Liquid Cell Transmission Electron Microscopy. *Advanced Functional Materials* **32**, 2105188 (2022).
85. Yu, Y. *et al.* Three-Dimensional Tracking and Visualization of Hundreds of Pt–Co Fuel Cell Nanocatalysts During Electrochemical Aging. *Nano Lett.* **12**, 4417–4423 (2012).
86. Beermann, V. *et al.* Real-time imaging of activation and degradation of carbon supported octahedral Pt–Ni alloy fuel cell catalysts at the nanoscale using in situ electrochemical liquid cell STEM. *Energy Environ. Sci.* **12**, 2476–2485 (2019).
87. Xin, H. L. *et al.* Atomic-Resolution Spectroscopic Imaging of Ensembles of Nanocatalyst Particles Across the Life of a Fuel Cell. *Nano Lett.* **12**, 490–497 (2012).
88. Zhao, J., Tu, Z. & Chan, S. H. Carbon corrosion mechanism and mitigation strategies in a proton exchange membrane fuel cell (PEMFC): A review. *Journal of Power Sources* **488**, 229434 (2021).
89. Bertier, P. *et al.* On the use and abuse of N<sub>2</sub> physisorption for the characterization of the pore structure of shales. in 151–161 (2016). doi:10.1346/CMS-WLS-21.12.
90. Neimark, A. V., Lin, Y., Ravikovitch, P. I. & Thommes, M. Quenched solid density functional theory and pore size analysis of micro-mesoporous carbons. *Carbon* **47**, 1617–1628 (2009).
91. Thommes, M. *et al.* Physisorption of gases, with special reference to the evaluation of surface area and pore size distribution (IUPAC Technical Report). *Pure and Applied Chemistry* **87**, 1051–1069 (2015).
92. Soboleva, T. *et al.* On the Micro-, Meso-, and Macroporous Structures of Polymer Electrolyte Membrane Fuel Cell Catalyst Layers. *ACS Appl. Mater. Interfaces* **2**, 375–384 (2010).
93. Kobayashi, A. *et al.* Effect of Pt Loading Percentage on Carbon Blacks with Large Interior Nanopore Volume on the Performance and Durability of Polymer Electrolyte Fuel Cells. *ACS Appl. Energy Mater.* acaem.1c02836 (2021) doi:10.1021/acsaem.1c02836.
94. Kobayashi, A. *et al.* Effect of Pt and Ionomer Distribution on Polymer Electrolyte Fuel Cell Performance and Durability. *ACS Appl. Energy Mater.* **4**, 2307–2317 (2021).
95. Garrick, T. R., Moylan, T. E., Carpenter, M. K. & Kongkanand, A. Electrochemically Active Surface Area Measurement of Aged Pt Alloy Catalysts in PEM Fuel Cells by CO Stripping. *J. Electrochem. Soc.* **164**, F55 (2016).
96. Chowdhury, A., Darling, R. M., Radke, C. J. & Weber, A. Z. Modeling Water Uptake and Pt Utilization in High Surface Area Carbon. *ECS Trans.* **92**, 247 (2019).

- 
97. Shinozaki, K., Yamada, H. & Morimoto, Y. Relative Humidity Dependence of Pt Utilization in Polymer Electrolyte Fuel Cell Electrodes: Effects of Electrode Thickness, Ionomer-to-Carbon Ratio, Ionomer Equivalent Weight, and Carbon Support. *J. Electrochem. Soc.* **158**, B467 (2011).
  98. Ikeda, K., Nonoyama, N. & Ikogi, Y. Analysis of the Ionomer Coverage of Pt Surface in PEMFC. *ECS Trans.* **33**, 1189–1197 (2010).
  99. Takeshita, T., Kamitaka, Y., Shinozaki, K., Kodama, K. & Morimoto, Y. Evaluation of ionomer coverage on Pt catalysts in polymer electrolyte membrane fuel cells by CO stripping voltammetry and its effect on oxygen reduction reaction activity. *Journal of Electroanalytical Chemistry* **871**, 114250 (2020).
  100. Schulenburg, H. *et al.* 3D Imaging of Polymer Electrolyte Fuel Cell Electrodes. *ECS Trans.* **33**, 1471–1481 (2010).
  101. Litster, S., Epting, W. K., Wargo, E. A., Kalidindi, S. R. & Kumbur, E. C. Morphological Analyses of Polymer Electrolyte Fuel Cell Electrodes with Nano-Scale Computed Tomography Imaging. *Fuel Cells* **13**, 935–945 (2013).
  102. Epting, W. K., Gelb, J. & Litster, S. Resolving the Three-Dimensional Microstructure of Polymer Electrolyte Fuel Cell Electrodes using Nanometer-Scale X-ray Computed Tomography. *Advanced Functional Materials* **22**, 555–560 (2012).
  103. Macauley, N. *et al.* Highly Durable Fluorinated High Oxygen Permeability Ionomers for Proton Exchange Membrane Fuel Cells. *Advanced Energy Materials* **n/a**, 2201063.
  104. Scheiba, F., Benker, N., Kunz, U., Roth, C. & Fuess, H. Electron microscopy techniques for the analysis of the polymer electrolyte distribution in proton exchange membrane fuel cells. *Journal of Power Sources* **177**, 273–280 (2008).
  105. Rieberer, S. & Norian, K. H. Analytical electron microscopy of Nafion ion exchange membranes. *Ultramicroscopy* **41**, 225–233 (1992).
  106. Cetinbas, F. C., Ahluwalia, R. K., Kariuki, N. N. & Myers, D. J. Agglomerates in Polymer Electrolyte Fuel Cell Electrodes: Part I. Structural Characterization. *J. Electrochem. Soc.* **165**, F1051–F1058 (2018).
  107. Van Cleve, T. *et al.* Tailoring electrode microstructure via ink content to enable improved rated power performance for platinum cobalt/high surface area carbon based polymer electrolyte fuel cells. *Journal of Power Sources* **482**, 228889 (2021).
  108. Cetinbas, F. C., Ahluwalia, R. K., Kariuki, N. N., De Andrade, V. & Myers, D. J. Effects of Porous Carbon Morphology, Agglomerate Structure and Relative Humidity on Local Oxygen Transport Resistance. *J. Electrochem. Soc.* **167**, 013508 (2020).
  109. Komini Babu, S., Chung, H. T., Zelenay, P. & Litster, S. Resolving Electrode Morphology's Impact on Platinum Group Metal-Free Cathode Performance Using Nano-CT of 3D Hierarchical Pore and Ionomer Distribution. *ACS Appl. Mater. Interfaces* **8**, 32764–32777 (2016).



110. Normile, S. J. & Zenyuk, I. V. Imaging ionomer in fuel cell catalyst layers with synchrotron nano transmission x-ray microscopy. *Solid State Ionics* **335**, 38–46 (2019).
111. Cetinbas, F. C. *et al.* Hybrid approach combining multiple characterization techniques and simulations for microstructural analysis of proton exchange membrane fuel cell electrodes. *Journal of Power Sources* **344**, 62–73 (2017).
112. Wu, J. *et al.* High-Resolution Imaging of Polymer Electrolyte Membrane Fuel Cell Cathode Layers by Soft X-ray Spectro-Ptychography. *J. Phys. Chem. C* **122**, 11709–11719 (2018).
113. Bessarabov, D. & Hitchcock, A. Advances in structural and chemical analysis of catalystcoated membranes for hydrogen fuel cell applications. *Membrane Technology* **2009**, 6–12 (2009).
114. Susac, D., Berejnov, V., Hitchcock, A. P. & Stumper, J. STXM Study of the Ionomer Distribution in the PEM Fuel Cell Catalyst Layers. *ECS Trans.* **41**, 629–635 (2011).
115. Susac, D. *et al.* Chemical Fingerprint Associated with the Formation of Pt in the Membrane in PEM Fuel Cells. *ECS Trans.* **33**, 391 (2010).
116. Melo, L. G. A. *et al.* Quantitative Mapping of Ionomer in Catalyst Layers by Electron and X-ray Spectromicroscopy. *ECS Trans.* **80**, 275–282 (2017).
117. Melo, L. G. A. & Hitchcock, A. P. Electron beam damage of perfluorosulfonic acid studied by soft X-ray spectromicroscopy. *Micron* **121**, 8–20 (2019).
118. Martens, I., Melo, L. G. A., Wilkinson, D. P., Bizzotto, D. & Hitchcock, A. P. Characterization of X-ray Damage to Perfluorosulfonic Acid Using Correlative Microscopy. *J. Phys. Chem. C* **123**, 16023–16033 (2019).
119. Takao, S. *et al.* Observation of Degradation of Pt and Carbon Support in Polymer Electrolyte Fuel Cell Using Combined Nano-X-ray Absorption Fine Structure and Transmission Electron Microscopy Techniques. *ACS Appl. Mater. Interfaces* **11** (2018).
120. Berejnov, V., Susac, D., Stumper, J. & Hitchcock, A. P. 3D Chemical Mapping of PEM Fuel Cell Cathodes by Scanning Transmission Soft X-ray SpectroTomography. *ECS Transactions* **50**, 361–368 (2013).
121. Wu, J. *et al.* 4D imaging of polymer electrolyte membrane fuel cell catalyst layers by soft X-ray spectro-tomography. *Journal of Power Sources* **381**, 72–83 (2018).
122. Pfeiffer, F. X-ray ptychography. *Nature Photon* **12**, 9–17 (2018).
123. Morawietz, T., Handl, M., Oldani, C., Friedrich, K. A. & Hiesgen, R. Quantitative in Situ Analysis of Ionomer Structure in Fuel Cell Catalytic Layers. *ACS Appl. Mater. Interfaces* **8**, 27044–27054 (2016).
124. Hiesgen, R., Morawietz, T., Handl, M., Corasaniti, M. & Friedrich, K. A. Atomic Force Microscopy on Cross Sections of Fuel Cell Membranes, Electrodes, and Membrane Electrode Assemblies. *Electrochimica Acta* **162**, 86–99 (2015).
125. Thiele, S. *et al.* Multiscale tomography of nanoporous carbon-supported noble metal catalyst layers. *Journal of Power Sources* **228**, 185–192 (2013).

- 
126. Vierrath, S. *et al.* Enhancing the quality of the tomography of nanoporous materials for better understanding of polymer electrolyte fuel cell materials. *Journal of Power Sources* **285**, 413–417 (2015).
  127. Thiele, S., Vierrath, S., Klingele, M. & Zengerle, R. Tomographic Analysis of Polymer Electrolyte Fuel Cell Catalyst Layers: Methods, Validity and Challenges. *ECS Trans.* **69**, 409 (2015).
  128. Zielke, L. *et al.* Three-dimensional morphology of the interface between micro porous layer and catalyst layer in a polymer electrolyte membrane fuel cell. *RSC Advances* **6**, 80700–80705 (2016).
  129. de A. Melo, L. G. *et al.* Evaluating focused ion beam and ultramicrotome sample preparation for analytical microscopies of the cathode layer of a polymer electrolyte membrane fuel cell. *Journal of Power Sources* **312**, 23–35 (2016).
  130. Suzuki, T., Koyama, T. & Tsushima, S. Analysis of Ionomer Distribution in Catalyst Layers by Two-Stage Ion-Beam Processing. *ECS Trans.* **80**, 419–423 (2017).
  131. Yu, H. *et al.* Tracking Nanoparticle Degradation across Fuel Cell Electrodes by Automated Analytical Electron Microscopy. *ACS Nano* acsnano.2c02307 (2022) doi:10.1021/acsnano.2c02307.
  132. Jurkiewicz, K., Pawlyta, M. & Burian, A. Structure of Carbon Materials Explored by Local Transmission Electron Microscopy and Global Powder Diffraction Probes. *C* **4**, 68 (2018).
  133. Uchida, M. *et al.* Effect of the state of distribution of supported Pt nanoparticles on effective Pt utilization in polymer electrolyte fuel cells. *Physical Chemistry Chemical Physics* **15**, 11236–11247 (2013).
  134. Park, Y.-C. *et al.* Investigation of the corrosion of carbon supports in polymer electrolyte fuel cells using simulated start-up/shutdown cycling. *Electrochimica Acta* **91**, 195–207 (2013).
  135. Wang, Z., Ke, X. & Sui, M. Recent Progress on Revealing 3D Structure of Electrocatalysts Using Advanced 3D Electron Tomography: A Mini Review. *Front. Chem.* **10**, 872117 (2022).
  136. Friedrich, H., de Jongh, P. E., Verkleij, A. J. & de Jong, K. P. Electron Tomography for Heterogeneous Catalysts and Related Nanostructured Materials. *Chem. Rev.* **109**, 1613–1629 (2009).
  137. Abrosimov, O. G., Moroz, E. M. & Chuvilin, A. L. Electron microtomography: A new method for studying the spatial structure of catalysts. *Kinet Catal* **47**, 464–466 (2006).
  138. Ito, T. *et al.* Three-Dimensional Spatial Distributions of Pt Catalyst Nanoparticles on Carbon Substrates in Polymer Electrolyte Fuel Cells. *Electrochemistry* **79**, 374–376 (2011).
  139. Schulenburg, H. *et al.* 3D Imaging of Catalyst Support Corrosion in Polymer Electrolyte Fuel Cells. *J. Phys. Chem. C* **115**, 14236–14243 (2011).
  140. Grothausmann, R. *et al.* Quantitative Structural Assessment of Heterogeneous Catalysts by Electron Tomography. *J. Am. Chem. Soc.* **133**, 18161–18171 (2011).

141. Jankovic, J., Susac, D., Soboleva, T. & Stumper, J. Electron Tomography Based 3D Reconstruction of Fuel Cell Catalysts. *ECS Trans.* **50**, 353–359 (2013).
142. Peng, Y. *et al.* New approach for rapidly determining Pt accessibility of Pt/C fuel cell catalysts. *J. Mater. Chem. A* **9**, 13471–13476 (2021).
143. Jenkinson, K., Liz-Marzán, L. M. & Bals, S. Multimode Electron Tomography Sheds Light on Synthesis, Structure, and Properties of Complex Metal-Based Nanoparticles. *Advanced Materials* **34**, 2110394 (2022).
144. Sentosun, K., Sanz Ortiz, M. N., Batenburg, K. J., Liz-Marzán, L. M. & Bals, S. Combination of HAADF-STEM and ADF-STEM Tomography for Core–Shell Hybrid Materials. *Particle & Particle Systems Characterization* **32**, 1063–1067 (2015).
145. Gontard, L. C., Dunin-Borkowski, R. E. & Ozkaya, D. Three-dimensional shapes and spatial distributions of Pt and PtCr catalyst nanoparticles on carbon black. *Journal of Microscopy* **232**, 248–259 (2008).
146. Gontard, L. C., Dunin-Borkowski, R. E., Chong, R. K. K., Ozkaya, D. & Midgley, P. A. Electron tomography of Pt nanocatalyst particles and their carbon support. *J. Phys.: Conf. Ser.* **26**, 203–206 (2006).
147. da Silva, A., David, T., Saghi, Z. & Guetaz, L. Multiple ADF-STEM Towards the Optimization of Electron Tomography Reconstructions of Pt/C fuel cell catalyst nanostructures. *Microsc Microanal* **27**, 978–980 (2021).
148. Yakovlev, S., Balsara, N. P. & Downing, K. H. Insights on the Study of Nafion Nanoscale Morphology by Transmission Electron Microscopy. *Membranes* **3**, 424–439 (2013).
149. Cullen, D. A. *et al.* Imaging and Microanalysis of Thin Ionomer Layers by Scanning Transmission Electron Microscopy. *J. Electrochem. Soc.* **161**, F1111–F1117 (2014).
150. Schuler, T. *et al.* Fuel-Cell Catalyst-Layer Resistance via Hydrogen Limiting-Current Measurements. *J. Electrochem. Soc.* **166**, F3020–F3031 (2019).
151. Scheiba, F., Benker, N., Kunz, U., Roth, C. & Fuess, H. Electron microscopy techniques for the analysis of the polymer electrolyte distribution in proton exchange membrane fuel cells. *Journal of Power Sources* **177**, 273–280 (2008).
152. Colletta, M., Yang, Y., Goodge, B. H., Abruña, H. D. & Kourkoutis, L. F. Overcoming Artifacts in Imaging Nanometer-thick Ionomer Layers in Anion Exchange Membrane Fuel Cells. *Microsc Microanal* **28**, 2210–2212 (2022).
153. Shimanuki, J., Imai, H., Ito, Y., Nishino, Y. & Miyazawa, A. Microstructural observation of the swollen catalyst layers of fuel cells by cryo-TEM. *Microscopy* dfac059 (2022) doi:10.1093/jmicro/dfac059.
154. Guétaz, L., Lopez-Haro, M., Bayle-Guillemaud, P., Morin, A. & Escribano, S. Contribution of Transmission Electron Microscopy to Proton Exchange Membrane Fuel Cell Electrodes Development and Degradation Understanding. *Microscopy and Microanalysis* **22**, 1282–1283 (2016).
155. Koga, M. *et al.* Microstructure Investigation of Polymer Electrolyte Fuel Cell Catalyst Layers Containing Perfluorosulfonated Ionomer. *Membranes* **11**, 466 (2021).

- 
156. Wen, Z. *et al.* Micromodification of the Catalyst Layer by CO to Increase Pt Utilization for Proton-Exchange Membrane Fuel Cells. *ACS Appl. Mater. Interfaces* **acsami.2c16524** (2022) doi:10.1021/acsami.2c16524.
  157. Lee, M.-R. *et al.* Effects of Ionomer Carbon Ratio and Ionomer Dispersity on the Performance and Durability of MEAs. *Fuel Cells* **18**, 129–136 (2018).
  158. Soleymani, A. P., Reid, M. & Jankovic, J. An Epoxy-Free Sample Preparation Approach to Enable Imaging of Ionomer and Carbon in Polymer Electrolyte Membrane Fuel Cells. *Advanced Functional Materials* **n/a**, 2209733 (2022).
  159. Venkatesan, S. V., El Hannach, M., Holdcroft, S. & Kjeang, E. Probing nanoscale membrane degradation in fuel cells through electron tomography. *Journal of Membrane Science* **539**, 138–143 (2017).
  160. Allen, F. I. *et al.* Morphology of Hydrated As-Cast Nafion Revealed through Cryo Electron Tomography. *ACS Macro Lett.* **4**, 1–5 (2015).
  161. Peltonen, A., Etula, J., Seitsonen, J., Engelhardt, P. & Laurila, T. Three-Dimensional Fine Structure of Nanometer-Scale Nafion Thin Films. *ACS Appl. Polym. Mater.* **3**, 1078–1086 (2021).
  162. Uchida, H. *et al.* Electron Tomography of Nafion Ionomer Coated on Pt/Carbon Black in High Utilization Electrode for PEFCs. *J. Phys. Chem. B* **110**, 13319–13321 (2006).
  163. Lopez-Haro, M. *et al.* Three-dimensional analysis of Nafion layers in fuel cell electrodes. *Nature Communications* **5**, 5229 (2014).
  164. Yakovlev, S. & Downing, K. H. Visualization of clusters in polymer electrolyte membranes by electron microscopy. *Phys. Chem. Chem. Phys.* **15**, 1052–1064 (2013).
  165. Ross, F. M. Opportunities and challenges in liquid cell electron microscopy. *Science* **350**, aaa9886 (2015).
  166. de Jonge, N., Houben, L., Dunin-Borkowski, R. E. & Ross, F. M. Resolution and aberration correction in liquid cell transmission electron microscopy. *Nature Reviews Materials* **4**, 61–78 (2019).
  167. *Liquid Cell Electron Microscopy*. (Cambridge University Press, 2016). doi:10.1017/9781316337455.
  168. Ruska, E. Beitrag zur übermikroskopischen Abbildung bei höheren Drucken. *Kolloid-Zeitschrift* **100**, 212–219 (1942).
  169. Abrams, I. M. & McBain, J. W. A Closed Cell for Electron Microscopy. **4**.
  170. Crozier, P. A. & Hansen, T. W. In situ and operando transmission electron microscopy of catalytic materials. *MRS Bulletin* **40**, 38–45 (2015).
  171. Williamson, M. J., Tromp, R. M., Vereecken, P. M., Hull, R. & Ross, F. M. Dynamic microscopy of nanoscale cluster growth at the solid–liquid interface. *Nature Materials* **2**, 532–536 (2003).
  172. Han, B. *et al.* Nanoscale structural oscillations in perovskite oxides induced by oxygen evolution. *Nature Materials* **16**, 121–126 (2017).

173. Chenna, S. & Crozier, P. A. Operando Transmission Electron Microscopy: A Technique for Detection of Catalysis Using Electron Energy-Loss Spectroscopy in the Transmission Electron Microscope. *ACS Catal.* **2**, 2395–2402 (2012).
174. Unocic, R. R. *et al.* Quantitative Electrochemical Measurements Using In Situ ec-S/TEM Devices. *Microscopy and Microanalysis* **20**, 452–461 (2014).
175. Pan, Y., Li, X. & Su, D. Understanding the structural dynamics of electrocatalysts via liquid cell transmission electron microscopy. *Current Opinion in Electrochemistry* **33**, 100936 (2022).
176. Chee, S. W., Lunkenbein, T., Schlögl, R. & Cuenya, B. R. In situ and operando electron microscopy in heterogeneous catalysis—insights into multi-scale chemical dynamics. *J. Phys.: Condens. Matter* **33**, 153001 (2021).
177. Shen, T.-H., Spillane, L., Peng, J., Shao-Horn, Y. & Tileli, V. Switchable wetting of oxygen-evolving oxide catalysts. *Nat Catal* **5**, 30–36 (2022).
178. Ortiz Peña, N. *et al.* Morphological and Structural Evolution of Co<sub>3</sub>O<sub>4</sub> Nanoparticles Revealed by in Situ Electrochemical Transmission Electron Microscopy during Electrocatalytic Water Oxidation. *ACS Nano* **13**, 11372–11381 (2019).
179. Zhu, G.-Z. *et al.* In Situ Liquid Cell TEM Study of Morphological Evolution and Degradation of Pt–Fe Nanocatalysts During Potential Cycling. *J. Phys. Chem. C* **118**, 22111–22119 (2014).
180. Kato, H. In-Situ Liquid TEM Study on the Degradation Mechanism of Fuel Cell Catalysts. *SAE Int. J. Alt. Power.* **5**, 189–194 (2016).
181. Nagashima, S. *et al.* Atomic-Level Observation of Electrochemical Platinum Dissolution and Redeposition. *Nano Lett.* **19**, 7000–7005 (2019).
182. Impagnatiello, A. *et al.* Degradation Mechanisms of Supported Pt Nanocatalysts in Proton Exchange Membrane Fuel Cells: An Operando Study through Liquid Cell Transmission Electron Microscopy. *ACS Appl. Energy Mater.* **3**, 2360–2371 (2020).
183. Vavra, J., Shen, T.-H., Stoian, D., Tileli, V. & Buonsanti, R. Real-time Monitoring Reveals Dissolution/Redeposition Mechanism in Copper Nanocatalysts during the Initial Stages of the CO<sub>2</sub> Reduction Reaction. *Angewandte Chemie* **133**, 1367–1374 (2021).
184. Grosse, P. *et al.* Dynamic transformation of cubic copper catalysts during CO<sub>2</sub> electroreduction and its impact on catalytic selectivity. *Nat Commun* **12**, 6736 (2021).
185. Li, Y. *et al.* Electrochemically scrambled nanocrystals are catalytically active for CO<sub>2</sub>-to-multicarbon. *Proceedings of the National Academy of Sciences* **117**, 9194–9201 (2020).
186. Yang, Y. *et al.* Operando studies reveal active Cu nanograins for CO<sub>2</sub> electroreduction. *Nature* **614**, 262–269 (2023).
187. Grogan, J. M., Schneider, N. M., Ross, F. M. & Bau, H. H. Bubble and Pattern Formation in Liquid Induced by an Electron Beam. *Nano Lett.* **14**, 359–364 (2014).

- 
188. Schneider, N. M. *et al.* Electron–Water Interactions and Implications for Liquid Cell Electron Microscopy. *J. Phys. Chem. C* **118**, 22373–22382 (2014).
  189. Ambrožič, B. *et al.* Controlling the radical-induced redox chemistry inside a liquid-cell TEM. *Chem. Sci.* **10**, 8735–8743 (2019).
  190. Williams, D. B. & Carter, C. B. *Transmission electron microscopy: a textbook for materials science.* (Springer, 2008).
  191. *Springer Handbook of Microscopy.* (Springer International Publishing, 2019). doi:10.1007/978-3-030-00069-1.
  192. Krumeich, F., Müller, E. & Wepf, R. A. Phase-contrast imaging in aberration-corrected scanning transmission electron microscopy. *Micron* **49**, 1–14 (2013).
  193. Crewe, A. V. & Wall, J. A scanning microscope with 5 Å resolution. *Journal of Molecular Biology* **48**, 375–393 (1970).
  194. Carter, C. B. & Williams, D. B. *Transmission Electron Microscopy.* (Springer US, 2016).
  195. Kirkland, E. J. *Advanced Computing in Electron Microscopy.* (Springer International Publishing, 2020). doi:10.1007/978-3-030-33260-0.
  196. Scherzer, O. The Theoretical Resolution Limit of the Electron Microscope. *Journal of Applied Physics* **20**, 20–29 (1949).
  197. Egerton, R. F., Li, P. & Malac, M. Radiation damage in the TEM and SEM. *Micron* **35**, 399–409 (2004).
  198. Egerton, R. F. Radiation damage to organic and inorganic specimens in the TEM. *Micron* **119**, 72–87 (2019).
  199. Russo, C. J. & Egerton, R. F. Damage in electron cryomicroscopy: Lessons from biology for materials science. *MRS Bull.* **44**, 935–941 (2019).
  200. Meyer, J. C. *et al.* Accurate Measurement of Electron Beam Induced Displacement Cross Sections for Single-Layer Graphene. *Phys. Rev. Lett.* **108**, 196102 (2012).
  201. Egerton, R. F. & Rauf, I. Dose-rate dependence of electron-induced mass loss from organic specimens. *Ultramicroscopy* **80**, 247–254 (1999).
  202. Leisegang, S. Zur Erwärmung elektronenmikroskopischer Objekte bei kleinem Strahlquerschnitt. in *Proc. 3rd Int. Conf. Elec. Microsc.* 176–188 (1954).
  203. Dubochet, J. *et al.* Cryo-electron microscopy of vitrified specimens. *Quart. Rev. Biophys.* **21**, 129–228 (1988).
  204. Homo, J.-C., Booy, F., Labouesse, P., Lepault, J. & Dubochet, J. Improved anticontaminator for cryo-electron microscopy with a Philips EM 400. *Journal of Microscopy* **136**, 337–340 (1984).
  205. McMullan, G. *et al.* Experimental observation of the improvement in MTF from backthinning a CMOS direct electron detector. *Ultramicroscopy* **109**, 1144–1147 (2009).
  206. McMullan, G., Faruqi, A. R. & Henderson, R. Direct Electron Detectors. in *Methods in Enzymology* vol. 579 1–17 (Elsevier, 2016).
  207. Turchetta, R. CMOS monolithic active pixel sensors (MAPS) for scientific applications: Some notes about radiation hardness. *Nuclear Instruments and*

- Methods in Physics Research Section A: Accelerators, Spectrometers, Detectors and Associated Equipment* **583**, 131–133 (2007).
208. Faruqi, A. R. & Henderson, R. Electronic detectors for electron microscopy. *Current Opinion in Structural Biology* **17**, 549–555 (2007).
209. Kühlbrandt, W. The Resolution Revolution. *Science* **343**, 1443–1444 (2014).
210. Ruskin, R. S., Yu, Z. & Grigorieff, N. Quantitative characterization of electron detectors for transmission electron microscopy. *Journal of Structural Biology* **184**, 385–393 (2013).
211. *Electron tomography: methods for three-dimensional visualization of structures in the cell*. (Springer, 2006).
212. Weyland, M., Midgley, P. A. & Thomas, J. M. Electron Tomography of Nanoparticle Catalysts on Porous Supports: A New Technique Based on Rutherford Scattering. *J. Phys. Chem. B* **105**, 7882–7886 (2001).
213. Midgley, P. A. & Weyland, M. 3D electron microscopy in the physical sciences: the development of Z-contrast and EFTEM tomography. *Ultramicroscopy* **96**, 413–431 (2003).
214. Saghi, Z., Xu, X. & Möbus, G. Electron tomography of regularly shaped nanostructures under non-linear image acquisition. *Journal of Microscopy* **232**, 186–195 (2008).
215. Padgett, E. *et al.* A Simple Preparation Method for Full-Range Electron Tomography of Nanoparticles and Fine Powders. *Microsc Microanal* **23**, 1150–1158 (2017).
216. Leary, R. K. & Midgley, P. A. Electron Tomography in Materials Science. in *Springer Handbook of Microscopy* (eds. Hawkes, P. W. & Spence, J. C. H.) (Springer International Publishing, 2019). doi:10.1007/978-3-030-00069-1\_26.
217. Mastronarde, D. N. Automated electron microscope tomography using robust prediction of specimen movements. *Journal of Structural Biology* **152**, 36–51 (2005).
218. Odstrčil, M., Holler, M., Raabe, J. & Guizar-Sicairos, M. Alignment methods for nanotomography with deep subpixel accuracy. *Opt. Express* **27**, 36637 (2019).
219. Scott, M. C. *et al.* Electron tomography at 2.4-ångström resolution. *Nature* **483**, 444–447 (2012).
220. Sanders, T., Prange, M., Akatay, C. & Binev, P. Physically motivated global alignment method for electron tomography. *Advanced Structural and Chemical Imaging* **1**, 4 (2015).
221. Houben, L. & Bar Sadan, M. Refinement procedure for the image alignment in high-resolution electron tomography. *Ultramicroscopy* **111**, 1512–1520 (2011).
222. Printemps, T. *et al.* Self-adapting denoising, alignment and reconstruction in electron tomography in materials science. *Ultramicroscopy* **160**, 23–34 (2016).
223. Kak, A. C. & Slaney, M. *Principles of Computerized Tomographic Imaging*. (Society for Industrial and Applied Mathematics, 2001). doi:10.1137/1.9780898719277.

- 
224. Leary, R., Saghi, Z., Midgley, P. A. & Holland, D. J. Compressed sensing electron tomography. *Ultramicroscopy* **131**, 70–91 (2013).
225. Bouman, C. A. *Model Based Imaging*. (2013).
226. Goris, B., Van den Broek, W., Batenburg, K. J., Heidari Mezerji, H. & Bals, S. Electron tomography based on a total variation minimization reconstruction technique. *Ultramicroscopy* **113**, 120–130 (2012).
227. Saghi, Z. *et al.* Three-Dimensional Morphology of Iron Oxide Nanoparticles with Reactive Concave Surfaces. A Compressed Sensing-Electron Tomography (CS-ET) Approach. *Nano Lett.* **11**, 4666–4673 (2011).
228. Venkatakrisnan, S. V. *et al.* A Model Based Iterative Reconstruction Algorithm For High Angle Annular Dark Field-Scanning Transmission Electron Microscope (HAADF-STEM) Tomography. *IEEE Transactions on Image Processing* **22**, 4532–4544 (2013).
229. Van den Broek, W., Van Aert, S. & Van Dyck, D. A model based atomic resolution tomographic algorithm. *Ultramicroscopy* **109**, 1485–1490 (2009).
230. Venkatakrisnan, S. V. *et al.* Model-Based Iterative Reconstruction for Bright-Field Electron Tomography. *IEEE Transactions on Computational Imaging* **1**, 1–15 (2015).
231. Ren, D., Ophus, C., Chen, M. & Waller, L. A multiple scattering algorithm for three dimensional phase contrast atomic electron tomography. *Ultramicroscopy* **208**, 112860 (2020).
232. Crowther, R. A., DeRosier, D. J. & Klug, A. The reconstruction of a three-dimensional structure from projections and its application to electron microscopy. *Proc. R. Soc. Lond. A* **317**, 319–340 (1970).
233. van Heel, M. & Schatz, M. Fourier shell correlation threshold criteria. *Journal of Structural Biology* **151**, 250–262 (2005).
234. Chen, D., Friedrich, H. & With, G. de. On Resolution in Electron Tomography of Beam Sensitive Materials. *J. Phys. Chem. C* **118**, 1248–1257 (2014).
235. Hasinoff, S. W. Photon, Poisson Noise. in *Computer Vision: A Reference Guide* (ed. Ikeuchi, K.) 608–610 (Springer US, 2014). doi:10.1007/978-0-387-31439-6\_482.
236. Russ, J. C. & Neal, F. B. *The Image Processing Handbook*.
237. Mevenkamp, N. *et al.* Poisson noise removal from high-resolution STEM images based on periodic block matching. *Adv Struct Chem Imag* **1**, 3 (2015).
238. Dabov, K., Foi, A., Katkovnik, V. & Egiazarian, K. Image Denoising by Sparse 3-D Transform-Domain Collaborative Filtering. *IEEE Transactions on Image Processing* **16**, 2080–2095 (2007).
239. Strong, D. & Chan, T. Edge-preserving and scale-dependent properties of total variation regularization. *Inverse Problems* **19**, S165–S187 (2003).
240. Domingos, P. A few useful things to know about machine learning. *Commun. ACM* **55**, 78–87 (2012).
241. Moen, E. *et al.* Deep learning for cellular image analysis. *Nat Methods* **16**, 1233–1246 (2019).



242. Nichols, J. A., Herbert Chan, H. W. & Baker, M. A. B. Machine learning: applications of artificial intelligence to imaging and diagnosis. *Biophys Rev* **11**, 111–118 (2019).
243. Ronneberger, O., Fischer, P. & Brox, T. U-Net: Convolutional Networks for Biomedical Image Segmentation. *arXiv:1505.04597* (2015).
244. Weigert, M. *et al.* Content-aware image restoration: pushing the limits of fluorescence microscopy. *Nat Methods* **15**, 1090–1097 (2018).
245. Belthangady, C. & Royer, L. A. Applications, promises, and pitfalls of deep learning for fluorescence image reconstruction. *Nat Methods* **16**, 1215–1225 (2019).
246. Lehtinen, J. *et al.* Noise2Noise: Learning Image Restoration without Clean Data. *arxiv.org:1803.04189* (2018).
247. Krull, A., Buchholz, T.-O. & Jug, F. Noise2Void - Learning Denoising from Single Noisy Images. *arXiv:1811.10980* (2019).
248. Buchholz, T.-O., Jordan, M., Pigino, G. & Jug, F. Cryo-CARE: Content-Aware Image Restoration for Cryo-Transmission Electron Microscopy Data. in *2019 IEEE 16th International Symposium on Biomedical Imaging (ISBI 2019)* 502–506 (2019). doi:10.1109/ISBI.2019.8759519.
249. Laine, R. F., Arganda-Carreras, I., Henriques, R. & Jacquemet, G. Avoiding a replication crisis in deep-learning-based bioimage analysis. *Nat Methods* **18**, 1136–1144 (2021).
250. Zhu, X. & Milanfar, P. Automatic Parameter Selection for Denoising Algorithms Using a No-Reference Measure of Image Content. *IEEE Transactions on Image Processing* **19**, 3116–3132 (2010).
251. Otsu, N. A Threshold Selection Method from Gray-Level Histograms. *IEEE transactions on systems, man, and cybernetics* **9**, 62–66 (1979).
252. Leary, R. *et al.* Quantitative High-Angle Annular Dark-Field Scanning Transmission Electron Microscope (HAADF-STEM) Tomography and High-Resolution Electron Microscopy of Unsupported Intermetallic GaPd<sub>2</sub> Catalysts. *J. Phys. Chem. C* **116**, 13343–13352 (2012).
253. Arganda-Carreras, I. *et al.* Trainable Weka Segmentation: a machine learning tool for microscopy pixel classification. *Bioinformatics* **33**, 2424–2426 (2017).
254. Falk, T. *et al.* U-Net: deep learning for cell counting, detection, and morphometry. *Nat Methods* **16**, 67–70 (2019).
255. Müller, S. *et al.* Deep learning-based segmentation of lithium-ion battery microstructures enhanced by artificially generated electrodes. *Nat Commun* **12**, 6205 (2021).
256. Taha, A. A. & Hanbury, A. Metrics for evaluating 3D medical image segmentation: analysis, selection, and tool. *BMC Med Imaging* **15**, 29 (2015).
257. Cullen, D. A., Sneed, B. T. & More, K. L. Overcoming the Challenges of Beam-sensitivity in Fuel Cell Electrodes. *Microscopy and Microanalysis* **23**, 2222–2223 (2017).

- 
258. Guetaz, L. *et al.* Catalyst-Layer Ionomer Imaging of Fuel Cells. *ECS Trans.* **69**, 455–464 (2015).
259. Fang, Z., Lee, M. S., Kim, J. Y., Kim, J. H. & Fuller, T. F. The Effect of Carbon Support Surface Functionalization on PEM Fuel Cell Performance, Durability, and Ionomer Coverage in the Catalyst Layer. *J. Electrochem. Soc.* **167**, 064506 (2020).
260. Blom, D. A., Dunlap, J. R., Nolan, T. A. & Allard, L. F. Preparation of Cross-Sectional Samples of Proton Exchange Membrane Fuel Cells by Ultramicrotomy for TEM. *J. Electrochem. Soc.* **150**, A414–A418 (2003).
261. Zheng, S. Q. *et al.* MotionCor2: anisotropic correction of beam-induced motion for improved cryo-electron microscopy. *Nat Methods* **14**, 331–332 (2017).
262. Schindelin, J. *et al.* Fiji: an open-source platform for biological-image analysis. *Nat Methods* **9**, 676–682 (2012).
263. Schneider, C. A., Rasband, W. S. & Eliceiri, K. W. NIH Image to ImageJ: 25 years of image analysis. *Nat Methods* **9**, 671–675 (2012).
264. Levin, B. D. A. *et al.* Tutorial on the Visualization of Volumetric Data Using tomviz. *Microscopy Today* **26**, 12–17 (2018).
265. van Aarle, W. *et al.* The ASTRA Toolbox: A platform for advanced algorithm development in electron tomography. *Ultramicroscopy* **157**, 35–47 (2015).
266. Palenstijn, W. J., Batenburg, K. J. & Sijbers, J. Performance improvements for iterative electron tomography reconstruction using graphics processing units (GPUs). *Journal of Structural Biology* **176**, 250–253 (2011).
267. Buchholz, T.-O. *et al.* Content-aware image restoration for electron microscopy. in *Methods in Cell Biology* (eds. Müller-Reichert, T. & Pigino, G.) vol. 152 277–289 (Academic Press, 2019).
268. Cryo-CARE: Content-Aware Image Restoration for Cryo-Transmission Electron Microscopy Data. [https://github.com/juglab/cryoCARE\\_T2T](https://github.com/juglab/cryoCARE_T2T) (2021).
269. YAPiC - Yet Another Pixel Classifier (based on deep learning). <https://yapic.github.io/yapic/>.
270. Bankhead, P. *et al.* QuPath: Open source software for digital pathology image analysis. *Sci Rep* **7**, 16878 (2017).
271. Image Science - FSC program. <https://imagescience.de/fsc.html>.
272. Legland, D., Arganda-Carreras, I. & Andrey, P. MorphoLibJ: integrated library and plugins for mathematical morphology with ImageJ. *Bioinformatics* **32**, 3532–3534 (2016).
273. Domander, R., Felder, A. A. & Doube, M. BoneJ2 - refactoring established research software. *Wellcome Open Research* **6**, 37 (2021).
274. Doube, M. Multithreaded two-pass connected components labelling and particle analysis in ImageJ. *Royal Society Open Science* **8**, 201784.
275. Gostick, J. T. *et al.* PoreSpy: A Python Toolkit for Quantitative Analysis of Porous Media Images. *Journal of Open Source Software* **4**, 1296 (2019).
276. Sawyer, L., Grubb, D. T. & Meyers, G. F. *Polymer Microscopy*. (Springer Science & Business Media, 2008).

277. Hildebrand, T. & Rügsegger, P. A new method for the model-independent assessment of thickness in three-dimensional images. *Journal of Microscopy* **185**, 67–75 (1997).
278. More, K., Borup, R. & Reeves, K. Identifying Contributing Degradation Phenomena in PEM Fuel Cell Membrane Electrode Assemblies Via Electron Microscopy. *ECS Trans.* **3**, 717–733 (2006).
279. Poojary, S., Islam, M. N., Shrivastava, U. N., Roberts, E. P. L. & Karan, K. Transport and Electrochemical Interface Properties of Ionomers in Low-Pt Loading Catalyst Layers: Effect of Ionomer Equivalent Weight and Relative Humidity. *Molecules* **25**, 3387 (2020).
280. Sinha, P. K., Gu, W., Kongkanand, A. & Thompson, E. Performance of Nano Structured Thin Film (NSTF) Electrodes under Partially-Humidified Conditions. *J. Electrochem. Soc.* **158**, B831 (2011).
281. Sui, S. *et al.* A comprehensive review of Pt electrocatalysts for the oxygen reduction reaction: Nanostructure, activity, mechanism and carbon support in PEM fuel cells. *J. Mater. Chem. A* **5**, 1808–1825 (2017).
282. Castanheira, L. *et al.* Carbon Corrosion in Proton-Exchange Membrane Fuel Cells: Effect of the Carbon Structure, the Degradation Protocol, and the Gas Atmosphere. *ACS Catal.* **5**, 2184–2194 (2015).
283. Hara, M. *et al.* Electrochemical and Raman spectroscopic evaluation of Pt/graphitized carbon black catalyst durability for the start/stop operating condition of polymer electrolyte fuel cells. *Electrochimica Acta* **70**, 171–181 (2012).
284. Harris, P. Transmission Electron Microscopy of Carbon: A Brief History. *C* **4**, 4 (2018).
285. Heidenreich, R. D., Hess, W. M. & Ban, L. L. A test object and criteria for high resolution electron microscopy. *J Appl Crystallogr* **1**, 1–19 (1968).
286. Apicella, B. *et al.* Soot nanostructure evolution in premixed flames by High Resolution Electron Transmission Microscopy (HRTEM). *Proceedings of the Combustion Institute* **35**, 1895–1902 (2015).
287. Huang, X., Tang, Y., Kübel, C. & Wang, D. Precisely Picking Nanoparticles by a “Nano-Scalpel” for 360° Electron Tomography. *Microsc Microanal* **28**, 1981–1988 (2022).
288. Ju, B.-F., Chen, Y.-L. & Ge, Y. The art of electrochemical etching for preparing tungsten probes with controllable tip profile and characteristic parameters. *Review of Scientific Instruments* **82**, 013707 (2011).
289. Berg, S. *et al.* ilastik: interactive machine learning for (bio)image analysis. *Nat Methods* **16**, 1226–1232 (2019).
290. Weyland, M. & Midgley, P. A. Chapter 6. Electron Tomography. in *Nanoscience & Nanotechnology Series* (eds Kirkland, A. I. & Haigh, S. J.) 211–299 (Royal Society of Chemistry, 2015). doi:10.1039/9781782621867-00211.
291. Przybilla, T. *et al.* Transfer of Individual Micro- and Nanoparticles for High-Precision 3D Analysis Using 360° Electron Tomography. *Small Methods* **2**, 1700276 (2018).

- 
292. Harris, P. J. F. New Perspectives on the Structure of Graphitic Carbons. *Critical Reviews in Solid State and Materials Sciences* **30**, 235–253 (2005).
293. Andreev, Y. G. & Bruce, P. G. Size and shape of graphene layers in commercial carbon blacks established by Debye refinement. *J Appl Crystallogr* **49**, 24–30 (2016).
294. Kikkawa, N. & Jinnouchi, R. Does an Ionomer Penetrate a Carbon Mesopore? Free-Energy Analysis Using Molecular Dynamics Simulations. *J. Phys. Chem. C* **126**, 11518–11528 (2022).
295. Cherevko, S., Kulyk, N. & Mayrhofer, K. J. J. Durability of platinum-based fuel cell electrocatalysts: Dissolution of bulk and nanoscale platinum. *Nano Energy* **29**, 275–298 (2016).
296. Ehelebe, K. *et al.* Platinum Dissolution in Realistic Fuel Cell Catalyst Layers. *Angewandte Chemie* **133**, 8964–8970 (2021).
297. Meier, J. C. *et al.* Design criteria for stable Pt/C fuel cell catalysts. *Beilstein J. Nanotechnol.* **5**, 44–67 (2014).
298. Hodnik, N., Dehm, G. & Mayrhofer, K. J. J. Importance and Challenges of Electrochemical in Situ Liquid Cell Electron Microscopy for Energy Conversion Research. *Accounts of Chemical Research* **49**, 2015–2022 (2016).
299. Dubau, L., Castanheira, L., Berthomé, G. & Maillard, F. An identical-location transmission electron microscopy study on the degradation of Pt/C nanoparticles under oxidizing, reducing and neutral atmosphere. *Electrochimica Acta* **110**, 273–281 (2013).
300. Mayrhofer, K. J. J. *et al.* Fuel cell catalyst degradation on the nanoscale. *Electrochemistry Communications* **10**, 1144–1147 (2008).
301. Soleymani, A. P., Parent, L. R. & Jankovic, J. Challenges and Opportunities in Understanding Proton Exchange Membrane Fuel Cell Materials Degradation Using In-Situ Electrochemical Liquid Cell Transmission Electron Microscopy. *Advanced Functional Materials* 2105188 (2021) doi:10.1002/adfm.202105188.
302. Nagashima, S. *et al.* Atomic-Level Observation of Electrochemical Platinum Dissolution and Redeposition. *Nano Letters* **19**, 7000–7005 (2019).
303. Zhu, G. Z. *et al.* In situ liquid cell TEM study of morphological evolution and degradation of Pt-Fe nanocatalysts during potential cycling. *Journal of Physical Chemistry C* **118**, 22111–22119 (2014).
304. Beermann, V. *et al.* Real-time imaging of activation and degradation of carbon supported octahedral Pt-Ni alloy fuel cell catalysts at the nanoscale using: In situ electrochemical liquid cell STEM. *Energy and Environmental Science* **12**, 2476–2485 (2019).
305. Guntern, Y. T. *et al.* Colloidal Nanocrystals as Electrocatalysts with Tunable Activity and Selectivity. *ACS Catal.* **11**, 1248–1295 (2021).
306. Vavra, J., Shen, T.-H., Stoian, D., Tileli, V. & Buonsanti, R. Real-time Monitoring Reveals Dissolution/Redeposition Mechanism in Copper Nanocatalysts during the Initial Stages of the CO<sub>2</sub> Reduction Reaction. *Angewandte Chemie* **133**, 1367–1374 (2021).
307. Vávra, J. Monitoring and understanding Cu catalyst dissolution. (EPFL, 2022).

308. Shen, T.-H. Electron probing of oxygen-evolving oxide catalysts. (EPFL, 2022).
309. Imokawa, T., Williams, K.-J. & Denuault, G. Fabrication and Characterization of Nanostructured Pd Hydride pH Microelectrodes. *Anal. Chem.* **78**, 265–271 (2006).
310. Luisier, F., Vonesch, C., Blu, T. & Unser, M. Fast interscale wavelet denoising of Poisson-corrupted images. *Signal Processing* **90**, 415–427 (2010).
311. Benck, J. D., Pinaud, B. A., Gorlin, Y. & Jaramillo, T. F. Substrate selection for fundamental studies of electrocatalysts and photoelectrodes: Inert potential windows in acidic, neutral, and basic electrolyte. *PLoS ONE* **9**, (2014).
312. Malinský, P., Slepíčka, P., Hnatowicz, V. & Švorčík, V. Early stages of growth of gold layers sputter deposited on glass and silicon substrates. *Nanoscale Research Letters* **7**, 241 (2012).
313. Brug, G. J., Sluyters-Rehbach, M., Sluyters, J. H. & Hemelin, A. The kinetics of the reduction of protons at polycrystalline and monocrystalline gold electrodes. *Journal of Electroanalytical Chemistry and Interfacial Electrochemistry* **181**, 245–266 (1984).
314. Henning, S., Herranz, J. & Gasteiger, H. A. Bulk-Palladium and Palladium-on-Gold Electrocatalysts for the Oxidation of Hydrogen in Alkaline Electrolyte. *J. Electrochem. Soc.* **162**, F178 (2014).
315. Jacobse, L., Raaijman, S. J. & Koper, M. T. M. The reactivity of platinum microelectrodes. *Phys. Chem. Chem. Phys.* **18**, 28451–28457 (2016).
316. Daubinger, P., Kieninger, J., Unmüssig, T. & Urban, G. A. Electrochemical characteristics of nanostructured platinum electrodes-A cyclic voltammetry study. *Physical Chemistry Chemical Physics* **16**, 8392–8399 (2014).
317. Cherevko, S., Zeradjanin, A. R., Keeley, G. P. & Mayrhofer, K. J. J. A Comparative Study on Gold and Platinum Dissolution in Acidic and Alkaline Media. *J. Electrochem. Soc.* **161**, H822 (2014).
318. Schneider, N. M. *et al.* Electron-Water interactions and implications for liquid cell electron microscopy. *Journal of Physical Chemistry C* **118**, 22373–22382 (2014).
319. Greeley, J., Jaramillo, T. F., Bonde, J., Chorkendorff, I. & Nørskov, J. K. Computational high-throughput screening of electrocatalytic materials for hydrogen evolution. *Nature Materials* **5**, 909–913 (2006).
320. Nørskov, J. K. *et al.* Trends in the Exchange Current for Hydrogen Evolution. *J. Electrochem. Soc.* **152**, J23 (2005).
321. Reier, T., Oezaslan, M. & Strasser, P. Electrocatalytic oxygen evolution reaction (OER) on Ru, Ir, and Pt catalysts: A comparative study of nanoparticles and bulk materials. *ACS Catalysis* **2**, 1765–1772 (2012).
322. Damjanovic, A. & Jovanovic, B. Anodic Oxide Films as Barriers to Charge Transfer in O<sub>2</sub> Evolution at Pt in Acid Solutions. *J. Electrochem. Soc.* **123**, 374 (1976).
323. Birss, V. I. & Damjanovic, A. Oxygen Evolution at Platinum Electrodes in Alkaline Solutions: I. Dependence on Solution pH and Oxide Film Thickness. *Journal of The Electrochemical Society* **134**, 113–117 (1987).

- 
324. Van der Linden, W. E. & Dieker, J. W. Glassy carbon as electrode material in electro- analytical chemistry. *Analytica Chimica Acta* **119**, 1–24 (1980).
325. Hassan, Y. M. *et al.* High temperature SU-8 pyrolysis for fabrication of carbon electrodes. *Journal of Analytical and Applied Pyrolysis* **125**, 91–99 (2017).
326. Zittel, H. E. & Miller, F. J. A Glassy-Carbon Electrode for Voltammetry. *Anal. Chem.* **37**, 200–203 (1965).
327. Wei, C. *et al.* Recommended Practices and Benchmark Activity for Hydrogen and Oxygen Electrocatalysis in Water Splitting and Fuel Cells. *Advanced Materials* **1806296**, 1–24 (2019).
328. Wightman, R. M., Deakin, M. R., Kovach, P. M., Kuhr, W. G. & Stutts, K. J. Methods to Improve Electrochemical Reversibility at Carbon Electrodes. *J. Electrochem. Soc.* **131**, 1578–1583 (1984).
329. Engstrom, R. C. Electrochemical pretreatment of glassy carbon electrodes. *Analytical Chemistry* **54**, 2310–2314 (1982).
330. Girod, R., Nianias, N. & Tileli, V. Electrochemical Behavior of Carbon Electrodes for In Situ Redox Studies in a Transmission Electron Microscope. *Microscopy and Microanalysis* **25**, 1304–1310 (2019).
331. Holtz, M. E. *et al.* Nanoscale Imaging of Lithium Ion Distribution During In Situ Operation of Battery Electrode and Electrolyte. *Nano Letters* **14**, 1453–1459 (2014).
332. Impagnatiello, A. *et al.* Degradation Mechanisms of Supported Pt Nanocatalysts in Proton Exchange Membrane Fuel Cells: An Operando Study through Liquid Cell Transmission Electron Microscopy. *ACS Appl. Energy Mater.* **3**, 2360–2371 (2020).
333. Guth, U., Gerlach, F., Decker, M., Oelßner, W. & Vonau, W. Solid-state reference electrodes for potentiometric sensors. *J Solid State Electrochem* **13**, 27–39 (2009).
334. *Handbook of Reference Electrodes.* (Springer, 2013). doi:10.1007/978-3-642-36188-3.
335. Alnoush, W., Black, R. & Higgins, D. Judicious selection, validation, and use of reference electrodes for in situ and operando electrocatalysis studies. *Chem Catalysis* (2021) doi:10.1016/j.cheecat.2021.07.001.
336. Shinwari, M. W. *et al.* Microfabricated Reference Electrodes and their Biosensing Applications. *Sensors* **10**, 1679–1715 (2010).
337. Sawyer, D. T., Sobkowiak, A., Roberts, J. L. & Sawyer, D. T. *Electrochemistry for chemists.* (Wiley, 1995).
338. Jerkiewicz, G. Standard and Reversible Hydrogen Electrodes: Theory, Design, Operation, and Applications. *ACS Catal.* **10**, 8409–8417 (2020).
339. Solchenbach, S., Pritzl, D., Kong, E. J. Y., Landesfeind, J. & Gasteiger, H. A. A Gold Micro-Reference Electrode for Impedance and Potential Measurements in Lithium Ion Batteries. *J. Electrochem. Soc.* **163**, A2265–A2272 (2016).
340. Hou, J. *et al.* Lithium-Gold Reference Electrode for Potential Stability During In Situ Electron Microscopy Studies of Lithium-Ion Batteries. *J. Electrochem. Soc.* **167**, 110515 (2020).

341. Xu, K., Kitazumi, Y., Kano, K. & Shirai, O. Electrochemical pH sensor based on a hydrogen-storage palladium electrode with Teflon covering to increase stability. *Electrochemistry Communications* **101**, 73–77 (2019).
342. Manchester, F. D., San-Martin, A. & Pitre, J. M. The H-Pd (hydrogen-palladium) System. *JPE* **15**, 62–83 (1994).
343. Castellan, G. W., Hoare, J. P. & Schuldiner, S. Electrochemical Behavior of the Palladium-Hydrogen System. II. Thermodynamic Considerations. *The Journal of Chemical Physics* **28**, 20–21 (1958).
344. Ghilane, J., Hapiot, P. & Bard, A. J. Metal/Polypyrrole Quasi-Reference Electrode for Voltammetry in Nonaqueous and Aqueous Solutions. *Anal. Chem.* **78**, 6868–6872 (2006).
345. Park, S. *et al.* pH-Sensitive Solid-State Electrode Based on Electrodeposited Nanoporous Platinum. *Anal. Chem.* **77**, 7695–7701 (2005).
346. Lim, J. *et al.* Origin and hysteresis of lithium compositional spatiodynamics within battery primary particles. *Science* **353**, 566–571 (2016).
347. Unocic, R. R. *et al.* Direct Visualization of Solid Electrolyte Interphase Formation in Lithium-Ion Batteries with In Situ Electrochemical Transmission Electron Microscopy. *Microscopy and Microanalysis* **20**, 1029–1037 (2014).
348. Chen, J. G., Jones, C. W., Linic, S. & Stamenkovic, V. R. Best Practices in Pursuit of Topics in Heterogeneous Electrocatalysis. *ACS Catal.* **7**, 6392–6393 (2017).
349. Yu, Y. *et al.* A review on performance degradation of proton exchange membrane fuel cells during startup and shutdown processes: Causes, consequences, and mitigation strategies. *Journal of Power Sources* **205**, 10–23 (2012).
350. Korpanty, J., Parent, L. R. & Gianneschi, N. C. Enhancing and Mitigating Radiolytic Damage to Soft Matter in Aqueous Phase Liquid-Cell Transmission Electron Microscopy in the Presence of Gold Nanoparticle Sensitizers or Isopropanol Scavengers. *Nano Lett.* **21**, 1141–1149 (2021).
351. Woehl, T. J. & Abellan, P. Defining the radiation chemistry during liquid cell electron microscopy to enable visualization of nanomaterial growth and degradation dynamics. *Journal of Microscopy* **265**, 135–147 (2017).
352. Shrestha, B. R., Tada, E. & Nishikata, A. Effect of Chloride on Platinum Dissolution. *Electrochimica Acta* **143**, 161–167 (2014).
353. Geiger, S., Cherevko, S. & Mayrhofer, K. J. J. Dissolution of Platinum in Presence of Chloride Traces. *Electrochimica Acta* **179**, 24–31 (2015).
354. Bozzetti, M. *et al.* On the role of pore constrictions in gas diffusion electrodes. *Chemical Communications* **58**, 8854–8857 (2022).
355. Odstrcil, M. *et al.* Ab initio nonrigid X-ray nanotomography. *Nat Commun* **10**, 2600 (2019).
356. Printemps, T., Bernier, N., Bleuet, P., Mula, G. & Hervé, L. Non-rigid alignment in electron tomography in materials science. *Journal of Microscopy* **263**, 312–319 (2016).

- 
357. Jones, L. *et al.* Smart Align—a new tool for robust non-rigid registration of scanning microscope data. *Advanced Structural and Chemical Imaging* **1**, 8 (2015).
358. Roiban, L. *et al.* Fast ‘Operando’ electron nanotomography. *Journal of Microscopy* **269**, 117–126 (2018).
359. Koneti, S. *et al.* Fast electron tomography: Applications to beam sensitive samples and in situ TEM or operando environmental TEM studies. *Materials Characterization* **151**, 480–495 (2019).
360. Kwon, O.-H. & Zewail, A. H. 4D Electron Tomography. *Science* **328**, 1668–1673 (2010).
361. Park, J. *et al.* 3D structure of individual nanocrystals in solution by electron microscopy. *Science* **349**, 290–295 (2015).
362. Zhou, J. *et al.* Observing crystal nucleation in four dimensions using atomic electron tomography. *Nature* **570**, 500–503 (2019).
363. Casablanca, J. G. & Nicolopoulos, S. Devices and Methods for High Angle Liquid Electron Tomography.
364. Das, P. P. *et al.* High Angle Liquid Cell TEM Tomography for In Situ Observation and 3D Reconstruction in Liquid. *Microscopy and Microanalysis* **28**, 854–856 (2022).
365. Xue, T., Trent, J. S. & Osseo-Asare, K. Characterization of nafion® membranes by transmission electron microscopy. *Journal of Membrane Science* **45**, 261–271 (1989).
366. Iden, H., Sato, K., Ohma, A. & Shinohara, K. Relationship among Microstructure, Ionomer Property and Proton Transport in Pseudo Catalyst Layers. *J. Electrochem. Soc.* **158**, B987 (2011).
367. Mäkinen, Y., Azzari, L. & Foi, A. Collaborative Filtering of Correlated Noise: Exact Transform-Domain Variance for Improved Shrinkage and Patch Matching. *IEEE Transactions on Image Processing* **29**, 8339–8354 (2020).
368. García-Cruz, L., Montiel, V. & Solla-Gullón, J. Shape-controlled metal nanoparticles for electrocatalytic applications. *Physical Sciences Reviews* **4**, (2019).
369. Arán-Ais, R. M., Solla-Gullón, J., Herrero, E. & Feliu, J. M. On the quality and stability of preferentially oriented (100) Pt nanoparticles: An electrochemical insight. *Journal of Electroanalytical Chemistry* **808**, 433–438 (2018).



# Curriculum Vitae

Chemin des Avelines, 1  
1004 Lausanne, SWITZERLAND

robin.girod@epfl.ch  
+41 78 855 70 80

## RESEARCH INTERESTS

Energy materials and sustainability, electron tomography, *in situ* electrochemical microscopy

## EDUCATION

Since 2018 **PhD candidate in materials science**, École Polytechnique Fédérale de Lausanne (EPFL), Switzerland. Graduation expected in spring 2023

Dissertation: “Multidimensional Electron Imaging of Catalyst Layer Materials”

Supervised by Prof. Vasiliki Tileli

2018 **MSc in chemistry and chemical engineering**, Lyon School of Chemistry, Physics and Electronic (CPE Lyon), France

Modules spanned from analytical and organic chemistry to process engineering. Final year included an exchange semester at EPFL

Dissertation: “Towards *in-situ* transmission electron microscopy visualisation of nano-electrocatalysts degradation during CO<sub>2</sub> reduction reaction”

Supervised by Prof. Vasiliki Tileli, Institute of Materials, EPFL, Switzerland

2015 **BSc in chemistry and chemical engineering**, Lyon School of Chemistry, Physics and Electronic (CPE Lyon), France

## RESEARCH AND PROFESSIONAL EXPERIENCE

Since 2018 **Doctoral researcher**, Institute of Materials, EPFL, Switzerland

- Develop methods and design experiments to probe fuel cell materials with electron microscopy and understand their morphology and degradation pathways
- Research and implement advanced data processing and analysis tools, making them available to colleagues
- Collaborate in an inter-disciplinary project to improve conventional and PGM-free fuel cell performance

Feb.-Aug. 2018 **Master thesis work**, Institute of Materials, EPFL, Switzerland

- Developed and implemented knowledge of the apparatus for *in situ* electrochemical electron microscopy
- Designed and conducted experiments to understand the behaviour of micro-scale carbon electrodes towards their use for CO<sub>2</sub> reduction in an electron microscope

Jul. 2016-Jul. 2017 **Gap year microscopy laboratory intern**, Analytical Service, Technology, and Innovation Department, SABIC, Netherlands

- Performed characterization by atomic force microscopy (AFM) to support research and innovation projects
- Implemented new AFM operation modes to improve the analytical capabilities of the laboratory

Jul.-Aug. 2015 **Laboratory technician and assistant to safety engineer**, Henkel Technologies, France

- Performed routine quality control of industrial adhesive production
- Updated the chemical hazard classification of the production plant

## TEACHING ACTIVITIES

Since 2020 **Supervision of laboratory semester projects**

- Supervised undergraduate and graduate students in conducting weekly experiments, analyzing data and scientific reporting

Spring 2022: Viollet, A. “Optimization of sample preparation for full range electron tomography”

Spring 2021: Gonçalves Coelho, M. “Denoising of electron microscopy images”

Fall 2020: Liu, G.-Y. “Deep learning for electron microscopy image segmentation”

Spring 2020: Simon Greminger, J. “Training of a model for content-aware restoration of electron microscopy images”

Since 2019 **Teaching assistant**, EPFL MSE-477 Nanomaterials, 3 ECTS master course taught yearly

- Helped with lectures preparation on nanomaterial synthesis, nanobiotechnologies and nanomagnetism
- Supervised and assisted students during group projects aiming at developing a research plan involving nanomaterials
- Participated in creating and grading course examination

## PUBLICATIONS

Ünsal, S.; Bozzetti, M.; Yen-Chun, C.; **Girod, R.**; Berger, A.; Diercks, J.S.; Gialamoidou, S.; Clark, A.H.; Lyu, J.; Medarde, M.; Gasteiger, H.A.; Büchi, F.; Tileli, V.; Schmidt, T.J.; Herranz, J. Effect of Catalyst Aggregate Size on the Mass Transport Properties of Non-Noble Metal Catalyst Layers in PEMFC Cathodes. *Under Review* **2023**.

**Girod, R.**; Shen, T.-H.; Vavra, J.; Tileli, V. Considerations for Liquid Phase Transmission Electron Microscopy Applied to Electrocatalysis. *J. Electrochem. Soc.* **2023**, *170* (5), 056502.

**Girod, R.**; Lazaridis, T.; Gasteiger, H.; Tileli, V. Three-Dimensional Nanoimaging of Catalyst Layers. *Nat. Cat.* **2023**, 1-9.

Ünsal, S.; **Girod, R.**; Appel, C.; Karpov, D.; Mermoux, M.; Maillard, F.; Saveleva, V.A.; Tileli, V.; Schmidt, T.J.; Herranz, J. Decoupling the Contributions of Different Instability Mechanisms to the PEMFC Performance Decay of Non-noble Metal O<sub>2</sub>-reduction Catalysts. *J. Am. Chem. Soc.* **2023**, *145* (14), 7845-7858.

Bozzetti, M.; Berger, A.; **Girod, R.**; Chen, Y.-C.; Büchi, F.; Gasteiger, H.; Tileli, V. On the Role of Pore Constrictions in Gas Diffusion Electrodes. *Chem. Commun.* **2022**, *58* (63), 8854-8857.

Hou, J.; **Girod, R.**; Nianias, N.; Shen, T.-H.; Fan, J.; Tileli, V. Lithium-Gold Reference Electrode for Potential Stability During In Situ Electron Microscopy Studies of Lithium-Ion Batteries. *J. Electrochem. Soc.* **2020**, *167* (11), 110515.

Hou, J.; Freiberg, A.; Shen, T.-H.; **Girod, R.**; Gonthier, J.; Kim, S.-J.; Maglia, F.; Gasteiger, H. A.; Tileli, V. Charge/Discharge Cycling of Li<sub>1+x</sub>(Ni<sub>0.6</sub>Co<sub>0.2</sub>Mn<sub>0.2</sub>)<sub>1-x</sub>O<sub>2</sub> Primary Particles Performed in a Liquid Microcell for Transmission Electron Microscopy Studies. *J. Phys. Energy* **2020**, *2* (3), 034007.

**Girod, R.**; Nianias, N.; Tileli, V. Electrochemical Behavior of Carbon Electrodes for In Situ Redox Studies in a Transmission Electron Microscope. *Microscopy and Microanalysis* **2019**, *25* (6), 1304–1310.

Cancelas, A. J.; Yang, L.; **Girod, R.**; de Heer, J.; Kleppinger, R.; Delsman, E.; Wang, J.; Gahleitner, M.; Monteil, V.; McKenna, T. F. L. The Effect of Reactor Conditions on High-Impact Polypropylene Properties and Gas Phase Polymerization Kinetics. *Macromolecular Reaction Engineering* **2018**, *12* (4), 1700063.

## POSTERS AND PRESENTATIONS

**Girod, R.**; Toleukhanova, S.; Tileli, V. Advanced denoising methods for electrocatalyst studies with electrochemical liquid phase TEM. Poster presented at *Microscopy Conference 2023*, Feb. 28-Mar. 2, **2023**

**Girod, R.**; Lazaridis, T.; Gasteiger, H.; Tileli, V. Cryo-Electron Tomography for Imaging and Quantitative Analysis of Beam-Sensitive Fuel Cell Materials. Platform presentation given at *Microscopy & Microanalysis 2022*, Jul. 31-Aug. 4, **2022**.

**Girod, R.**; Lazaridis, T.; Gasteiger, H.; Tileli, V. Probing Ionomer Coverage in Proton Exchange Membrane Fuel Cell with Cryo-Electron Tomography and Advanced Image Processing Methods. Poster presented at *Microscopy Conference 2021*, Aug. 22-26, **2021**

## TECHNICAL SKILLS AND LANGUAGES

Languages **French:** native speaker  
**English:** professionally operational, Cambridge C2 Proficiency obtained

Scientific Instrumentation and Techniques **Transmission Electron Microscopy:** TFS (F20, Osiris, Talos, double-corrected Titan Themis) and JEOL (2200FS) instruments and S/TEM, HRTEM, EDS, tomography, cryo-transfer, ultra-microtomy, *in situ* electrochemical microscopy (Hummingbird) techniques  
**Scanning Electron Microscopy:** imaging and EDS with Zeiss and TFS instruments

**Atomic Force Microscopy:** Tapping, quantitative nanomechanical mapping and tunnelling AFM modes with Bruker instruments

**Electrochemical analysis:** potentiodynamic and potentiostatic techniques

IT **Microsoft Office** (Word, Excel, Power Point)

**Python 3:** scientific computing (scipy, numpy), image processing and analysis (sci-kit image, porespy), machine learning (sci-kit learn, keras, tensorflow, ODL) and TEM data processing (hyperspy, ASTRA) libraries

**FIJI / ImageJ, Origin 9.5, EC-Lab V11**

Other Management of disabled persons in the work environment: part of a training program organised by Sopra Group and ADAPT

Afterschool lessons to young students with disabilities and difficulties in school